

Durham E-Theses

Structural evolution of the Nam Con Son Basin: quantitative fault analysis applied to a 3-simensional seismic dataset

Pugh, Adam

How to cite:

Pugh, Adam (2007) Structural evolution of the Nam Con Son Basin: quantitative fault analysis applied to a 3-simensional seismic dataset, Durham theses, Durham University. Available at Durham E-Theses Online: http://etheses.dur.ac.uk/2497/

Use policy

The full-text may be used and/or reproduced, and given to third parties in any format or medium, without prior permission or charge, for personal research or study, educational, or not-for-profit purposes provided that:

- ullet a full bibliographic reference is made to the original source
- a link is made to the metadata record in Durham E-Theses
- the full-text is not changed in any way

The full-text must not be sold in any format or medium without the formal permission of the copyright holders.

Please consult the full Durham E-Theses policy for further details.

STRUCTURAL EVOLUTION OF THE NAM CON SON BASIN: QUANTITATIVE FAULT ANALYSIS APPLIED TO A 3-DIMENSIONAL SEISMIC DATASET

by Adam Pugh

The copyright of this thesis rests with the author or the university to which it was submitted. No quotation from it, or information derived from it may be published without the prior written consent of the author or university, and any information derived from it should be acknowledged.

A thesis submitted for the degree of Doctor of Philosophy at the Department of Earth Sciences, University of Durham.

2007

0 6 OCT 2008



COPYRIGHT

The copyright of this thesis rests with the author. No quotation from it should be published without prior written consent and information derived from it should be acknowledged.

No part of this thesis has been submitted for a degree at this university or any other university. The work described in this thesis is entirely that of the author, except where reference is made to previous published or unpublished work.

© 2007 Adam Philip Pugh

ABSTRACT

The Nam Con Son Basin is one of several Tertiary rift basins located on the continental shelf, offshore Indochina. It has received relatively little attention until recently and remains a poorly understood sedimentary basin. The discovery and production of significant volumes of hydrocarbons from within fault-bounded structural highs has spurred a drive to better understand the basin structure. Previous interpretations of regional 2-dimensional seismic data suggested a complex structure, with E-W trending Eocene-Oligocene faults, overprinted by a rhomboidal pattern of mainly N-S and NE-SW trending Miocene faults and the possible involvement of compressional and/or strike-slip tectonics. The driving mechanism for extension on the continental shelf is not fully understood, but the Cenozoic structural evolution was undoubtedly influenced by a heterogeneous crust cut by a number of pre-existing Palaeozoic and Mesozoic structures. Crucially, the western extent of South China Sea rifting in the region may have been controlled by the ~N-S trending edge of the Indochina craton, a major rheological boundary that likely underlies the Nam Con Son Basin. In addition to its economic importance, the proximity of the basin to the tip of the South China Sea, the possible involvement of wrench tectonics and the potential influence of pre-existing fabrics, makes it an ideal target for academic study.

A 3-dimensional seismic dataset from the centre of the Basin has been used to build a fault/horizon model of the Early-Middle Miocene syn-rift sequence. The faults have a wide range of orientations and, in all cases, the hangingwall is down-thrown consistent with apparent normal offsets; there is no evidence for strike-slip or reverse faulting. By accurately modelling the fault surfaces and the fault/horizon intersections, the dip, strike, dip-azimuth and offset of 225 faults have been calculated and used to quantitatively analyse the fault sample.

The timing of fault activity has been constrained for each fault and shows that all the faults are broadly contemporary but that the number of active faults increased through time. This is partly attributed to continuing subsidence on graben bounding faults, which focussed faulting and extension within the graben. There is no correlation between fault strike and fault age and the faults show no significant rotation about vertical axes with progressive deformation. The range of fault orientations likely reflects the conflicting influences of the ~NW-SE regional extension direction and the dominant ~N-S trending basement fabric.

A systematic variation in maximum dip-slip fault offset (defined as the distance between the footwall and hangingwall cutoffs measured parallel to the fault surface) with fault strike has revealed an 'ideal' fault orientation, which can be used to infer the direction of maximum horizontal extension. The relationship between this extension direction, the dominant pre-existing basement fabric and the regional displacement direction is consistent with a model of moderately extension-dominated dextral transtension for the Nam Con Son Basin synchronous with the opening of the South China Sea. At a local scale, the influence of the underlying Eocene-Oligocene structures has produced offset depocentres, along strike fault polarity flips, and complex accommodation zones.

ACKNOWLEDGEMENTS

The project has been made possible by NERC (Natural Environment Research Council) who have provided funding in the form of an Industrial Case Studentship and BP (Industrial Case partner) who have provided additional funding and the seismic data that I have used for this project. I wish to thank the people at BP for their help and hospitality on those occasions when I have visited the company, in particular Steve Matthews at BP Sunbury and James Stewart and the Asset Team at BP Ho Chi Minh City.

A big thanks to my supervisors for their guidance, support and advice, Bob Holdsworth, Ken McCaffrey and Jonny Imber at Durham University and Steve Matthews at BP Sunbury. Jonny deserves additional thanks for loading the 2D and 3D seismic data that I have used and for working to overcome a number of software and data issues that have been encountered along the way. I would also like to thank the other academic staff and support staff within the Earth Science department who have helped me during my time at Durham.

On a personal note, I have made some great friends whilst at Durham who have made the whole process much more enjoyable. So a very big thanks to all of them. This thesis marks the end of over 7 years at university in full time education. Throughout the whole time my family have been a great support, both financially when it was needed and by taking such an interest in what I have been doing and encouraging me all the way. I am lucky to have such a caring family. For the last four years I have had my girlfriend Kerry with me. To say that she has improved my time in Durham would be a gross understatement. I am incredibly grateful that she moved up to Durham to be with me. Together we have really enjoyed our time here.

LIST OF TABLES AND FIGURES

CHAPTER 1

Figure 1.1	1
CHAPTER 2	
Figure 2.1	6
Figure 2.2	7
Figure 2.3	10
Figure 2.4	11
Figure 2.5	12
Figure 2.6	13
Figure 2.7	14
Figure 2.8	16
Figure 2.9	18
Figure 2.10	19
Figure 2.11	21
Figure 2.12	24
Figure 2.13	27
CHAPTER 3	
Figure 3.1	31
Figure 3.2	33
Figure 3.3	35
Figure 3.4	37
Figure 3.5	38
Figure 3.6	40
Figure 3.7	43
Figure 3.8	45
Figure 3.9	47
Figure 3.10	49
Figure 3.11	50
Figure 3.12	52
Figure 3.13	54
Figure 3.14	55
Figure 3.15	56
Figure 3.16	58-59
Figure 3.17	60-6
Figure 3.18	62-63
Figure 3.19	64-63
Figure 3.20	66-6
Figure 3.21	68-69
Figure 3.22	70-7
Figure 3.23	72-73
Figure 3.24	74-73
Figure 3.25 Figure 3.26	76-7° 78-7°
TIRNE 1 70	/ N= / `

Figure 3.27	81
Figure 3.28	82
Figure 3.29	84
Figure 3.30	87-89
Figure 3.31	90
Figure 3.32	92
Figure 3.33	95
Figure 3.34	98
Figure 3.35	99
Figure 3.36	101
Figure 3.37	102
Figure 3.38	104
Figure 3.39	106
Figure 3.40	107
Figure 3.41	108
Figure 3.42	109
Figure 3.43	114
CHAPTER 4	
Figure 4.1	119
Figure 4.2	122
Figure 4.3	123
Figure 4.4	124
Figure 4.5	128
Figure 4.6	129
Figure 4.7	130
Figure 4.8	131
Figure 4.9	132
Figure 4.10	133
Figure 4.11	135
Figure 4.12	138
CHAPTER 5	
Figure 5.1	143
Figure 5.2	145
Figure 5.3	149
Figure 5.4	151
Table 5.1	153
Figure 5.5	154
Figure 5.6	155
Figure 5.7	156
Figure 5.8	157
Figure 5.9	160
Table 5.2	161
Figure 5.10	162
Figure 5.11	163
Figure 5.12	166

CHAPTER 6

170
171
172
174
178
179
180
185

CONTENTS

TITL	E	i
COPY	YRIGHT	i
ABST	FRACT	ii
ACKI	NOWLEDGEMENTS	iv
LIST	OF TABLES AND FIGURES	v
1	INTRODUCTION	1
1.1	AIMS AND CONTENTS	4
2	STRUCTURAL GEOLOGICAL BACKGROUND	6
2.1.2	STRAIN 3-dimensional strain Faulting during 3-D strain Analogue modelling of 3-D strain Folding during transtension	6 9 12 13
2.2 2.2.1 2.2.2 2.2.3	FAULTING Post-sedimentary normal faults Syn-sedimentary normal faults Fault growth, linkage and fault population evolution	19 19 21 23
2.3	REACTIVATION	26
3	STRUCTURE AND EVOLUTION OF THE NAM CON SON BASIN	29
3.1	INTRODUCTION	29
3.2	REGIONAL GEOLOGICAL SETTING	30
3.3 3.3.1 3.3.2 3.3.3	METHOD AND DATASET Sampling faults Depth conversion Constraining the timing of fault movement	42 48 49 51
3.4.4	STRUCTURAL MODEL DERIVED FROM THE 3-D SURVEY Cross sections Structure The fault pattern Structural evolution Folding	56 56 80 86 94

	Strain Fault kinematics Summary of results	111 113 116
4	A NEW STRAIN DISTRIBUTION MODEL FOR RIFT BASINS WITH A CASE STUDY FROM THE CENTRAL NAM CON SON BASIN, OFFSHORE VIETNAM	118
4.1	INTRODUCTION	118
4.2	CONCEPTUAL MODEL OF STRAIN DISTRIBUTION	122
4.3	APPLICATION TO THE NAM CON SON BASIN	126
4.4	THE NAM CON SON FAULT SAMPLE	128
4.5	STRAIN DISTRIBUTION WITHIN THE NAM CON SON BASIN	130
4.6 4.6.1 4.6.2 4.6.3	DISCUSSION Maximum extension direction Strain distribution Fault growth rate	136 136 136 137
4.6.4 4.6.5	Reactivation Application to fractured reservoirs	139 141
4.7	CONCLUSIONS	141
5	THE RECOGNITION OF TRANSTENSIONAL RIFT BASINS USING SUB-SURFACE FAULT GROWTH DATASETS: A CASE STUDY FROM THE NAM CON SON BASIN, OFFSHORE VIETNAM	143
5.1	INTRODUCTION	143
5.2	SUMMARY OF THE REGIONAL TECTONICS AND BASIN STRUCTURE	147
5.3 5.3.1 5.3.2 5.3.3	TYPES OF FAULT ROTATION Type 1: Fault orientation vs. age Type 2: Rotation during vertical fault growth Type 3: Rotation during lateral fault growth	148 150 152 155
5.4 5.4.1	DISCUSSION Transtension	159 162
5.5	CONCLUSIONS	165

6	DISCUSSION AND CONCLUSIONS	168
6.1	BASIN EVOLUTION	168
6.1.1	Eocene-Oligocene rifting	168
6.1.2	Graben geometry	169
6.2	THE EFFECTS OF TRANSTENSION AND	
	REACTIVATION ON THE MIOCENE STRUCTURE	176
6.2.1	Offset graben and along strike dip polarity flips	177
6.2.2	Transtensional folding	180
6.3	IMPLICATIONS FOR HYDROCARBON PROSPECTIVITY	183
6.4	CONCLUSIONS	187
	REFERENCES	190

CHAPTER 1. INTRODUCTION

The Nam Con Son Basin, on the Vietnamese continental shelf (Fig. 1.1), has received relatively little attention until recently and the kinematics and driving mechanisms of basin formation remain poorly understood. The discovery and production of significant volumes of hydrocarbons trapped within fault-bounded structural highs has spurred a drive to better understand the structure of the basin. In particular, an investigation of the southern half of the basin, carried out by BP and published in Matthews *et al.* (1997), has revealed a complex tectonic evolution, which includes two separate rifting episodes, a rhomboidal pattern of mainly N-S and NE-SW trending faults and the possible involvement of compressional and/or strike-slip tectonics.

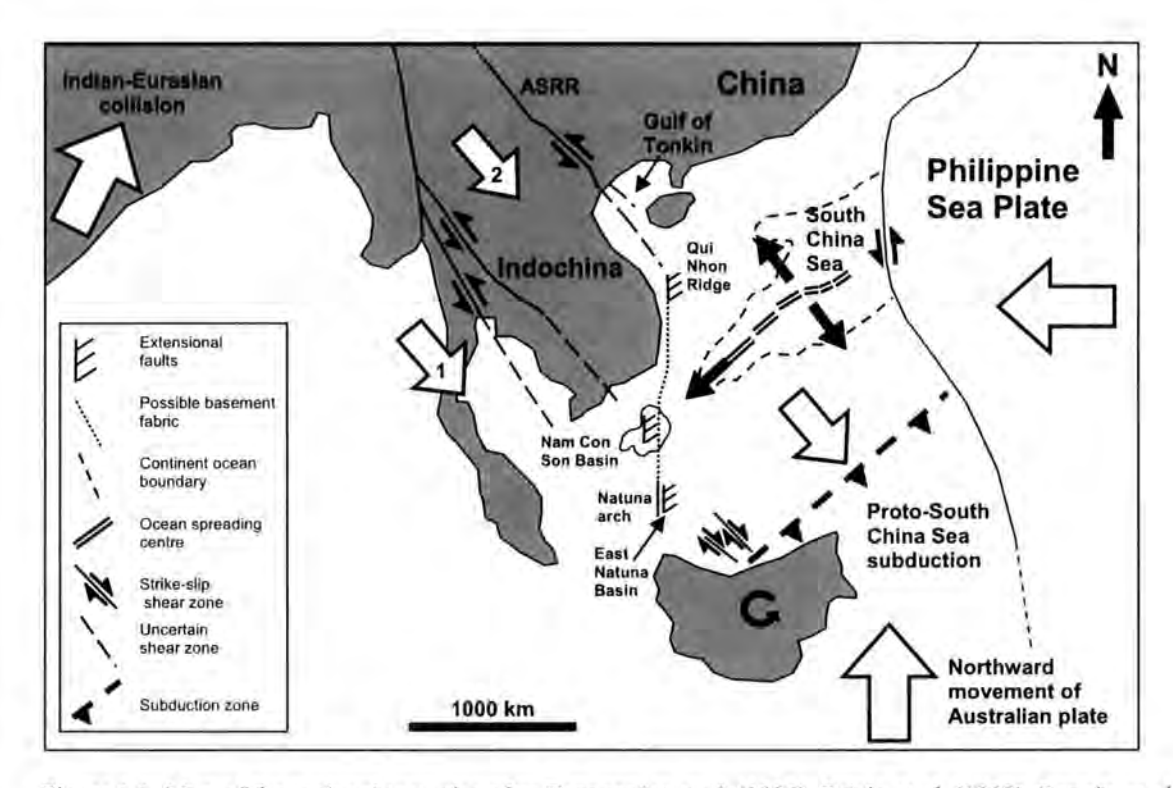


Figure 1.1: Map of the regional tectonics after Tapponnier et al. (1986), Briais et al. (1993), Rangin et al. (1995), Hall (1997), Mat-zin & Swarbrick (1997), Roques et al. (1997) and Morley (2002). Large arrows represent the tectonic displacements in the region. Numbered arrows represent the successive extrusion of the continental blocks. Extrusion progresses northwards with the northwards identation of India into Eurasia (block 1 was extruded first followed by block 2).



The Tertiary tectonics of the SE Asia region are thought to have been driven by the northward movement of the Indian indenter, the northward movement and eventual collision of the Indian-Australian plate and the westward subduction of the Pacific plate (Fig. 1.1; Hall, 1997). The tectonic stresses arising from these plate movements have interacted with Palaeozoic and Mesozoic structural architectures preserved within the continental crust of SE Asia. These basement heterogeneities have undoubtedly influenced the Tertiary deformation, including the strike-slip reactivation of ancient sutures throughout Indochina (Metcalfe, 1996). The possible involvement of strike-slip tectonics, the potential for reactivation of pre-existing fabrics and the location of the basin in close proximity to the SW tip of the South China Sea spreading centre (Fig. 1.1) makes the Nam Con Son Basin a key location on the Vietnamese continental shelf for better understanding the Tertiary tectonics of SE Asia. Improved knowledge of basin evolution will also provide better constraints on hydrocarbon exploration and petroleum play definition in offshore Vietnam.

2-dimensional and especially 3-dimensional seismic data remain the primary tools for hydrocarbon exploration in offshore basins but many of the traditional techniques of the structural geologist cannot be applied to such sub-surface data. A kinematic analysis of fault slip vectors and shear sense indicators is not possible and 3-dimensional seismic data has a much lower spatial resolution compared to surface-based outcrop studies (tens of metre verses millimetre scales). However, it does provide a complete, 3-dimensional picture of the structures that is not possible in surface outcrops where the available exposure limits the complete 3-dimensional view of the structures to some extent. Additionally, in basins where the sedimentation rate kept pace with the subsidence rate, it is possible to use well-calibrated 3-dimensional seismic data to reconstruct the growth histories of syn-sedimentary faults. These "displacement

backstripping" techniques (Peterson et al., 1992; Childs et al. 1993) use down-dip and along strike variations in throw to constrain the growth of individual syn-sedimentary faults (Childs et al., 2003) and, in favourable circumstances, to track fault system evolution at the basin scale (Walsh et al., 2003).

For this thesis, a 3-dimensional seismic dataset from the central area of the Nam Con Son Basin has been used to construct a detailed 4-dimensional model of the fault population evolution. By accurately modelling the fault/horizon intersections, fault attributes such as throw, heave and dip-azimuth have been calculated and used as a basis for the development of new quantitative fault analysis techniques. The work provides new insight into the Early to Middle Miocene evolution of the Nam Con Son Basin and, in particular, suggests that the basin opened during a phase of moderately extension-dominated dextral transtension. This finding has broader implications for understanding the evolution of fault populations in regions of oblique extension or transtension and also places new constraints on models of the regional tectonics of South East Asia.

1.1 AIMS AND CONTENTS

The aim of the thesis is to construct a new, detailed model of the Miocene fault population and associated syn-rift strata in the central Nam Con Son Basin using 3-dimensional seismic data. The fault model is analysed using new and existing quantitative techniques in order to constrain the timing of faulting and folding within the area, to understand how the strain was accommodated by the fault population and how the fault population evolved through time. Specifically, the timing of fault growth, the geometries of fault surfaces, the way in which the faults interact and the distribution of strain can constrain the boundary conditions of the deformation and provide insight into the nature of the regional tectonics during the Miocene.

Chapter 2 introduces the concept of 3-dimensional strain and summarises previous numerical and analogue modelling studies into the faulting and folding patterns produced during transtension. This section is followed by an overview of fault geometry, growth, linkage and interaction. Finally, reactivation is reviewed including the relationship between reactivation and oblique extension.

In Chapter 3 the geological setting of the Nam Con Son Basin is outlined, including its regional structure and stratigraphic infill. The seismic dataset and the methodology used throughout the thesis is described. The bulk of the chapter is a presentation and discussion of the basic structural model for the Miocene faults, derived from the interpretation of the 3-dimensional seismic dataset. The faults and folds are described and the timing of fault movement and the amount of extension are analysed using a quantitative approach.

In Chapter 4, a new conceptual model of strain distribution within extensional and extension-dominated transfersional basins is presented and applied to the Nam Con

Son dataset. The model predicts a correlation between the maximum amount of dip-slip offset on a fault and the orientation of that fault relative to the maximum extension direction. It is shown to be applicable to the fault pattern in the central Nam Con Son Basin and the analysis suggests the influence of basement reactivation in controlling Miocene faulting.

Chapter 5 addresses the specific question of whether the Miocene deformation is transtensional. The existence of major onshore strike-slip shear zones throughout Indochina (Fig. 1.1), coupled with the unusual structural geometry of the Nam Con Son Basin has led many workers to propose the involvement of strike-slip tectonics in its evolution. This chapter presents a new quantitative approach to identifying non-coaxial deformation by analysing the faults for evidence of rotations about vertical axes.

Finally, Chapter 6 brings together the discussions from the previous chapters. An overall kinematic model for the structural evolution of the basin is presented and the implications that the model has for the regional tectonics and for hydrocarbon exploration is discussed.

CHAPTER 2. STRUCTURAL GEOLOGICAL BACKGROUND

2.1 STRAIN

Strain is the change in volume and shape of a body during deformation and any rotation or translation of the body relative to a fixed frame of reference. The change in volume and shape can be described by changes in the lengths of material lines (longitudinal strains or extension) and changes in the angles between initially perpendicular lines (shear strains) (Twiss and Moores, 1992).

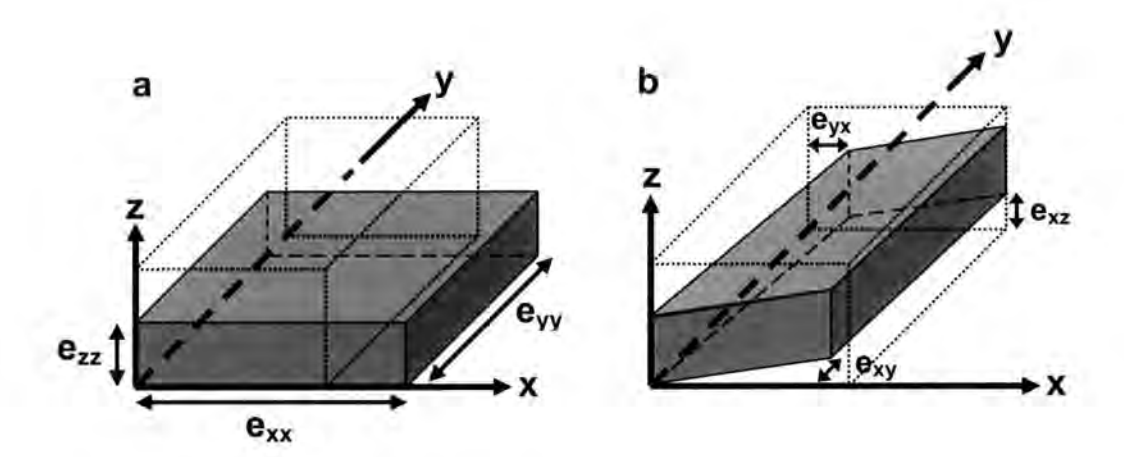


Figure 2.1: a) Orthogonal strains. b) Shear strains.

The extension of a line (e_{ii}) is measured relative to the initial length:

$$e_{ii} = \frac{I - I_0}{I_0} \tag{2.1}$$

where l is the deformed length and l_{θ} is the original length. The subscript characters refer to the components of strain (Fig. 2.1). The first indicates which axis was parallel to the

undeformed line and the second indicates the axis along which the strain is measured. Orthogonal strains are those in which the lines do not rotate during the deformation, e.g. e_{xx} (Fig. 2.1a). Whereas, shear strains require lines to rotate, e.g. e_{xy} (Fig. 2.1b) (Twiss and Moores, 1992).

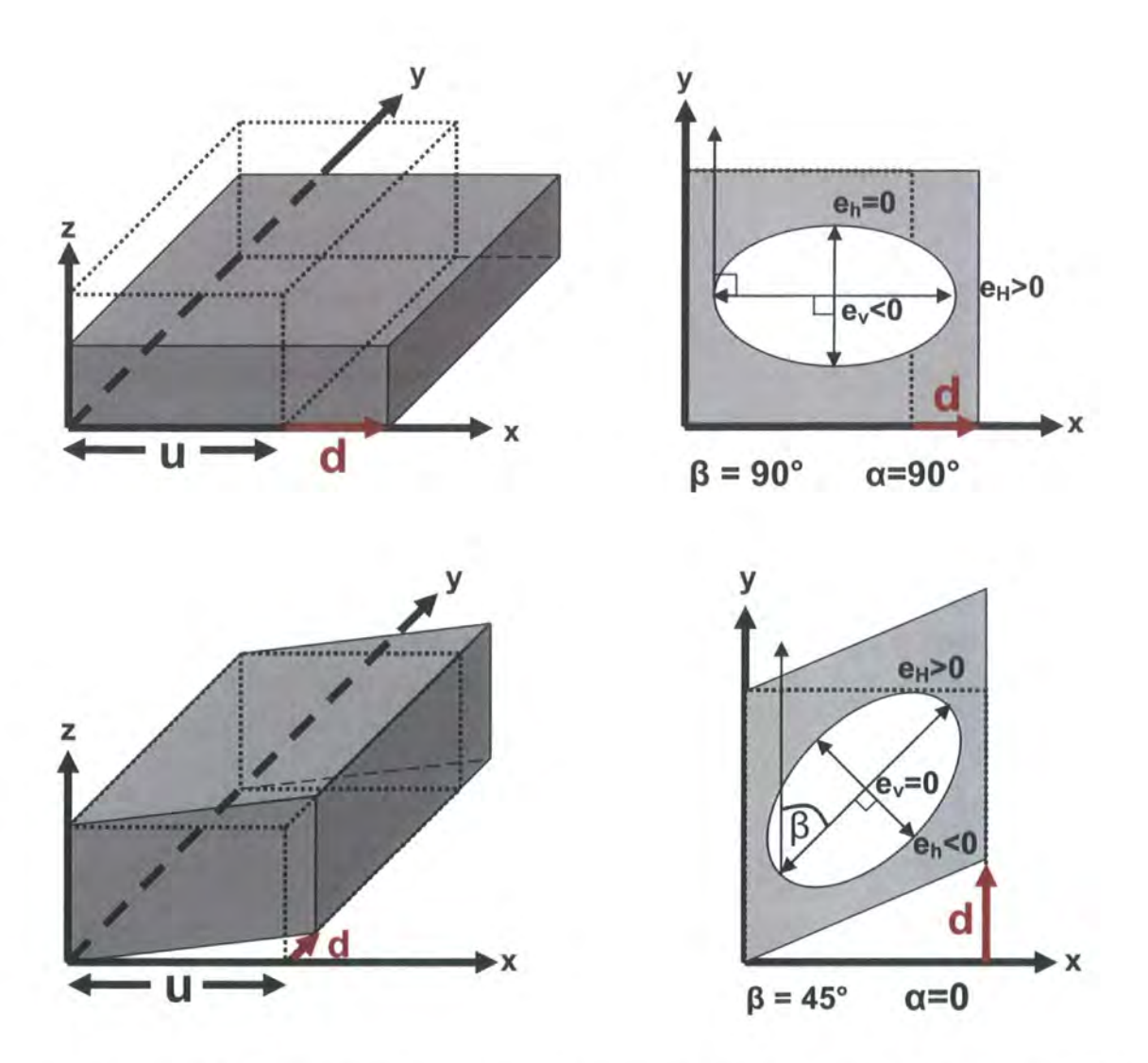


Figure 2.2: Models of infinitesimal strain (d<<u). 3-dimensional block diagrams and plan views showing infinitesimal strain axes. After strain models of Withjack and Jamison (1986), in which $e_H=0.5$ (d/u) (sin $\alpha+1$), $e_h=0.5$ (d/u) (sin $\alpha-1$), $e_v=-(v/1-v)$ (d/u) sin α , $\beta=90^\circ$ - 0.5 tan⁻¹ (cot α). a) Model of planestrain orthogonal extension where $\alpha=90^\circ$ and $\beta=90^\circ$. b) Model of plane-strain wrench deformation where $\alpha=0^\circ$ and $\beta=45^\circ$.

To model the deformation in a volume of crust we can use a rectangular plate of initial width, u, set in a reference Cartesian coordinate system with three mutually orthogonal axes labelled x,y,z (Fig. 2.2). For simplicity, the plate is linearly elastic, homogenous and isotropic. The plate is deformed by displacing one edge by a distance, d, in a direction oriented α degrees from the y axis. This model is appropriate for infinitesimal strains (d<<u). The deformation produced by the displacement is modelled as follows (Withjack and Jamison, 1986):

$$e_{xx} = (d/u)\sin\alpha \tag{2.2}$$

$$e_{yy} = 0 ag{2.3}$$

$$e_{zz} = -(v/1-v) (d/u) \sin \alpha \tag{2.4}$$

$$e_{xy} = e_{yx} = 0.5 \ (d/u) \cos \alpha$$
 (2.5)

$$e_{xz} = e_{zx} = e_{zy} = e_{yz} = 0 (2.6)$$

where v is Poisson's ratio and extension is positive. If we are modelling a vertical deformation zone where $e_H=e_1,\ e_h=e_2$ or e_3 and $e_v=e_2$ or e_3 , the corresponding infinitesimal principle strains are:

$$e_H = 0.5 (d/u) (\sin \alpha + 1)$$
 (2.7)

$$e_h = 0.5 (d/u) (\sin \alpha - 1)$$
 (2.8)

$$e_{\nu} = -(\nu/1 - \nu) (d/u) \sin \alpha \tag{2.9}$$

where e_H and e_h are the maximum and minimum infinitesimal principle horizontal strains respectively and e_v is the vertical infinitesimal principle strain. The maximum principle strain axis is oriented β degrees measured clockwise from the y axis:

$$\beta = 90^{\circ} - 0.5 \tan^{-1}(\cot \alpha) \tag{2.10}$$

Equations 2.2-2.10 can be solved for orthogonal extension ($\alpha = 90^{\circ}$) and wrench deformation ($\alpha = 0^{\circ}$), assuming a Poisson's ratio, v = 0.5, i.e. that of an ideal incompressible material (Fig. 2.2). The direction of maximum principle strain, β , in relation to the deformation zone boundary (y axis) is 90° in the case of an orthogonal extension (Fig. 2.2a) and 45° in the case of a wrench deformation (Fig. 2.2b).

2.1.1 3-dimensional strain

Orthogonal extension and wrench deformation are two examples of plane strain (a 2-dimensional pure shear and a simple shear respectively) in which the intermediate axis of strain, e₂, is equal to zero (Fig. 2.2). The maximum and minimum axes of strain, e₁ and e₃ respectively, are non-zero and are contained within a single 2-dimensional plane oriented perpendicular to the intermediate axis. If all strain axes are non-zero, the deformation is 3-dimensional and cannot be described within a 2-dimensional plane. Pure shear is a non-rotational strain, during which material lines that are parallel to the principle axes of finite strain remain parallel. Simple shear, on the other hand, is a rotational strain, in which all material lines rotate with respect to the coordinate system, except those parallel to the shear plane. During progressive simple shear, the principle axes of finite strain rotate with respect to the principle axes of incremental strain -

equivalent to the principal stress axes - which remain fixed in their orientation during steady state deformation (Twiss and Moores, 1992).

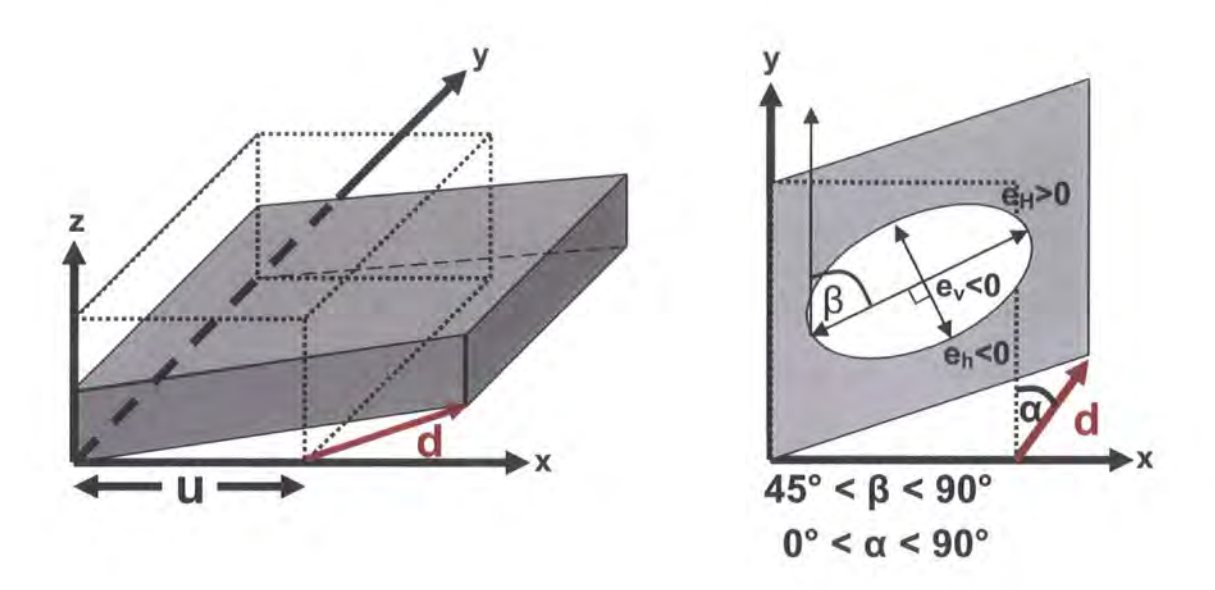


Figure 2.3: Model of non-plane strain transtension, in which the principle axes of strain are all non-zero, $0^{\circ}<\alpha<90^{\circ}$ and $45^{\circ}<\beta<90^{\circ}$. 3-d block diagrams and plan views showing infinitesimal strain axes. After strain models of Withjack and Jamison (1986), in which $e_H=0.5$ (d/u) (sin $\alpha+1$), $e_h=0.5$ (d/u) (sin $\alpha-1$), $e_v=-(v/1-v)$ (d/u) sin α , $\beta=90^{\circ}-0.5$ tan⁻¹ (cot α).

A 2-dimensional pure shear extension and a wrench simple shear can be considered as end members of transtensional deformation or oblique extension, in which $0^{\circ} < \alpha < 90^{\circ}$. Transtension gives rise to 3-dimensional strains, where $e_H > 0$ and e_h and $e_v < 0$ (Fig. 2.3). Withjack and Jamison (1986) calculated the principle axes of infinitesimal strain for several values of α (Fig. 2.4). For all values of α , the axis of greatest extension is horizontal, e_H . However, the axis of greatest shortening, e_3 , switches from being vertical to horizontal with decreasing α (Fig. 2.4a). The point at which this occurs (~20° in models where Poisson's ratio, v = 0.5, i.e. an ideal incompressible material) separates the extension dominated transtension strain field, where $e_3 = e_v$ from the wrench dominated transtensional strain field where $e_3 = e_h$ (Fig. 2.5).

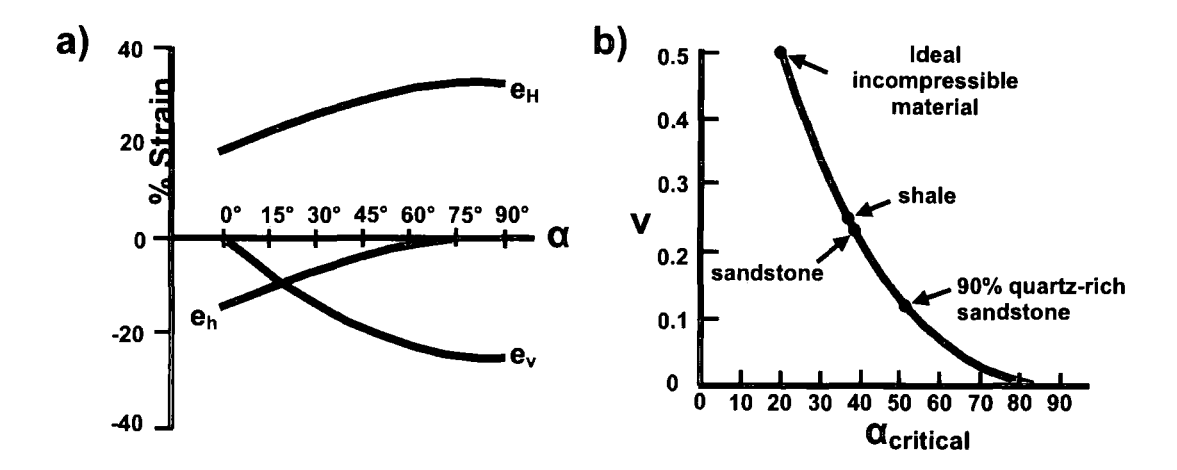


Figure 2.4: a) From Withjack and Jamison (1986). Magnitudes of the principal strains for several values of α ,. The ratio of the displacement to the original plate width is d/u = 0.33. Extension is positive. b) After DePaola *et al.* (2005). Plot of Poisson's ratio, ν , ν s. $\alpha_{critical}$, the point that marks a switch between extension dominated transtension and wrench dominated transtension. Values for the lithologies are taken from DePaola *et al.* (2005).

The critical angle ($\alpha_{critical}$) which separates these deformation domains is a function of Poisson's ratio (v) and can vary considerably in natural examples depending on lithology (Fig. 2.4b; DePaola *et al.*, 2005a). DePaola *et al.*, (2005a) calculated dynamic Poisson's ratio values and $\alpha_{critical}$ for a range of typical igneous, metamorphic and sedimentary rocks following Christensen (1996) and Johnston & Christensen (1992). Figure 2.4b includes those values for sand and shale, which will be used in chapter 5 of this thesis.

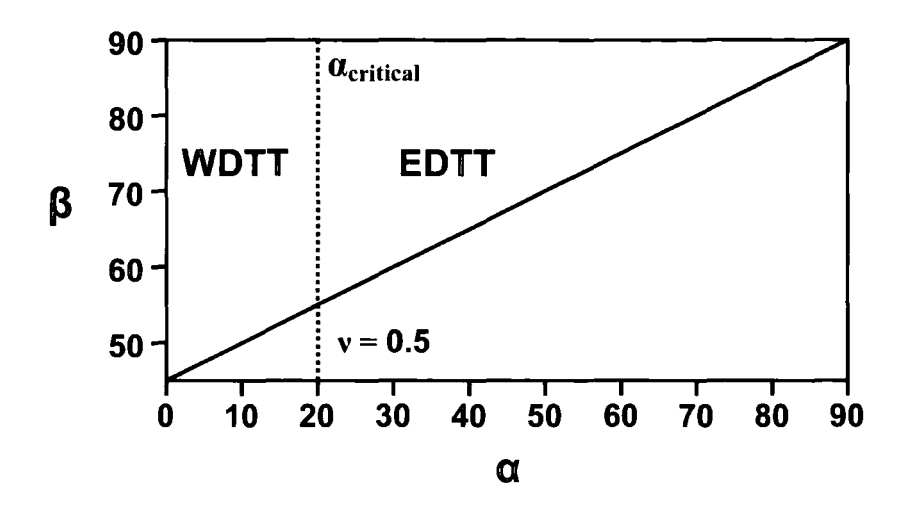


Figure 2.5: Plot of the relationship between α and β and $\alpha_{critical}$ which separates the wrench dominated transtension domain (WDTT) and the extension dominated transtension domain. $\alpha_{critical}$ is 20° for a material with a Poison's ratio (v) of 0.5. After DePaola *et al.* (2005a).

In lithologies with a low Poisson's ratio, such as quartz-rich sandstones, the switch in the axis of maximum shortening, e_3 , from vertical to horizontal can occur during extensions with relatively high α .

2.1.2 Faulting during 3-dimensional strain

The familiar models of Andersonian faulting predict two sets of conjugate faults with a bimodal pattern during 2-dimensional strain (Anderson, 1951). Multimodal rhomboidal fault patterns comprising two or more coeval sets of conjugate normal faults have been observed widely both in the field and on subsurface datasets (Reches, 1978; Krantz, 1988). These have been attributed to 3-dimensional strain, in which all three axes of principle strain are non-zero. The slip model of Reches (1978) considers faulting during a coaxial (pure shear) 3-dimensional, non-plane strain. The model predicts that three to four sets of faults, with orthorhombic symmetry about the principle strain axes, are required to accommodate 3-dimensional strain and that none of the fault planes or slip

vectors lie parallel to any of the principle axes of stress or strain (Reches, 1978; Reches and Dieterich, 1983).

2.1.3 Analogue modelling of 3-dimensional strain

Physical models using clay and sand have provided insight into the patterns of faulting, fracturing and folding that may be produced during oblique extension (Withjack and Jamison, 1986; McClay and White, 1995; Schlische *et al.*, 1996, Schlische *et al.*, 2002). In the analogue experiments of Withjack and Jamison (1986) a rig is used with a metal base plate, half of which is fixed and the other half moveable (Fig. 2.6).

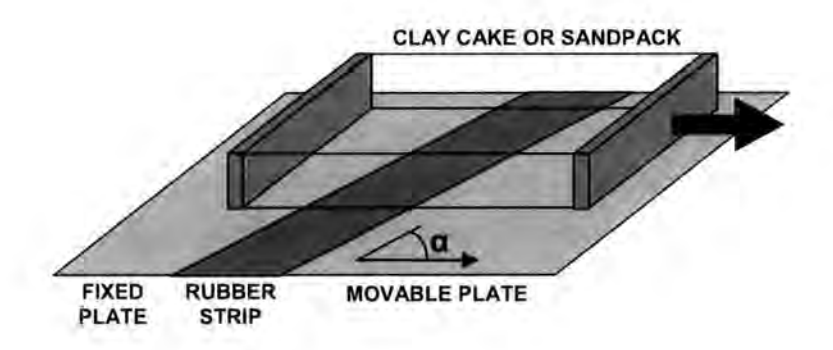


Figure 2.6; Schematic modelling rig used by Withjack and Jamison (1986) and McClay and White (1995).

The two halves of the base plate are bridged by a rubber strip, which represents the upper surface of the ductile crust. A cake of soft clay, representing the brittle upper crust, is rested on the base plate and the moveable half of the plate is displaced relative to the fixed half. The rubber is deformed beneath the clay, which in turn induces deformation within the clay. The angle between the rubber strip, representing the rift trend and the displacement direction, is equivalent to the angle α . For each experiment, this angle, α , was varied from 0° , simulating a (plane strain) wrench simple shear, to

15°, 30°, 45°, 60°, 75° (all non-plane strain transfension) and 90°, which simulates an extensional (plane strain) pure shear (Fig. 2.7).

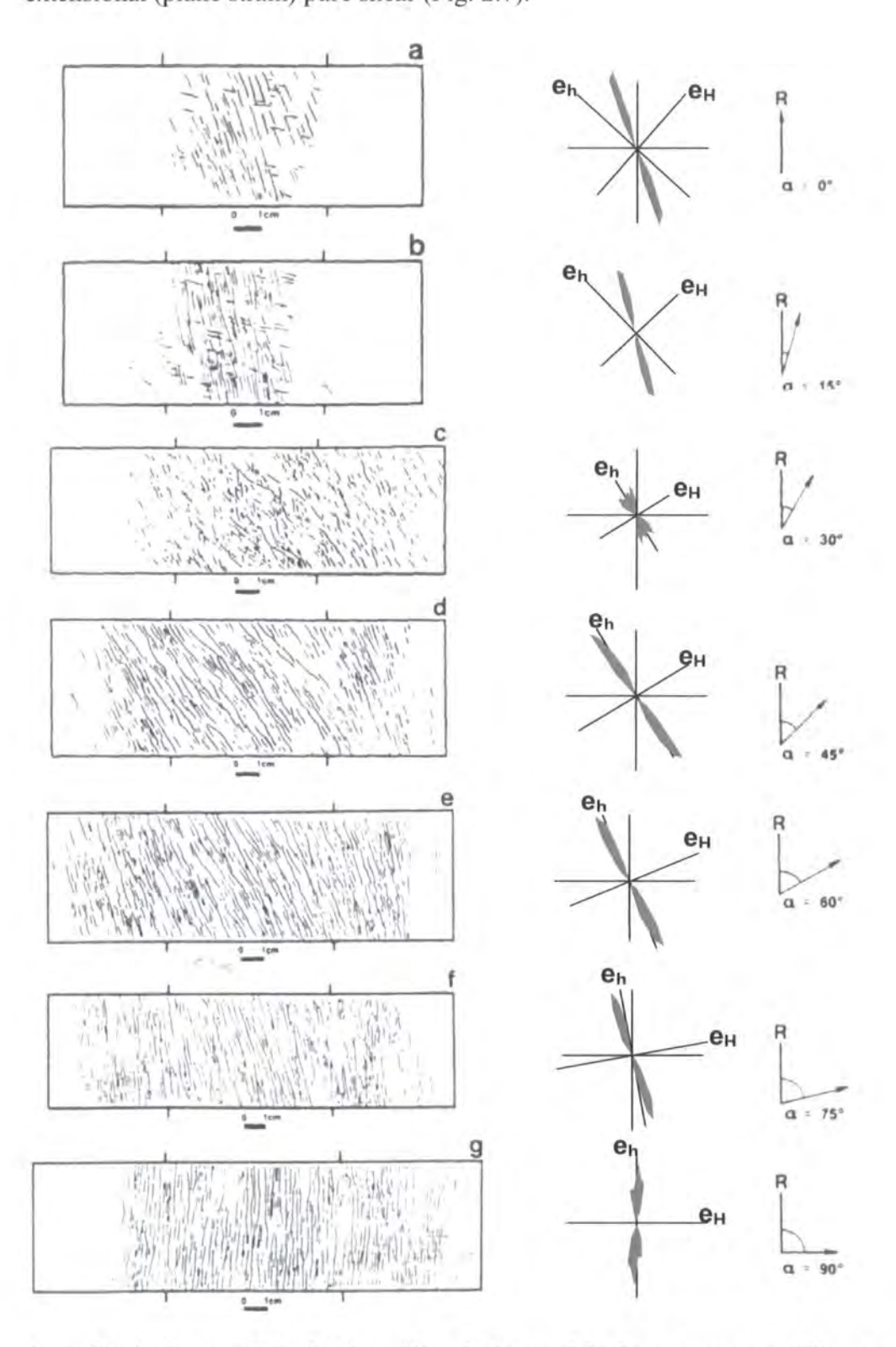


Figure 2.7: Analogue models of oblique rifting. Each part of the figure represents a different experiment. For each part of the figure there is a line drawing of the resultant fault pattern, a rose diagram of the fault distribution and a schematic diagram of the displacement direction relative to the rift trend. From Withjack and Jamison (1986).

The sense of lateral displacement of the base plate was sinistral in all cases and the angles of the faults, described below, are measured counter-clockwise relative to the rift trend.

With $\alpha=0^\circ$, 50% of faults formed at an angle of between 15°-25° to the rift trend and had sinistral strike-slip displacements, whilst a second set, ~10% of faults, made a higher angle to the rift trend of between 75°-85° and had dextral strike-slip displacements (Fig. 2.7a). The acute angle between the two sets bisects the axes of maximum shortening, $e_h=e_3$ (Withjack and Jamison, 1986). These faults are equivalent to Riedel shears (Woodcock and Schubert, 1994 and references therein). As the experiment continues, the faults that form at high angles to the rift, rotate several degrees counter-clockwise with progressive deformation (Withjack and Jamison, 1986).

The fault pattern that develops at $\alpha=15^\circ$ is very similar to that of $\alpha=0^\circ$ but with a slightly lower proportion of strike-slip faults (Fig. 2.7b). The faulting pattern is also similar to that predicted for wrench plane strain by Andersonian faulting models. At $\alpha=30^\circ$, the pattern of faults is significantly different from those of the experiments with $\alpha=0^\circ$ and $\alpha=15^\circ$ (Fig. 2.7c). This likely reflects the switch, at ~20°, from wrench-dominated to extension-dominated deformation, as predicted by the numerical models described above (Withjack and Jamison, 1986). In this experiment, normal faults predominate but there are also faults with sinistral and dextral strike-slip displacements and oblique-slip displacements. The faults show a wide range of orientations, with ~50% striking perpendicular to the direction of maximum extension, $e_1=e_H$, with predominantly normal displacements. There is little evidence of fault rotation with progressive deformation. With increasing α , the obliquity of the faults lessens. Specifically, ~50% of faults strike between 30°-40° of the rift trend when $\alpha=1$

45°, between 20°-30° of the rift trend when $\alpha = 60^{\circ}$ and between 10°-20° of the rift trend when $\alpha = 75^{\circ}$ (Fig. 2.7d, e and f, respectively). At $\alpha = 90^{\circ}$, the normal faults have moderate dips and trend parallel to the rift trend, similar to Andersonian-style faulting (Fig 2.7g). In all cases the faults show greater obliquity in the rift, above the rubber strip, than at the margins (Withjack and Jamison, 1986).

In the analogue models of McClay and White (1995), a sandpack is deformed using a rig very similar to that of Withjack and Jamison (1986), described above (Fig. 2.6). During oblique extension, $\alpha = 60^{\circ}$, the faults that border the rift are clearly controlled by the underlying rift geometry (Fig. 2.8).

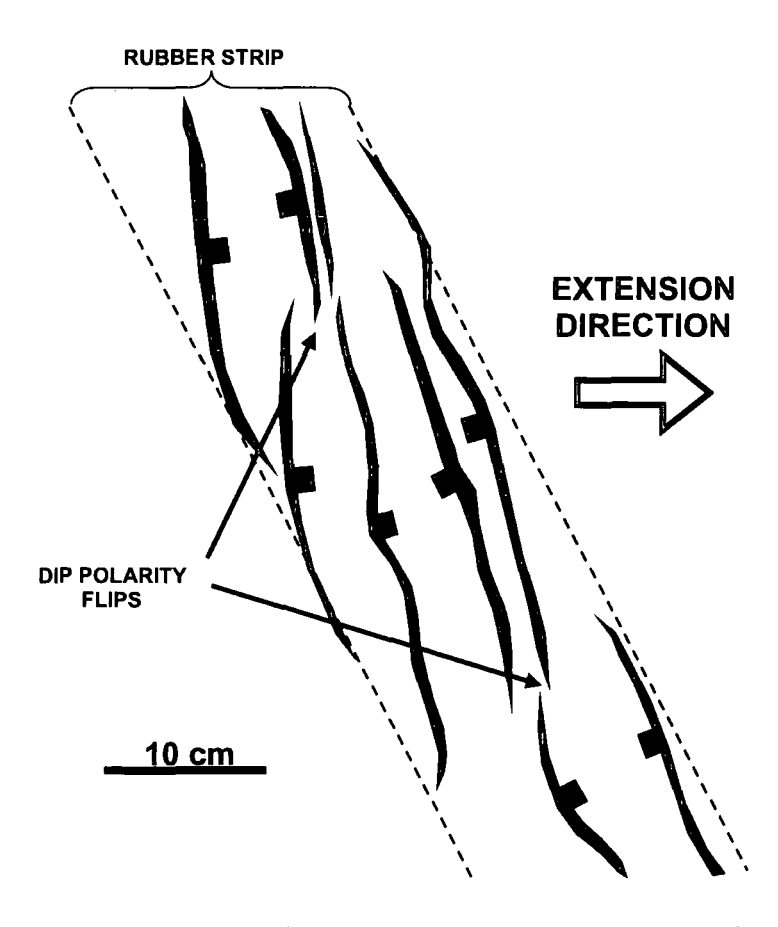


Figure 2.8: Results of sandbox model of oblique extension, $\alpha = 60^{\circ}$. Graben offset is accommodated by along strike fault dip polarity flips. After McClay and White (1995).

The border fault system is a segmented array of en-echelon, curvilinear faults, which form parallel to the base plate edge. The tips of the border faults tend to align parallel to the rift and with increased extension, propagate laterally and link via relay ramps (Section 2.2.3). The faults within the rift form at high angles to the displacement direction. Distinct, offset depocentres form in the rift, separated by accommodation zones of overlapping faults with along-strike polarity flips. The degree of segmentation and en-echelon character of the border fault system was lessened in experiments with less obliquity, $\alpha = 75^{\circ}$ but increased in experiments with a greater obliquity, $\alpha = 45^{\circ}$. Unlike the clay cake models of Withjack and Jamison (1986), deformation of the sandpack involved no oblique-slip or strike-slip faulting. In particular, the depocentre offsets are wholly accommodated by dip-slip normal faulting. This could be due to the absence of any strong underlying offset or step in the base-plate, the rheological differences between clay and sand or it could be a function of the amount of extension, β , which in this case was a maximum of $\beta = 1.5$ and perhaps not enough to produce transfer faults. The sand-pack was sliced to produce vertical cross-sections perpendicular to the rift trend. The faults are planar or slightly curved in cross-section, with some having sigmoidal profiles. In the accommodation zones the faults form conjugate sets and symmetrical graben (McClay and White, 1995).

2.1.4 Folding during transtension

During wrench dominated transtension, the wrench component of the deformation often results in the formation of folds. The physical models of Venkat-Ramani and Tikoff (2002) have successfully reproduced folding during wrench dominated transtension (α < 30°) (Fig. 2.9). The folds form parallel to the maximum infinitesimal extension

direction and rotate during progressive deformation towards parallelism with the divergence direction.

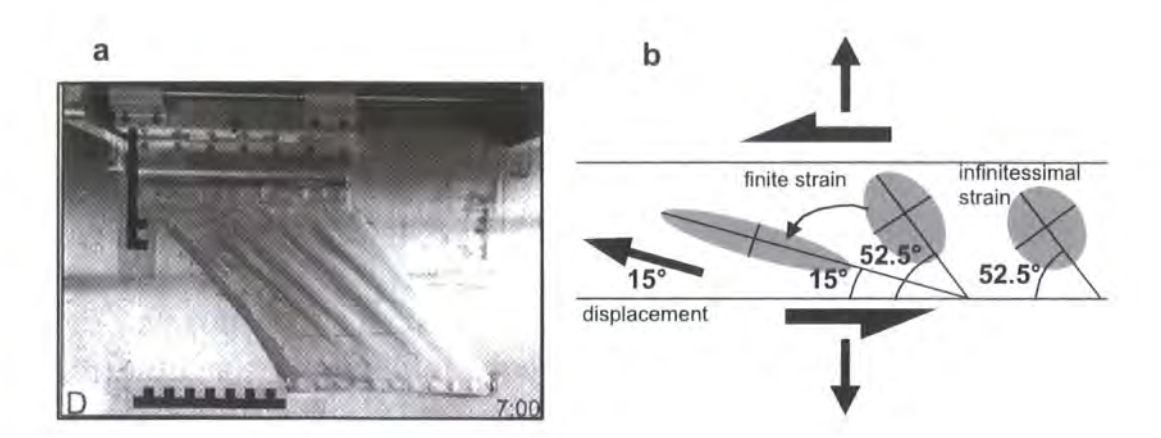


Figure 2.9: Experimental models of transtensional folding. a) Analogue model using a rubber sheet. The sheet is extended and sheared to simulate wrench dominated transtension. Scale bar shows centimetre gradations (15 cm in length). b) During the experiment folds form at 52.5° to the boundary and rotate with continued shearing towards parallelism with the displacement direction. (After Venkat-Ramani and Tikoff, 2002).

The fold amplitude increases with decreasing divergence angle (α angle of section 2.1.2) or, put another way, the amount of horizontal shortening is greater if the wrench component of deformation is greater. The fold axial planes consistently form vertically and are unaffected by variations in the divergence angle. During transtension, the extensional component of deformation is dominant and so folding is accompanied by hinge parallel extension. Whilst folding is the result of the wrench component, extension is the result of both the wrench and pure shear components. Consequently the horizontal extension (hinge-parallel) is always greater than the horizontal shortening (hinge-perpendicular).

2.2 FAULTING

2.2.1 Post-sedimentary normal faults

The idealised geometry of an isolated post-sedimentary normal fault is described by Barnett *et al.* (1987) (Fig. 2.10).

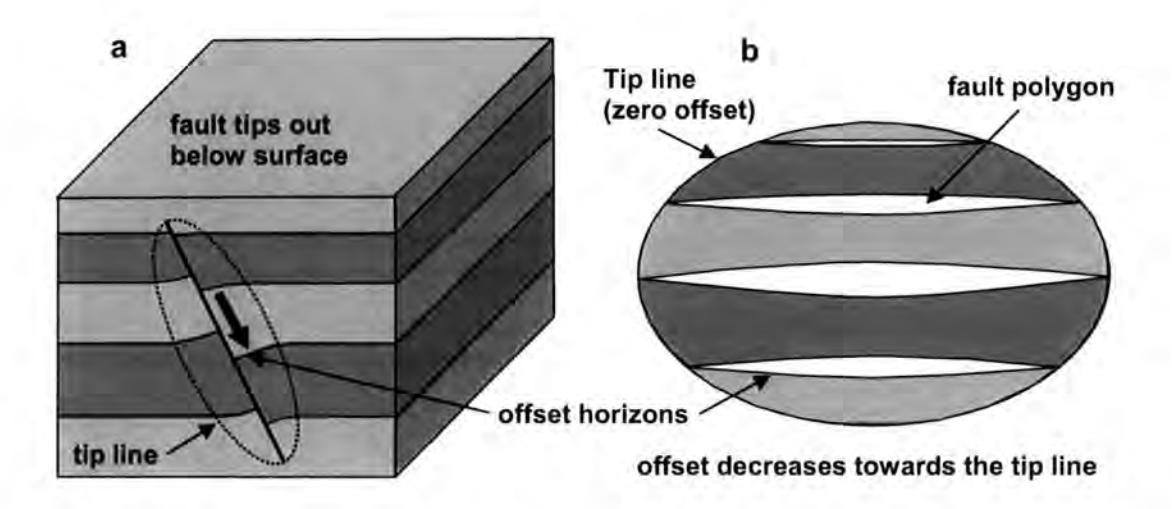


Figure 2.10: Conceptual model of an ideal post-sedimentary blind fault. a) Fault in cross section. Fault tips out below the Earth's surface. Offset decreases towards the tip line and note the reverse drag (footwall uplift; hangingwall rollover) in the wallrocks. b) Strike view of the fault surface. Fault polygons are in white. Offset decreases towards the tip line.

The fault surface is elliptical, with an average aspect ratio of ~2 and a sub-horizontal major axis (Walsh and Watterson, 1989). The displacement decreases in all directions from a maximum at the fault centre to zero at the tip line loop, with displacement contours forming concentric ellipses (Barnett *et al.*, 1987; Fig. 2.11c). In 3-dimensions the displacement also decreases away from the fault, normal to the fault surface to form an ellipsoidal tip surface that defines a volume of near field strain (Fig. 2.10a). The variation in strain across the fault surface must be accommodated by ductile strain (distortion, dilation) of the hangingwall and footwall rocks and results in reverse drag adjacent to the fault surface (Barnett *et al.*, 1987; Fig. 2.10a).

The displacement gradient is the rate of change in displacement across the fault surface in a particular direction and can be measured vertically or horizontally (Barnett et al., 1987; Walsh and Watterson, 1989; Nicol et al. 1996). In an ideal fault model, where the length of the horizontal axis is roughly twice that of the vertical axis, the horizontal displacement gradient should be roughly half that of the vertical displacement gradient (Nicol et al. 1996). The gradient is influenced by the material properties of the rock volume, particularly the shear modulus, and the size of the fault. The non-linear growth relationship predicted by analysing fault displacement-length populations (Eq. 2.1, see below) implies that larger faults should have higher displacement gradients compared with smaller faults. This contention is supported by values for throw gradients reported in Nicol et al. (1996), from faults measured on mining plans and seismic datasets. Coal-field faults, with widths of 0.2-2.6 km have gradients of 0.001 to 0.007 (horizontal) and 0.007 to 0.03 (vertical), whilst seismically imaged faults with widths of 1.3-9.7 km have gradients of 0.007-0.06 (horizontal) and 0.04-0.22 (vertical).

The ideal geometry described above is relevant only for isolated normal faults. The majority of faults interact with neighbouring faults or the Earth's surface, restricting the vertical or lateral growth of the fault. This results in reduced curvature of the tip line and displacement contours (Nicol *et al.*, 1996), locally increased displacement gradients (Walsh and Watterson, 1989) and changes to the fault surface aspect ratio.

2.2.2 Syn-sedimentary normal faults

Syn-sedimentary normal faults or growth faults are those that were active during the deposition of the sedimentary sequence that they cut and offset (Fig. 2.11).

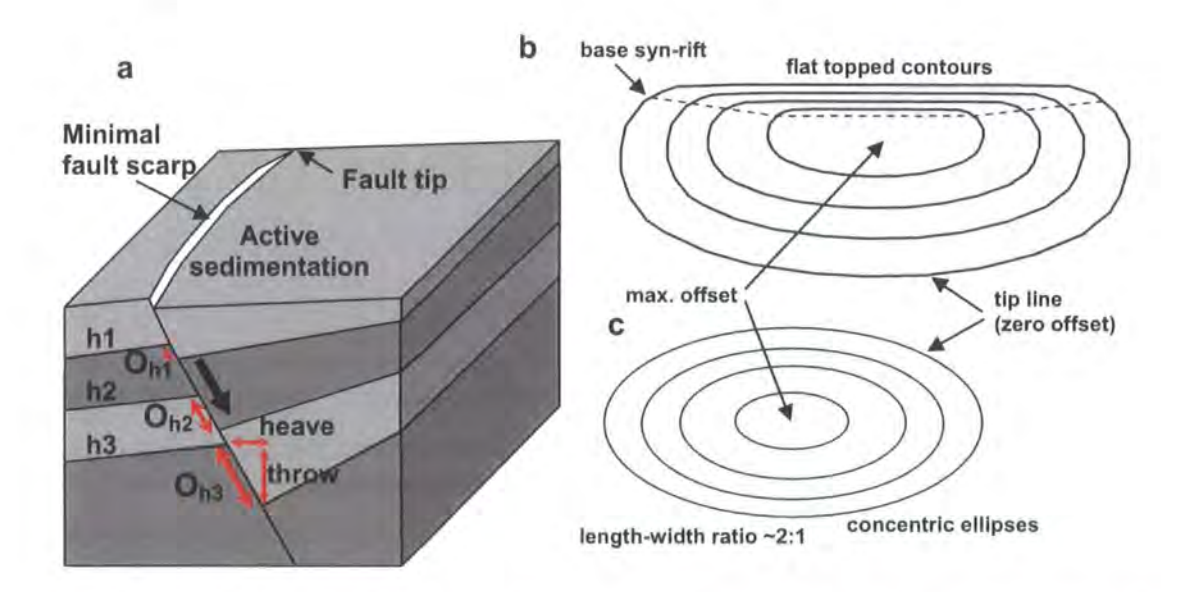


Figure 2.11: Model of syn-sedimentary faulting. a) Block diagram of a syn-sedimentary fault. The fault intercepts the Earth's surface. b) Displacement contours for an ideal syn-sedimentary fault. Maximum displacement is in the fault centre. The contours are flat topped above the maximum displacement indicating syn-sedimentary fault movement. The dashed line marks the base of the syn-sedimentary part of the fault, recognised by the horizontal contours. Below this line the fault is post-sedimentary and the contours resemble those of a post-sedimentary fault. After Childs *et al.* (2003). c) Displacement contours for an ideal post-sedimentary blind fault. Contours are concentric ellipses and the fault has a ~2:1 length to width ratio. After Barnett *et al.* (1987).

In contrast to the blind fault described above, syn-sedimentary faults intercept the Earth's surface. The downthrown hangingwall creates an asymmetric depression into which sediment can be deposited. The footwall is often uplifted and, depending on the overall basin subsidence, the location of the fault within the basin and the eustatic sea level, may be subject to erosion. Provided the sedimentation rate keeps pace with the fault displacement rate, the difference in elevation between the footwall and hangingwall controls the relative sediment thickness across the fault and produces a thicker sedimentary sequence in the hangingwall (Childs *et al.*, 2003).

Because the sediment is deposited during fault movement, an older stratigraphic unit is generally subjected to a longer history of fault movement than the younger sequence and the amount of offset on a stratigraphic horizon is the accumulation of all fault movements subsequent to its deposition. This results in increasing offsets with depth but is different to the variation in offset from a maximum at the fault centre to zero at the tip line as seen in the case of post-sedimentary faults (Barnett *et al.*, 1997; Fig. 2.11c). The displacement gradients on syn-sedimentary faults can be much larger than those of post-sedimentary faults. Nicol *et al.* (1997) report vertical displacement gradients of 0.16 to 1.5 for onshore and offshore syn-sedimentary faults of a range of sizes from 30 m to 6 km maximum displacement. They suggest that these values are larger than post-sedimentary faults of a comparable size by a factor of at least 2.

Interactions between neighbouring faults can cause the active fault trace of a syn-sedimentary fault to propagate, remain static or retreat during syn-sedimentary growth (Childs et al., 2003). The shapes of the upper tip line and displacement contours on syn-sedimentary faults reflect the high vertical displacement gradients where fault intersects the Earth's surface and are horizontal rather than curved (Fig. 2.11b and c; Childs et al., 2003). In reality, many faults include a syn-sedimentary section and a post-sedimentary section in which the fault geometry resembles that of a blind fault. The post-sedimentary section is that part of the fault that cuts the pre-faulting sequence, which was deposited prior to fault initiation. Such faults would show sub-horizontal, closely spaced displacement contours in the younger, syn-kinematic sequence and concentric displacement contours in the pre-faulting sequence (Fig. 2.11b; Childs et al., 2003). In seismic datasets in which the faults penetrate below the depth imaged by the data, the lower, curved tip line and the lower concentric contours of the post-sedimentary section can be absent. In such cases, the pre-faulting sequence is identified

by the curved, sub-vertical displacement contours that define the lateral component of fault growth. The point on the fault surface where there is a switch from sub-vertical contours to sub-horizontal contours marks the base of the syn-kinematic sequence (Fig. 2.11b; Childs *et al.*, 2003). A shift in the lateral position of this point reflects the lateral propagation of the fault tip during syn-sedimentary activity and can be used to identify fault growth or fault retreat.

2.2.3 Fault growth, linkage and fault population evolution

By plotting maximum displacement against width for a variety of faults, Watterson (1986) proposed a fault growth model:

$$D = W^2/P \tag{2.11}$$

where D is maximum displacement, W is the maximum dimension of the fault surface normal to the slip direction and P is a variable relating to rock properties. The model shows a non-linear relationship, i.e. the displacement increases disproportionately more than the fault width (or length). Conventional models of fault growth based on mathematical analyses of fault displacement-length populations suggest that faults grow by the simultaneous accumulation of both displacement and length (Walsh and Watterson, 1988). A more recent model proposed by Walsh *et al.* (2002), which was based upon an analysis of syn-sedimentary growth faults, suggests that the displacement to length ratio of faults progressively increases as they grow. In this model, fault growth is divided into two stages. During the first stage, the fault grows predominantly through the rapid (near-instantaneous on geological timescales) lateral propagation of the fault tips until the length of the fault is established. In the second stage, lateral growth is

retarded and the fault continues to grow mainly by the accumulation of displacement. This model is consistent with reactivated normal faults in the Timor Sea, in which the fault lengths in the cover sequence are inherited by rapid up-dip propagation from pre-existing basement structures (Walsh *et al.*, 2002). It may also be applicable to many other fault populations which are not necessarily reactivated (Childs *et al.*, 2003). The switch from lateral growth to displacement accumulation could occur because the lateral growth is impeded, as the faults in a population begin to interact at the fault tips (Walsh *et al.*, 2002; Nicol *et al.*, 1996; Walsh and Watterson, 1989).

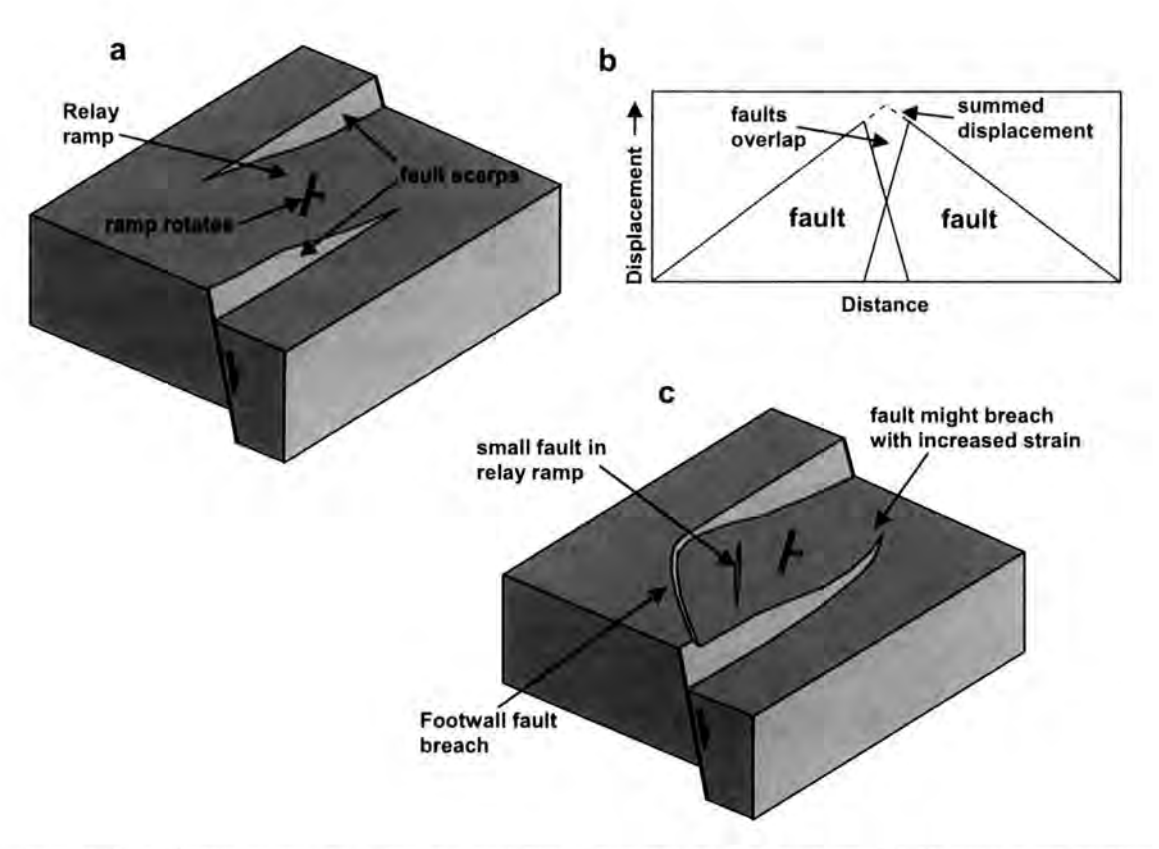


Figure 2.12: Relay ramps. a) 3-dimensional block diagram of a relay ramp. b) Displacement profiles. Displacement decreases on the two faults as they overlap. The profile of the summed fault displacement is that of a single fault with no deficit in the displacement. c) With increasing displacement and fault growth the relay ramp is breached by one or both fault tips or by newly formed faults. After Peacock and Sanderson (1991).

As faults grow, they interact and link with neighbouring faults. Synthetic faults, which have the same polarity of dip, can overlap and act as a single coherent fault. The displacement on the two faults is accommodated by ductile strain in the form of a relay ramp, which develops in the overlap zone (Fig. 2.12; Peacock and Sanderson, 1991). The faults show an abrupt decrease in displacement and increased horizontal displacement gradients within the zone of overlap (Childs et al., 1995; Fig. 2.12b). If the displacement on the two faults is summed and contoured, the resultant displacement pattern will resemble that of an ideal isolated fault and will show very little net displacement deficit (Fig. 2.12b; Peacock and Sanderson, 1991; Walsh and Watterson, 1991; Childs et al. 1995). The faults in this case are said to be "soft-linked", at least at the scale of observation (Fig. 2.12a). It is often the case that some deficit will remain when the displacements are summed in this way. This could be due to a ductile component of strain within the relay zone - for example, due to shear strain accommodated on small faults that exist on a scale too small to be seen on seismic reflection data (Walsh and Watterson, 1991). Faults with aggregate displacements that show significant deficits do not form a coherent structure and might have been active at different times.

With increasing displacement on the faults, a relay ramp can breach (Fig. 2.12c). Either or both of the faults will propagate across the relay ramp to physically link with the other. Alternatively, a new fault could initiate within the overlap zone and link with both faults (Peacock and Sanderson, 1991; Imber *et al.*, 2004). The faults are then hard-linked. This process of growth by linkage results in an increasing amount of the strain being accommodated on fewer, larger faults as the system evolves (Meyer *et al.*, 2002; Walsh *et al.*, 2003).

2.3 REACTIVATION

Structural reactivation is defined as "the accommodation of geologically separable displacement events on pre-existing structures" (Holdsworth et al. 1997). The reactivation of pre-existing faults and fabrics in the continental crust is known to influence the locations and structural architectures of rift basins. Structures such as faults and shear zones are thought to be long-lived zones of weakness that can reactivate repeatedly and may do so in preference to the formation of new faults (Holdsworth et al. 1997). Geometric reactivation describes a situation in which a deformation inherits the location or geometry of a pre-existing structure but with a different sense of movement. During kinematic reactivation the sense of displacement is similar between successive reactivation events (Holdsworth et al. 1997). Pre-existing fabrics can be discrete or pervasive (Morley, 1999). Discrete fabrics include faults, shear zones or major rheological or compositional boundaries. Pervasive fabrics are present throughout a large rock volume and induce a marked strength anisotropy. These include metamorphic fabrics such as cleavage, schistosity and gneissic foliation (Morley, 1999). Pervasive fabrics tend to influence the majority of the faults within a rift whereas discrete fabrics tend to influence more isolated structures to produce faults which may be atypical in terms of their location, geometry or orientation.

Fault orientations can directly reflect the orientation of the regional stress field, with localised re-orientation of structures due to the influence of pre-existing fabrics within the rift. Often, faults are either parallel to the basement fabric or perpendicular to the regional extension direction, or some combination of these two end-member types (Fig. 2.13).

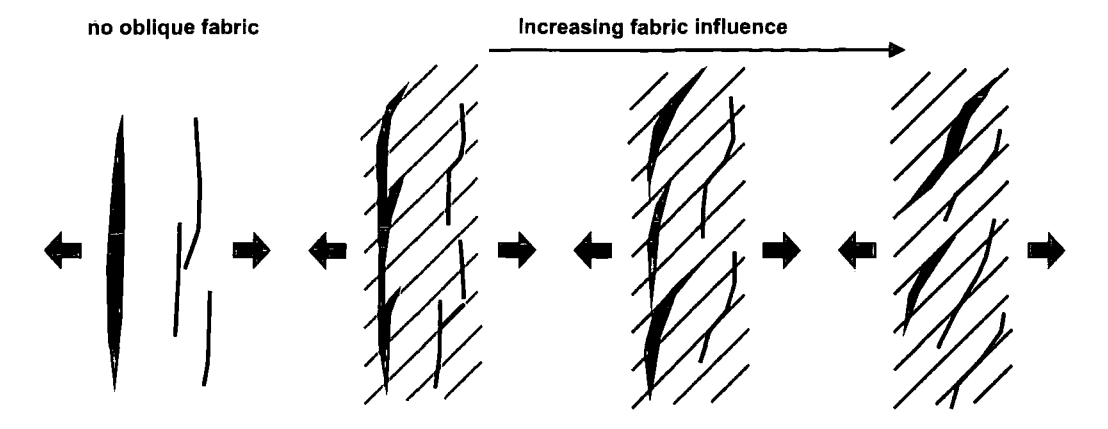


Figure 2.13: The influence of an oblique pre-existing fabric on fault geometry. After Morley et al. (2004).

Natural rifts commonly develop where there are a variety of pre-existing fabric orientations, locations and types, some of which may be exploited whilst others are ignored (Morley *et al.*, 2004). For example, the structure of the Mesozoic rifts of the North Sea has most likely been influenced by basement heterogeneity (Bartholomew *et al.*, 1993). It is often difficult to confidently identify reactivation, particularly in offshore settings where the basement or deep structure may be below the range of the seismic data, whilst the relatively poor resolution of the data prevents the use of traditional outcrop scale identification criteria (Holdsworth *et al.* 1997). Often geometric similarity ('trendology') – in which offshore structures have the same orientation as basement faults and shear zones exposed onshore – is relied upon to infer reactivation but this is not always a reliable indicator (Holdsworth *et al.* 1997).

The study of onshore and offshore examples and the use of physical analogue models have provided useful insights into the structural styles associated with reactivation. Pre-existing structures are often orientated obliquely to later directions of rifting and if reactivated will inevitably lead to transtensional deformation where the angles between the pre-exiting feature and the regional transport direction (α) will be important in determining the resultant fault patterns, as are the relative rheological strengths and intensities of the fabrics (Fig. 2.13). The range of fault orientations may

be increased by the influence of pre-existing fabrics and this effect varies depending on α (Withjack and Jamison, 1986; Fig. 2.7). Individual faults can form curved and sigmoidal geometries in plan view (McClay and White, 1995; Fig. 2.8). At most angles, faults will curve to follow the fabric but at higher angles (e.g. >70°) faults are more likely to cross the fabric (Morley, 1999 citing Blanton, 1982) or alternatively fault growth may be inhibited, resulting in a fault pattern with more numerous, closely spaced faults (Morley *et al.*, 2004). In the Timor Sea, the presence of a pre-existing fabric may have controlled the style of fault growth by encouraging very rapid lateral growth early in the evolution of the fault system and so establishing a near final length before accumulating displacement (Walsh *et al.*, 2002; Section 2.2.3).

CHAPTER 3. STRUCTURE AND EVOLUTION OF THE NAM CON SON BASIN

3.1 INTRODUCTION

The aims of this chapter are to describe and analyse the structures that have been modelled and to provide an overall appreciation of the structural evolution of the Nam Con Son basin. In the first section the structure is qualitatively described, including the distribution and geometries of the depocentres and structural highs. The deeper Oligocene-Eocene succession and the pre-Tertiary basement have proved difficult to constrain, with the basement only clearly seen on the 3-dimensional seismic data in the eastern corner of the survey area. The second section is a quantitative analysis of the faulting within the area, including the orientations and dip angles of the faults and how that varies spatially. The third section addresses the evolution of the structures through time using two methods. Firstly, isochron maps are used to establish which areas subsided the most and which subsided least during a particular time interval and, secondly, displacement backstripping techniques are used to constrain the timing of each fault. Another section addresses the folding within the area. A variety of small folds are mapped and described. The timing of folding is established using variations in the fold amplitude, and compared with the timing of the faulting. The amount of extension across the area is also addressed. To calculate the amount of extension, bed lengths and fault heaves have been measured on several 2-dimensional cross sections, which traverse the area through each graben. Finally, a study of the fault kinematics is presented. A small channel is identified within the syn-rift succession that is offset by a fault surface. This has been used to provide a finite slip vector for that fault.

3.2 REGIONAL GEOLOGICAL SETTING

The Nam Con Son Basin is one of several Tertiary rift basins on the continental shelf, offshore Indochina. It is located ~250 km southwest of the tip of the South China Sea ocean basin (Fig. 3.1a). The geometry of the Nam Con Son Basin is unusual when compared with many extensional rift basins. It is as much as 13 km deep, ~350 km long and ~200 km wide, a length to width ratio of < 2:1 (Fig. 3.1b). The dominant fault trend is N-S to NE-SW. The pre-Tertiary basement has been drilled on structural highs and is an assemblage of volcanic, igneous and metasedimentary rocks. The earliest rift fill has not been drilled but is thought to have been deposited in E-W trending half graben that formed during the Eocene to Early Oligocene based on interpretation of 2-dimensional seismic data and comparison with sedimentary fill in neighbouring basins (Matthews et al., 1997). The oldest, drilled sedimentary cover is the Late Oligocene Cau Formation (Fig. 3.2a), which is broadly distributed throughout the entire basin. This may have been deposited during a thermal sag phase following the earlier rifting (Matthews et al., 1997). By contrast to the older basin fill, the Miocene sequence, which comprises the Dua, Thong and Mang Cau Formations, is deposited in N-S and NE-SW trending graben and represents the main syn-rift phase (Fig. 3.2a). Throughout most of the basin, the top of the syn-rift sequence is defined by a regional unconformity that has eroded footwall highs and is associated with major channels/scours that locally truncate the Miocene rift faults (Matthews et al., 1997). This unconformity is dated as end-Middle Miocene and probably represents a major eustatic sea-level fall at 10.5 Ma (Haq et al., 1988). A Late Miocene to present-day post-rift sequence, comprising the Nam Con Son and Bien Dong Formations, overlies the unconformity and was deposited during thermal subsidence (Fig. 3.2a; Matthews et al., 1997).

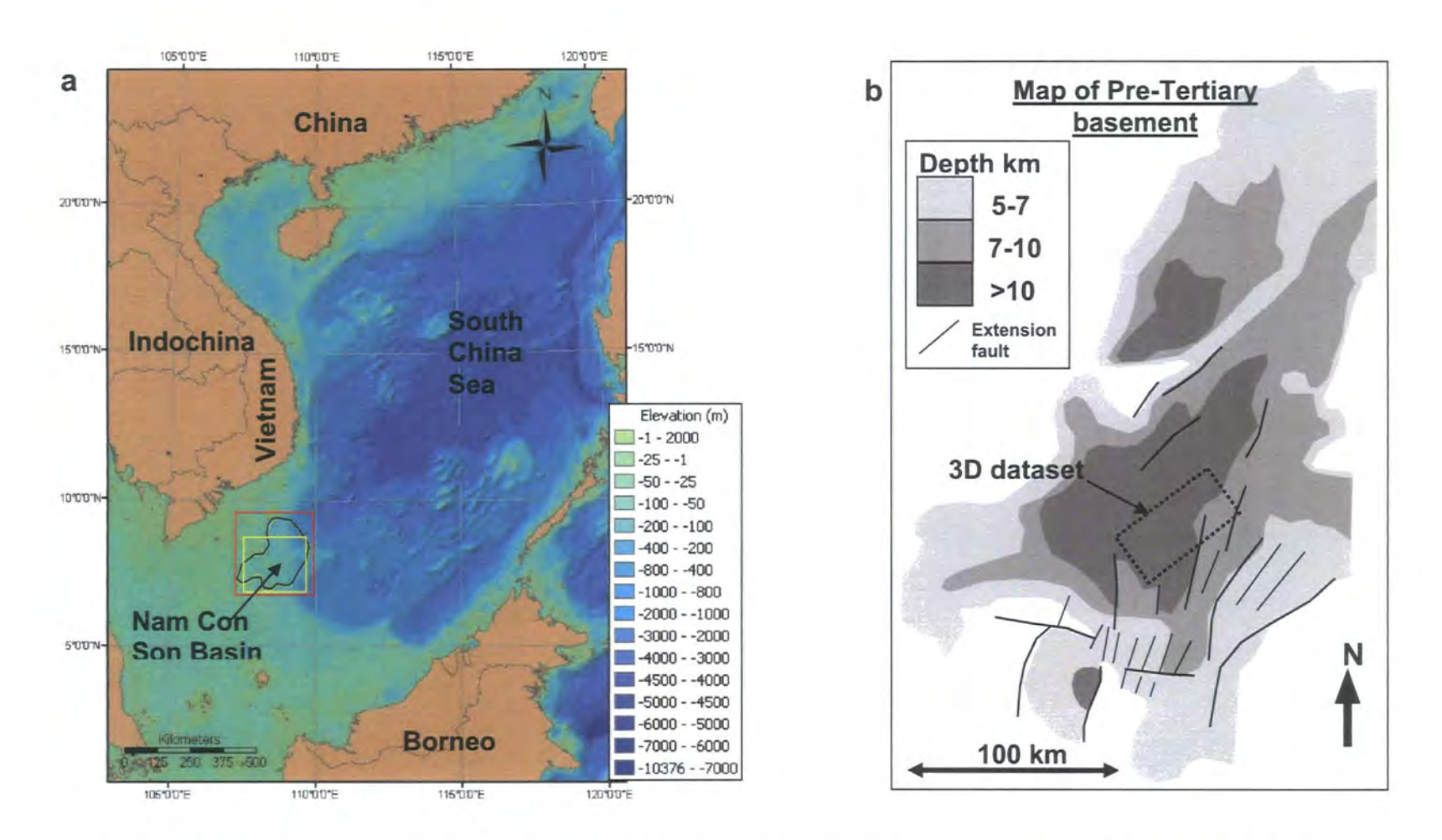


Figure 3.1: a) Map showing the bathymetry of the South China Sea and adjacent continental shelf. Bathymetry map is produced using the free air anomaly gravity data of Smith and Sandwell. The red outline shows the location of Fig. 3.1b and the yellow outline shows the location of Fig. 3.3. b) Depth to top basement with prominent faults. The east of the basin is open to the South China Sea rift. The area of 3-dimensional seismic data used for this thesis is located. After Huchon *et al.*, (1998); Matthews *et al.*, (1997) and BP Internal reports.

The post-rift sequence is mostly mudrock with isolated channel sands and represents the prograding Mekong Delta. The pre- to syn-rift sequence shows an overall deepening upstratigraphy from coastal deposits of sand and mudrock in the pre-rift Oligocene, to outer shelf and bathyal deposits of mostly mudrock in the syn-rift Middle Miocene (Matthews *et al.*, 1997). There are significant carbonate deposits on some footwall highs, particularly at basin margins (Matthews *et al.*, 1997). However, there is no evidence for their existence within the 3-dimensional seismic survey area and therefore this does not affect the parameters used in the depth conversion algorithm described in section 3.3.2.

Within the basin centre, in the area covered by the 3-dimensional seismic dataset, several wells have been drilled into the Early Miocene but have not reached the Oligocene sequence or basement (Vietnam Licence Team, 1995). The Early-Middle Miocene stratigraphy in this area is mostly mudrock with some thin sands (Fig. 3.2c). In places the amount of sand increases in the Early Miocene sequence. Unlike in the southeast of the basin, there is no evidence for significant carbonate deposits in the basin centre, although the wells do penetrate very thin carbonate layers in the Middle Miocene.

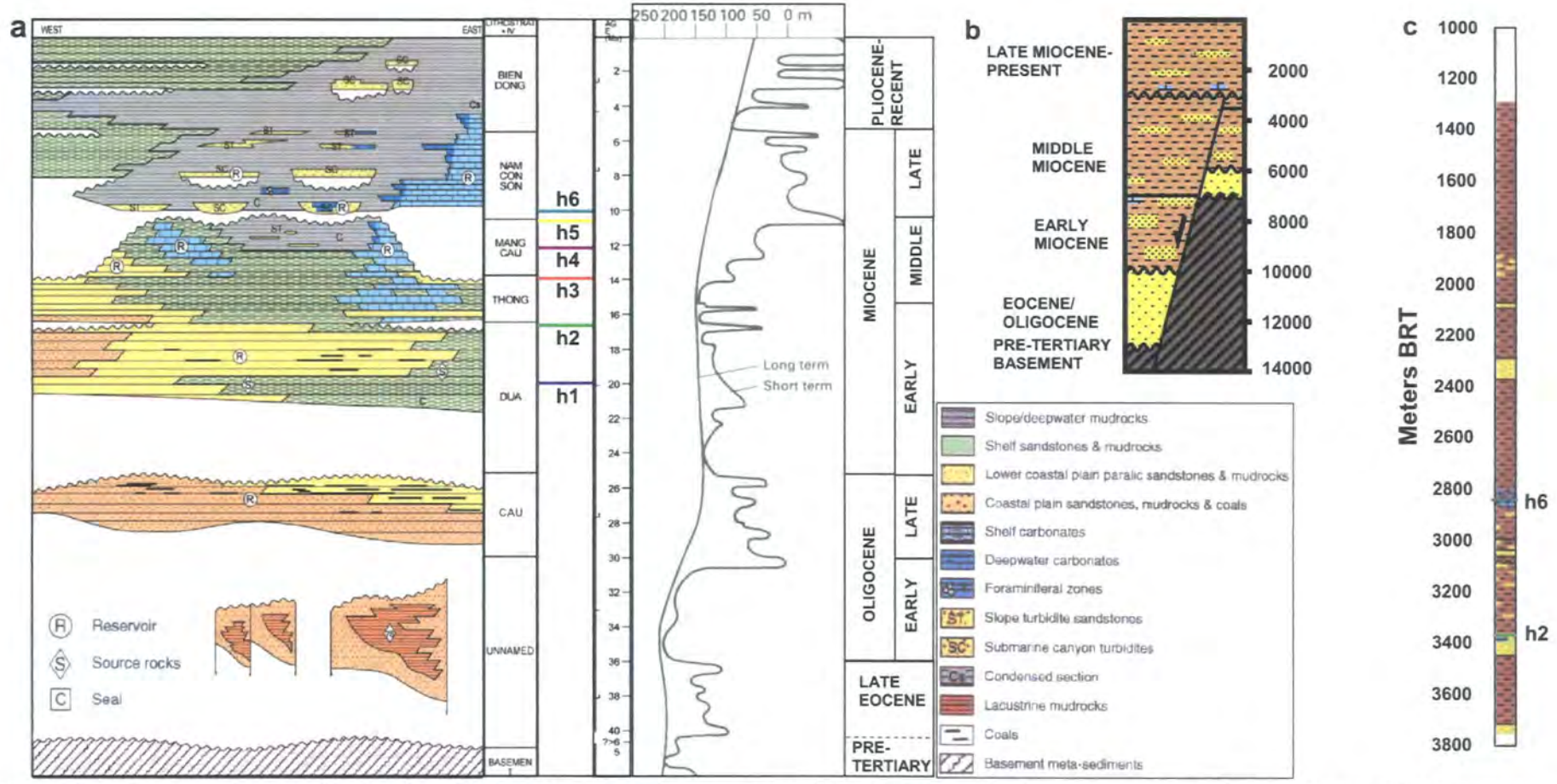


Figure 3.2: a) Chronostratigraphy of the Southeast Nam Con Son Basin (Matthews et al., 1997). Eustatic sea level curve from Haq et al., 1988. Horizons h1-h6 are marked. b) Generalised tectono-stratigraphy from the area of the 3-dimensional seismic dataset in the basin centre. Eocene/Oligocene is not drilled in the basin centre but is probably coastal plane sands based on the Oligocene stratigraphy in the southeast and a comparison with similar Eocene basin fill in region (After Huchon et al., 1998, Matthews et al., 1997 and Vietnam Licence Team, 1995). c) A well from within the area of the 3-dimensional seismic dataset. For location see Enclosure 1. Horizons h6 and h2 are marked and define the area of interest.

Figure 3.3 shows two maps that have been produced by the Asset team at BP using a regional grid of 2-dimensional seismic data. The first is a map of the top pre-Tertiary basement and the second is a map of an intra Early Miocene horizon (equivalent to horizon h2 described in section 3.3). The E-W trending faults that may have controlled Eocene-Early Oligocene rifting are evident on the top basement map but are buried by the Early Miocene sedimentary cover. Therefore, for tectonic faults the upper age of E-W faulting is Early Miocene (Fig. 3.3). The E-W fault trend suggests that during the Eocene-Early Oligocene the extension direction was ~N-S (Matthews *et al.*, 1997). This is consistent with the oldest magnetic lineations (~32 Ma) in the South China Sea which are oriented ~E-W (Briais *et al.*, 1993).

The Middle Miocene rifting was accompanied by the formation of large extensional rollover anticlines in the hangingwalls of graben bounding faults. It is possible that these rollover structures have been further deformed by a mild, contractional tightening but this is uncertain (Matthews *et al.* 1997). A number of graben centres appear to have been eroded as a result of mild uplift (Fig. 3.4; Matthews *et al.* 1997). It is possible that the Miocene folding was controlled in some way by the earlier E-W trending structures and that in places the anticlinal uplifts are locally developed orthogonal to the major Middle Miocene faults. There is no evidence, however, for net-reverse stratigraphic offsets on any Miocene faults (Fig. 3.4; Matthews *et al.*, 1997).

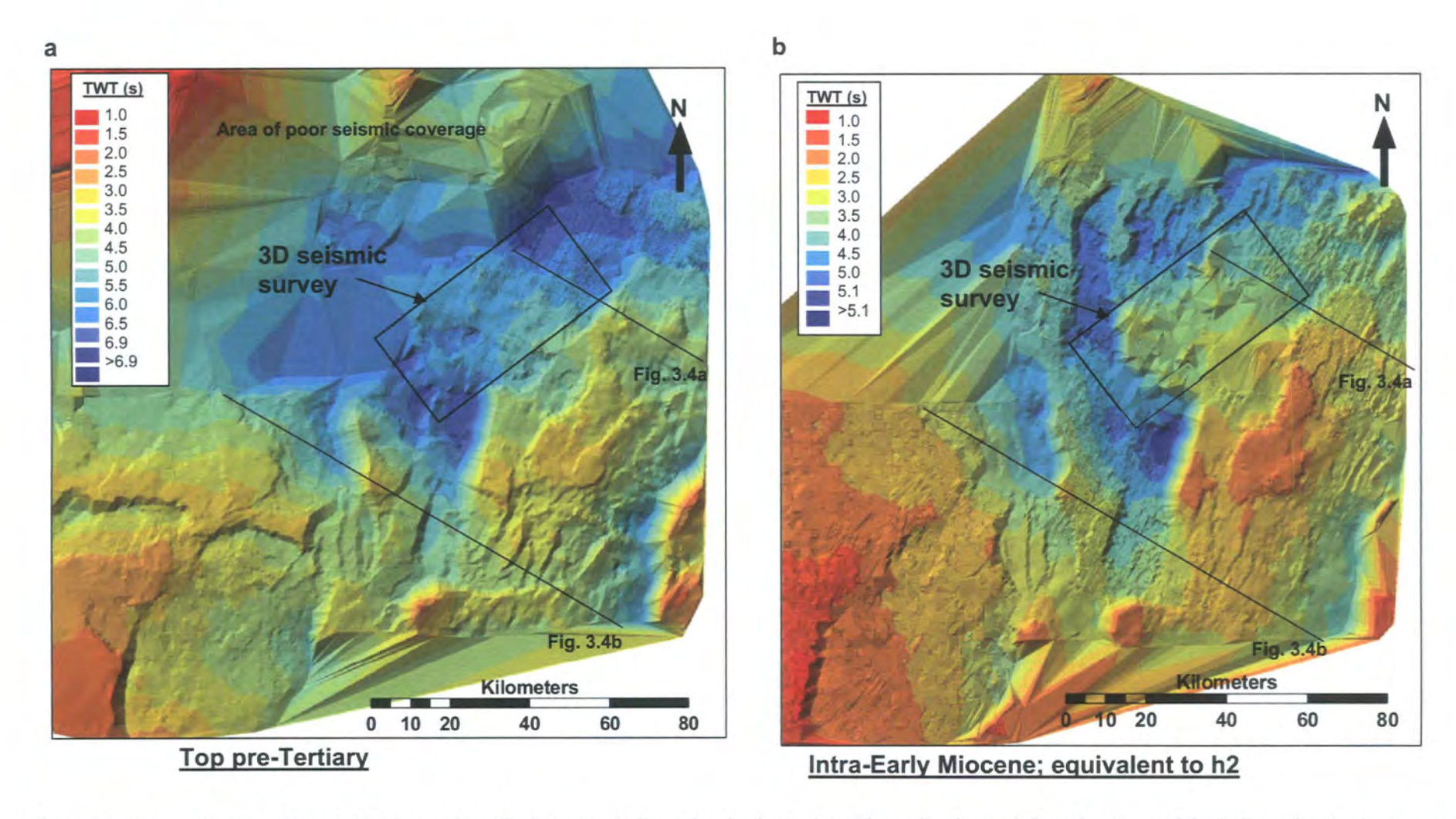


Figure 3.3: Maps of the Nam Con Son Basin, produced by BP using 2-dimensional seismic data. The outlined area defines the extent of the 3-dimensional seismic survey used for this thesis. a) Top pre-Tertiary basement. b) Intra-Early Miocene (syn-rift) horizon dated at ~16 Ma and equivalent to horizon h2 mapped during this thesis.

The contemporary stress azimuths for the Southeast Asia region give an indication of the complexity of the tectonic plate interactions that have persisted throughout the Tertiary (Fig. 3.5). A study of the magnetic lineations in the South China Sea by Briais et al. (1993) has dated the oldest oceanic crust here as 32 Ma (middle Early Oligocene) and the youngest as 15.5 Ma (end Early Miocene). During the Early Miocene the spreading centre propagated towards the southwest, reaching its present day position by 20.5 Ma (Briais et al. (1993); Fig. 3.6a). The driving mechanism of extension in the region is unknown and a number of tectonic models have proposed solutions to this fundamental problem. The Tertiary tectonics of South East Asia are thought to have been driven by a number of plate interactions, including the northward movement of the Indian indenter, the northward movement and eventual collision of the Indian-Australian plate and the westward subduction of the Pacific plate (Hall, 1997; Fig. 3.6a). The resulting regional-scale tectonic stresses interacted with the complex pre-existing Palaeozoic and Mesozoic structural architecture in the crust of SE Asia, which has undoubtedly influenced the Tertiary deformation, including the strike-slip reactivation of ancient sutures throughout Indochina (Metcalfe, 1996). Which of these plate interactions are significant or dominant and how the pre-existing structure may have influenced Tertiary deformation is not yet fully understood.

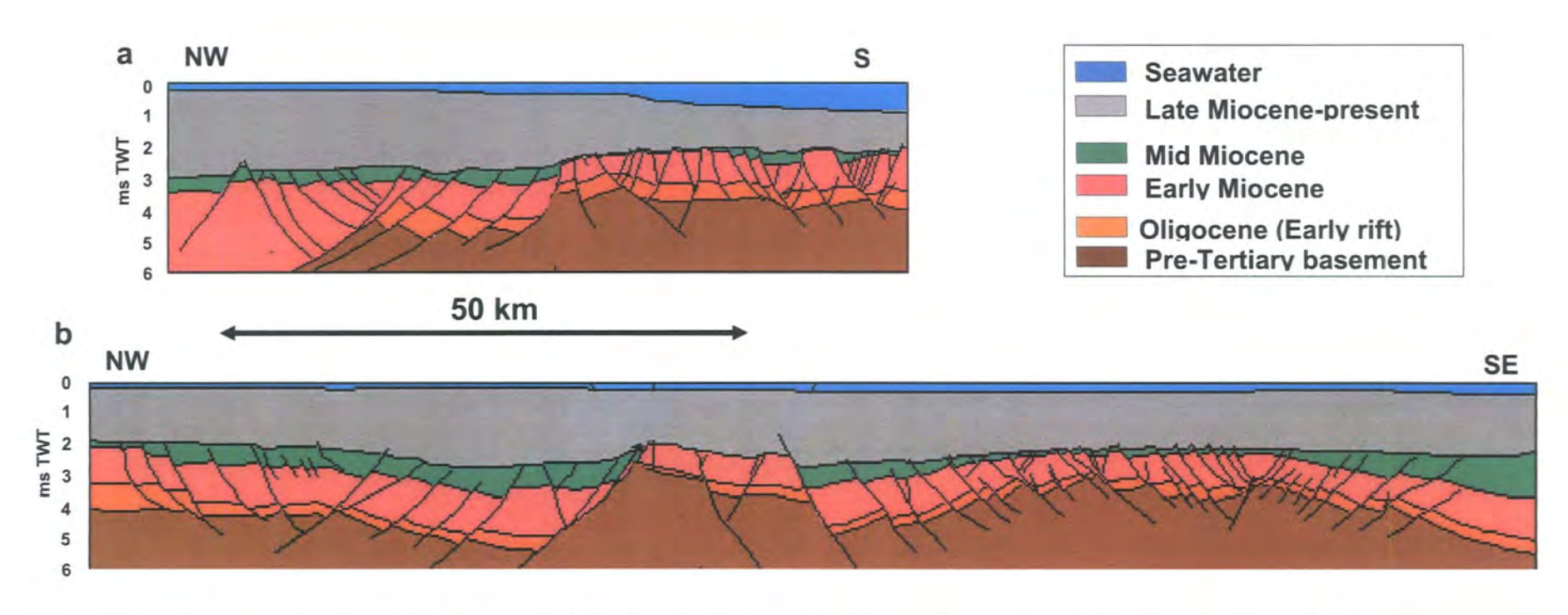


Figure 3.4: a) and b) Cross sections showing the structure to the east and south of the 3-dimensional seismic data, respectively (Matthews *et al.*, 1997). For locations see Fig. 3.3.

There are several major strike-slip shear zones that cross the Indochina continent and possibly continue offshore into the continental shelf region (Fig. 3.6a). The involvement of wrench tectonics in basin rifting is a possibility and a number of tectonic models have favoured this solution. In some models, rifting was a direct result of movement along strike-slip shear zones (e.g. Tapponnier *et al.*, 1986; Lui *et al.*, 2004; Tjia and Liew, 1996), whilst in others, the shear zones act as transfer faults and simply accommodate the extension rather than being the primary control on rifting (e.g. Morley, 2002; Hall, 1997; Huchon *et al.*, 1998).

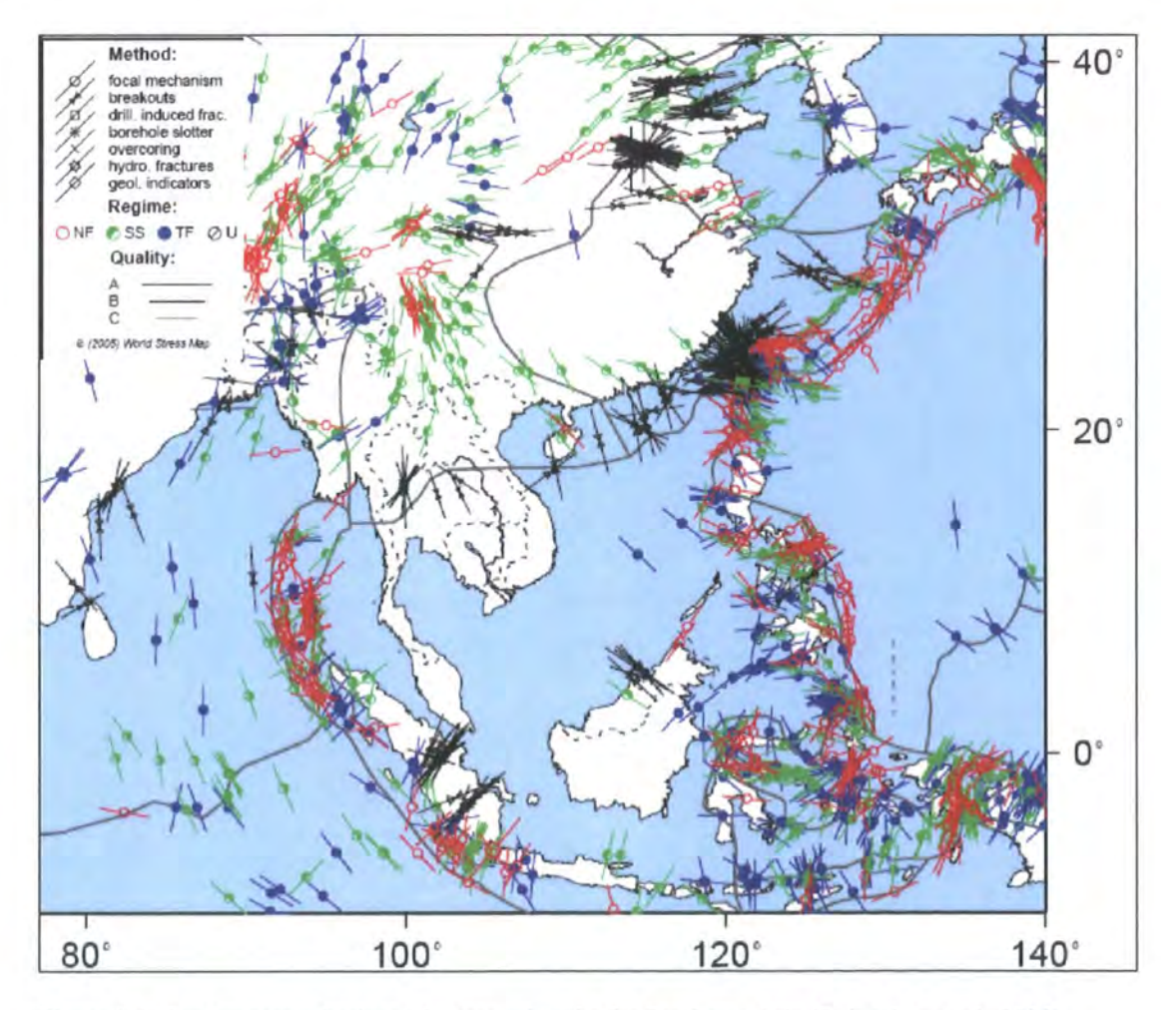


Figure 3.5: Contemporary horizontal stress azimuths for Southeast Asia (Reinecker et al., 2005).

Although there is little evidence for the existence of strike-slip structures within the Nam Con Son Basin, there could be major shear zones beyond the limits of the regional seismic data. The role of strike-slip tectonics in both the Eocene-Early Oligocene and the Miocene rifting phases is a possibility (Matthews et al. 1997). The conflicting data from onshore investigations of the shear zones and the lack of firm evidence for their offshore continuation means that their timing, shear sense and locations are not at all well constrained. Most models favour the area adjacent to the east Vietnamese coast as a location for a through-going shear zone but the sense of shear and whether this shear zone accommodates or drives South China Sea spreading varies between models (Tapponnier et al., 1986; Roques et al., 1997; Huchon et al., 1998; Morley, 2002). Seismic data from the Qui Nhon Ridge, off the east Vietnam coast, suggest a dextrally transtensional fault pattern with N-S and NE-SW trending normal faults some of which curve towards parallelism with the N-S trending Qui Nhon Ridge (Roques et al., 1997). Dating of the post-rift carbonates across this structure constrains the upper age of fault movement to 21 Ma, which coincides with the end of South China Sea spreading centre propagation (Roques et al., 1997).

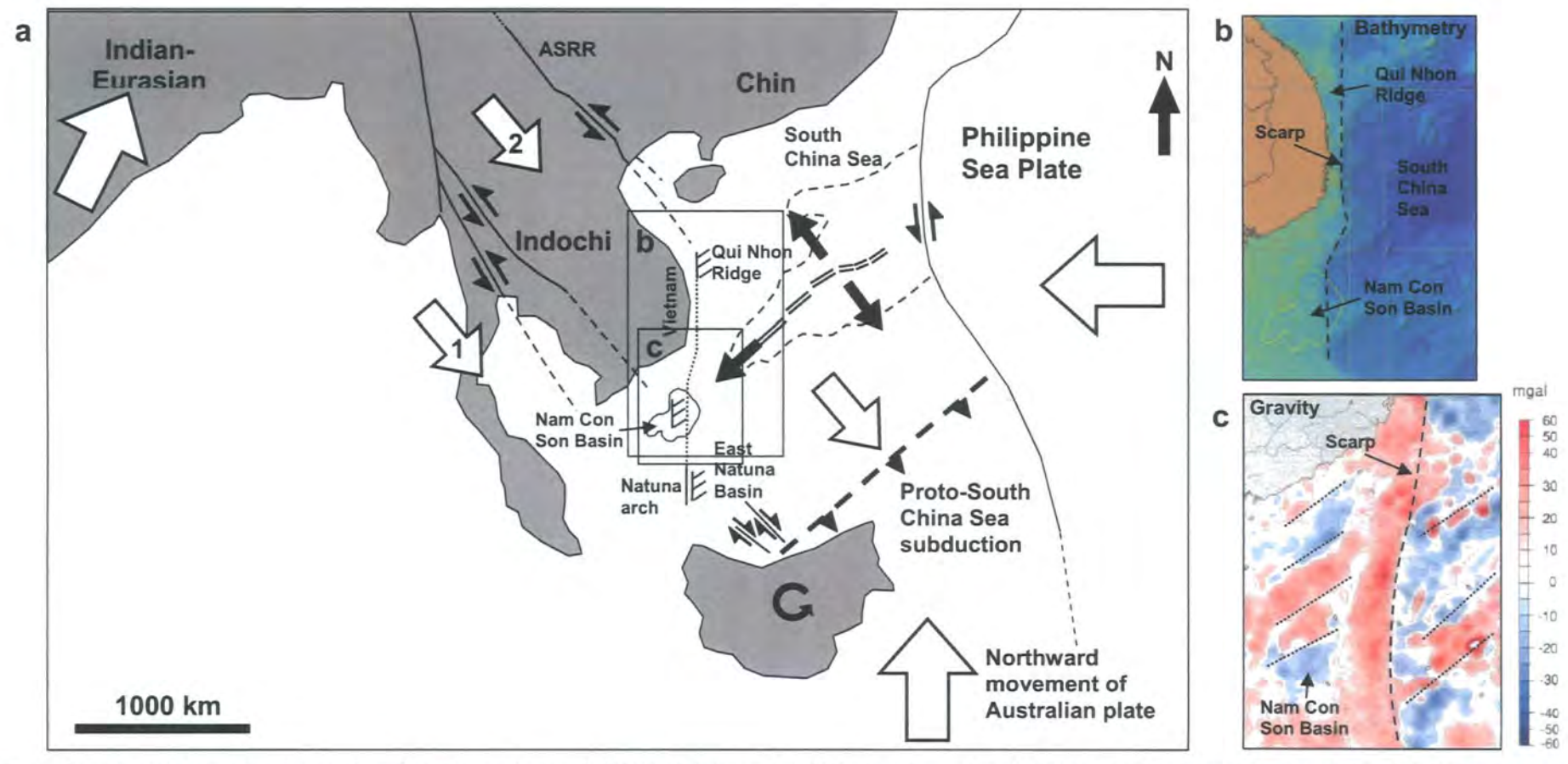


Figure 3.6: Map of the regional tectonics after Tapponnier *et al.* (1986), Briais *et al.* (1993), Rangin *et al.* (1995), Hall (1997), Mat-zin & Swarbrick (1997), Roques *et al.* (1997) and Morley (2002). Large arrows represent the tectonic displacements in the region. Numbered arrows represent the successive extrusion of the continental blocks (the escape tectonics model of Tapponnier *et al.* (1986). Extrusion progresses northwards with the northwards identation of India into Eurasia. b) Bathymetry map showing the location of the N-S trending scarp that defines the westernmost extent of South China Sea rifting. Satellite altimetry data from Sandwell and Sanderson (for colour-bar see Fig. 3.1). c) Gravity map (Huchon *et al.* 1998) showing the N-S trending scarp (bold dashed line) that defines the westernmost extent of South China Sea rifting and the dominant NE-SW trending structure (dotted lines). The scarp represents the proposed location and trend of the edge of the Indochina Craton (see text for explanation).

The western boundary of South China Sea rifting is defined by a linear 1 km high N-S trending scarp, which marks the edge of the continental shelf (Fig. 3.6b). The scarp runs along the eastern Vietnam coastline and through the Nam Con Son area. Gravity data highlights the scarp which defines a boundary between extended and thinned continental crust to the east and thicker continental crust to the west (Fig. 3.6c). This N-S structural trend continues south and is reflected in the N-S trend of the Natuna Arch, a structural high that bounds the western edge of the East Natuna Basin. Miocene faulting within the Nam Con Son Basin, the East Natuna Basin to the south and along the Qui Nhon Ridge to the north shows a consistent pattern of NE-SW and N-S trending faults (Fig. 3.6a; Roques et al., 1997; Matthews et al. 1997; Huchon et al., 1998). The NE-SW trending faults reflect the trend of the magnetic lineations in the South China Sea and are probably controlled by the ~NW-SE regional extension direction. It is possible that the N-S trending faults are controlled by a regional pre-existing basement fabric that corresponds to the rifted margin of the Indochina Craton which formed when the craton separated from Gondwanaland during Devonian (Metcalfe, 1996). The boundary between the Palaeozoic Indochina Craton to the west from Mesozoic ophiolitic crust to the east likely represents a strong rheological contrast which could have both localised and geometrically controlled later deformation. It is possible that this boundary inhibited the westward propagation of the South China Sea resulting in the prominent N-S trending scarp.

3.3 METHOD AND DATASET

The 3-dimensional time-migrated seismic dataset used for this study covers an area of 54.6 x 26.3 km or 1435 km² with lines spaced at 12.5 m intervals. The quality of the seismic data is very good, particularly within the Miocene-Recent syn-rift to post-rift interval and reaches a maximum two-way travel time of 6500 milliseconds (ms). Several wells have been drilled within the area of the 3-dimensional seismic survey, which provide velocity data, lithological data, depositional environment and dated formation tops, as used by BP. The dataset compliments an extensive grid of regional 2dimensional seismic data that has been used to map the basin, in particular the southeastern area (e.g. Fig. 3.3; Matthews et al. 1997). The 3-dimensional dataset is located in the basin centre, where the depth to top basement is greatest. The top basement has been modelled using an inversion of gravity data (Huchon et al., 1998). This indicates that in the area of the 3-dimensional seismic dataset, the highest point of the basement lies at a depth of 8-9 km in the eastern corner of the area and that it dips down towards the north and west down to a maximum depth of ~13 km (Fig. 3.1b). It predicts that the basement will be below the base of the seismic data throughout most of the survey area.

A fault/horizon model has been constructed using a combination of Schlumberger's IESXTM and Badley's TraptesterTM software. Fault segments were picked on inlines, crosslines and arbitrary lines in IESXTM and then imported into TraptesterTM to be modelled into gridded fault surfaces. Figure 3.7 is a 3-dimensional image of the fault surfaces. In total 225 fault surfaces have been modelled.

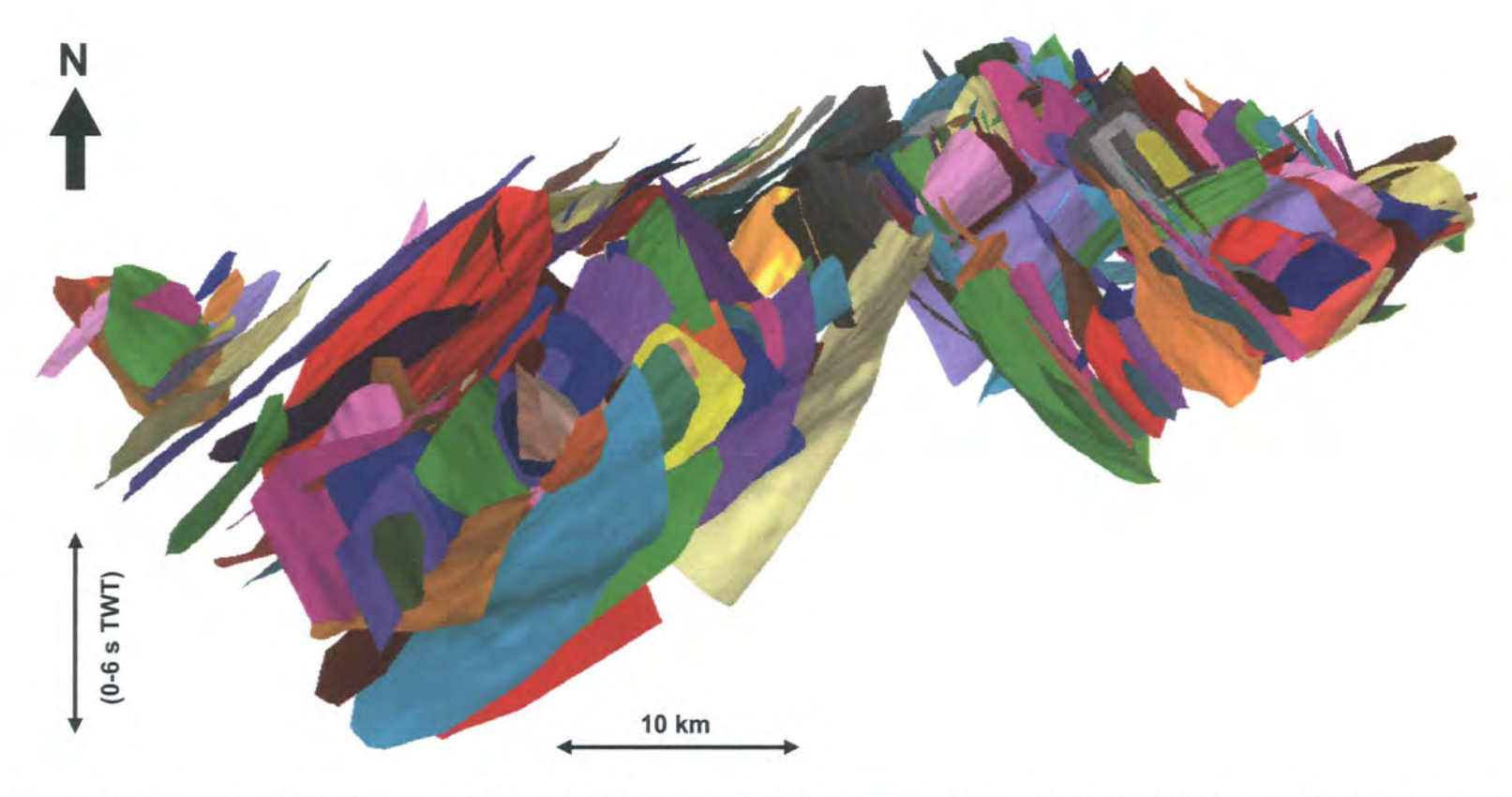


Figure 3.7: 3-dimensional image of the modelled fault surfaces from Badley's Traptester software. The image is in the time domain and has a x2 vertical exaggeration. In total 225 fault surfaces have been modelled.

Six stratigraphic horizons have been interpreted within the syn-rift sequence and are labelled h1-h6 from the oldest to the youngest, respectively (Fig. 3.8). The horizons were picked on strong, laterally continuous seismic events rather than being tied to stratigraphic well picks. It was important for this study that the horizons could be confidently picked across the whole survey area. Synthetic seismograms were not used due to a lack of well data. Interpretations were made on every 20 inlines and crosslines across the whole survey area. The density of seed picking was increased in areas of complex faulting or folding and adjacent to some fault surfaces and tips. In addition, arbitrarily oriented (composite) sections were used to tie horizons around fault tips and through areas of complex structure. The use of this technique is crucial in such a densely faulted area. The faults were interpreted on sections aligned roughly orthogonal to the fault strike, with a maximum 250 m (20 inlines or crosslines) between fault sticks/segments.

Although the horizons were picked using seismic character only, a comparison between the horizon-well intersections and the available BP well picks/formation tops provided approximate ages for the horizons, which range from ~18 Ma to ~10 Ma, respectively, Early Miocene to the end of the Middle Miocene. Horizons h1-h3 are within the Early Miocene sequence, h2 is dated as ~16.5 Ma and h3 roughly coincides with the end of the Early Miocene. Horizons h4-h6 are within the Middle Miocene, h6 is dated at ~10.5 Ma, the end of the Middle Miocene. In the eastern part of the survey area, the youngest three horizons, h4-h6, are incised by an undulating erosional surface (Fig. 3.8). However, the eroded area is relatively small and the results of the quantitative fault analysis presented within the thesis are not significantly affected.

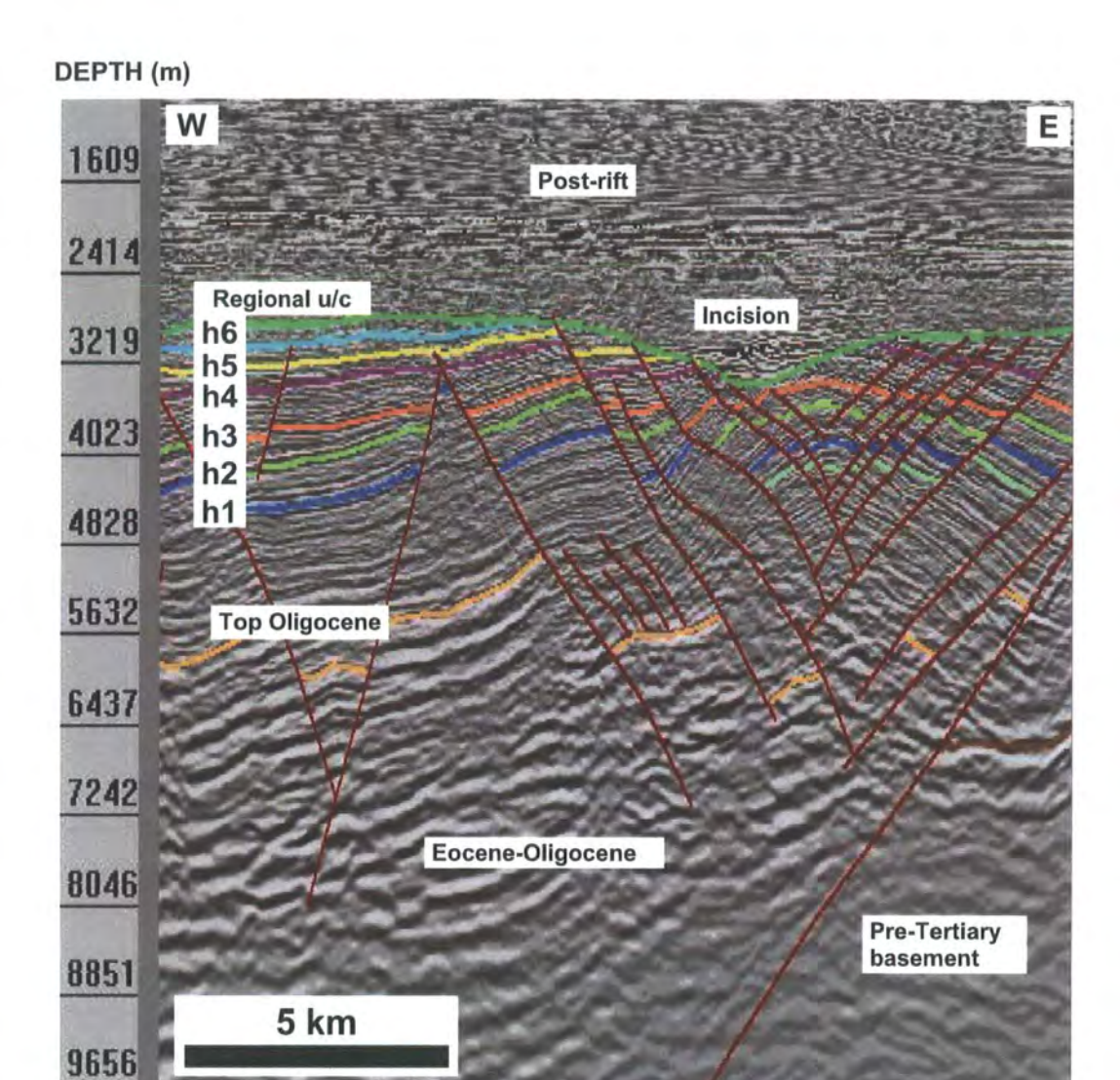


Figure 3.8: Example seismic cross section from the southeastern part of the 3-dimensional seismic dataset. For location see Fig. 3.9.

Figure 3.9 shows the h2 horizon (Intra-Early Miocene), interpreted using the 3-dimensional seismic dataset (outlined), superimposed upon the equivalent horizon as mapped by BP using 2-dimensional seismic data (see Fig. 3.3b). This demonstrates the increased structural detail that has been achieved using the 3-dimensional seismic data. The two interpretations were produced independently of each other and yet the similarity between them is clear. The deeper areas of the basin and the structural trends including major fault scarps that were mapped using 2-dimensional seismic data 'mesh' seamlessly with the structures mapped using 3-dimensional seismic data. This provides a high level of confidence that the interpretations are accurate.

The study presented within this thesis focuses on the Early to Middle Miocene syn-rift succession, which coincides in timing with the southwestward propagation of the South China Sea towards the Nam Con Son area. The majority of faulting within the basin is focussed within this succession and the apparent complexity of the fault pattern is of interest. At the depth of the Early to Middle Miocene, the quality of the 3dimensional seismic data are high and are ideally suited to the use of quantitative techniques which require a high level of accuracy. Despite the poorer data quality at depth, the top Oligocene and top Basement have been picked in some sections/areas but with less certainty or accuracy and so have not been used for the quantitative analysis. The top of the Oligocene has been picked as a clearly defined change in the seismic character from shorter wavelength reflectors in the Miocene to stronger reflectors with longer wavelengths in the Oligocene (Fig. 3.8). This change is not gradual such as that due to the attenuation of the seismic energy. The top-Pre-Tertiary basement is picked as a strong laterally continuous reflector that defines the top of an area of relatively transparent seismic character (Fig. 3.8). The interpretation of the top basement has been further constrained using the top basement map of Huchon et al. (1998), produced using

an inversion of gravity data (Fig. 3.1b). There is clearly a complex structure at depth but it has proved very difficult to interpret this with any degree of certainty. It has not been possible to interpret the 3-dimensional geometries of stratigraphic or structural surfaces at depth as many potential targets imaged on 2-dimensional sections have proved to be laterally discontinuous in 3-dimensions.

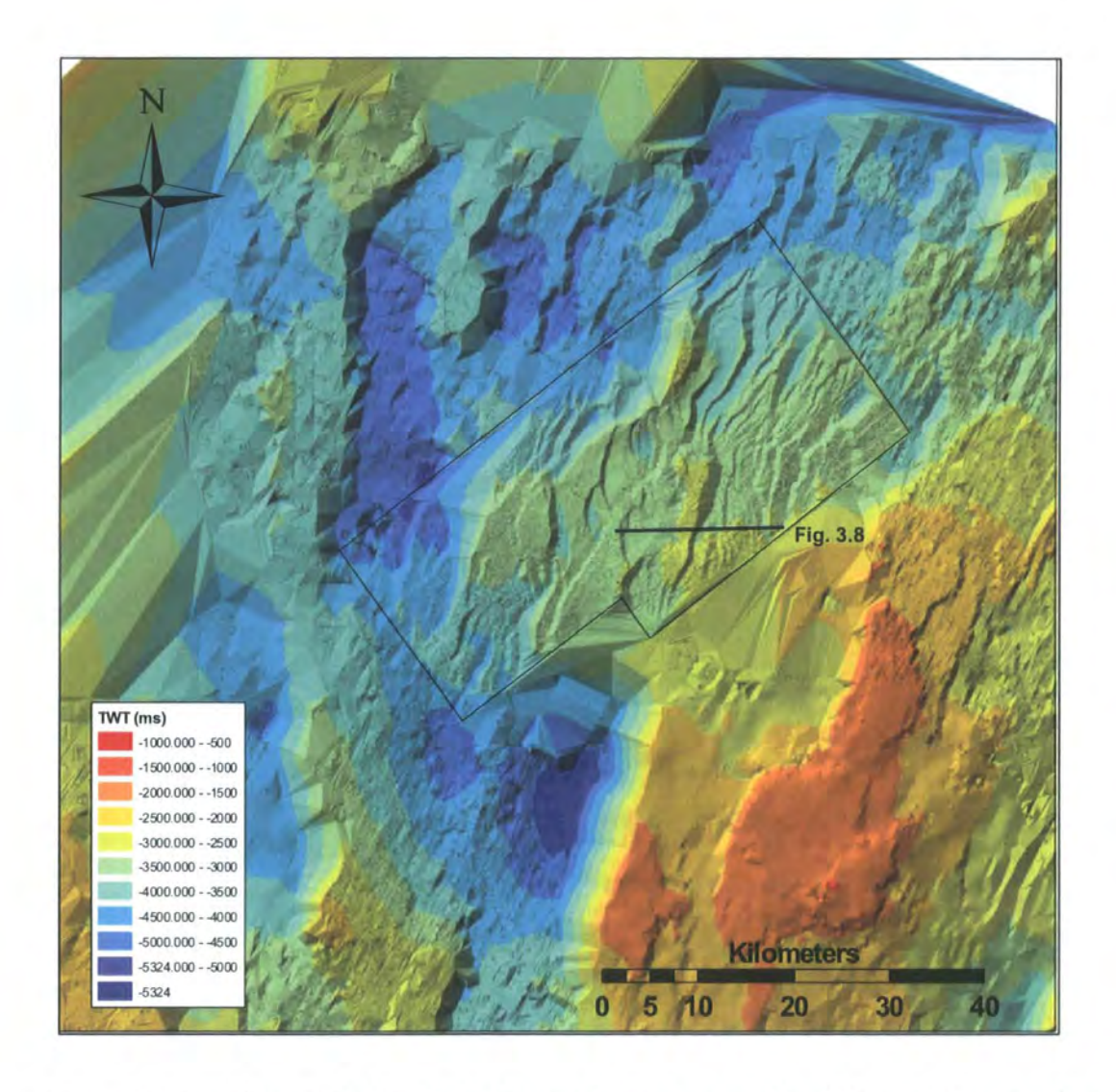


Figure 3.9: Central part of the Intra-Early Miocene horizon as mapped by BP using 2-dimensional seismic data (central part of Fig. 3.3b). The equivalent horizon, h2, interpreted from the 3-dimensional seismic data is superimposed. The area of 3-dimensional seismic data is outlined.

3.3.1 Sampling faults

By using Badley's TraptesterTM software, the hangingwall and footwall intersections for each horizon can be accurately modelled on the fault surface. Throughout this thesis, the hangingwall and footwall cutoffs of a given stratigraphic horizon on a fault surface define a fault polygon. Once modelled, TraptesterTM uses the fault polygons to calculate various fault attributes including apparent throw, apparent heave and dip azimuth. The software extracts fault attributes from the polygons using two different sampling strategies (Fig. 3.10). The first method uses an array of regularly spaced sample lines, each of which is automatically aligned orthogonal to the dip azimuth of the fault surface at each sample point (Fig. 3.10a). The second uses a grid of regularly spaced lines with a fixed azimuth that has been manually set by the interpreter (Fig. 3.10b). The first method describes the geometry and orientation of the fault polygons without making any assumption regarding the slip direction of the fault. This method has been used to calculate dip azimuth and fault offset, which is defined in section 4.2 (Fig. 4.2). The second method quantifies the amount of offset in a particular direction. This method has been used to constrain the timing of fault movement and the grids were aligned parallel to the mean dip azimuth of each fault.

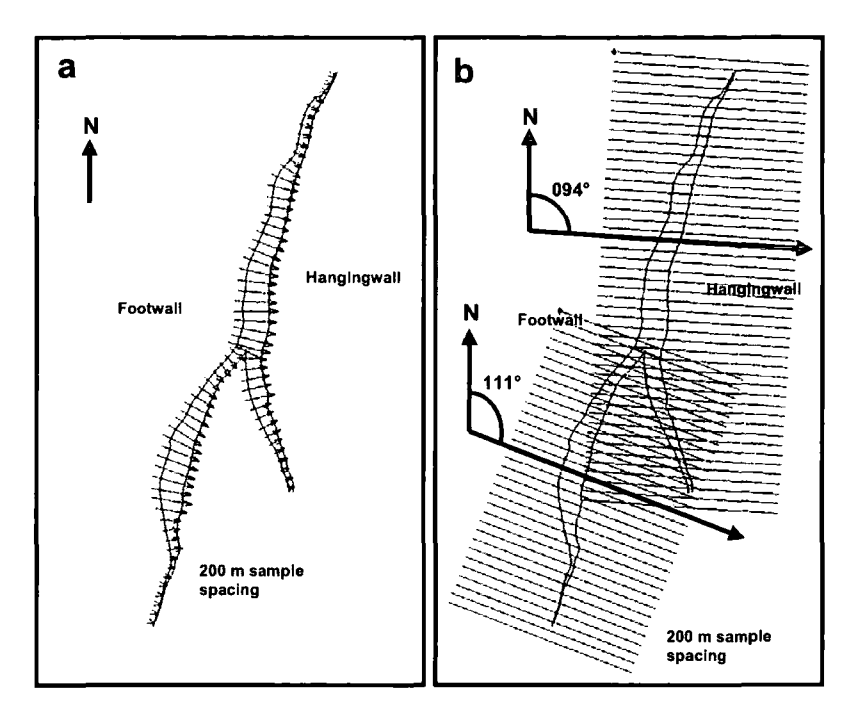


Figure 3.10: Sampling methods used by Badley's Traptester software. The fault polygons for one horizon are shown for two linked faults. Both faults dip towards the ESE. a) trace sampling method (set by the interpreter). b) grid sampling method (set automatically). In both cases the sample spacing is 200 m. The azimuths of the grids in b are the mean dip azimuths calculated from the trace sampling method shown in a.

The data have been exported in ascii file format and imported into Microsoft Excel, GEOrient and EZ-Rose (Baas, 2000) for analysis. The result is a database of fault attributes that describe the dip and dip azimuth of the fault surface and the amount of offset (in ms two way time) on each horizon at regularly spaced points along the length of each fault.

3.3.2 Depth conversion

The exported fault data were depth converted prior to analysis using the equation:

$$Z = V_0(e^{kt} - 1)/k (3.1)$$

where Z is depth, V_0 is the interval velocity, t is the one way travel time and k is the change of velocity with depth (Marsden, 1998). In order to determine values for V_0 and k, the algorithm was used to plot a curve of depth versus time and V_0 and k were adjusted until a best fit was found with the available well data from the area, which extend to ca. 4.5 km depth (Fig. 3.11).

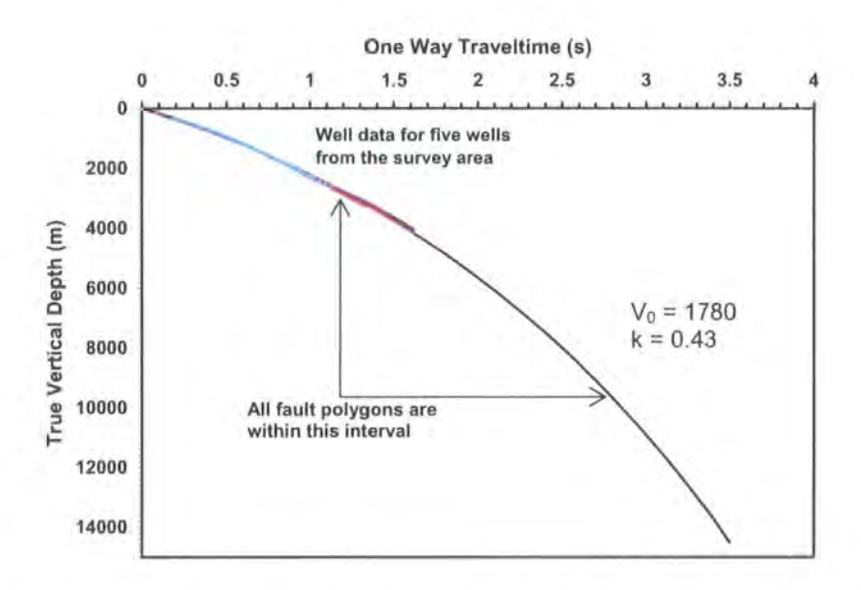


Figure 3.11: Depth versus time plot. A curve $Z = V_0(e^{kt}-1)/k$ is plotted with V_0 =1780 and k=0.43. The parameters V_0 (velocity at the surface) and k (change of velocity with depth) were adjusted until a best fit was found with the available well data. The time/depth data from five wells, from within the area of the 3-dimensional seismic data, are plotted as coloured points.

Within this part of the basin the stratigraphy is relatively uniform and there is no evidence for evaporites or thick carbonate deposits (section 3.2). Well data show that the post-rift and syn-rift stratigraphy is mostly mudrock, with some thin sandstone units that become slightly more prominent towards the base of the syn-rift section (Fig. 3.2). The depth versus time data from the available wells plot as continuous, smooth curves with no evidence for significant velocity changes across stratigraphic units. The relatively uniform section and the absence of any strong lateral velocity changes justifies the use of a single depth conversion for the whole section (one interval) and across the entire survey area. Inspection of the seismic data also precludes the presence

of thick evaporite or carbonate units below the depth of well penetration. Thus, although it is not possible to rule out other factors that could cause an abrupt change in velocity (e.g. the presence of deeper, overpressured layers), these observations provide a rationale for using the same depth conversion parameters down to ca. 10 km depth (Fig. 3.11).

The validity of the depth conversion method is supported by two independent studies. Firstly, the predicted depth to the top basement is consistent with that of Huchon *et al.* (1998) who mapped out the top basement using gravity data (Fig. 3.1b). Secondly, the depth to horizon h2 coincides, in two wells, with that of the equivalent horizon, interpreted at BP and depth converted using a more complex velocity model. In addition, the sensitivity of the data analysis to the depth conversion method has been tested. This reveals that varying the V_0 and k values within the range of the available well data does not significantly affect the results of the data analysis.

3.3.3 Constraining the timing of fault movement

The timing of fault activity has been constrained for 225 modelled faults using a variety of quantitative and qualitative techniques. The most important of these techniques is based on an analysis of the amount of offset on each horizon cut by the fault (e.g. Childs *et al.* 2003). By using this method, syn-sedimentary fault growth can be identified.

Syn-sedimentary tectonic normal faults are those that were active during the deposition of the sedimentary sequence. The difference in elevation between the footwall and hangingwall controls the relative sediment thickness across the fault and, assuming that sedimentation keeps pace with subsidence, produces a thicker sedimentary sequence in the hangingwall (Petersen *et al.* 1992; Childs *et al.* 2003). Because the sediments are being deposited whilst the fault is active, the older sediments

will have been subject to a longer history of fault movement than the younger sediments. Thus, pre-faulting and older syn-faulting horizons will record greater offsets than younger syn-faulting horizons. It is this variation in offset of different stratigraphic horizons that has enabled the timing of fault activity to be established (Childs *et al.* 2003).

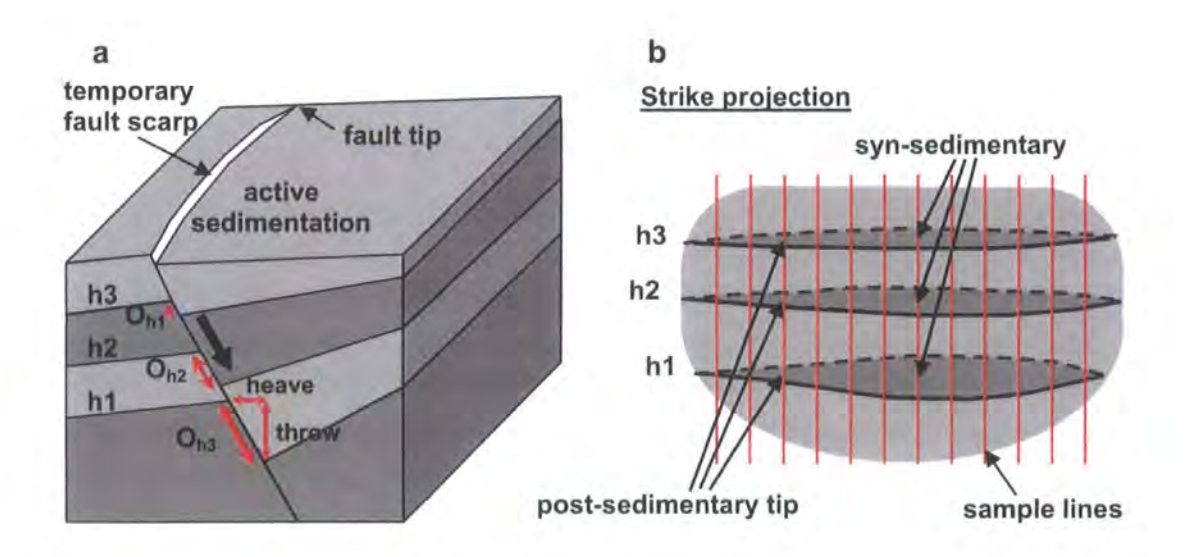


Figure 3.12: a) 3-dimensional cartoon of a syn-sedimentary tectonic fault intersecting three horizons h1-h3. The upward decrease in offset between horizons may indicate syn-sedimentary fault movement. b) A strike projection of the same fault surface with an orthogonal sample grid. The amount of offset on the horizons is sampled along each grid line. The fault centre shows a decreasing upwards offset consistent with syn-sedimentary fault movement from horizon h1 onwards. The fault tip shows equal offset on all three horizons indicated that movement occurred after the deposition of h3. The fault tip is younger than the fault centre, thus the fault has grown laterally through time.

Displacement backstripping techniques can only be accurately applied if the rate of sedimentation into the fault hangingwall kept pace with the rate of displacement and so preserving the thickness changes across the fault (Prosser, 1993; Childs *et al.* 2003). The Early to Middle Miocene depositional environment in the central Nam Con Son Basin was an inner to outer continental shelf (Vietnam Licence Team, 1995), where there would probably have been an adequate supply of siliclastic sediment to keep pace with basin subsidence. A thorough inspection of the seismic character in the survey area

has revealed no onlap or offlap relationships (Prosser, 1993) and no footwall erosion (Nicol *et al.*, 1997) during the Early to Middle Miocene syn-rift interval, any one of which could indicate a lull in the sediment supply rate relative to the rate of subsidence. It is therefore reasonable to conclude that in this part of the basin, the sediment supply rate kept pace with the rate of subsidence and that the use of fault offsets to determine the timing of fault movement is justified.

The offset across each fault surface has been sampled at different stratigraphic levels using a grid with a fixed azimuth aligned parallel to the mean dip azimuth of the fault surface (Fig. 3.12b). The mean dip azimuth was determined initially using the trace sampling method (Fig. 3.10a). The grid sampling enables the amount of offset on one horizon to be compared with that on the horizon above at the same point along the fault strike. An increase in the amount of offset between a younger horizon and an older horizon, as measured along a sample grid line, is an indication that the fault was active during the time between the deposition of those two horizons. However, the variation in offset can only be interpreted as a reliable indicator of syn-sedimentary faulting when the change in offset up the fault plane exceeds a critical value. Small variations in offset can result from the systematic decrease in strain from a maximum at the fault centre to zero at the tip line, as modelled for post-sedimentary faults (Section 2.2.1; Barnett *et al.* 1997). To discriminate between syn- and post-sedimentary faults, the variation in offset between two horizons can be quantified using vertical displacement gradients:

$$G = d_1 - d_2/z (3.2)$$

where G is the vertical gradient, d_1 and d_2 are the apparent displacements (offsets) on the older and younger horizon respectively and z is the distance measured

down dip and parallel to the fault surface, between the centre points of the fault polygons. The minimum displacement gradient below which the variations in offset could be due to strain variation on a blind fault is not precisely quantified. However, the value does increase with increasing fault size and is thought to be relatively large for seismically imaged faults compared to those studied in mining plans and outcrop (Nicol et al., 1996). For this study a minimum gradient figure of 0.22 was used based on vertical displacement gradients reported in Nicol et al. (1996). Hence in Chapter 3, all those faults referred to as 'syn-sedimentary' have vertical displacement gradients > 0.22.

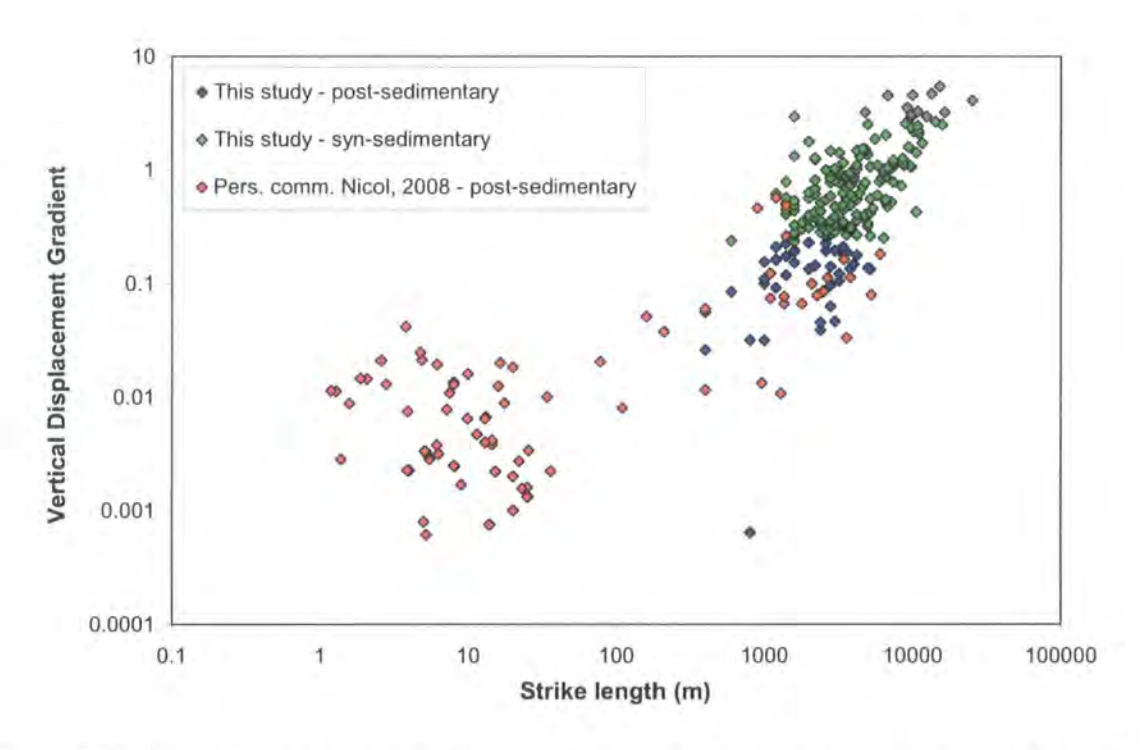


Figure 3.13: Comparison of vertical displacement gradients for post-sedimentary and syn-sedimentary faults. Fault data supplied by A. Nicol (pers. comm. Nicol, 2008) of predominantly post-sedimentary faults from outcrop, coal mine plans and seismic data. Fault data for this study are divided into syn-sedimentary and post-sedimentary faults, i.e. those faults with displacement gradients of greater than 0.22 and less than 0.22, respectively.

Figure 3.13 is a comparison between post-sedimentary and syn-sedimentary faults. The vertical displacement gradients increase with increasing fault size and this increase is greater for syn-sedimentary faults than for post-sedimentary faults.

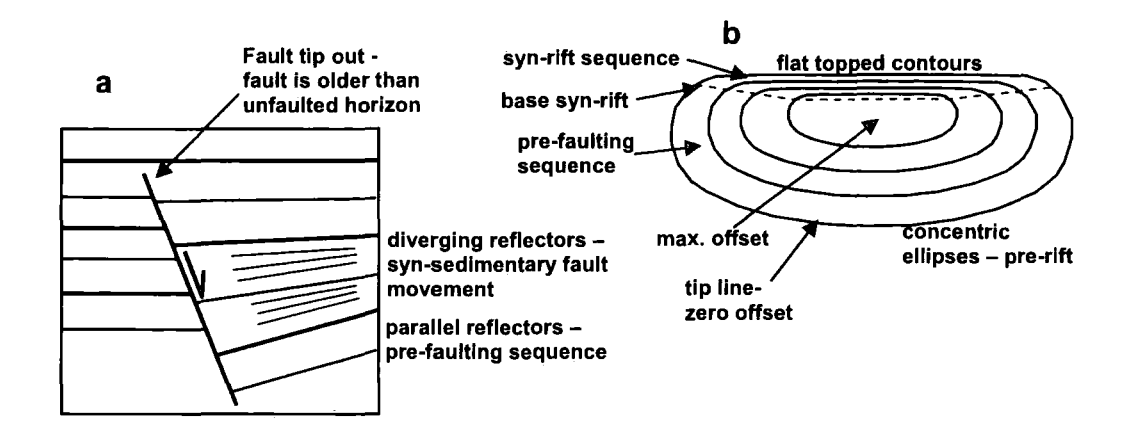


Figure 3.14: Cartoon to demonstrate the use of seismic reflector geometry (a) and displacement contours (b) to identify the timing of syn-sedimentary fault movement.

Additional qualitative evidence such as displacement contours (Childs *et al.*, 2003), divergent hangingwall reflectors (Cartwright, 1991), the vertical positions of fault tips and the interactions between adjacent faults, e.g. cross cutting relationships, have been used wherever possible to further constrain fault timing (Fig. 3.14). The position of the upper and lower fault tips can provide very reliable age constraints. For syn-sedimentary faults the position within the stratigraphy of the upper and lower tips provides a very reliable minimum and maximum age for fault activity, respectively. In this dataset the maximum age for 34% of faults was constrained using this method.

3.4 THE STRUCTURAL MODEL

3.4.1 Cross sections

The 3-dimensional seismic volume has been sliced to produce eleven 2-dimensional cross sections that illustrate the key structural aspects of the model (Figs. 3.16 to 3.26). The locations of the cross sections are shown on figure 3.15, which is a structure map of horizon h2. The cross sections are labelled by figure number.

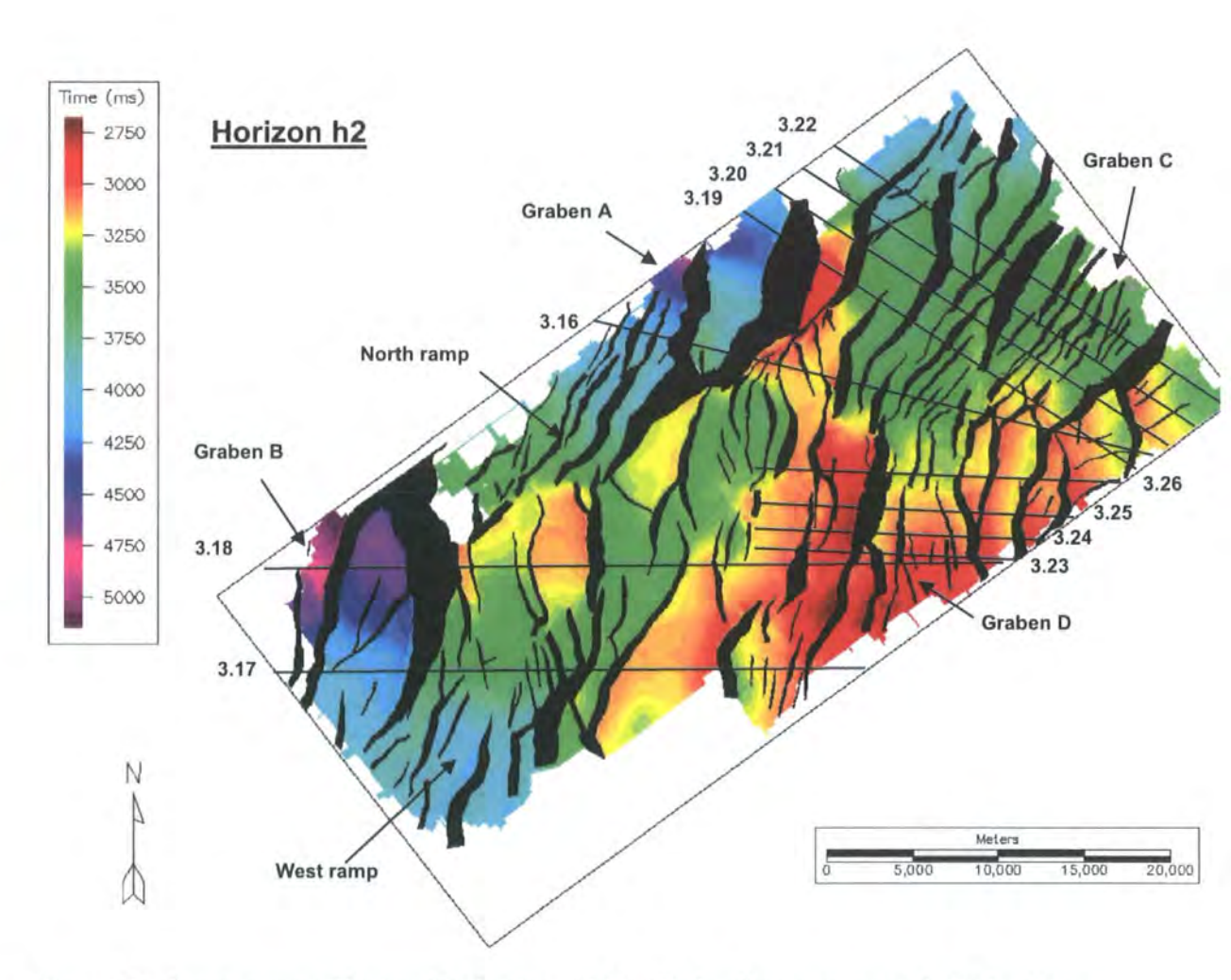


Figure 3.15: Structure map of horizon h2, dated to ~16 Ma. Black polygons represent the fault polygons. Colour bar is in TWT (ms). The main structural features are labelled and the locations of the cross sections are shown.

The seismic data and structural interpretation have been imported into Midland Valley's 2-dimensional Move software and depth converted using an identical method and

algorithm to that discussed in section 3.3.2 (Eq. 3.1). Therefore, the depth converted 2-dimensional cross sections and the depth converted fault attribute data used for quantitative analysis are comparable and consistent. The depth sections are displayed with an aspect ratio of 1:1, they are not vertically exaggerated. In all cases the cross sections have been aligned so that they are perpendicular to the faults that they intersect. Each cross section is presented with and without seismic data. In addition to horizons h1-h6, the Late Miocene unconformity, an intra-Early Miocene stratigraphic horizon, the top-Oligocene and the top-pre-Tertiary basement are also shown. The cross sections are referred to throughout chapter 3.

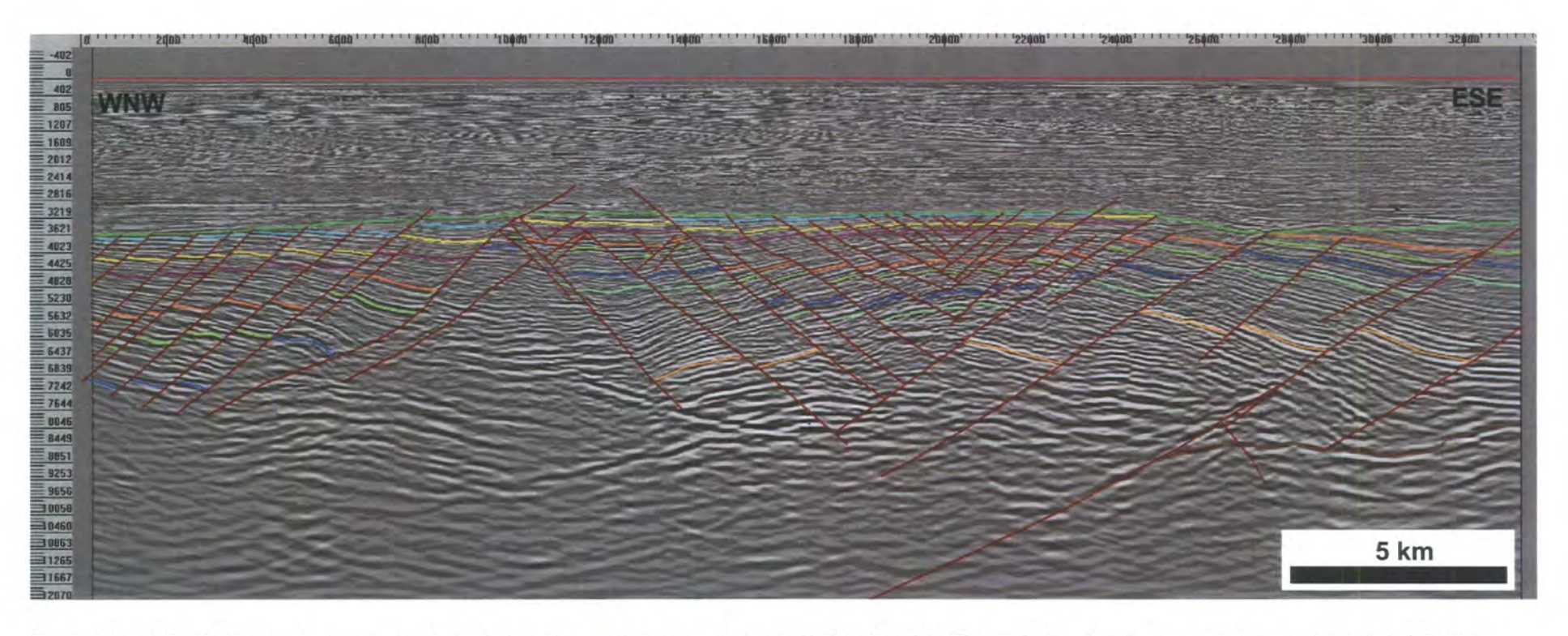


Figure 3.16: a) Depth converted cross section through the accommodation zone between Graben C and D. The vertical scale is in metres and the aspect ratio is 1:1. For location see Figure 3.11 and Enclosure 1.

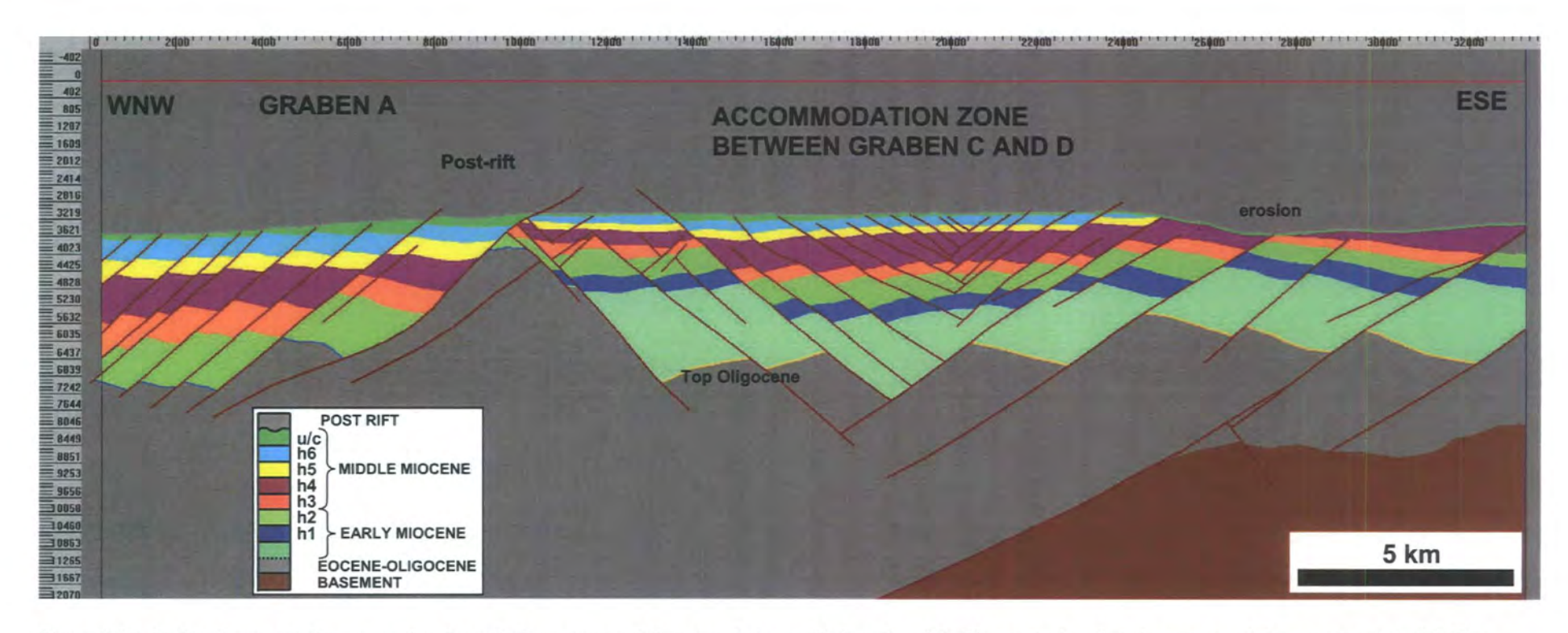


Figure 3.16: b) Depth converted cross section through the accommodation zone between Graben C and D. The vertical scale is in metres and the aspect ratio is 1:1. For location see Figure 3.11 and Enclosure 1. The cross section cuts through Graben A at the western end and the accommodation zone that separates Graben C and D. Graben A is separated from the accommodation zone by a horst. The basement can be seen at the eastern end of the section. The faults are typically planar in cross section in both Graben A and in the accommodation zone.

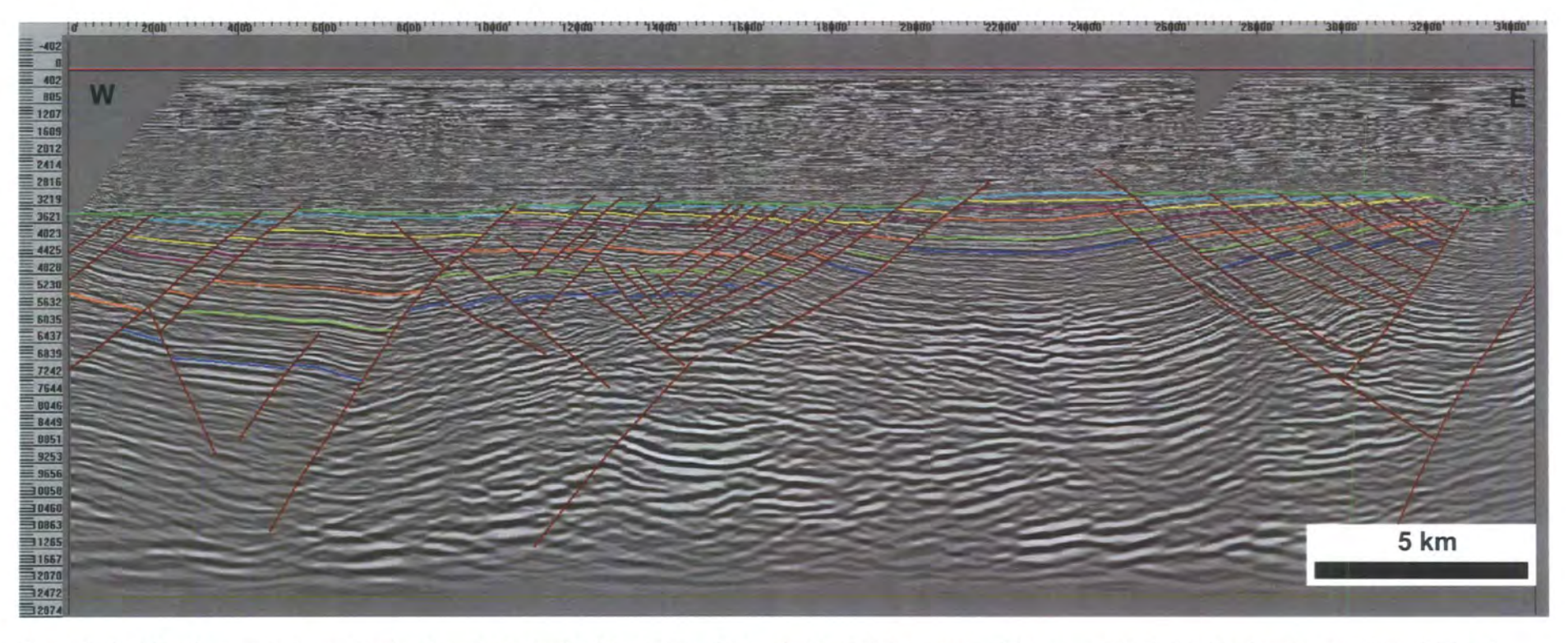


Figure 3.17: a) Depth converted cross section through the south of the dataset. The vertical scale is in metres and the aspect ratio is 1:1. For location see Figure 3.11 and Enclosure 1.

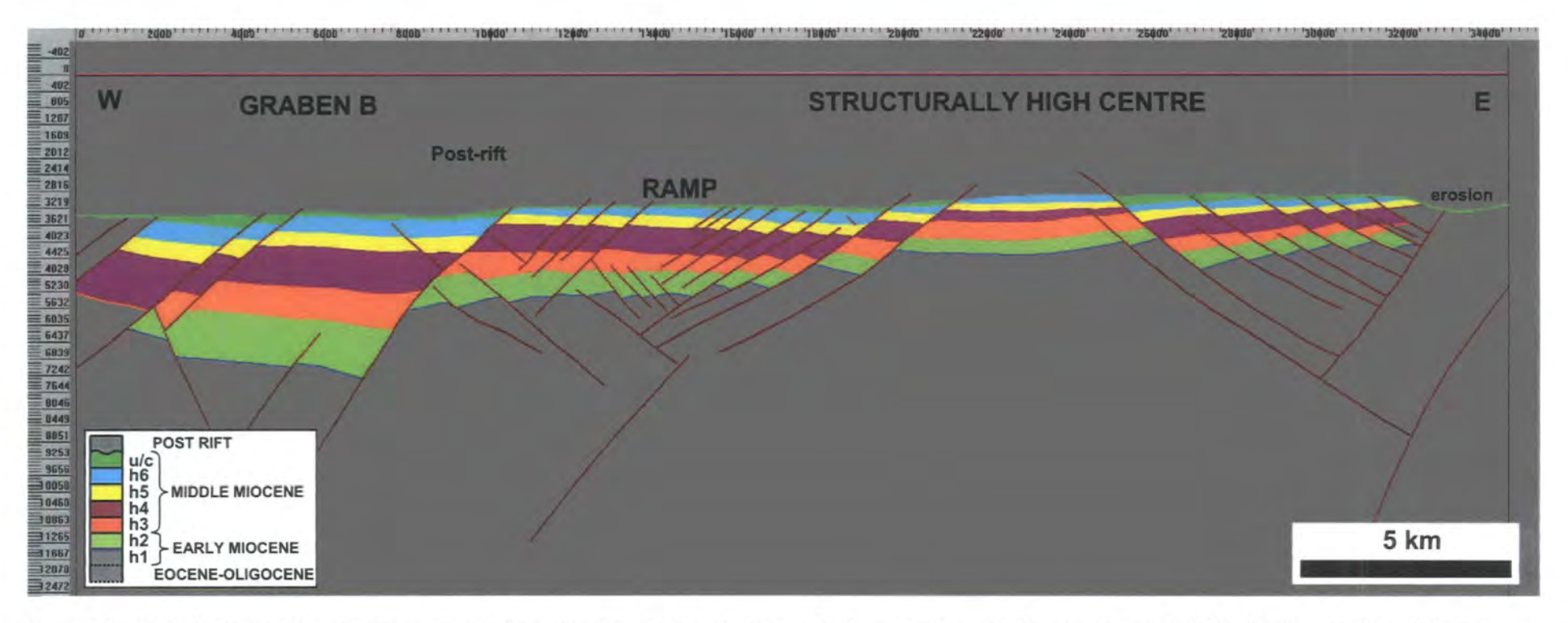


Figure 3.17: b) Depth converted cross section through the south of the dataset. The vertical scale is in metres and the aspect ratio is 1:1. For location see Figure 3.11 and Enclosure 1. The cross section through the south of the dataset. The western end of the section cuts through Graben B, the graben bounding fault is clearly shown. The ramp that connects Graben B to the structurally high centre is shown, with the sequence H1 to H3 thickening towards the graben.

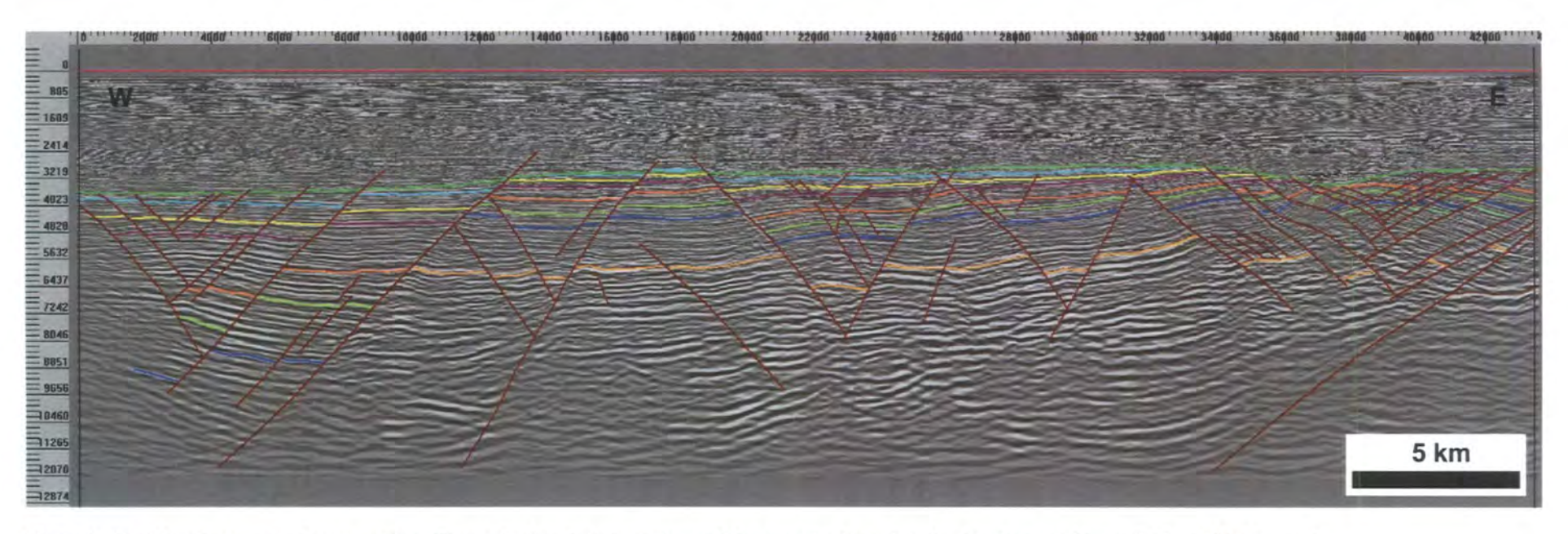


Figure 3.18: a) Depth converted cross section. The vertical scale is in metres and the aspect ratio is 1:1. For location see Figure 3.11 and Enclosure 1.

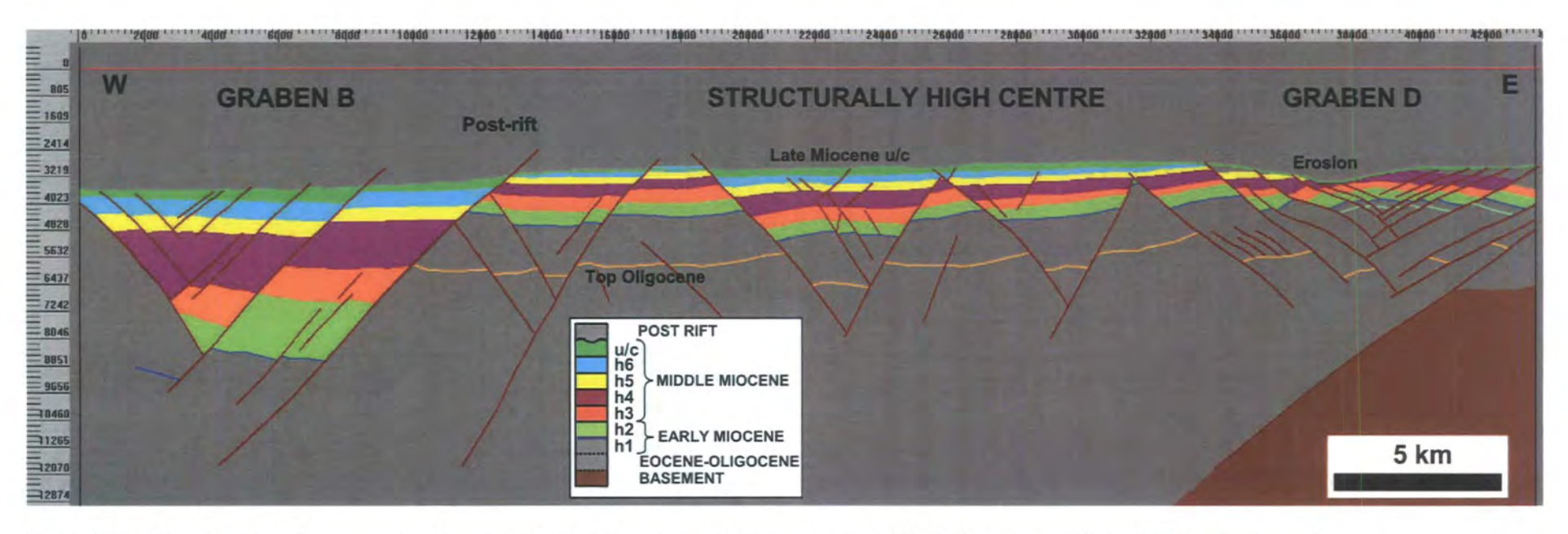


Figure 3.18: b) Depth converted cross section. The vertical scale is in metres and the aspect ratio is 1:1. For location see Figure 3.11 and Enclosure 1. Cross section through Graben B and D and the structurally high centre. Graben B to the west is separated from Graben D to the east by the structurally high centre. The unusual symmetrical geometry of Graben D can be seen.

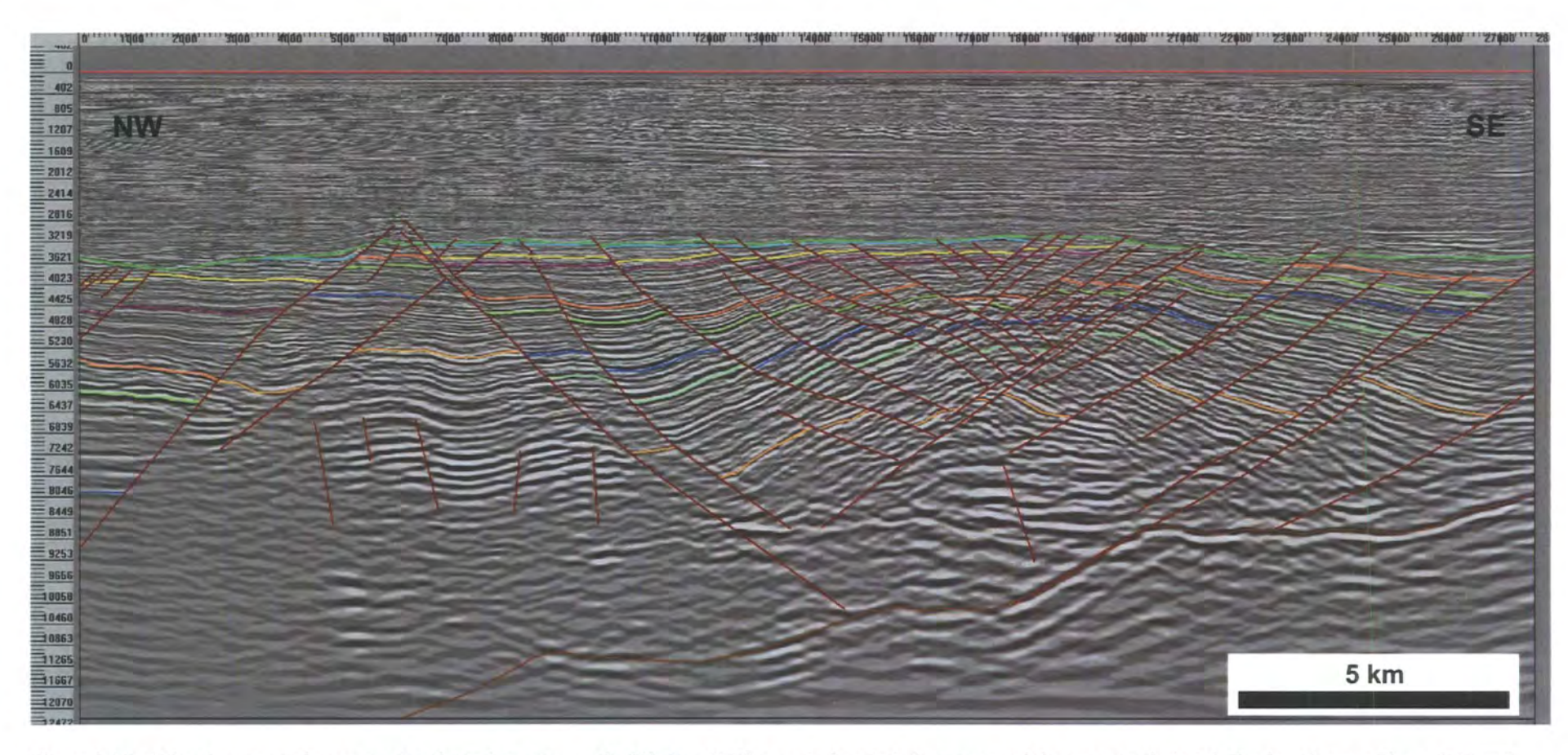


Figure 3.19: a) Depth converted cross section through western end of Graben C. The vertical scale is in metres and the aspect ratio is 1:1. For location see Figure 3.11 and Enclosure 1.

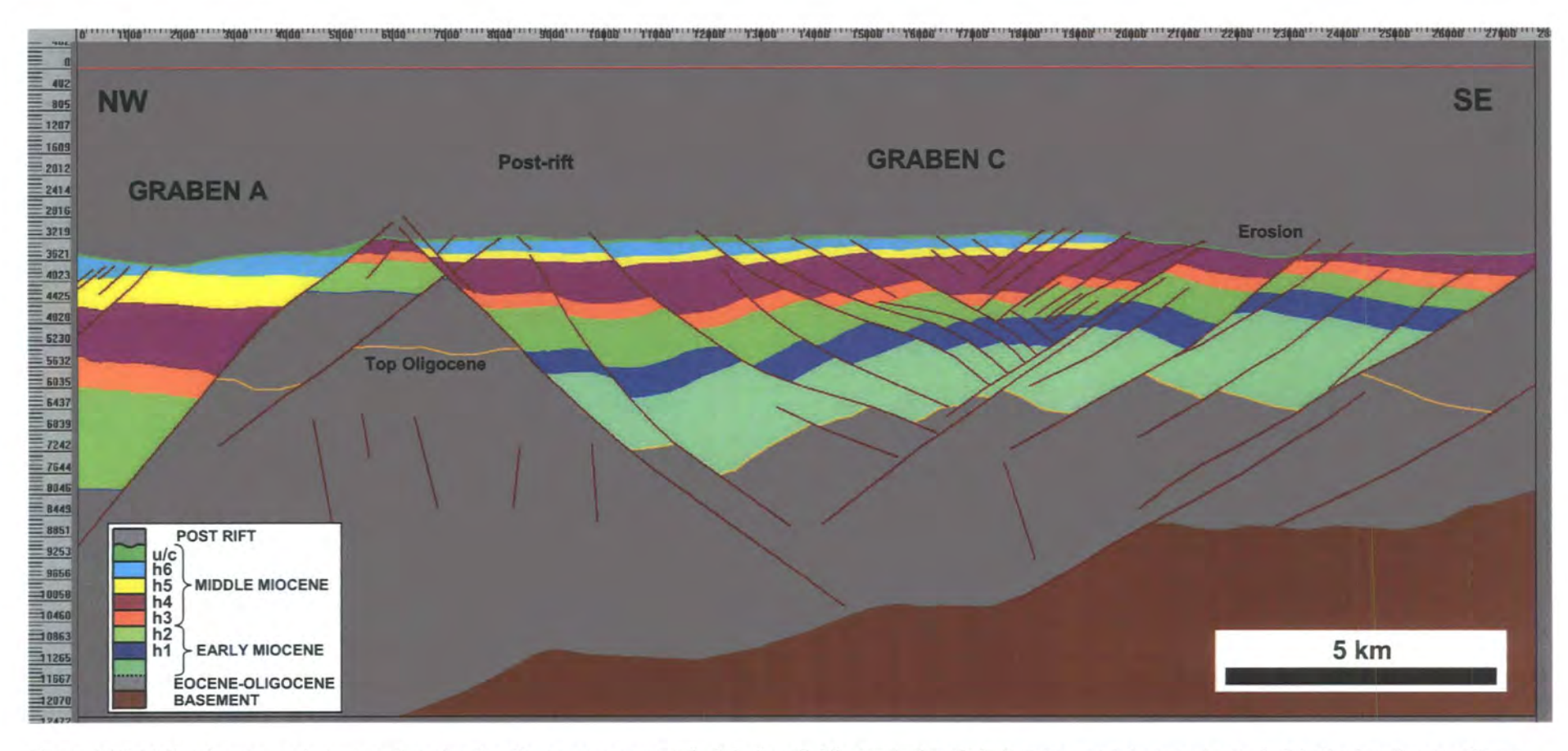


Figure 3.19: b) Depth converted cross section showing the western most end of Graben C. The vertical scale is in metres and the aspect ratio is 1:1. For location see Figure 3.11 and Enclosure 1. Graben A and Graben C are separated by a horst, the top of which is eroded flat.

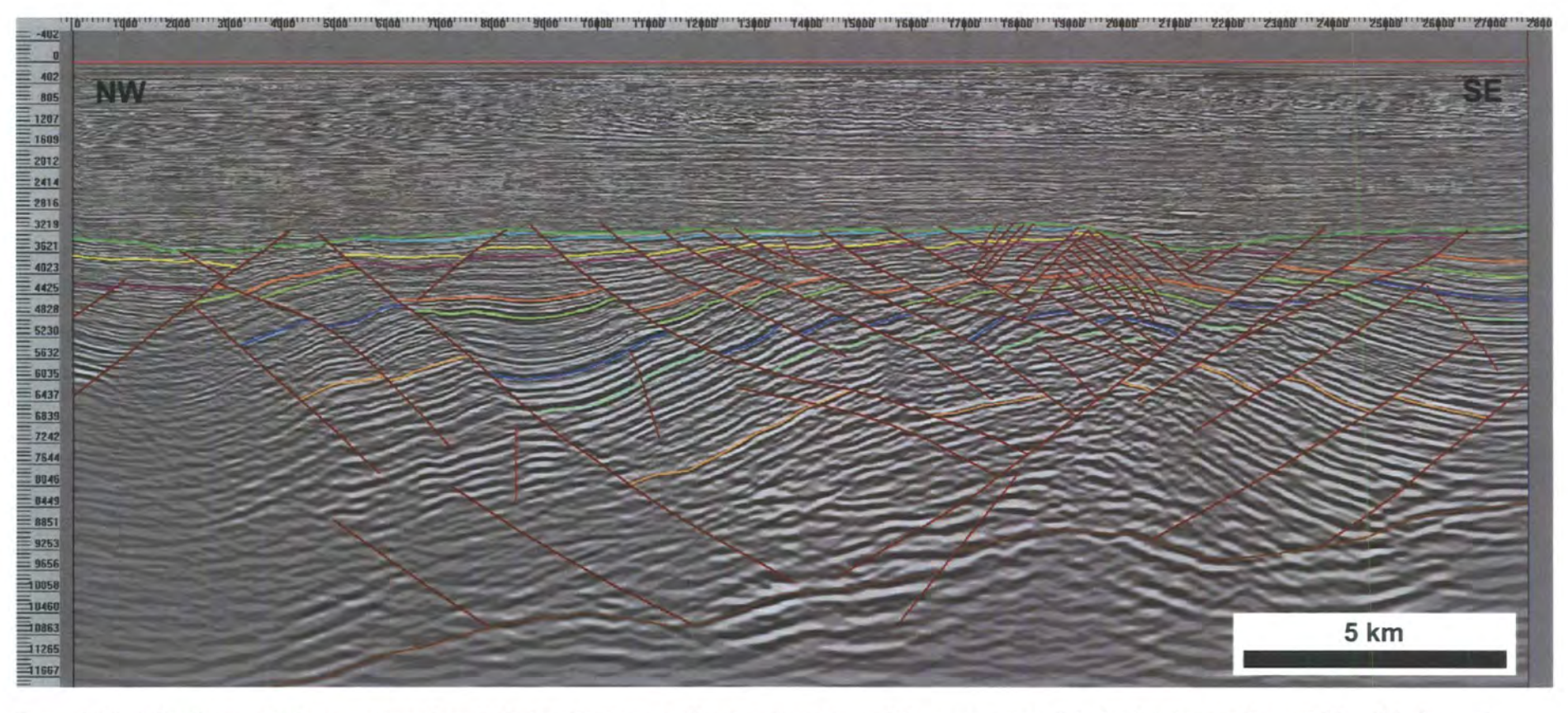


Figure 3.20: a) Depth converted cross section through Graben C. The vertical scale is in metres and the aspect ratio is 1:1. For location see Figure 3.11 and Enclosure 1.

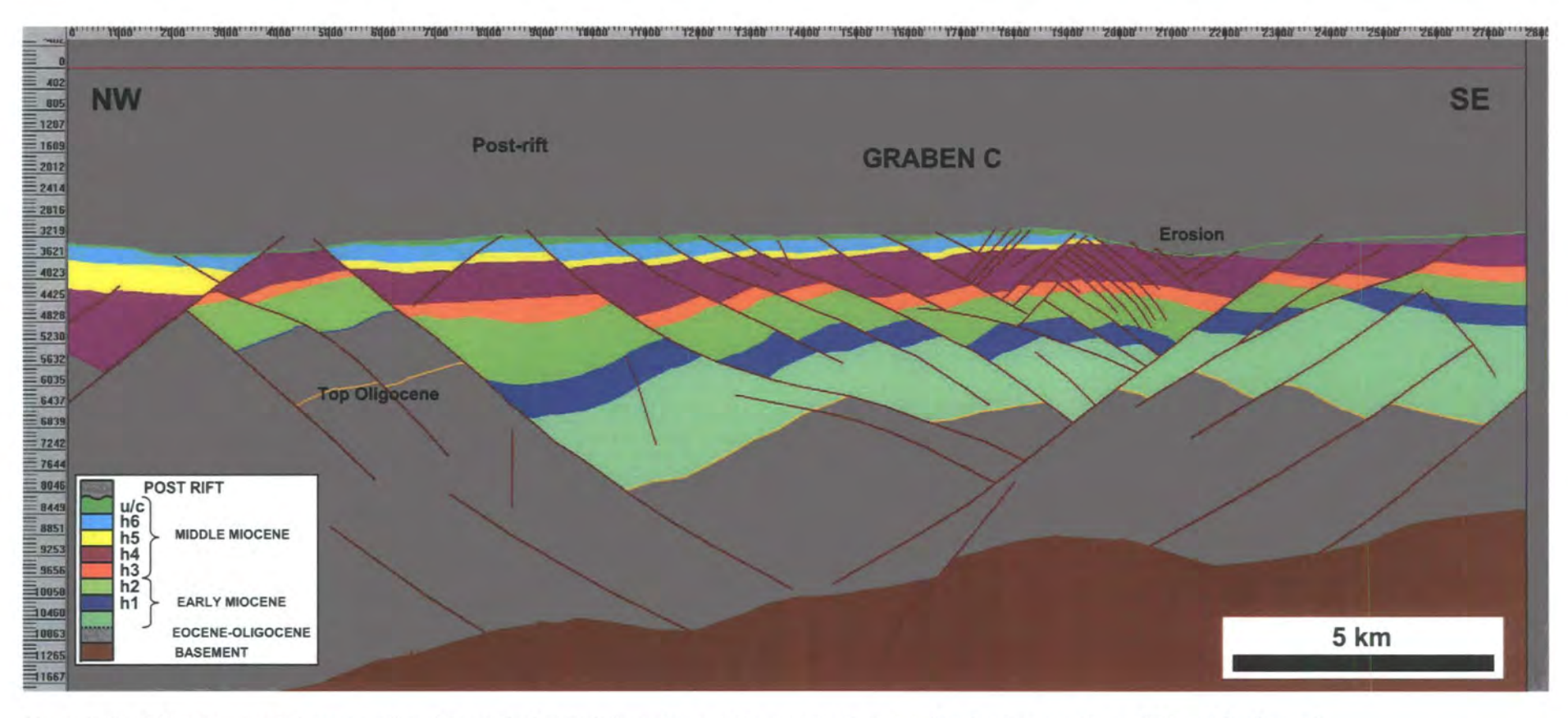


Figure 3.20: b) Depth converted cross section. The vertical scale is in metres and the aspect ratio is 1:1. For location see Figure 3.11 and Enclosure 1.

The cross section shows the centre of Graben C. Excepting one small fault, the basement appears to be unfaulted. The Miocene faults possibly detach onto the top basement.

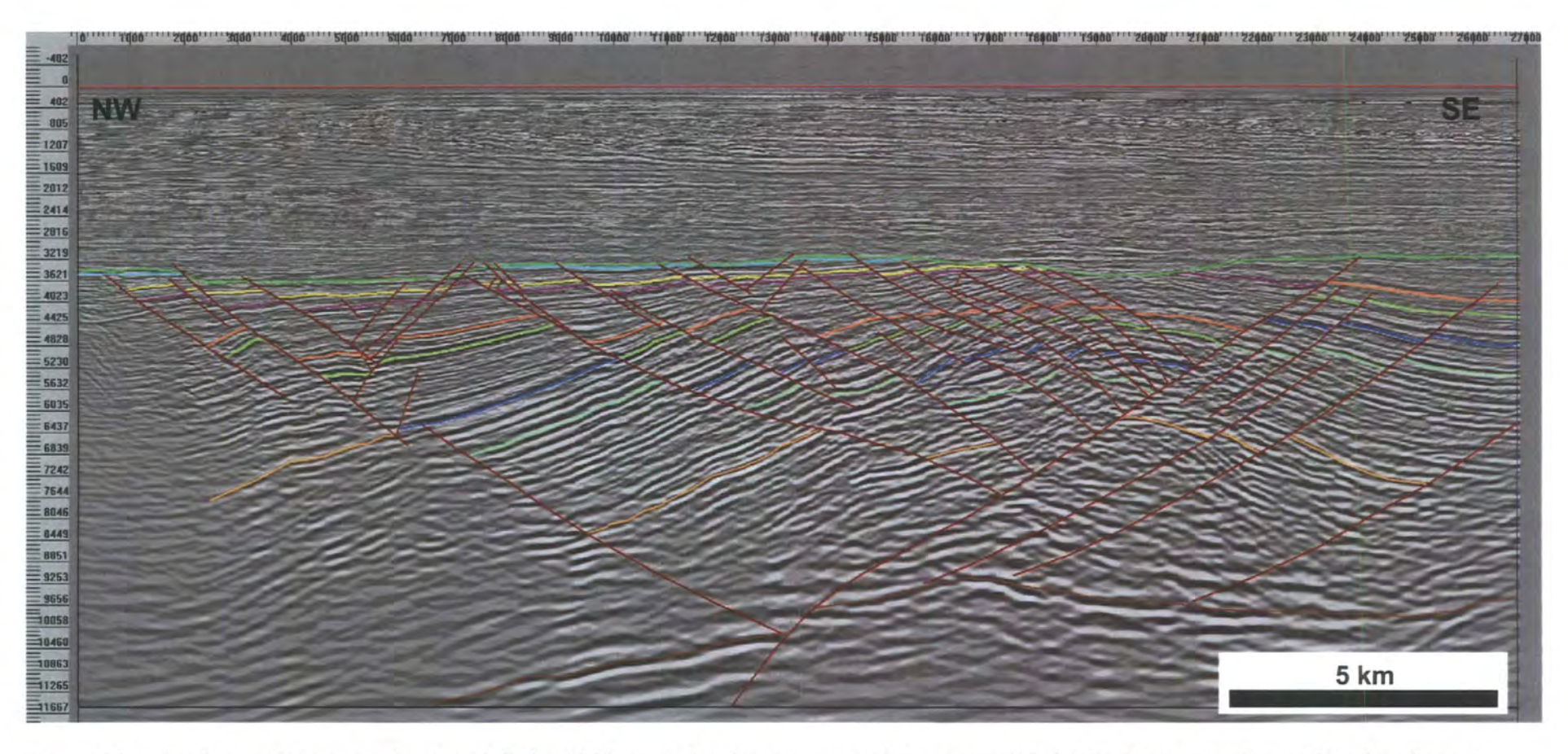


Figure 3.21: a) Depth converted cross section through Graben C. The vertical scale is in metres and the aspect ratio is 1:1. For location see Figure 3.11 and Enclosure 1.

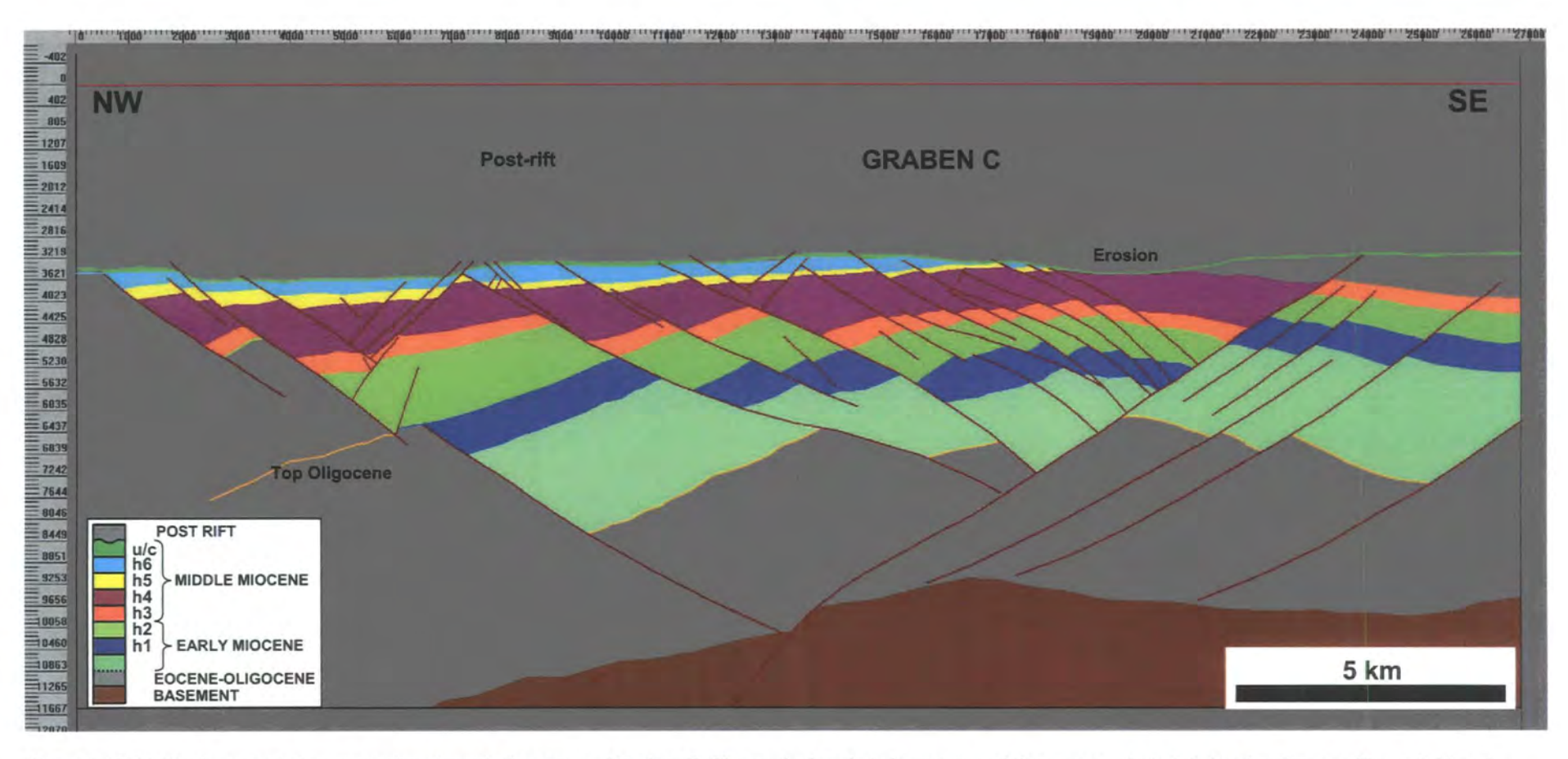


Figure 3.21: b) Depth converted cross section through the centre of Graben C. The vertical scale is in metres and the aspect ratio is 1:1. For location see Figure 3.11 and Enclosure 1.

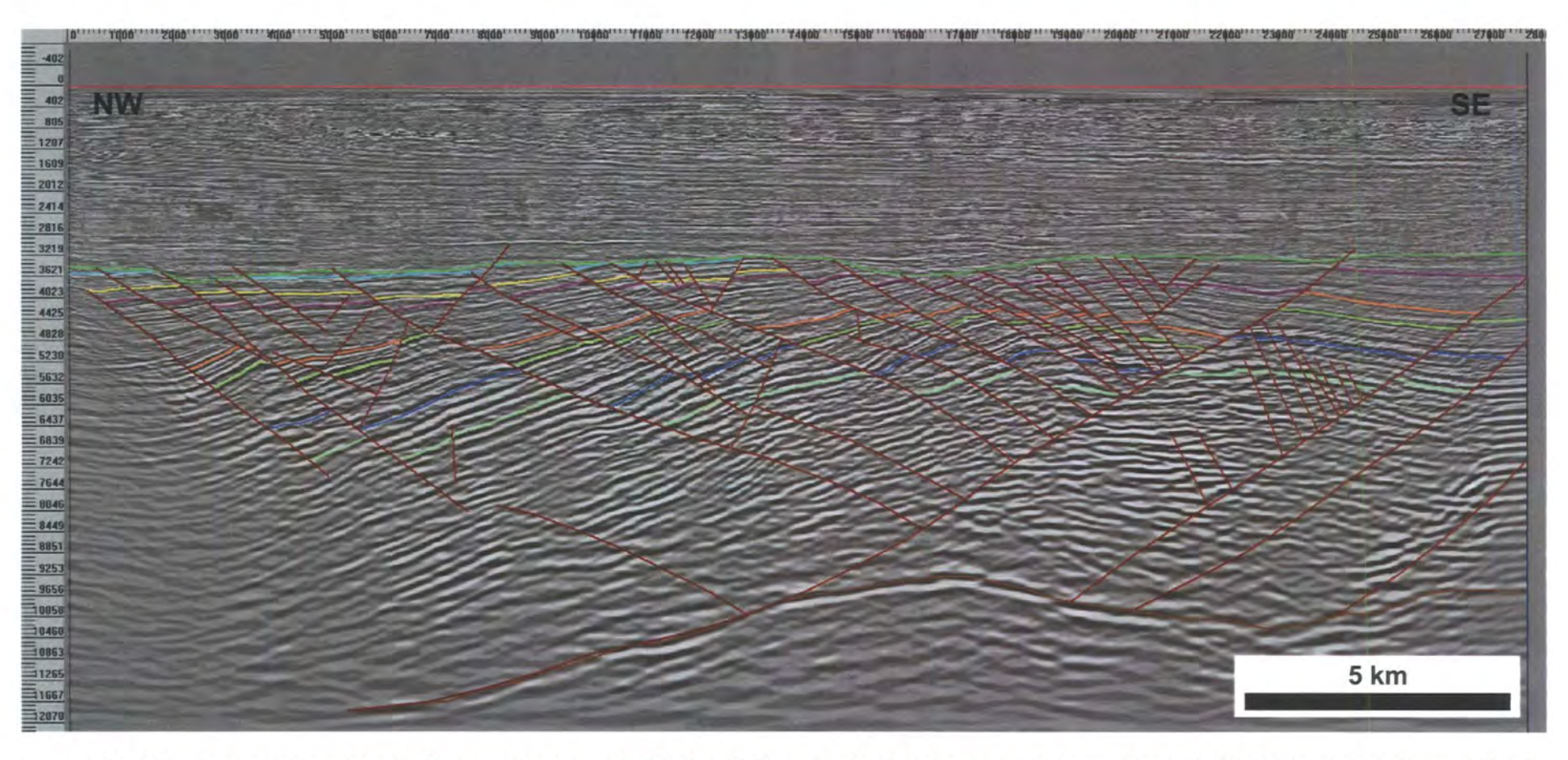


Figure 3.22: a) Depth converted cross section through the eastern end of Graben C. The vertical scale is in metres and the aspect ratio is 1:1. For location see Figure 3.11 and Enclosure 1.

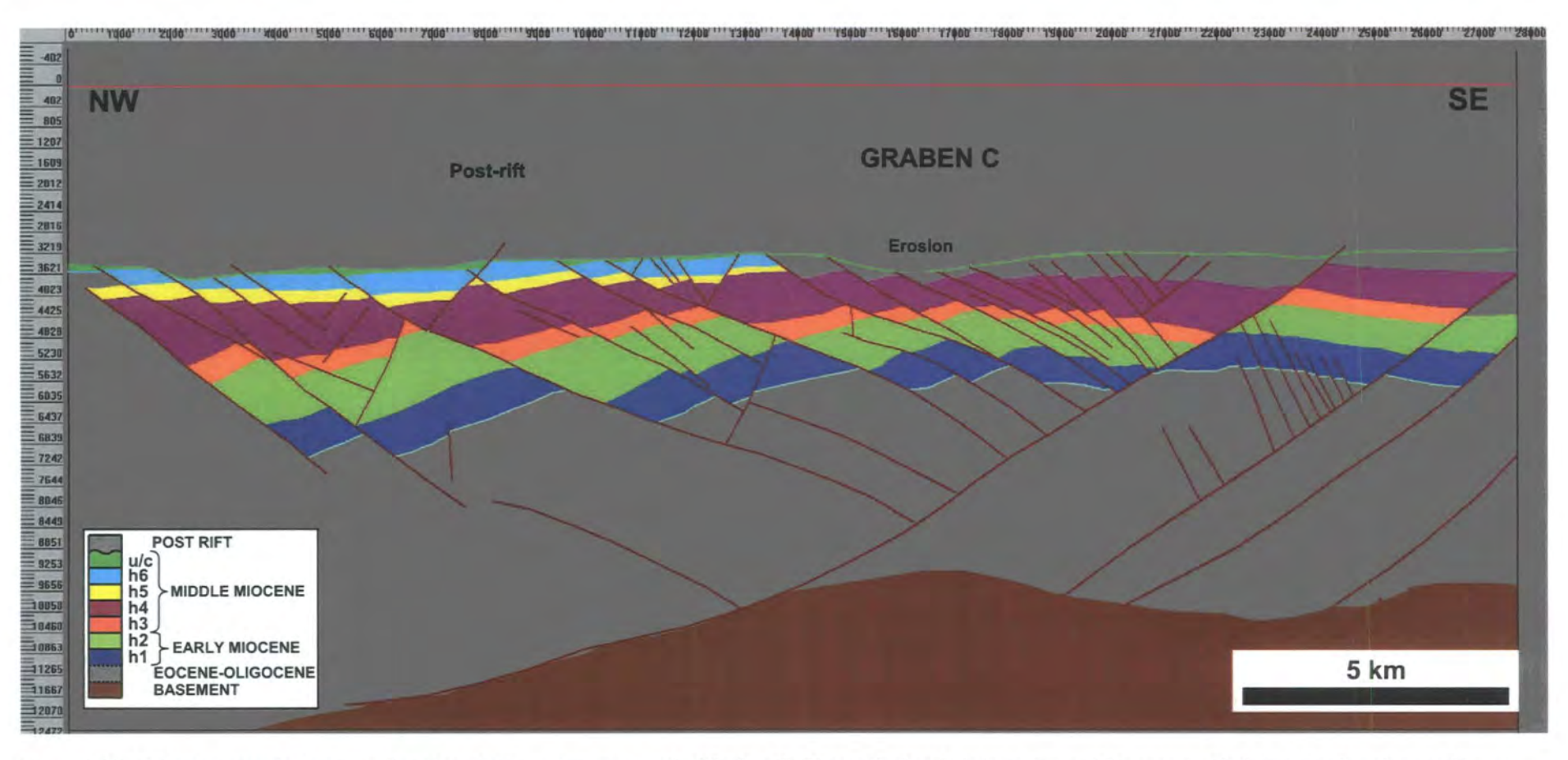


Figure 3.22: b) Depth converted cross section through the eastern most end of Graben C. The vertical scale is in metres and the aspect ratio is 1:1. For location see Figure 3.11 and Enclosure 1. The basement does not appear to be offset. The Miocene faults possibly detach onto the top basement.

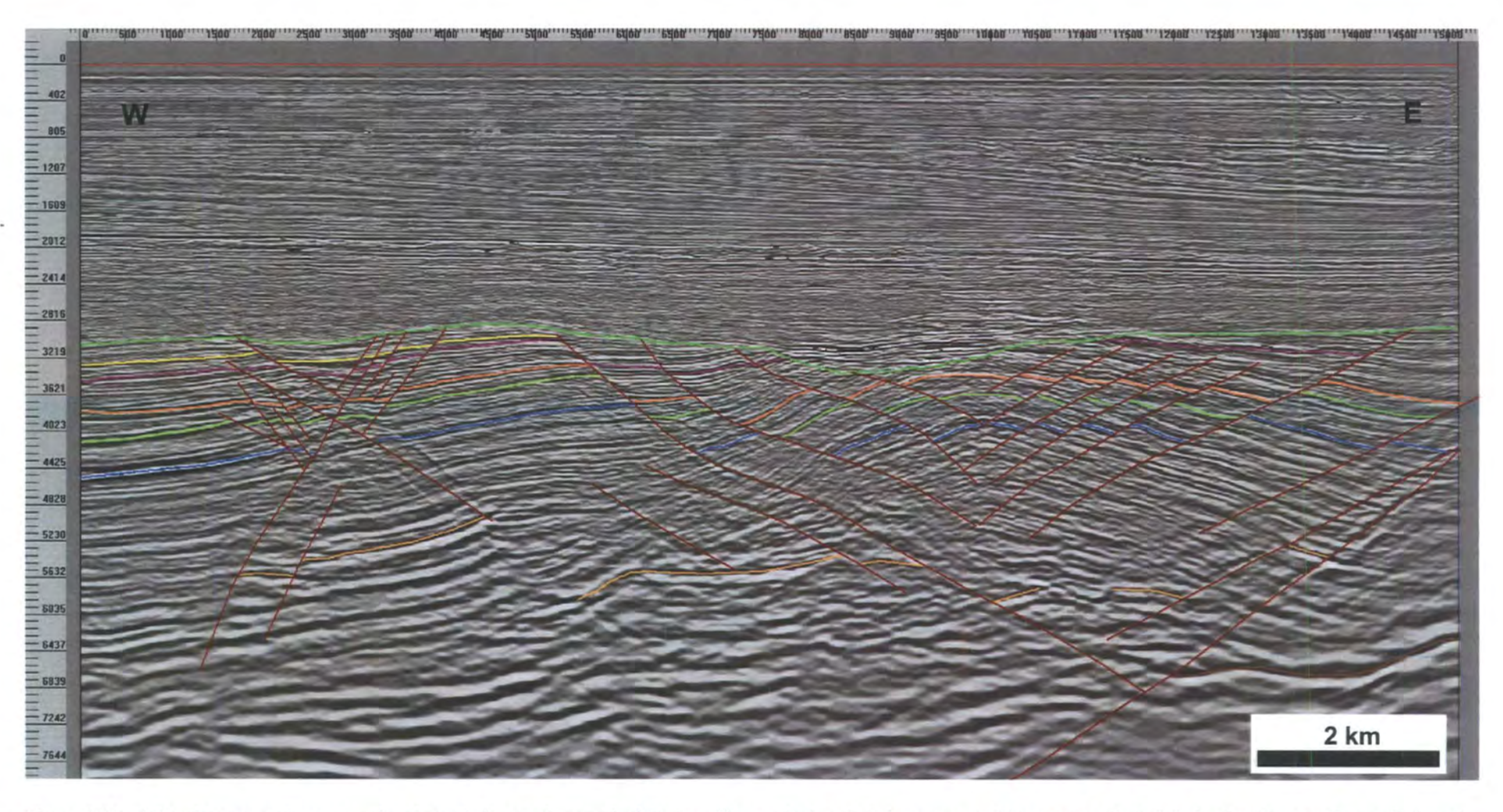


Figure 3.23: a) Depth converted cross section through the southern end of Graben. The vertical scale is in metres and the aspect ratio is 1:1. For location see Figure 3.11 and Enclosure 1.

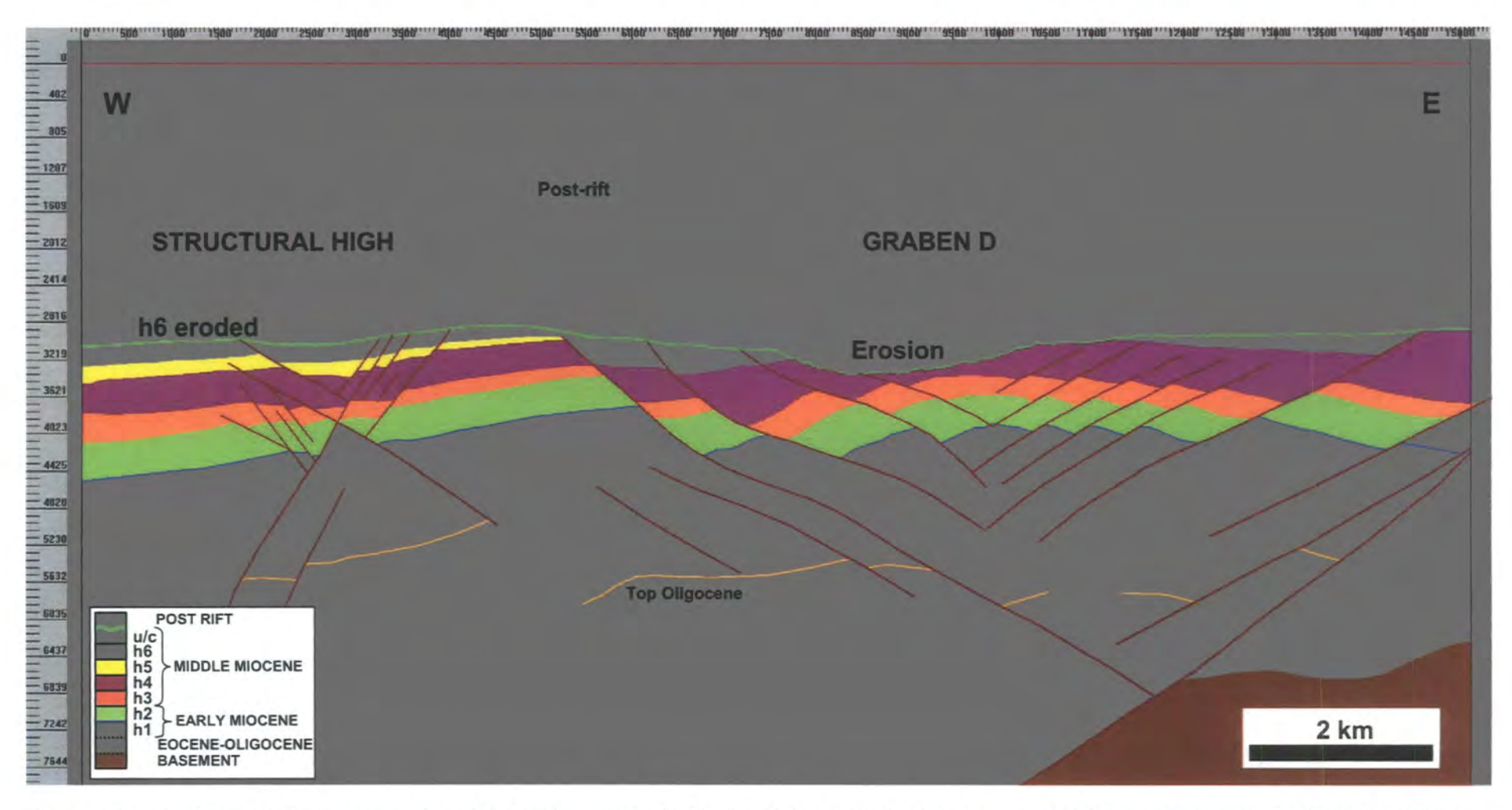


Figure 3.23: b) Depth converted cross section through the southern most end of Graben D. The vertical scale is in metres and the aspect ratio is 1:1. For location see Figure 3.11 and Enclosure 1.

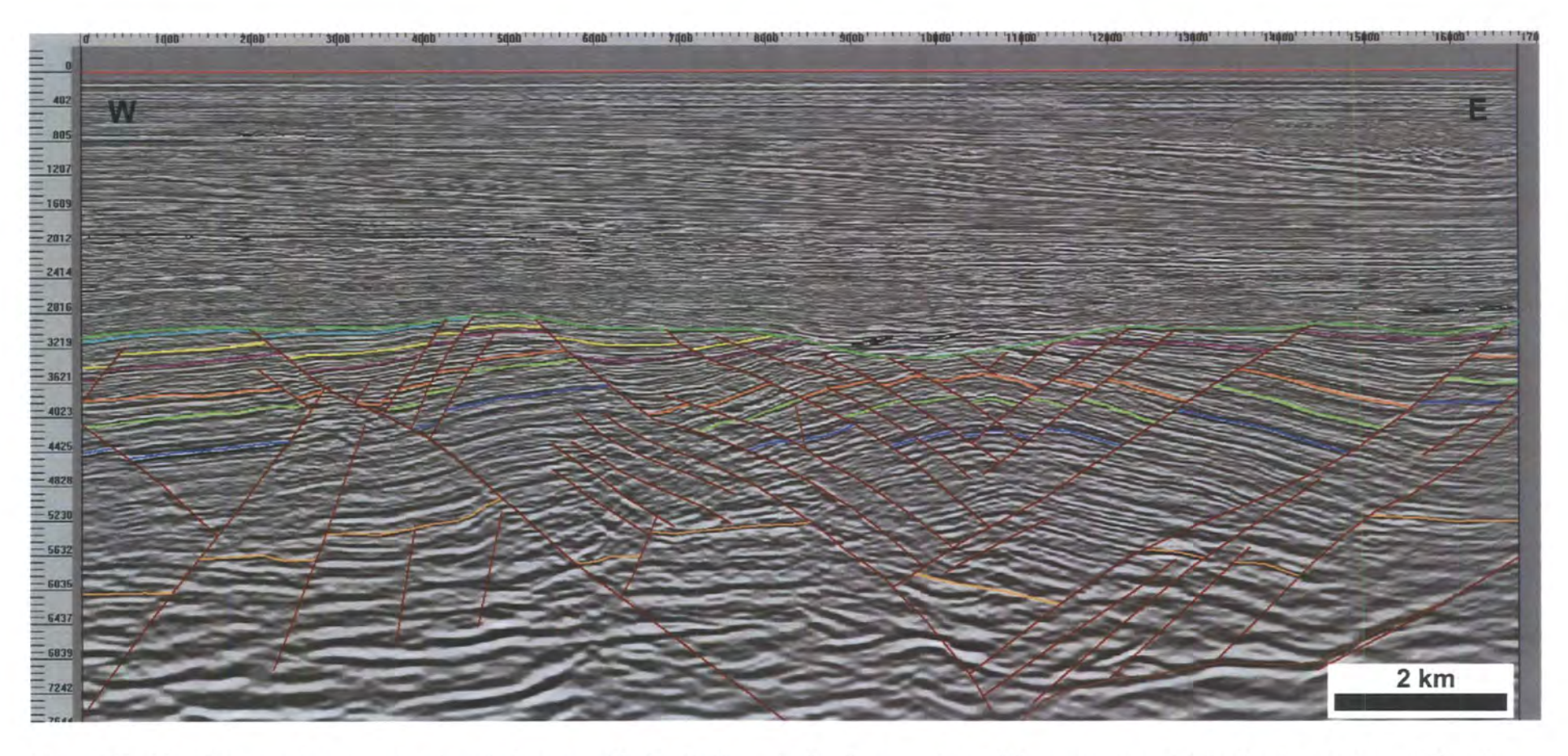


Figure 3.24: a) Depth converted cross section through the centre of Graben D. The vertical scale is in metres and the aspect ratio is 1:1. For location see Figure 3.11 and Enclosure 1.

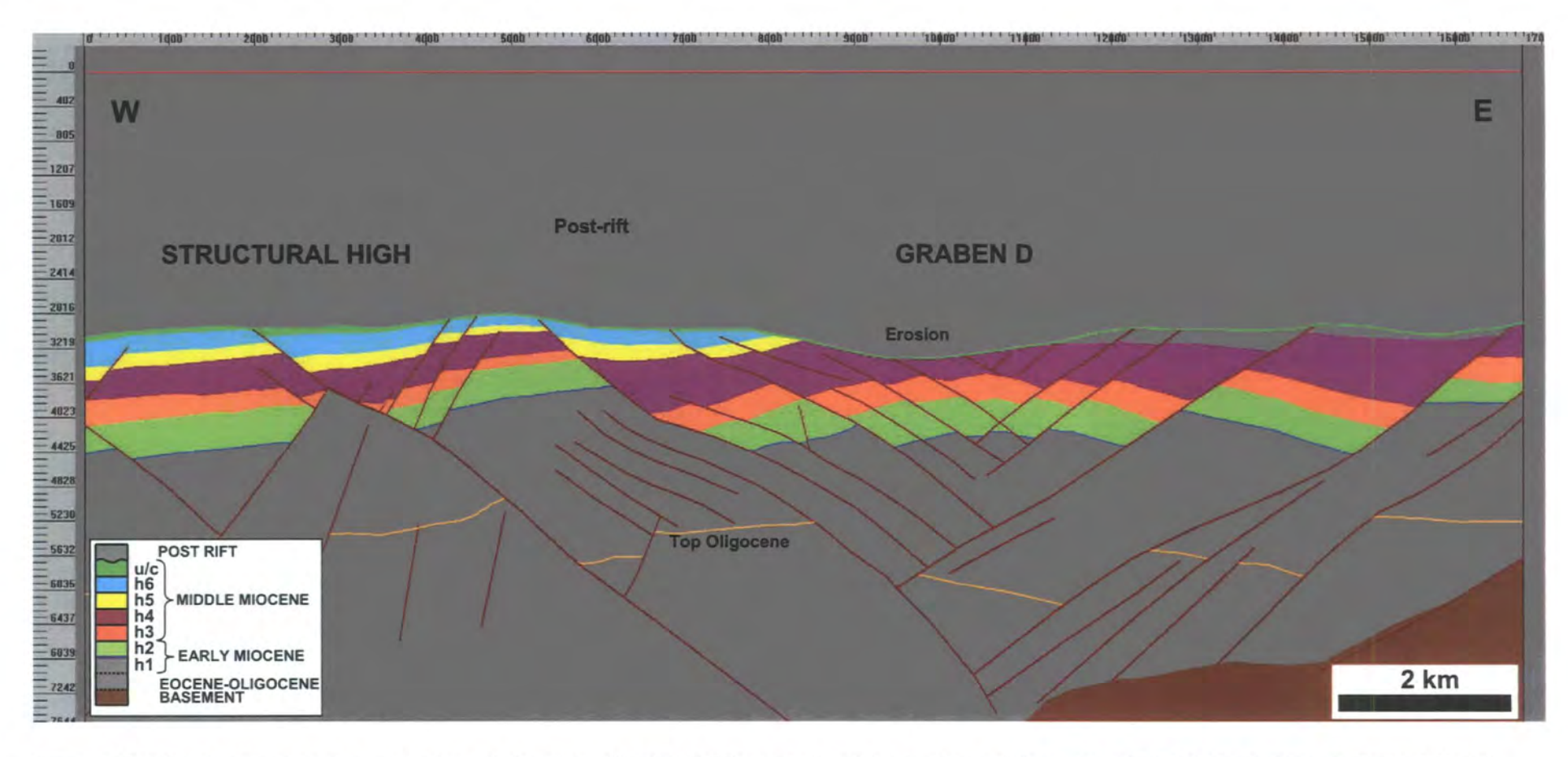


Figure 3.24: b) Depth converted cross section through the centre of Graben D. The vertical scale is in metres and the aspect ratio is 1:1. For location see Figure 3.11 and Enclosure 1.

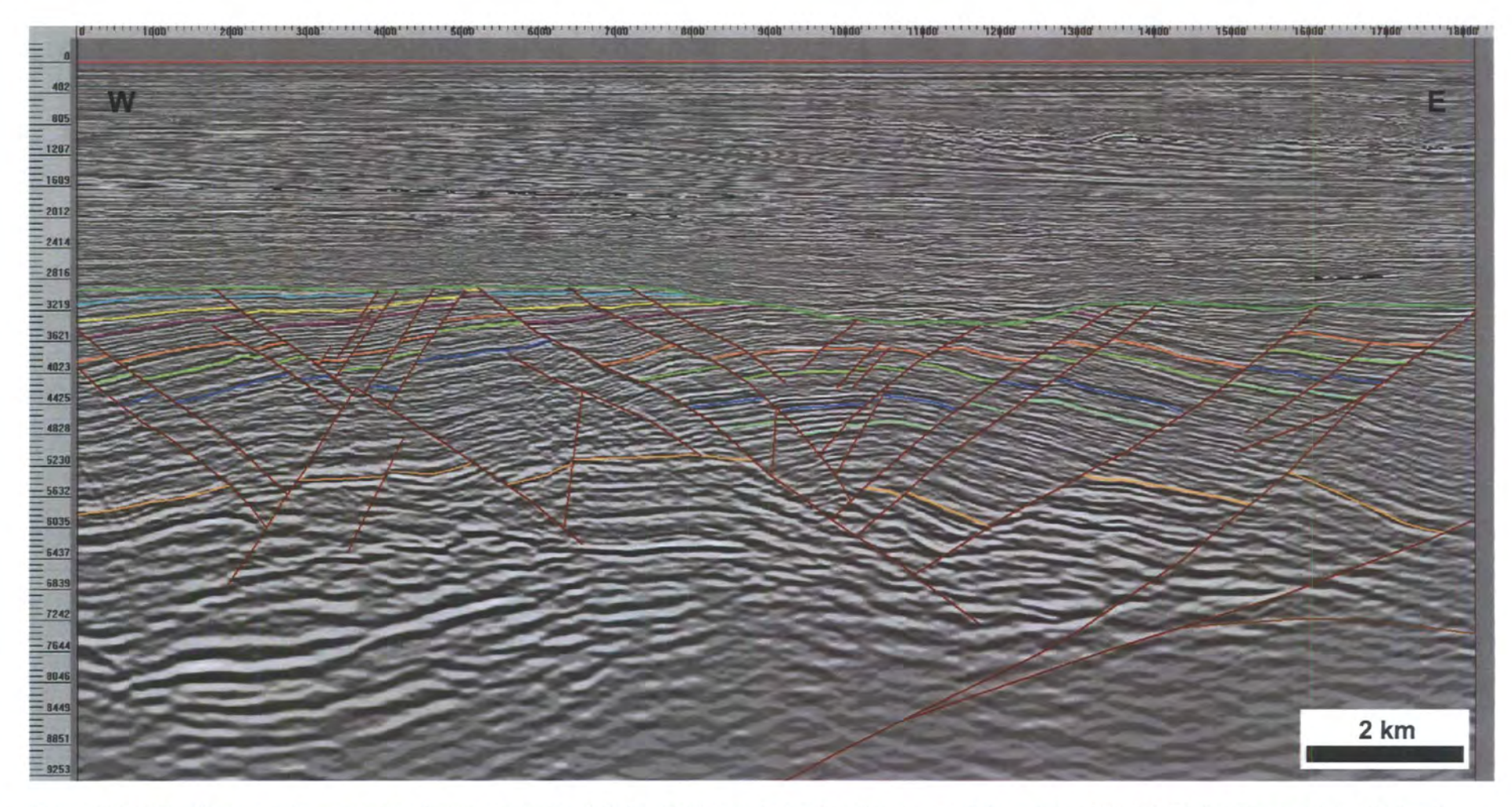


Figure 3.25: a) Depth converted cross section through the centre of Graben D. The vertical scale is in metres and the aspect ratio is 1:1. For location see Figure 3.11 and Enclosure 1.

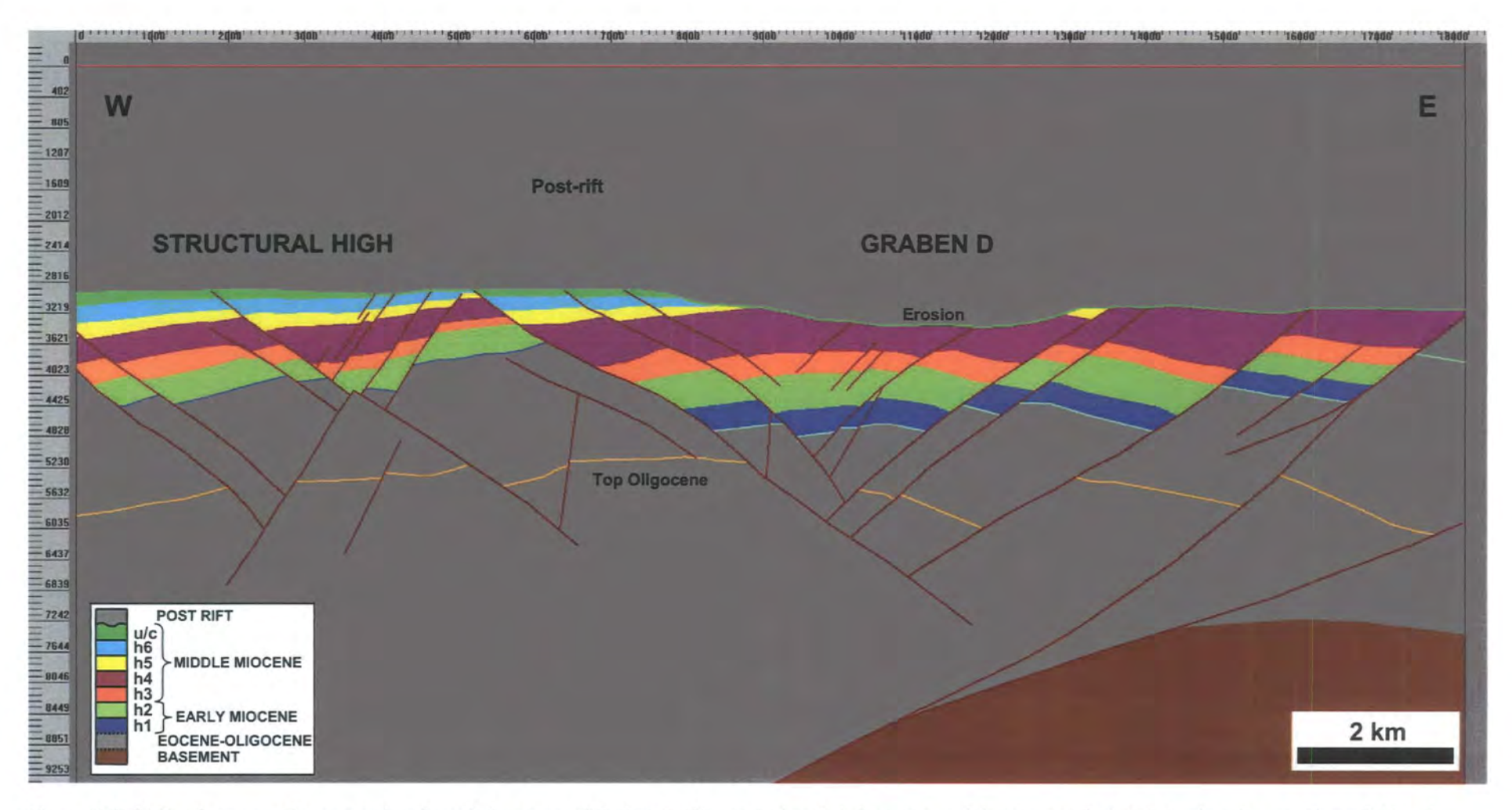


Figure 3.25: b) Depth converted cross section through the centre of Graben D. The vertical scale is in metres and the aspect ratio is 1:1. For location see Figure 3.11 and Enclosure 1.

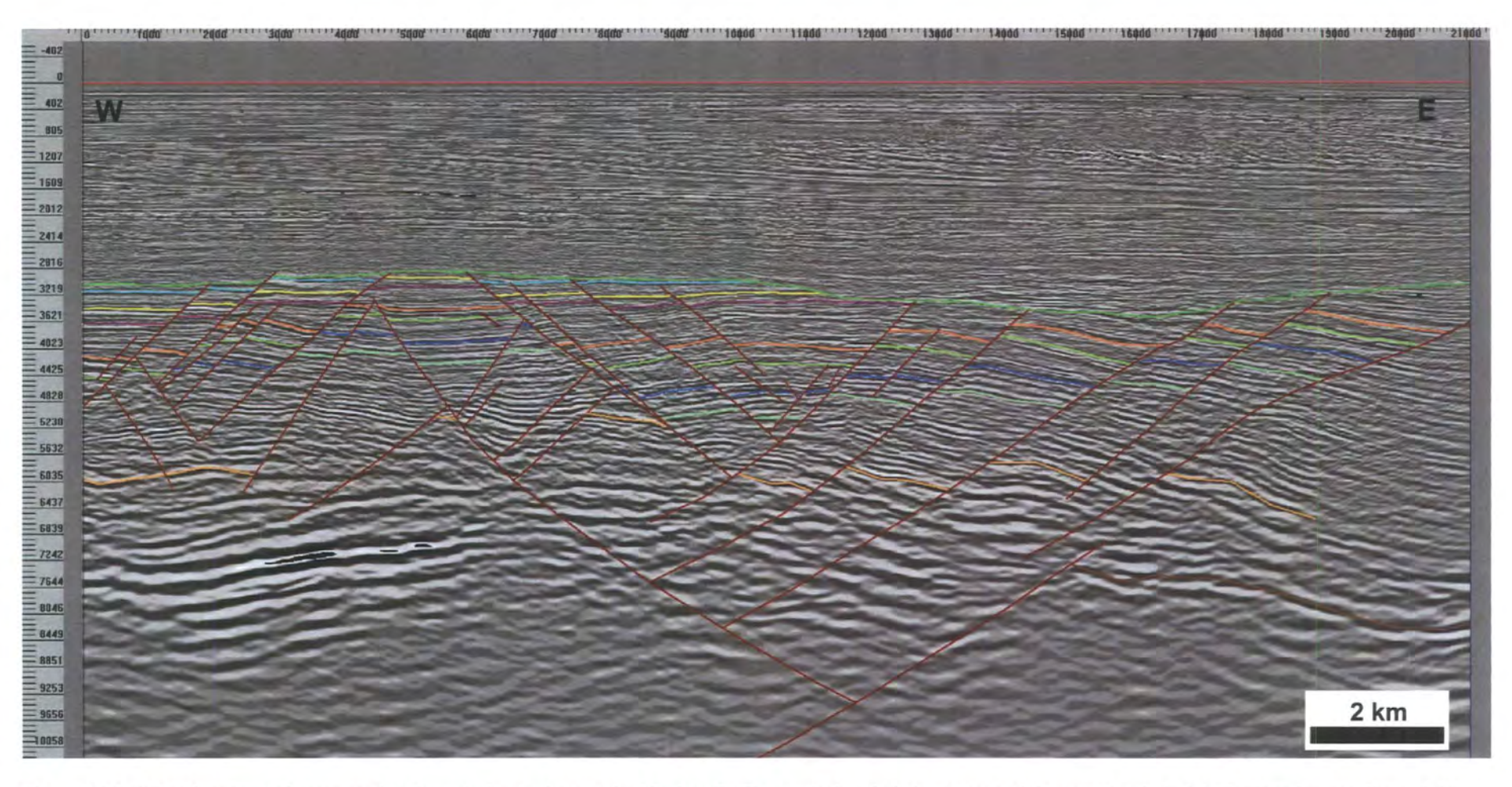


Figure 3.26: a) Depth converted cross section through the northern end of Graben D. The vertical scale is in metres and the aspect ratio is 1:1. For location see Figure 3.11 and Enclosure 1.

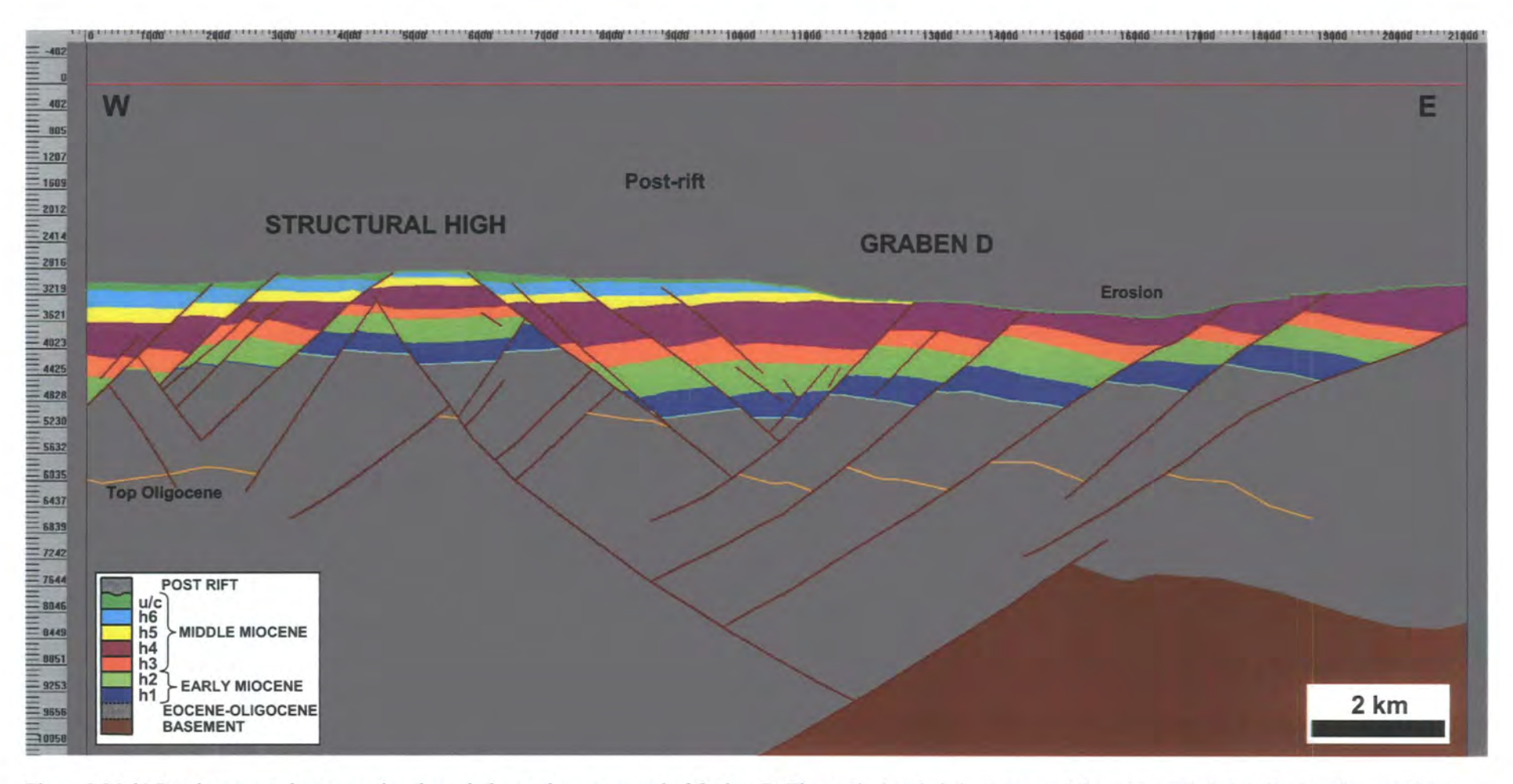


Figure 3.26: b) Depth converted cross section through the northern most end of Graben D. The vertical scale is in metres and the aspect ratio is 1:1. For location see Figure 3.11 and Enclosure 1.

3.4.2 Structure

The two structurally deepest parts of the survey area lie in graben to the north and west of the area, labelled Graben A and B, respectively (Figs. 3.16-3.18). Here the syn-rift Early to Middle Miocene sequence is >6 km thick. The graben lie in part of the deepest area in the basin centre, where the basement could be as much as 13 km deep (Huchon et al. 1998). Two other structures, in the east of the survey area, are labelled Graben C and D (Figs. 3.19-3.26). They are heavily faulted areas but an inspection of sequence thicknesses on the depth-converted cross section suggests that Graben C and D experienced less fault-related subsidence compared to Graben A and B. The graben bound a structurally high centre, which is itself heavily faulted (Fig. 3.18).

Graben A and B are bounded by large faults, which tip out along strike. Because of this they are not isolated but are connected to the structurally high centre by hinged trapdoor-style ramps (Fig. 3.27). Another ramp connects graben C in the east to the structural high in the centre. These ramps are faulted but the strikes of the faults are mostly parallel to the dip of the ramps. Therefore, the ramps have the potential to provide continuous pathways for hydrocarbon migration from the deeper graben into the structural highs (Gawthorpe and Hurst, 1993). During rifting they would also have provided pathways for sediment transport from the basin margins into the graben and deep basin centre (Prosser, 1993; Gawthorpe and Hurst, 1993; Gawthorpe and Leeder, 2000).

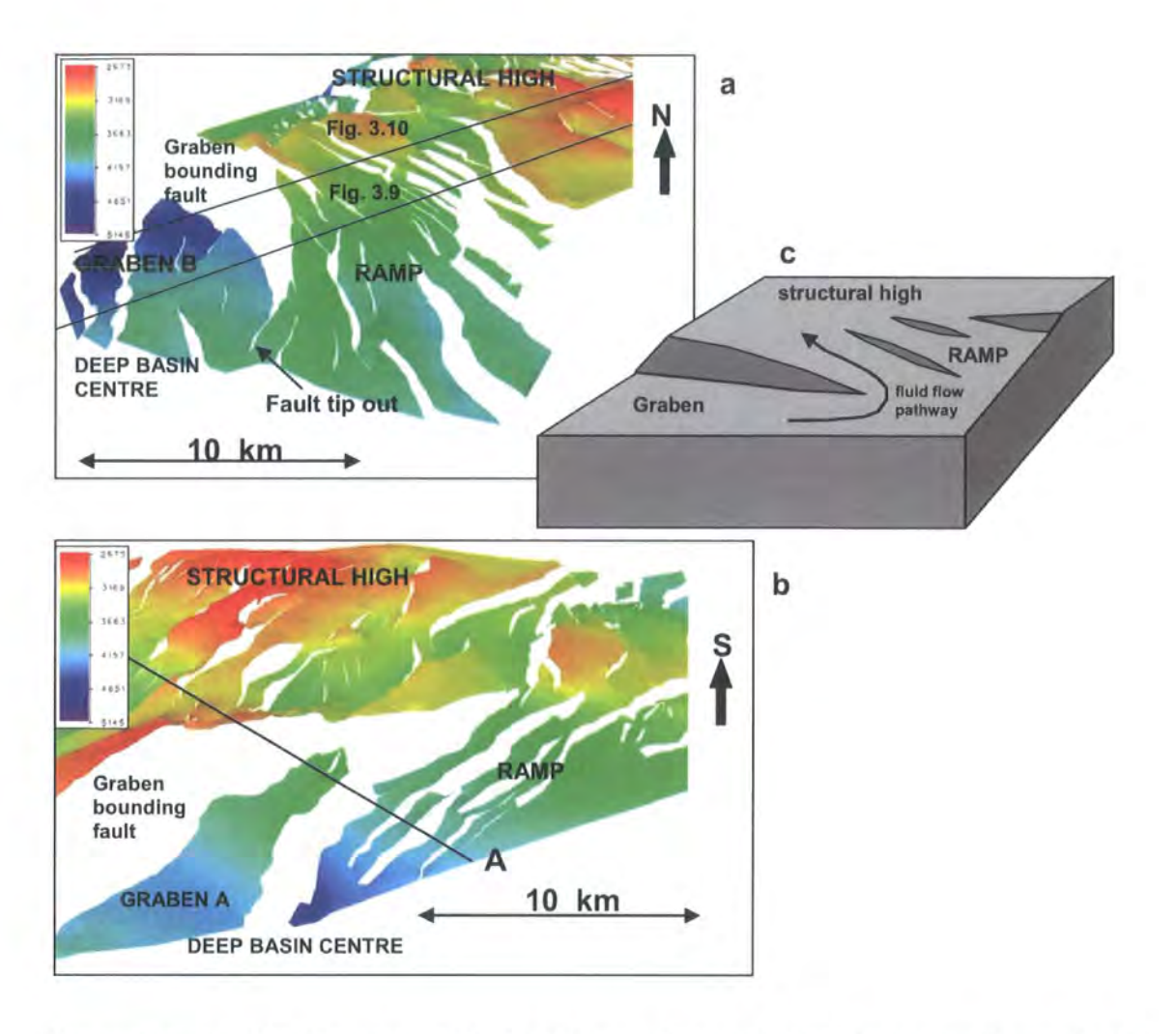


Figure 3.27: a) and b) 3-dimensional display of horizon h2 from Badley's Traptester software showing ramps connecting graben B and A, respectively, to the structurally high centre. The surfaces are displayed in TWT and have x2 vertical exaggeration. The locations of the cross sections are shown. Longitudinal faults cut and offset reflectors within the ramps but do not isolate the graben. The ramps serve to connect the deeper basin centre to the basin margins. c) 3-dimensional block model of this type of ramp structure.

Graben C and D are bounded on both sides by symmetrical, oppositely-dipping faults with roughly equal offsets. This has given the graben centres anticlinal geometries that more closely resemble compressional folds than extensional rollover anticlines (Figs. 3.19, 3.23). The graben centres are heavily faulted with faults dipping towards the structure centre. Graben D is structurally higher in the centre than at the margins (Fig. 3.28). The cause of this unusual geometry is discussed in Chapter 6. The faults in Graben D trend ~N-S, whilst those in Graben C trend ~NE-SW. The two graben are separated by a densely faulted accommodation zone, in which the fault strike abruptly

switches. Western-dipping faults that bound the eastern edge of Graben D pass along strike into eastern-dipping faults within Graben C. The graben are therefore offset and the polarity of the faults switches along strike (Fig. 3.28). To the west of the Graben C, and along strike of Graben D, the ~NE-SW trending faults form a ~NNE-SSW trending en-echelon array.

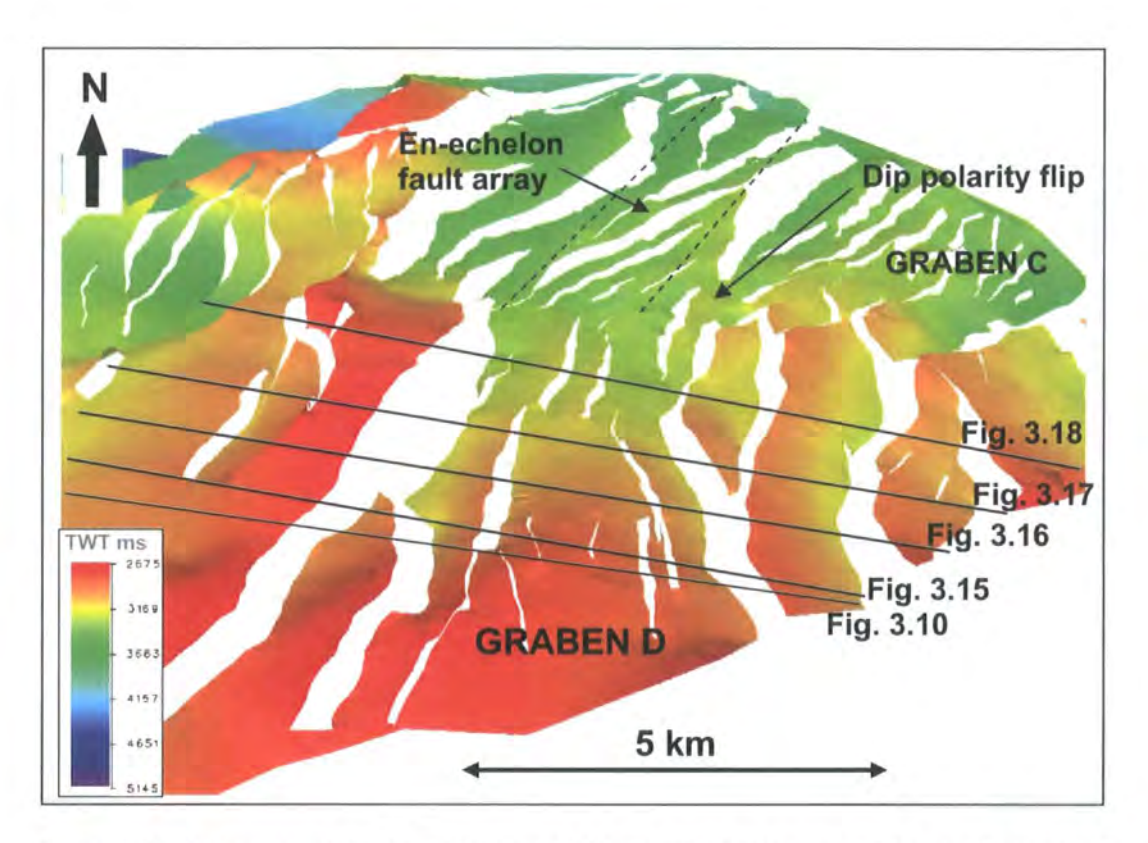


Figure 3.28: 3-dimensional display of horizon h2 from Badley's Traptester software showing graben D. The model is displayed in TWT and has a x2 vertical exaggeration. The locations of the cross sections are shown.

Across Graben C and D - but not in Graben A and B - horizons h4, h5 and h6 are eroded (Figs. 3.19, 3.23). It is possible that the erosion, coupled with the apparent lack of subsidence in the graben centres, is an indication that the grabens have been mildly uplifted as suggested by Matthews *et al.* (1997). A thorough examination of the 3-dimensional seismic data and additional 2-dimensional seismic lines from across the basin has revealed no evidence for reverse fault offsets, however in many cases mild

compression can be accommodated without fault inversion and resulting in an underestimation of the amount of shortening (Eisenstadt and Withjack, 1995). The mechanism and cause of this apparent uplift remains enigmatic.

The deeper syn-rift and pre-rift succession has proved difficult to constrain. In general the top-Oligocene appears to be conformable with the overlying Miocene succession, consistent with the findings of Lee *et al.* (2001) for the basin centre. The top-Oligocene is offset by the Miocene faults and there is no evidence for significant earlier faulting. Intra-Oligocene horizons have been interpreted over small areas but no significant thickness variations have been identified, e.g. no syn-tectonic growth of intra-Oligocene strata into faults. On most cross sections (Fig. 3.16-3.26) the top-Oligocene is shown along with an intra-Early Miocene horizon beneath h1. These interpretations show very little thickness variation in the sequence below h1.

It is unclear whether any of the deep succession represents the earliest Eocene rifting event. In the centre of the survey area, the basement is faulted below the base of the seismic data and yet the Miocene succession is at its thinnest. Therefore, the Eocene-Oligocene succession must be thickest in this area. It is possible that the deep basin centre is filled with Eocene sediment deposited during an early rift phase.

The top basement is interpreted in the eastern part of the survey area (Fig. 3.29). The top basement is represented by a package of strong reflectors overlying a sequence of low energy reflectors (Fig. 3.8). It is ~6.5 km deep at the highest point and dips towards the northwest. The western edge of the top basement is difficult to constrain. In the south it appears to be faulted down below the base of the seismic data (Fig. 3.8). Further north, the top basement does not appear to be faulted but instead dips gently to below the base of the seismic data. The depth to top-basement and the geometry of the top-basement interpreted using seismic data is broadly similar to that modelled by

Huchon *et al.* (1998) with two exceptions. Firstly, the area of basement in the centre of the 3-dimensional survey could be within the lower limit of the seismic data but has not been picked due to the poor quality of seismic data at this depth. Secondly, the highest point of the basement pick (~6.5 km depth) to the east of Graben D, is as much as 3 km higher than that predicted by Huchon *et al.*, (1998).

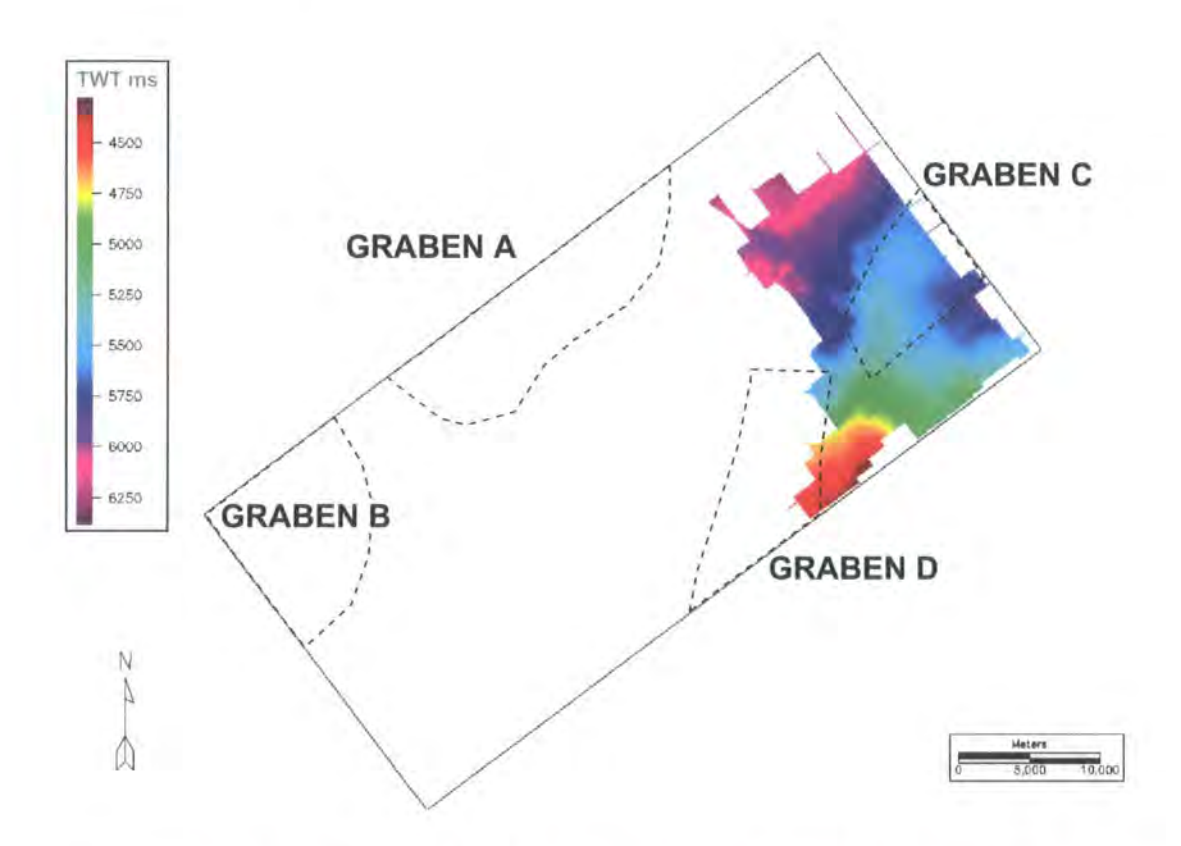


Figure 3.29: Structure map of the top pre-Tertiary basement, in TWT. For reference, the dashed lines represent the locations of the Miocene graben discussed in the text. The basement is below the bottom of the seismic data in the central and western part of the 3-dimensional seismic survey.

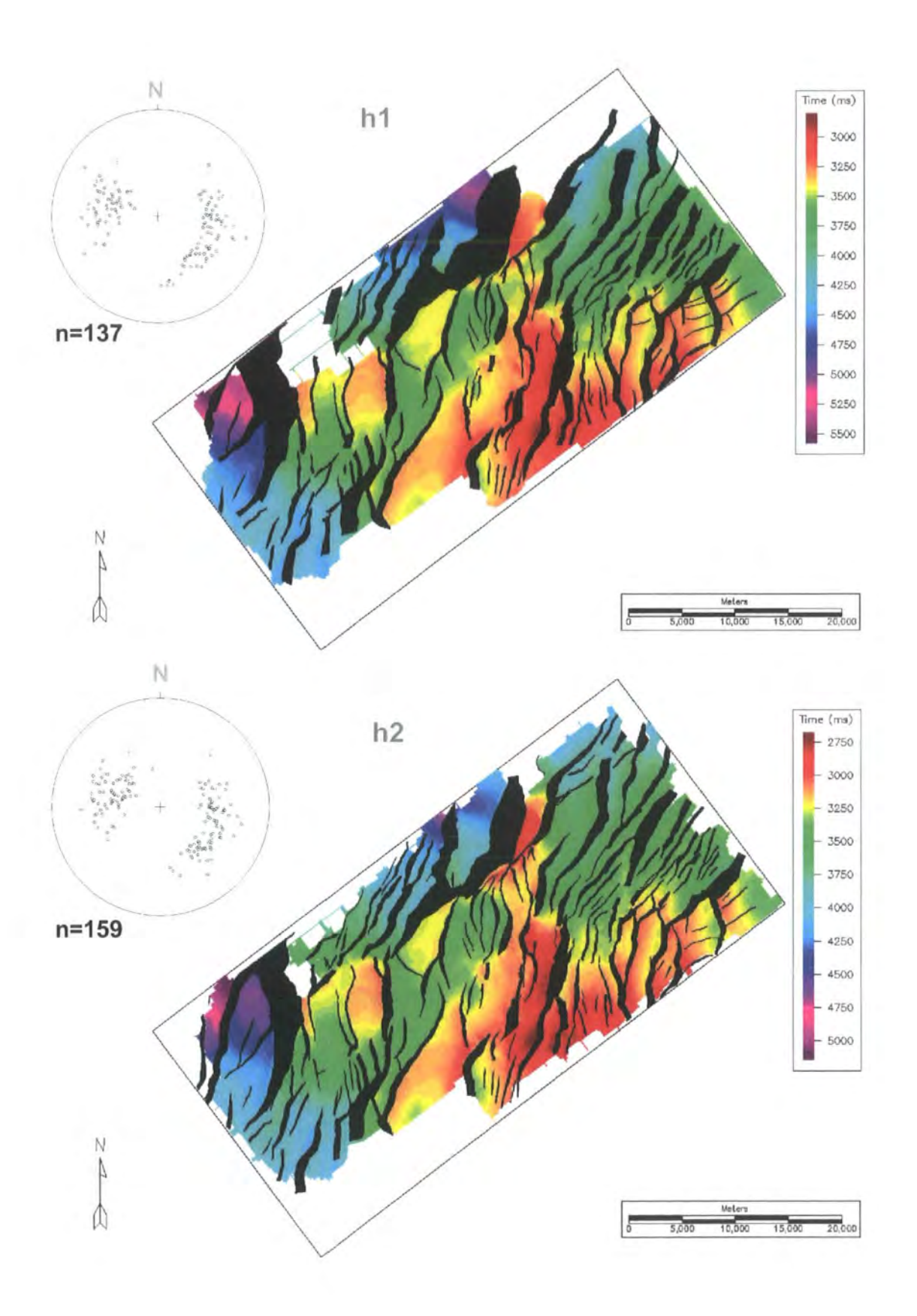
This area of basement is relatively small and may have been beyond the resolution of the gravity data. Furthermore, the shallow basement pick is appropriate, as the depth to basement immediately south of the survey area is even shallower, ~4.6 km (from the interpretion of the 2-dimensional seismic data, Fig. 3.3a).

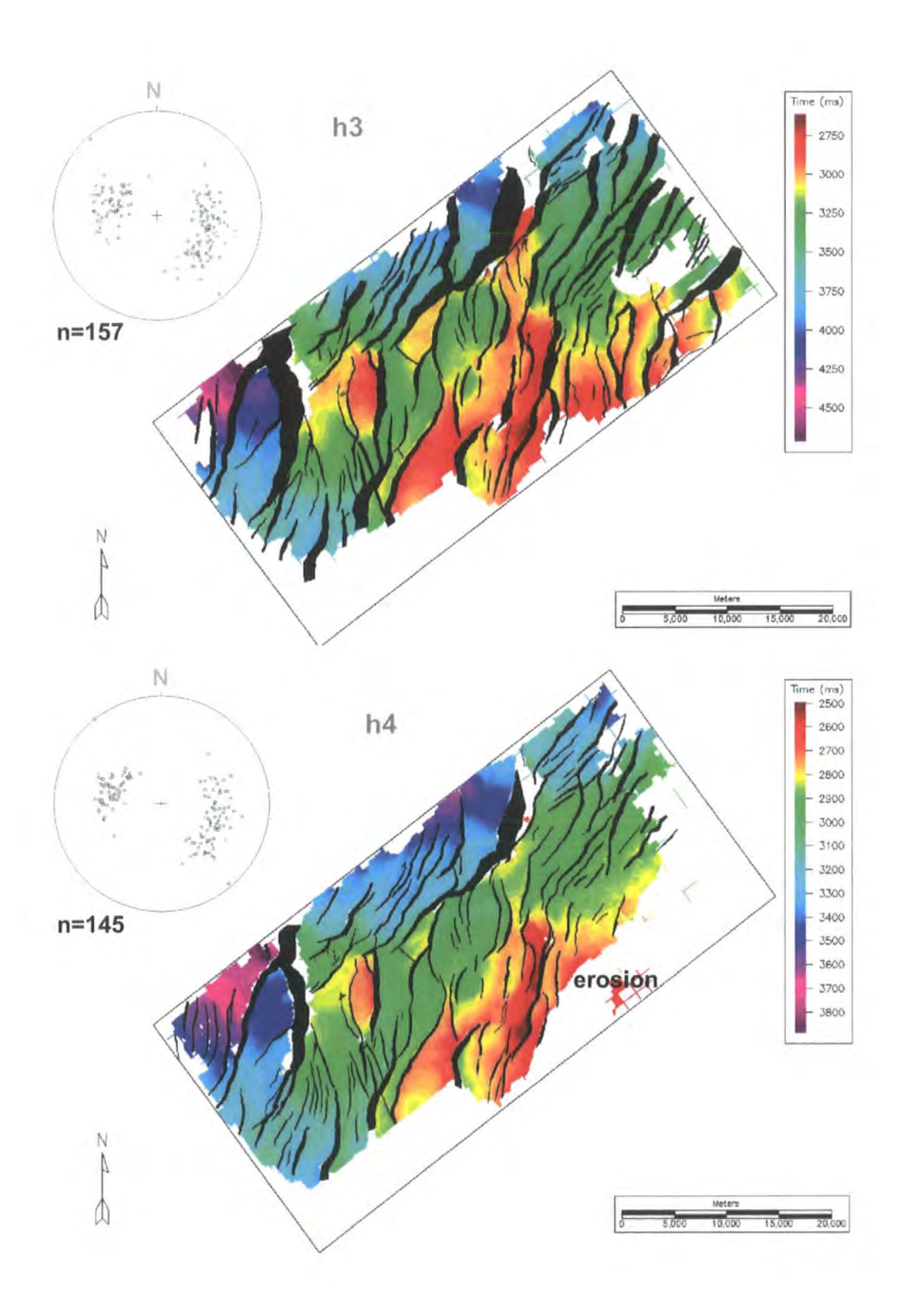
Except for the western edge of the basement, where it appears to be offset, the basement seems to be largely unfaulted, with a number of faults being imaged down to

the top-basement but not significantly offsetting it. The southern bounding fault of Graben C has a slightly listric geometry and locally appears to detach onto the top-basement (Fig. 3.19-3.22). However, the basin-scale map of top-basement and the cross sections from the southeastern area (Fig.3.3; Matthews *et al.* 1997) show that this geometry is probably atypical of the basin as a whole. It is speculated that this area of the basement was dipping to the northwest prior to the onset of Miocene faulting as a result of Eocene-Oligocene subsidence. The dip and dip-azimuth of the surface, which was broadly orthogonal to the NE-SW trending Miocene faults and the rheological contrast between the crystalline basement and the overlying mudrock cover sequence, may have caused the top-basement to act as a detachment surface resulting in localised thin-skinned extension.

3.4.3 The fault pattern

The faults have a variety of orientations, with a dominant \sim N-S and NE-SW trend. In total, 225 faults have been interpreted that offset at least one of the six horizons (h1-h6). The faults appear to be very densely spaced, with no more than 1 km between each fault and its nearest neighbour. The density of faulting is similar on all six horizons (Fig. 3.30). The modelled faults vary in size from <1 km to 25 km in length, with a mean length of 4.4 km. The maximum offset on each modelled fault varies from 19 m to \sim 6.2 km and the mean and median maximum offsets for the 225 fault sample are 603 m and 336 m, respectively. Fault offsets are discussed in Chapter 4.





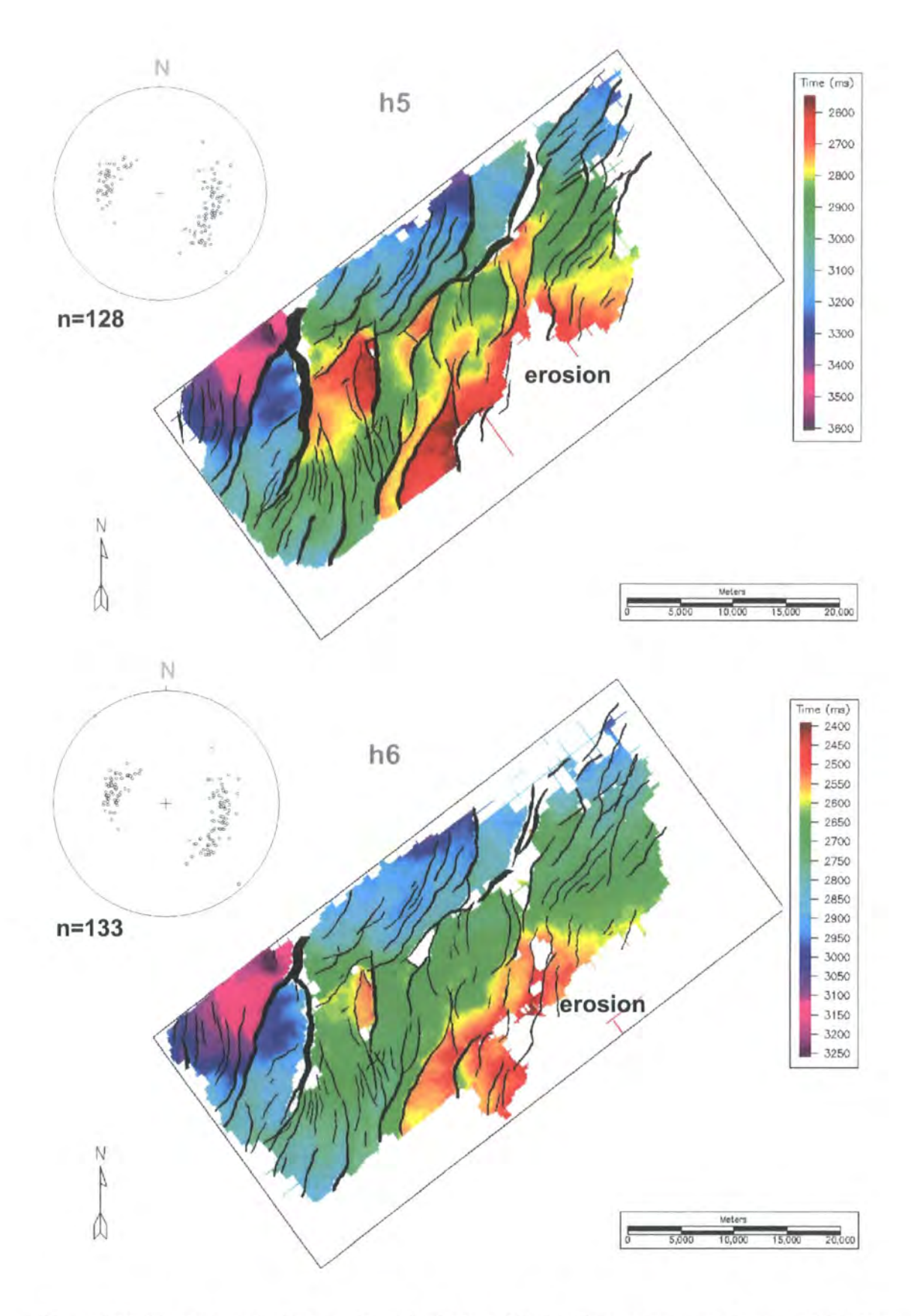


Figure 3.30: Six stratigraphic horizons from the Early to Middle Miocene sequence shown in TWT. The fault polygons are shown in solid black. The poles to planes of the fault polygons on each horizon are plotted on equal area, lower hemisphere stereonets. The poles to planes are calculated from the depth converted fault attribute database using the vectorial mean dip azimuth and the mean dip for each polygon.

The lower hemisphere stereographic projections show that the faults have a range of dips and dip azimuths. The poles to fault planes are calculated using a mean fault surface dip and a vector mean fault surface dip-azimuth for each fault. The vector mean is calculated using EZ-Rose (Baas, 2000) and is defined as (Agterberg, 1974):

$$\hat{\gamma} = \arctan \frac{\sum \sin x_i}{\sum \cos x_i}$$
 (3.3)

In this case, x_i is the dip-azimuth of the fault surface at each sample point. For all fault surfaces sampled, the measurements of dip azimuth are normally distributed and the vector mean dip azimuth and the arithmetic mean dip azimuth are practically equal, within 0.5° for 99% of faults, with a maximum difference of 1.03°.

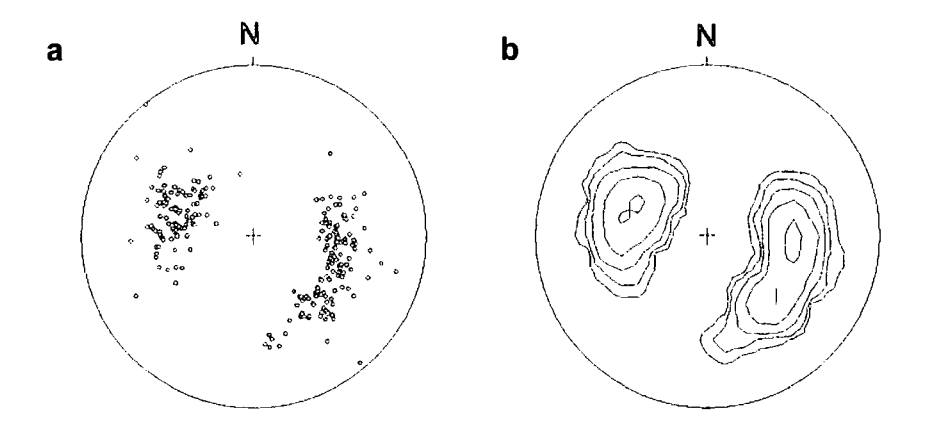


Figure 3.31: a) Stereonet for the whole fault sample, n = 225. Each point is a pole to fault plane plotted using a mean surface dip and a vector mean strike. b) Density plot of the same data.

The poles to fault planes typically plot as two clusters (Fig. 3.31), with one set of faults dipping moderately to steeply east and southeast and one set of faults dipping moderately to steeply west and northwest. The number of faults in each cluster is quite even, with 95 faults dipping east to southeast and 130 faults dipping west to northwest. The greater fault number dipping west to northwest reflects the location of the survey area on the southeastern margin of the main basin depocentre. The faults have a wide range of dip azimuths (and therefore strikes). The measurements of dip azimuth are of the vector mean dip-azimuth of each fault, calculated from numerous samples of the fault surface, taken along strike for each polygon. Because of this, the effects of fault surface geometry, such as curvature at the tips, is reduced. The range in dip azimuths (strike) is greater for faults dipping west and northwest (131°) than those dipping east and southeast (109°). The mean fault strike for the entire sample is 019°.

Depth conversion of the data using the methods discussed in section 3.3.2 has enabled an analysis of the fault dip angles. The range of fault dip is similar for both clusters. Overall, fault dips range from 19°-89° (Fig. 3.31), with 93% of faults having dips between 30°-60°. The mean dip for the 225 faults is 43° with a standard deviation of 9°. The mean fault dips for each of the horizons are all within 2°, with no systematic variation in mean dip with horizon age. The lowest dip recorded is significantly lower on the older horizons than the younger horizons. Horizons h1 and h2 have faults with lowest dips of 19° and 20°, respectively, whilst h5 and h6 have faults with lowest dips of 31° and 28°, respectively. This could reflect the apparent listric geometry of some of the faults. Although it must be noted that the simplicity of the depth conversion method used may not be adequate to correctly resolve subtle fault geometry.

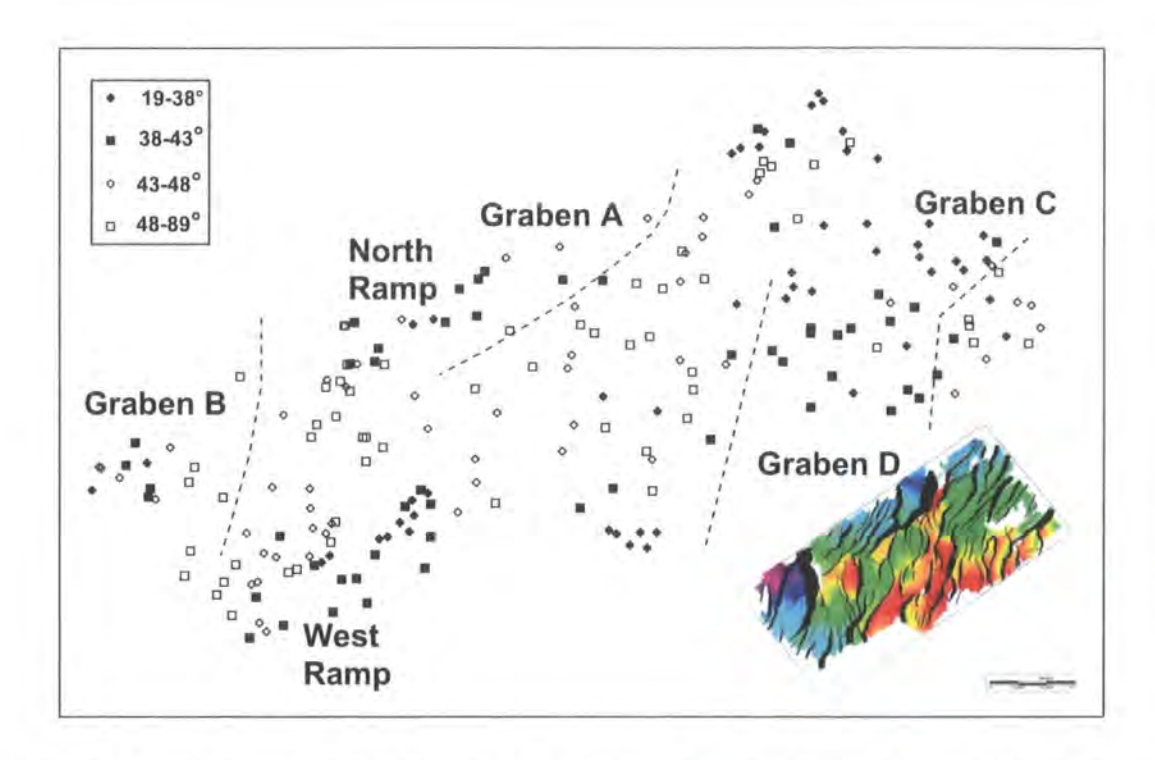


Figure 3.32: Map showing spatial distribution of fault dip angle. Each point is located at the fault centre n=225. The points are grouped into quartiles of fault dip. 1st quartile fault dips range 19-38°, 2nd quartile range 38-43°, 3rd quartile range 43-48° and 4th quartile range 48-89°. The dashed lines indicate the approximate boundaries of the graben.

Figure 3.32 is a map showing the locations of the 225 faults. Each point represents a single fault and is located at the fault centre, which has been calculated by taking a mean of the x-y coordinates for each fault. The faults are divided into four quartiles of fault dip angle. The median dip and the mean dip of the 225 fault sample are within 0.5° of each other. The map shows a correlation between fault dip and the spatial distribution. The faults within the four graben and on the connecting ramps have lower dip angles than those outside of the graben. This observation is not an artefact of the seismic data relating to the depth of the faults or the thickness of the overburden. Much of the eastern area, where the faults show lower dips, is structurally higher and has a thinner post-rift sequence than in some areas with steeper fault dips. However, the possible effect of sedimentary compaction on fault angle is uncertain and is difficult to constrain.

The fault geometry varies in different parts of the basin. In Graben A and B and much of the structurally high centre, the faults are planar in cross section but in Graben C and D many faults have listric or sigmoidal geometries (Figs. 3.17-3.26). The cross sections through Graben D show more sigmoidal faults at the southern end where the anticlinal geometry is most pronounced (Figs. 3.23-3.26).

Many of the faults are also curved or sigmoidal in plan view (Fig 3.30). In the majority of cases the fault surface is concave towards the dip direction. The density of faulting means that few faults are isolated and the majority of faults are hard linked. Due to the wide range of fault orientations, linkage is mostly between faults that meet at high angles rather than faults that overlap and link via relay ramps (see section 2.2.3). It is possible that the seismically imaged faults evolved through linkage via temporary and possibly sub-seismic relay ramps that were breached during continuing extension resulting in few obvious examples of relay ramps in the present day structure.

3.4.4 Structural evolution

Isochron maps have been produced for two intervals (Fig. 3.33). They show the difference measured vertically, in milliseconds two-way-time between two horizons. They are sensitive to changes in horizon dip and so cannot be used for the accurate analysis of fault movement. However, they do provide a useful picture of the overall thickness variations, which in turn indicates which areas were subsiding more than others during the time period separated by the deposition of the two horizons. Interpretation of the thickness variations seen in the isochron maps rests on the assumption that the sedimentation rate kept pace with the subsidence rate throughout the deposition of the studied interval and that at this scale of observation, sedimentation is considered to be uniform.

The first isochron map (Fig. 3.33a) shows the older part of the succession, between h1-h3, ~20 Ma to ~14 Ma. It shows that during that time, the deep graben were subsiding and were bounded by the large faults seen on the present-day fault maps. Furthermore, it shows that the area subsiding least at this time was a N-S trending horst, which is equivalent to the structurally highest area on the present-day maps. Graben D, adjacent to this horst also shows relatively little subsidence. This suggests that the present-day height of this graben is not necessarily the result of subsequent inversion.

The isochore map shows very little thickness variation across the central area of the survey, with most of the interval between 400-500 ms thick. This suggests that much of the faulting in this area did not occur until after the deposition of h3.

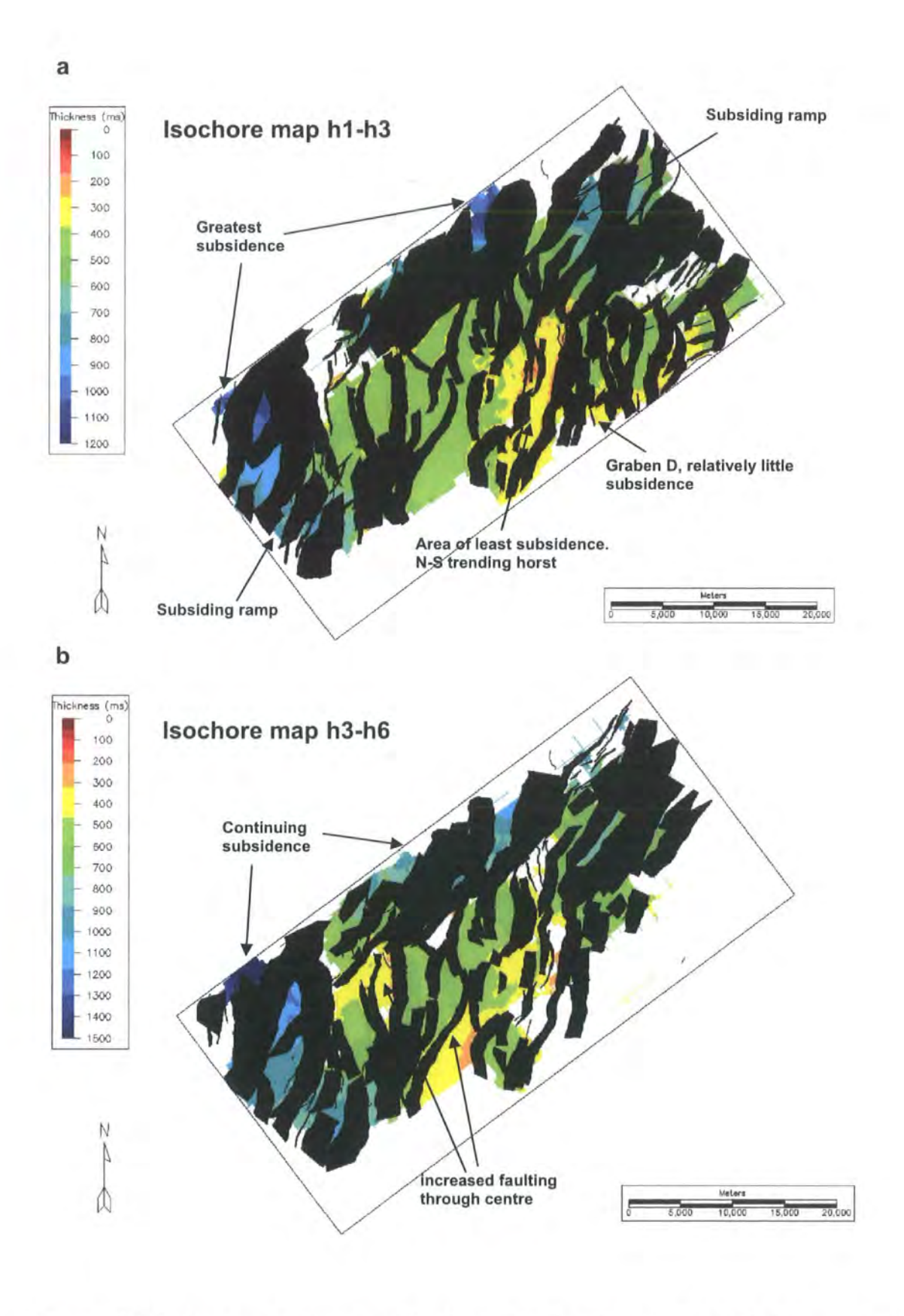


Figure 3.33: Isochore maps of two intervals, showing the time difference (ms TWT) between two horizons. The fault polygons are wider than shown on structure maps of a single horizon because they represent the distance between the footwall cutoff on the upper horizon and the hangingwall cutoff on the lower horizon. a) h1 to h3. b) h3 to h6.

The second isochore map (Fig. 3.33b) shows the younger part of the sequence, between h3-h6, ~14 Ma to ~10 Ma. This shows that the deep graben continued to subside during this time relative to the structural high. The central area shows more thickness variation during this time, which indicates that faulting increased across this area. The present-day graben are deep because of continued subsidence throughout the rifting episode. Likewise, the structural highs were relatively elevated throughout but began to become rifted during this later period.

The thickness variations shown on the isochore maps can also be seen in detail on the cross sections. The increased sediment thickness in Graben A and B can be seen on figure 3.16 and figures 3.17-3.18, respectively. Figure 3.18 shows very little thickness variation across the centre of the area, particularly between horizons h1-h3. Figure 3.17 shows Graben B and the ramp that connects the graben to the structurally high centre. Across the ramp, the older sequence thickens slightly towards the east, which indicates that during this time, the ramp was subsiding and rotating towards the depocentre in the graben. The younger sequence does not show this pattern of thickening. It is possible that at this location the ramp was initially linked to Graben B until the graben bounding fault propagated south to offset the ramp at this point.

The sedimentary sequence thickens into Graben D across the graben bounding faults, which indicates that the graben was subsiding throughout the Miocene rifting event (Figs. 3.23-3.26). However, within the graben there is little thickness variation until after h3 is deposited, indicating that much of this faulting post-dates h3. This is also the case in Graben C (Figs. 3.19-3.22). The sediment thickens across the graben bounding faults and also shows slight growth into these faults. However, the sediment shows little thickening across faults within the structure centre. Overall the Early Miocene sediment, h1-h3 shows a thickening towards the northwest, which suggests

that during this time faults to the northwest and possibly beyond the edge of the 3dimensional seismic survey were the controlling structures.

The timing of fault activity has been calculated for 225 modelled faults using the methods discussed in previously. Prior to the deposition of h2, many of the largest faults were active, including the large faults bounding Graben A and B (Fig. 3.34). This is consistent with the isochore map of the older sequence, which shows that these areas had subsided the most during this time (Fig. 3.33a). In addition, the faults bounding the southeast and east margins of Graben C and D, respectively, are also established along with a number of smaller faults. Thus at this early stage, the main elements of the present-day structure were likely already established.

The next set of faults, which formed prior to the deposition of h3, include most of the remaining large faults. In particular, the majority of the faults in the two deep fault-bounded structures, Graben A and B, formed at this time. These faults appear to be focussed within the existing graben, with very few forming in the centre of the area.

The subsequent fault set, which formed prior to the deposition of h4 show a similar pattern, particularly in Graben C where several faults form within the hangingwall of the bounding fault. However, this fault set includes some large faults in the centre of the area.

The timing of three subsequent fault sets has been constrained and mainly includes faults with relatively small offsets. The majority of these faults belong to the youngest fault set in the area that formed after the deposition of h6.

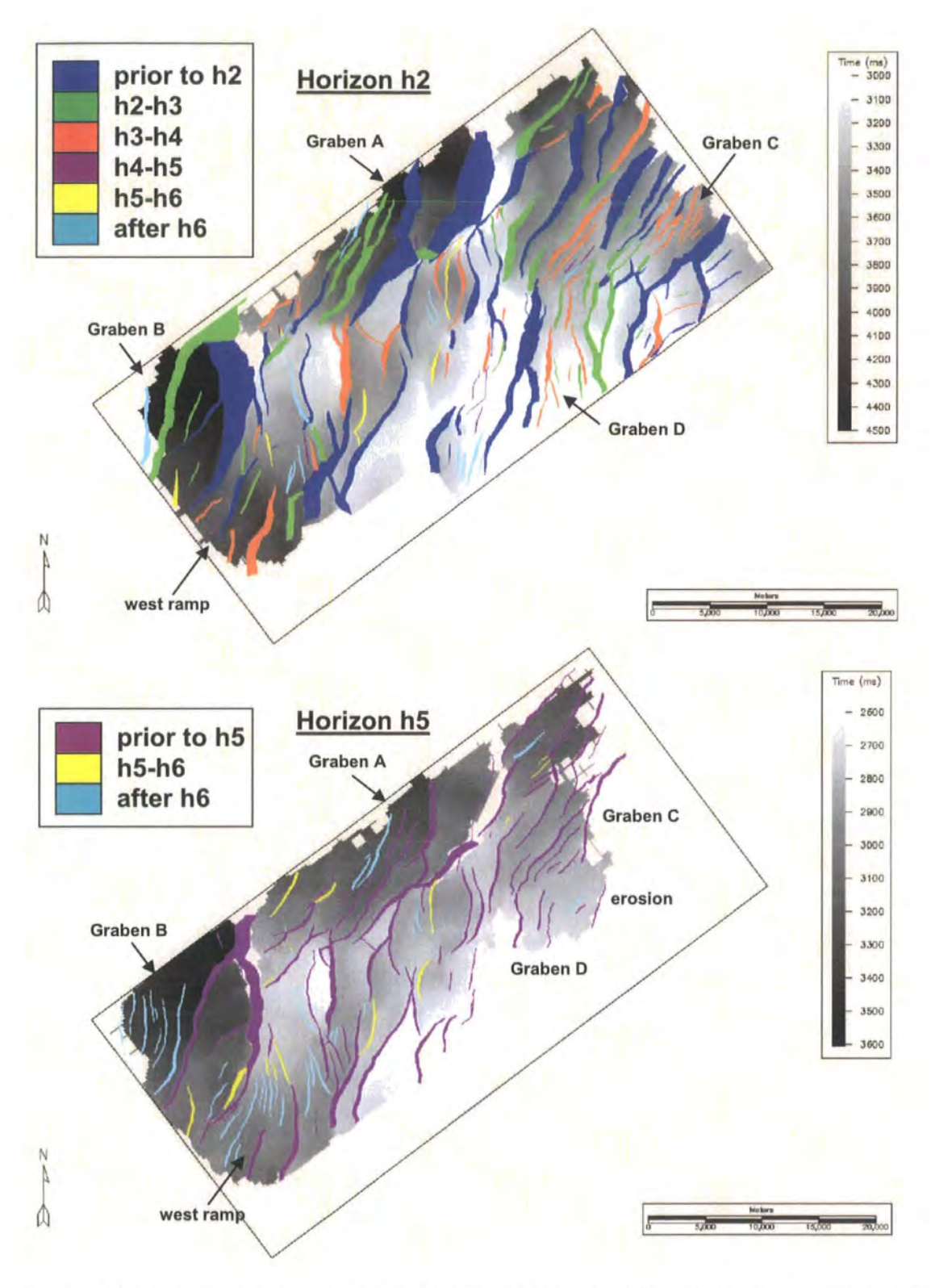


Figure 3.34: Structure maps in ms two-way time showing the age of the faults. Faults are colour coded based on the period during which they initiated. a) Map of faults as they offset horizon h2. b) Map of faults as they offset horizon h5.

Using the methods of fault timing discussed in Chapter 1, these faults either offset h6 only or they show an equal amount of offset on h6 and any other horizons. This faulting is very late in the rifting episode, ~10 Ma. Once again they are generally focussed within the graben or the hangingwalls of larger faults. Three areas in particular show concentrations of these youngest faults. Four faults form in a small depocentre to the southwest of Graben D, a number form within Graben B and many form across the hinged ramp structure in the west, which connects Graben B to the structurally high centre.

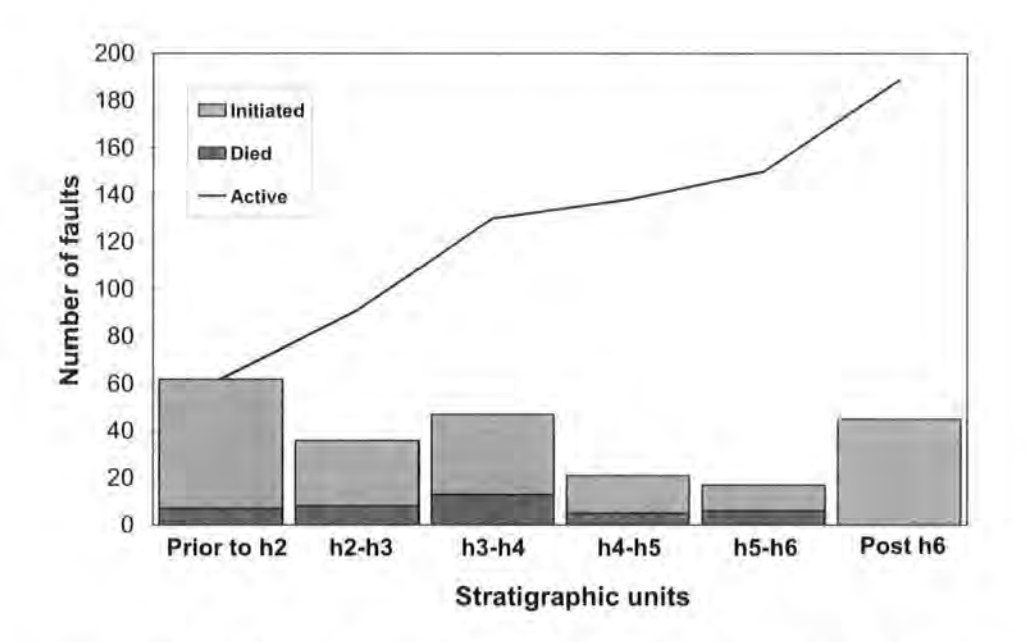


Figure 3.35: Plot showing the number of faults that initiated and died during each constrained time period. The 'Post h6' time period does not include the number of faults that died post h6 deposition. Most of the faults in the basin do not offset the regional Late Miocene u/c and none of the faults in the basin reach the present day seabed. The curve indicates the number of faults that were active during each time period.

Figure 3.35 summarises the number of faults that initiated and the number that had stopped propagating during each constrained time period. The curve indicates the number of faults that were actively propagating during each time period. The data show that the number of faults that had initiated was significantly greater than the number of faults that had ceased activity during each time period, resulting in a net increase in the

number of active faults. The number of faults that initiated during each time period does not show a systematic pattern. More faults initiated prior to the deposition of h2 than during any other single time period. The number of faults that initiated after the deposition of h6 is relatively high considering the earliest post-rift sequence is dated by well data as ~9-10 Ma (Vietnam Licence Team, 1995). The number of faults that were active increases systematically through time. This is also shown by the isochore maps, which show continued subsidence of the graben throughout the entire rifting sequence with increasing thickness variations during the deposition of the younger sequences.

3.4.5 Folding

Ninety three fold hinges have been mapped within the survey area, 56 of which are synclines and 37 anticlines (Fig. 3.36).

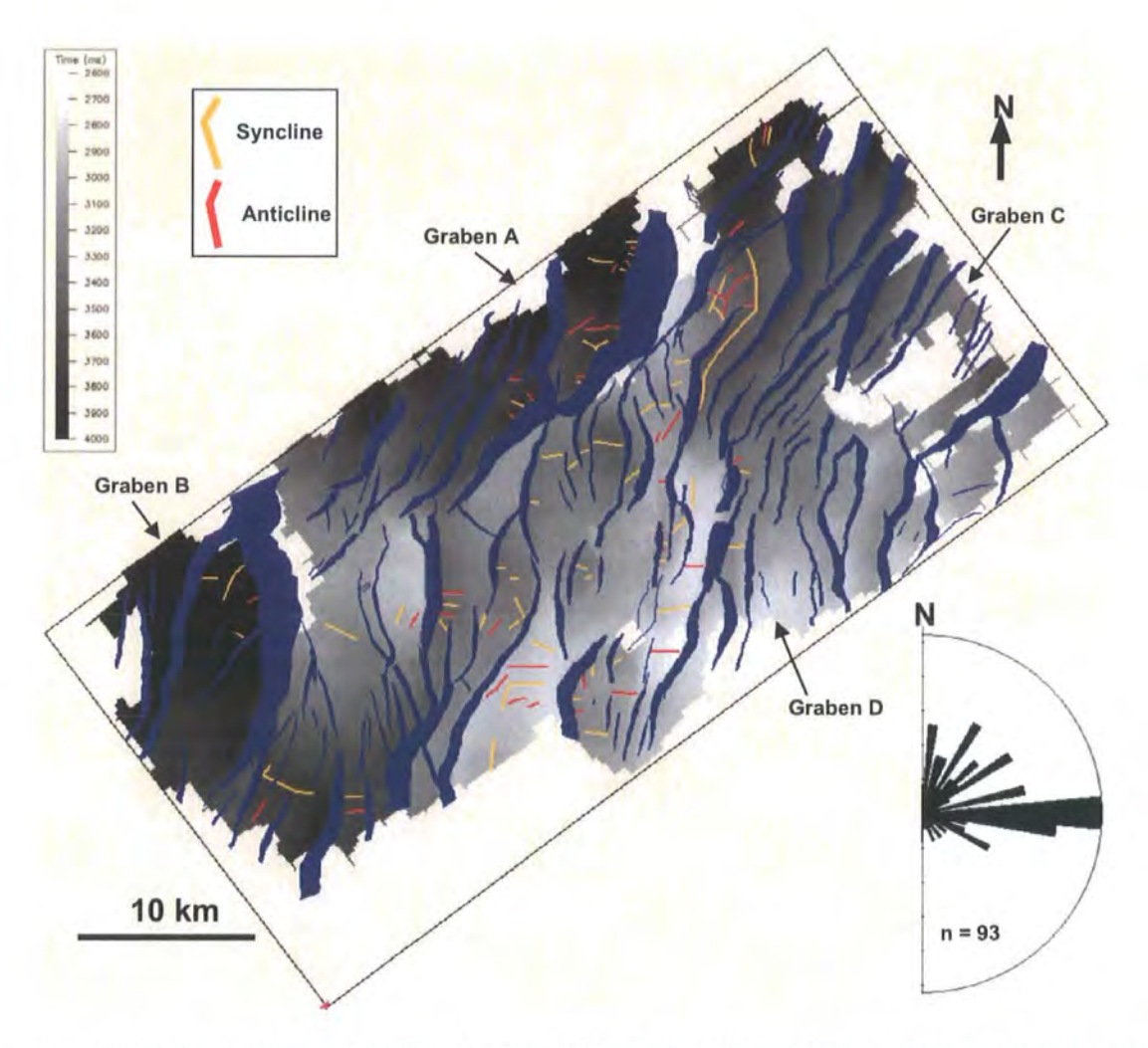


Figure 3.36: Structure map of horizon h3 in ms TWT including 93 mapped fold hinges and a rose diagram of the fold hinge azimuths. Most folds are sampled once but curved fold hinges are sampled at multiple points to accurately represent the variation in azimuth.

By investigating how the amplitudes of folds change through the folded sequence, the timing of folding has been constrained (Fig. 3.37). Equal fold amplitude indicates that the fold post-dated the sequence, whilst decreasing fold amplitude represents the growth strata (Suppe, 1997). Care has been taken to observe the fold geometry on sections perpendicular to the fold at each horizon in order to avoid artificial changes in the dip of



the fold limbs due to fold hinge rotation. The analysis rests on the assumption that fold amplification rate was comparable with the sedimentation rate during the period of folding.

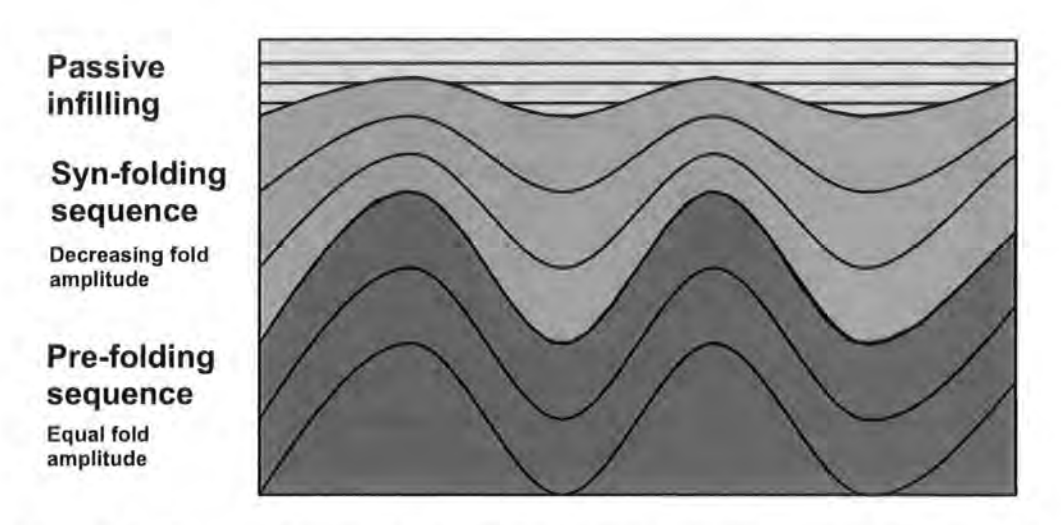


Figure 3.37: Cartoon to illustrate the use of fold amplitude variation to constrain the timing of folding.

Most fold hinges are <1 km in length, which is much shorter than the average fault length of 4.4 km. The folds are distributed throughout the structurally high centre and within Graben A and B. There is no evidence for folding within Graben C and D to the east, excepting three folds at the edge of Graben D. This may be a sampling or preservation issue relating to the erosion in Graben C and D. Most of the mapped folds are clearer on the younger horizons h3-h6, which have been eroded from this area.

The folds have been categorised into four types based on their geometries, timing and locations relative to adjacent faults. Type 1 folds form more than half of the total number of mapped folds (57 out of 93) (Fig. 3.38). These folds are located within fault hangingwalls immediately adjacent to the fault surfaces and are sub-perpendicular to the fault surface (transverse). They have relatively small wavelengths of up to 1 km and most have hinge lengths of ~500 m. The fold amplitude is greatest, for a given

stratigraphic horizon, adjacent to the fault surface and the folds plunge away from the fault into the hangingwall.

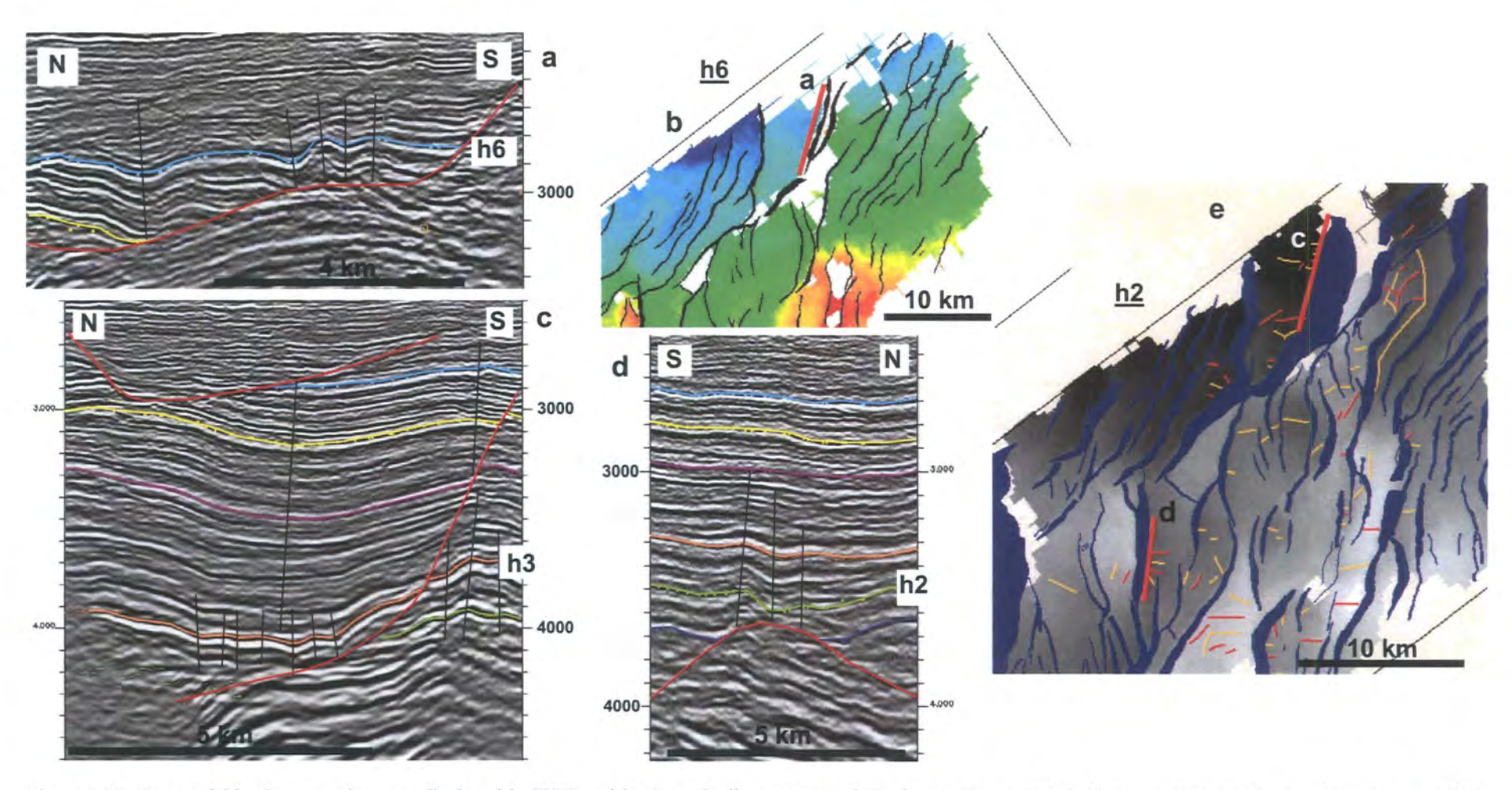


Figure 3.38: Type 1 folds. Cross sections are displayed in TWT and is x2 vertically exaggerated. Faults are shown in red. Cross sections a and c are from the same fault hangingwall. a) Folds are seen in h6 adjacent to the fault. b) location of cross section a. Shown on a map of h5. c) Type 1 folds are seen in horizon h3 adjacent to the fault surface. In addition, larger scale type 2 folds can be seen in the same hangingwall. d) Location of cross section c as shown on the fault hinge map of h2. All folds included not just type 1. e) Type 1 folds seen in h2 and h3. f) location of cross section e as shown on the fault hinge map of h2. All folds included not just type 1.

The trend of the fold hinge is sub-perpendicular to that part of the fault surface where the fold and fault intersect. This is particularly clear on faults with curved surfaces and multiple hangingwall folds, in which the fold trends vary along the fault strike. Two such faults have salient fault surface geometries; they are convex (in a horizontal plane) towards the dip direction and two have recessed fault geometries; they are concave towards the dip direction. The folds within the hangingwalls of the salient faults have divergent hinges, those within the hangingwalls of the recessed faults have convergent hinges (Fig. 3.39). A fifth fault has no curvature in the horizontal plane and has folds within the hangingwall with parallel hinges. Closer examination of Figure 3.36 shows that the fold hinges are subtly counter-clockwise of perpendicular, which is consistent with the sample as a whole. The rose diagram (Fig. 3.36) of fold hinge azimuth shows a dominant hinge trend of ~E-W. The mean fault strike is 019°, so the dominant fold hinge trend is ~20° counter-clockwise of perpendicular. The analysis of fault timing shows that Type 1 folds are relatively young and date from after the deposition of h4. They are synchronous with activity on the adjacent faults but do not necessarily coincide with the earliest activity on the fault.

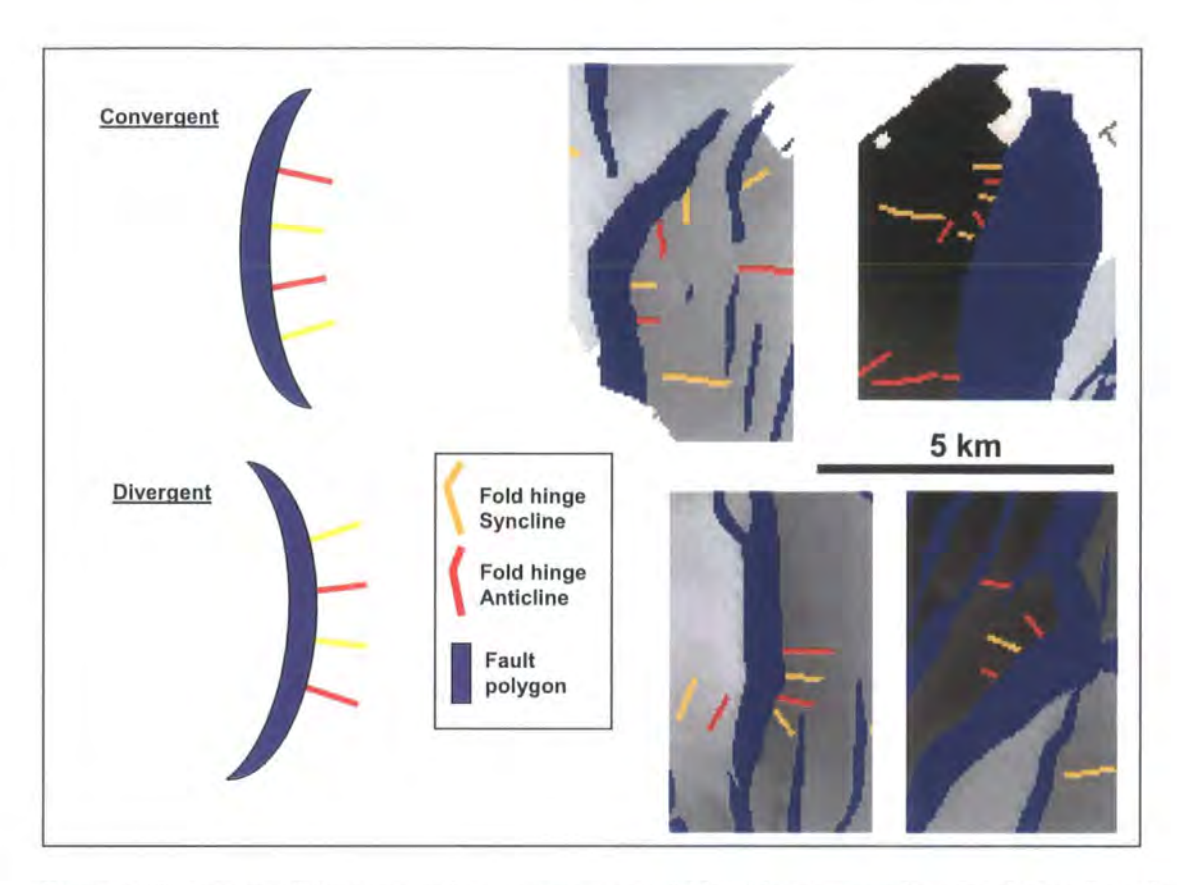


Figure 3.39: Cartoon of divergent and convergent type 1 folds with two examples of each type from the fault/horizon model. The examples show the fold hinges and fault polygons on horizon h2. The fold hinges of synclines and anticlines are coloured yellow and red, respectively.

Type 2 folds are located within the hangingwalls or footwalls of faults, are transverse to the fault, have significantly greater wavelengths (e.g. ~5 km) and longer hinges (mostly ~2 km) than Type 1 folds (Fig. 3.40). Furthermore they appear to be older than Type 1 folds. Nineteen of the folds are classified as being of Type 2. The folds of this group within Graben A and within the ramp area to the west date from h1 onwards, which is synchronous with movement on the large graben bounding fault. Folds of this type within a footwall, also show growth from h1 onwards. This demonstrates a clear association between Type 2 folds and fault movement.

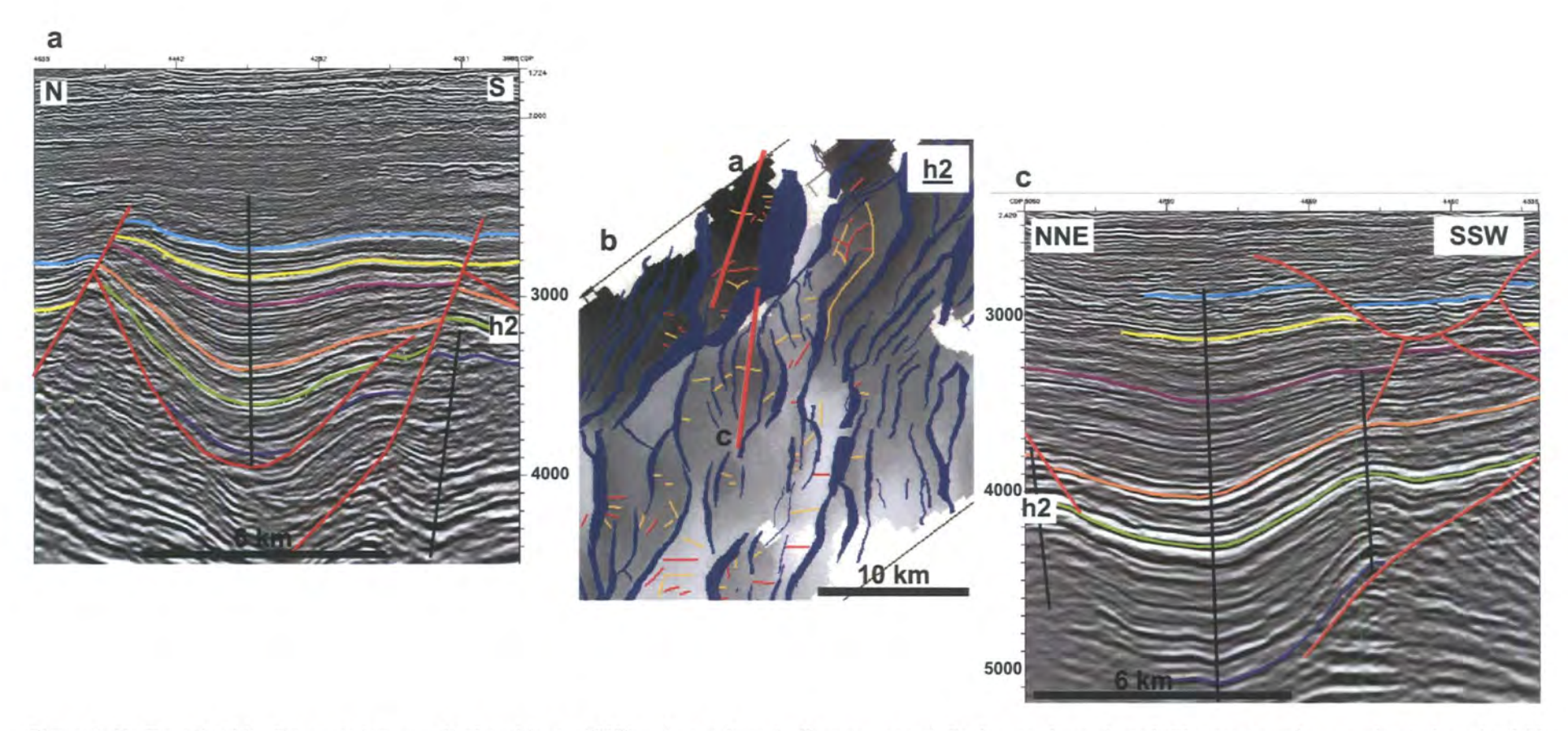


Figure 3.40: Type 2 folds. Cross sections are displayed in ms TWT and are x2 vertically exaggerated. Faults are shown in red. The cross sections are located on the fold structure maps and fold hinge maps (all folds are included on the map not just type 1).

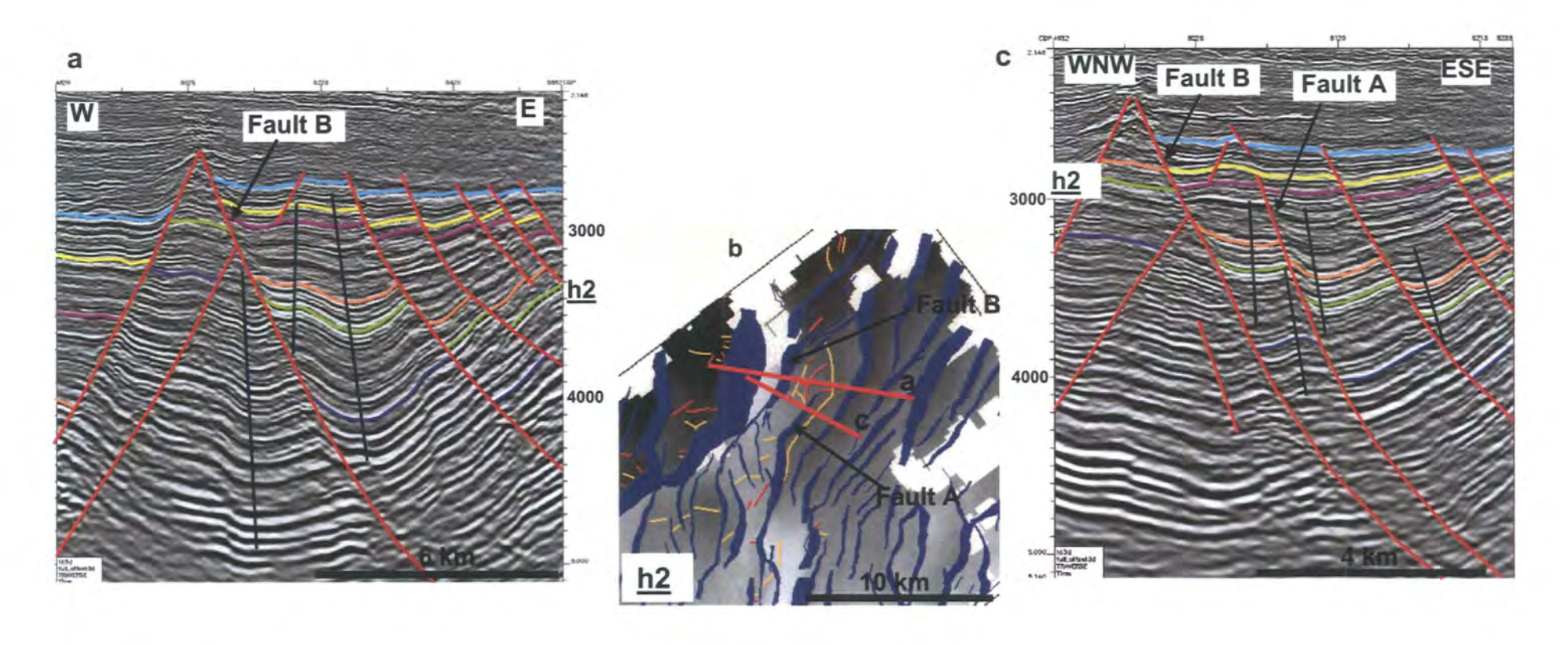


Figure 3.41: Type 3 folds. Folds are longitudinal - parallel to the faults. Cross sections are displayed in TWT and is x2 vertically exaggerated. Faults are shown in red and two of the faults are labelled A and B for reference a) Cross section ahead of the fault tip. Fault B only can be seen, fault A is not evident but the stratigraphy is folded. b) Cross section through Fault A. Fault B is shown for reference. c) Location of the two cross sections and the two faults. d) A possible model for the faults is that of forced folding (After Schlische, 1995).

Type 3 folds have trends that are longitudinal or sub-parallel to the faults (Fig. 3.41). They are shown on the rose diagram in Figure 3.36 with ~N-S to ~NE-SW trending fold hinges. Thirteen of the folds are classified as this type and they have a range of hinge lengths from 1 km up to the longest fold in the survey area, which has a length of ~10 km. This particular fold is atypical of folding within the basin. It has a wavelength of ~2 km and a curvilinear fold hinge that mimics the curved trace of the adjacent fault. Growth on this fold is dated from h1 onwards, and appears to pre-date fault movement on the adjacent fault. It is suggested that the timing of this fold and the longitudinal geometry may indicate that this is a forced fold, which grew ahead of the propagating fault tip (Withjack *et al.*, 1990; Schlische, 1995; Hardy and McClay, 1999).

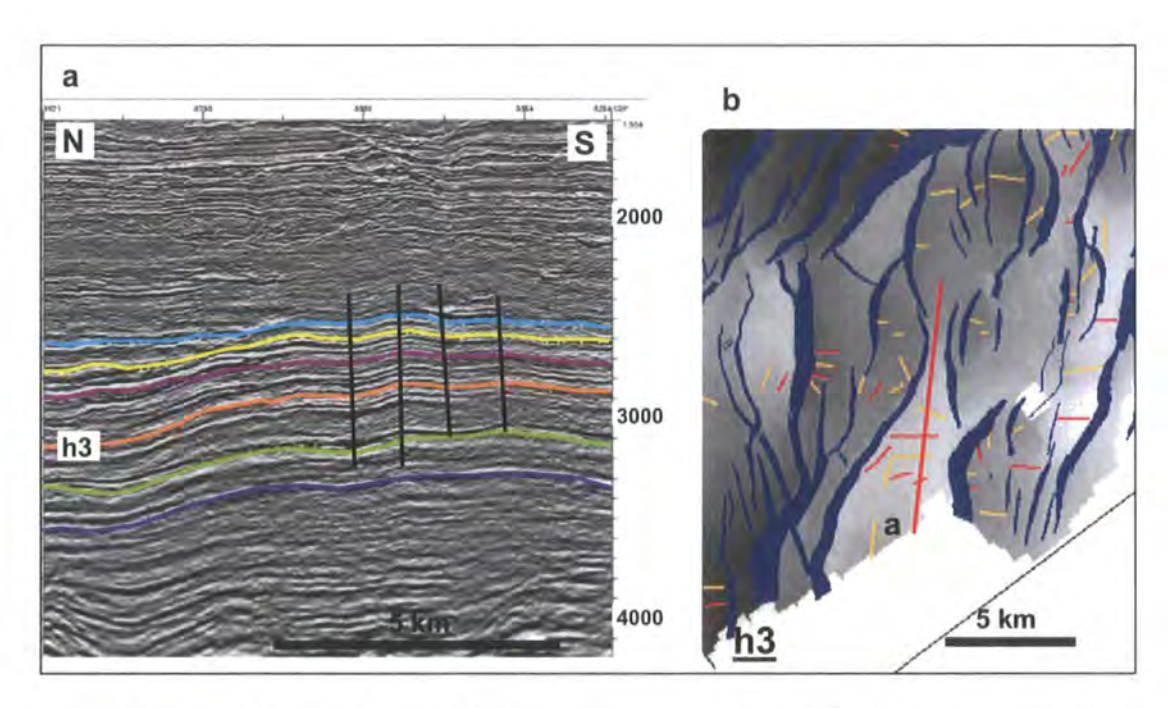


Figure 3.42: Type 4 folds in horst. a) Seismic cross-section showing the Type 4 folds. The vertical scale is in ms TWT. Horizon h3 is identified and is shown in b. Type 4 folds post-date h6. They have greatest amplitude on horizon h6 whilst the horizons below have equal or less amplitude. b) Map of horizon h3, the location of a is shown as a bold red line. The fault heave polygons are coloured blue whilst the anticline and syncline fold hinges are coloured red and yellow, respectively.

Type 4 folds are located within a N-S trending horst and are ~E-W trending, transverse to the bounding faults (Fig. 3.42). Four folds are classified in this group. They have a wavelength of ~3 km and do not show a clear plunge. They are dated as post-h6 deposition, as the amplitude on horizon h6 is equal to that of the horizons beneath. Folding may be synchronous with the latter stages of faulting or may have slightly post-dated faulting but this cannot be determined from the available temporal data. The faults that bound the horst formed prior to the folding.

3.4.6 Strain

The lengths of the horizons have been measured on the cross sections and compared with the horizontal length of the section. In this way the amount of extension has been calculated along each 2-dimensional line of section:

$$e = \frac{l/l_0}{l_0} \tag{3.4}$$

where I is the horizontal length of the section (deformed length) and I₀ is the length of the horizon. The values of strain calculated using this method are likely to underestimate the actual amount of horizontal extension since as much as 40% of extension may be accommodated by sub-seismic resolution faulting (Walsh *et al.*, 1991). However, assuming that the sub-seismic faults are as evenly distributed throughout the area as the resolvable faults, the values calculated allow a useful comparison of the amount of extension in different locations and across different structures.

All of the horizons measured show a net extension. In most cases, the maximum extension is recorded on horizon h1 and the amount of extension decreases upwards between horizons due to the syn-sedimentary nature of the faults. The graben show higher amounts of horizontal extension than the structurally high centre. Figure 3.18 has an overall E-W extension of 36% (β = 1.36) on horizon h1 but an E-W extension of 16% (β = 1.16) on horizon h1 across the structural high. The greatest recorded extensions of 50% (β = 1.5) are recorded on horizon h1 along Figure 3.16 (WNW-ESE) and 3.19 (NW-SE), which cross the area between Graben C and D, where the two fault sets cross. As stated above, the amount of net extension (or shortening) is a function of

the total amount of fault heave, which extends the section and folding, bed rotations and net reverse fault heaves, which shorten the section. In this area there is no evidence for net reverse fault heaves. The contributions of extension and shortening to the finite strain can be separated for analysis. On Figure 3.18 the contribution of shortening to the net E-W extension is 2%. This low value is consistent with the E-W trend of the fold hinges discussed in the previous section. Also, excepting Graben D at the eastern end of the section, there is relatively little bed rotation. If the structural high alone is analysed on Figure 3.18, the contribution of shortening to the E-W net extension is even less, at <1%. However, within the graben the amount of bed rotation is considerable, particularly in Graben C and D.

The E-W extension across Graben D has been measured on four cross sections, at different locations along the strike of the structure (Figs. 3.23-3.26). The amount of E-W extension decreases northwards along the structure from 33% (β = 1.33) to 16% (β = 1.16) on horizon h1 (the maximum measured extension). The contribution of shortening to the E-W extension also decreases northwards along the structure from 5% to 1%. The southern end of the structure (Fig. 3.23) has the greatest E-W extension despite also having the most bed rotation. Again it can be seen that the beds within this structure have an antiformal geometry and are significantly rotated. Increasing extension could result in increased bed rotation as the hangingwalls rotate to accommodate the extension. However, this relationship is not consistent in the majority of sections measured. There is no correlation between the amount of extension and the amount of folding and bed rotation. Alternatively, the greater amount of folding and bed rotation within the graben could have resulted if the faults and fault bound blocks had been rotated about horizontal axes following rifting. This would increase both the bed dip and the amount of fault heaves, or apparent extension.

Graben C has a maximum NW-SE extension of 35%, which is measured on horizon h1 at the northeastern end of the structure (Fig. 3.22). The graben also has significant bed rotations and an antiformal structure similar to that in Graben D. As stated previously, in most cases the greatest extension is measured on horizon h1 and then decreases upwards through the sequence as a result of the syn-sedimentary nature of the fault population. However, at the southwestern end of Graben C the greatest NW-SE net extension and the greatest amount of fault heave is measured on horizon h3 (Fig. 3.19). This increased extension upwards through the sequence may indicate that the antiformal geometry is due to bending or orthogonal flexure of the graben, which has resulted in greater NW-SE extension across the convex or upper side of the folded sequence. Unfortunately, the erosion across the hangingwall has prevented a measurement of the extension on horizons 4 to 6.

3.4.7 Fault kinematics

As is the case with most offshore datasets, the fault slip-vectors are difficult to establish. It is often unknown whether a fault with a normal offset has dip-slip or oblique-slip kinematics. Two of the faults do have sub-vertical dips of 86° and 89°. They are two of the smallest faults in the sample with lengths of < 1 km and lie within the hangingwall of a larger fault. Apart from these two minor faults, there are no other vertical or sub-vertical faults. Numerous published examples exist of seismically imaged strike-slip shear zones (Rangin *et al.*, 1995; Hsiao *et al.*, 2004; Williams *et al.*, 2005). The 3-dimensional seismic data and additional 2-dimensional seismic lines from across the basin have been carefully examined for evidence of strike-slip structures using the criteria discussed by Harding (1990). None of the seismic data shows any obvious geometric evidence for strike-slip faulting.

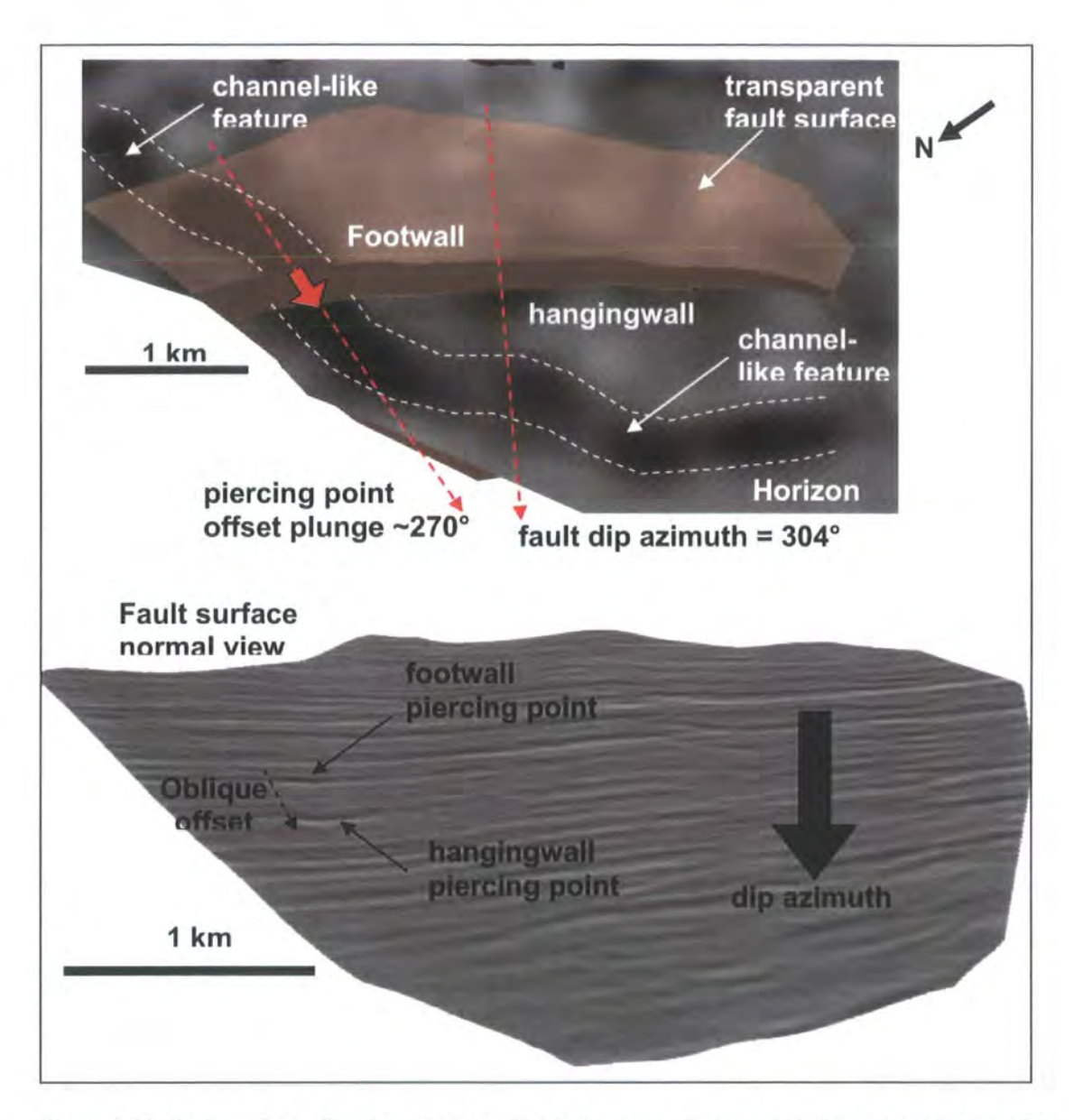


Figure 3.43: Fault surface offsetting a channel-like sedimentary feature. a) 3-dimensional image of the fault surface (transparent) and horizon h4 (in time). The horizon has been used to slice the seismic amplitude volume, which is then projected onto the horizon surface. The horizon is offset by the fault. The channel-like feature is an elongate 'patch' of strong positive amplitude. b) Fault-plane-normal view of the fault surface (in time). The fault surface has been used to slice the seismic amplitude volume, which is then projected onto the fault surface. The channel-like feature intersects the fault surface in two places, representing the footwall and hangingwall intersections. The feature is evident as a thin, laterally constrained, positive amplitude anomaly. The hangingwall intersection shows subtle incision into the reflector beneath.

Sometimes offset channels or other piercing points can provide a means to establish the kinematics of a fault. The 3-dimensional seismic data has been carefully examined for possible fault piercing points. The seismic data can then be sliced using the fault surface and displayed on the fault surface to show the relative juxtaposition of

the channel piercing point. Timeslices, which are horizontal sections through the seismic volume, have been examined for evidence of channels. Channels could be represented by amplitude changes, resulting from a contrast between the acoustic response of the channel fill, e.g. sand and the adjacent sediment e.g. shale (Davies and Posamentier, 2005). They should have thin, narrow, elongate geometries and are not necessarily represented by significant incision at the scale of the seismic data. For a channel to be recognisable on a horizontal section, either the stratigraphy must also be horizontal or the channel must be deeply incised. The less deeply incised the channel is, the nearer to horizontal the stratigraphy must be for the channel to be recognisable. The TraptesterTM software provides an alternative to using horizontal timeslices. The software allows the interpreter to slice the seismic amplitude volume using a modelled horizon and to display the seismic amplitude character on that horizon. This method is equivalent to the more widely used method of amplitude extraction within a specified time/depth window.

Both methods have been used to search for channels within the syn-rift stratigraphy (Fig. 3.43). An investigation of the timeslices through the volume did not show any channel like features, probably due to the dipping strata and the number of faults. However, by using the alternative method and slicing the seismic volume using each horizon, a sedimentary feature, possibly a channel, has been detected. The feature is located in Graben A on horizon h4. It is a long, narrow 'patch' of strongly positive amplitude and is slightly curved in plan view. It is evident on the same stratigraphic horizon in the footwall and hangingwall of a fault. This should be the case as the horizon represents a single depositional surface.

Once a channel-like feature has been indentified, the fault surface is used to slice the seismic volume. The laterally constrained, positive amplitude anomaly is evident on the fault slice where it intersects the fault in the hangingwall and footwall. In the hangingwall, the channel shows slight incision into the reflector beneath but it is mostly limited to one reflectors width. The offset of the channel represents the finite fault movement subsequent to its deposition. By joining the piercing points in the hangingwall and footwall slices, the finite slip vector of the fault can be established. The slip vector appears to be oblique relative to the dip azimuth of the fault surface, with a dip azimuth of 304° and a slip vector plunge of 270°, i.e. sinistral-normal oblique slip.

3.4.8 Summary of results

- The faulting represents one rifting event during the Miocene and there is no correlation between fault age and fault orientation.
- Graben A and B are the deepest parts of the survey area and were subsiding throughout the Miocene rifting event.
- Ramps connect the deeper graben to the structural highs and may provide pathways for fluid migration and sediment transport.
- The beds in Graben C and D, in the east of the survey, have unusual antiformal geometries.
- Graben C and D were subsiding throughout the rifting event but show relatively little subsidence compared to Graben A and B.
- The southern end of Graben D is higher in the centre than at the flanks but was structurally high at an early stage due to reduced subsidence, not necessarily subsequent uplift.
- There is no evidence for net reverse fault offsets anywhere within the basin.

- The graben bounding faults were established at an early stage and remained active throughout the rifting episode.
- The number of faults increased through time and later faulting appears to have been focussed within the graben.
- The mean dip of the fault sample is 43° and the mean strike is 019°.
- Faults within the graben have lower dips than those outside of the graben.
- Graben C and D in the east, include apparently listric and sigmoidal faults.
- The antiformal beds of Graben C have increasing extension upwards through the sequence.
- Horizons h4, h5 and h6 are eroded within Graben C and D.
- Four types of fold have been identified: a forced longitudinal fold that developed ahead of a propagating fault tip; folds that are synchronous with fault movements; small folds within hangingwalls that date from h4 onwards (younger than the earliest fault movement) and have hinges that trend slightly counter-clockwise of the fault dip azimuth; ~E-W trending folds on a horst that post date h6 deposition.
- The greatest extension measured is 50% whilst an extension of 16% is measured across the structural high. Figures of 33-37% extension are typical for the graben.
- The fault kinematics have been established for one oblique slip fault. The azimuth of the piercing point offset is ~270° compared to the fault dip azimuth of 304°.

CHAPTER 4. A NEW STRAIN DISTRIBUTION MODEL FOR RIFT BASINS WITH A CASE STUDY FROM THE CENTRAL NAM CON SON BASIN, OFFSHORE VIETNAM

4.1 INTRODUCTION

Fault populations observed in rock outcrops and from interpretations of 3-dimensional seismic datasets are more complex than those predicted by simple models of faulting (Reches, 1978; Krantz, 1988; De Paola et al., 2005 a & b; Wilson et al., 2006). Rather than seeing a single set of bimodal, conjugate faults with an orientation and slip vector that reflect the regional stress system, as predicted by simple Andersonian models (Anderson, 1951), many rift basins develop multiple fault sets with a range of orientations, with both dip-slip and oblique-slip kinematics. In some cases, the differently oriented fault sets show consistent cross-cutting relationships, indicating that they may be related to different tectonic episodes (Davies et al., 2001). However, in many examples this is not the case and the faults are broadly coeval, multimodal systems (e.g. De Paola et al., 2005 a & b; Wilson et al., 2006). In many extensional basins, such multiple sets of normal faults form rhomboidal patterns in plan view, and may show a quadrimodal distribution when plotted on a stereographic projection (Reches, 1978; Krantz, 1988).

The odd axis model of Krantz (1988) describes the geometry and slip vectors for faulting during 3-dimensional strain, in which none of the axes of principal strain are equal to zero (i.e. non-plane strain, Fig. 4.1a). The model was compared with field data from the Chimney Rock fault array, Utah, a natural example of a rhomboidal fault pattern (Fig. 4.1b). Analogue clay models have also been successful in reproducing complex fault patterns by applying an extension vector that is oblique relative to an

underlying heterogeneity (Withjack and Jamison, 1986) (Fig. 4.1c). This has led to the suggestion that multimodal faulting patterns may be a characteristic feature of oblique extensional – or transfersional – rift basins (De Paola *et al.*, 2005a & b).

Unfortunately, the analyses and models described above require kinematic information derived from either analysis of fault slickenlines preserved in the field or from a prior knowledge of the experimental boundary conditions.

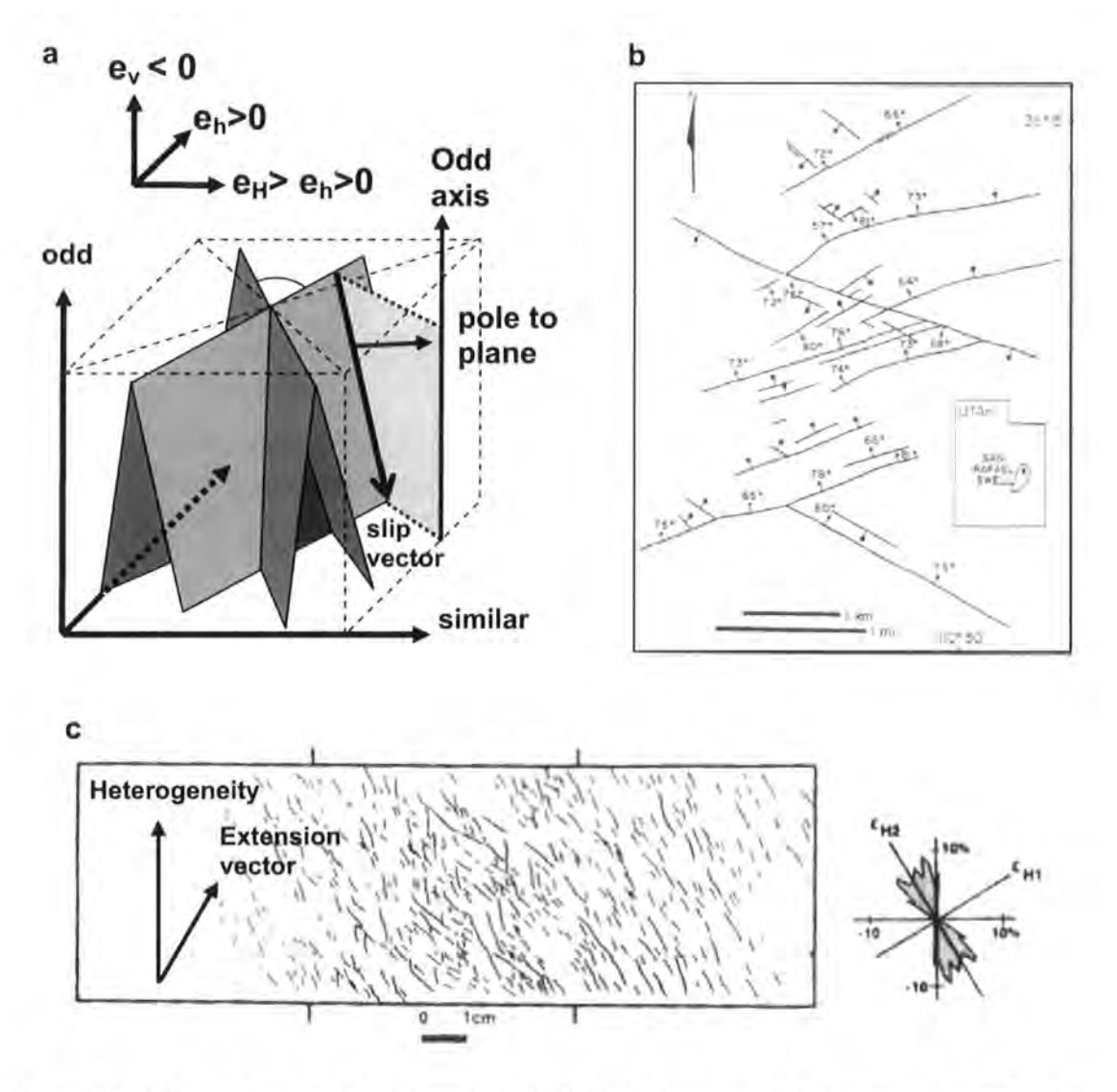


Figure 4.1: a) The odd axis model of Krantz (1988). b) The Chimney Rock fault array, an example of a 3-dimensional fault pattern from Krantz (1988). c) Analogue model of oblique extension after Withjack and Jamison (1986).

In general, subsurface datasets lack fault kinematic data, meaning that it is not clear whether the offset on a fault is the result of dip-slip or oblique-slip movement. Without this information, it is difficult to apply traditional methods of fault analysis (e.g. stress inversion techniques) or to make inferences about the far-field strain. Further complications arise if the reactivation of pre-existing structures or heterogeneities occurs within the basement or an older sequence. It is usually difficult to unambiguously identify and quantify the contribution of reactivation to the overall fault pattern (Holdsworth *et al.*, 1997). This ultimately means that it is difficult to assess whether the orientation of a fault set reflects either the regional stress regime or has been modified by the influence of an underlying basement fabric.

In this chapter a conceptual model is presented that uses variations in fault offsets to predict the most likely orientation for the maximum horizontal extension direction irrespective of whether or not reactivation has occurred. The model predicts an ideal fault orientation (strike) based on the distribution of fault dip-slip offsets throughout a fault population. The amount of offset systematically decreases on faults that are oblique to this ideal orientation.

The model is tested using a high resolution 3-dimensional seismic reflection dataset from the central Nam Con Son Basin, on the Vietnamese continental shelf. A fault/horizon model has been developed for the Early-Middle Miocene syn-rift sequence, which reveals a pattern of predominantly N-S to NE-SW-trending normal faults with a ~130° range of strikes. By comparing the amount of dip-slip offset to the orientation of each fault, the strike associated with the greatest offsets can be identified, the so-called 'ideal fault orientation'. The offset decreases systematically as fault strike becomes more oblique to the ideal orientation.

Although the model predicts the amount of fault offset, it does not predict the number of faults in a particular orientation. The Nam Con Son Basin data show a discrepancy between the orientation of faults with greatest offsets compared to the orientation associated with the greatest number of faults. It is suggested that this discrepancy could reflect the influence of a pre-existing fabric within the area. If correct, the model may provide a means of quantifying the contribution of reactivation to the development of a fault population during rifting.

4.2 CONCEPTUAL MODEL OF STRAIN DISTRIBUTION

The model exploits the observed variations in dip-slip offset with fault strike that typically occur in rift basins worldwide. Dip-slip offset is here defined as "the distance, measured parallel to the fault surface, in the dip direction, between the footwall and hangingwall cut-offs for a given stratigraphic horizon". For each fault, the maximum dip-slip offset is used, which represents the total strain accommodated by that fault (Fig. 4.2).

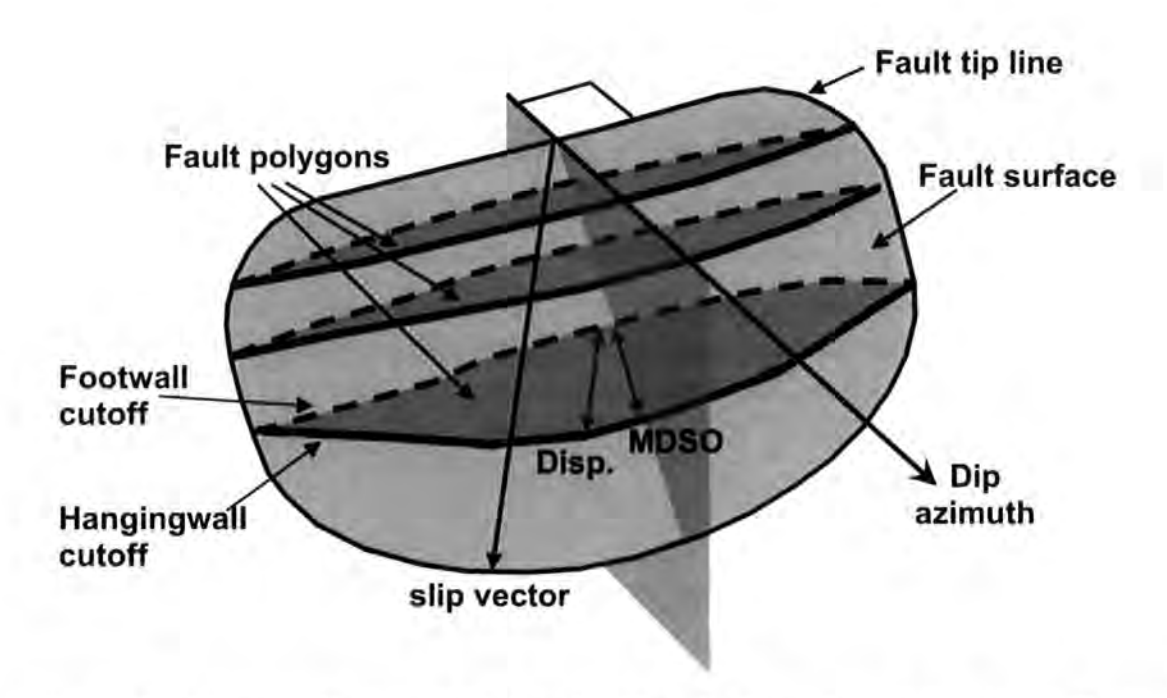


Figure 4.2: 3-dimensional image of a fault surface illustrating the definitions used herein. The fault polygons are defined by a footwall cutoff (dashed line) and a hangingwall cutoff (solid line). Displacement (Disp.) is the distance between the hangingwall and footwall cutoffs of a particular horizon measured parallel to the fault surface and the slip vector. Dip-slip offset is the distance between the hangingwall and footwall cutoffs of a particular horizon measured parallel to the fault surface and the dip azimuth. Maximum dip-slip offset (MDSO) is the greatest dip-slip offset measured on a particular fault surface, as shown in the example.

Figure 4.3a is a cartoon that shows a 2-dimensional plan view (for illustrative purpose) of three fault polygons (in grey), which are defined as the area of a fault surface that is enclosed by the footwall and hangingwall cut-offs for a particular

stratigraphic horizon. The bold arrows represent the magnitude and direction of the maximum fault displacement (plan-view component), whilst the thinner arrows represent the magnitude and direction of the maximum dip-slip offset (plan-view component). For this 2-dimensional illustration the fault dip angle is ignored but will be considered later.

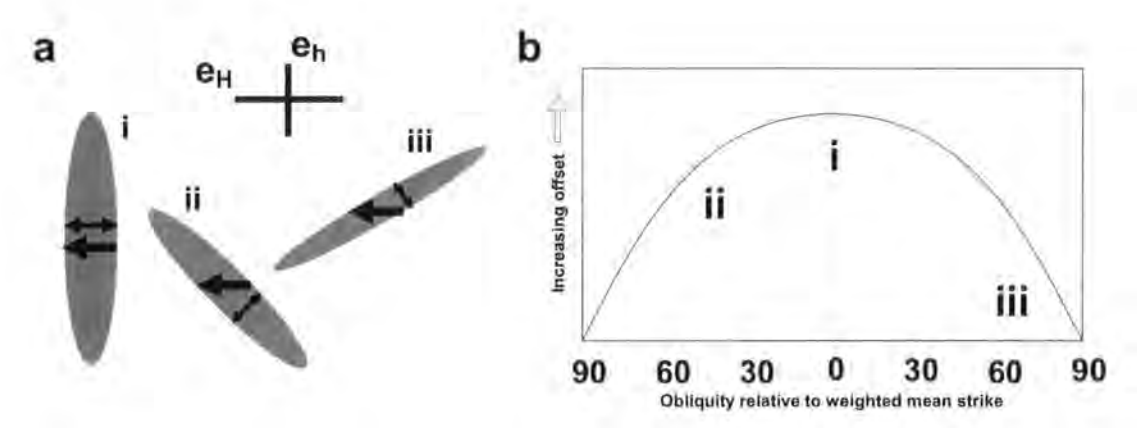


Figure 4.3: Strain distribution model. a) Plan-view cartoon of fault orientation relative to e_H. On faults i, ii, and iii the thick arrows, which represent the magnitude of the displacement (plan-view component), are equal in length. On fault i the fault dip-slip offset is equal to the displacement but on faults ii and iii the dip-slip offset offset is less than the displacement. b) The three theoretical faults from a are plotted beneath a theoretical curve which describes the geometric relationship between the offset and the strike of a fault relative to the weighted mean strike of the sample. The exact shape of the curve is a function of fault dip (see text).

Fault i strikes orthogonal to e_H and has the greatest dip slip offset. It has dip-slip kinematics and so the dip-slip offset is equal to the displacement. Faults ii and iii are oriented oblique to fault i and have strikes that are not orthogonal to e_H and oblique-slip kinematics. Hence, the maximum dip-slip offsets on all oblique faults are reduced relative to that of fault i, the ideally oriented fault. The maximum displacement on faults ii and iii is equal to that of fault i because the slip vectors are parallel to e_H. However, the dip-slip offset, which is measured parallel to the dip direction, is reduced because the slip-vector is oblique.

If fault strike is plotted against maximum fault offset for a sample of faults, a peak offset value will correspond to the ideal fault orientation that is orthogonal to e_H (Fig. 4.3b). Other faults plot away from the ideal orientation and have reduced maximum offsets. The exact centre of the sample can be calculated using a weighted mean strike, which takes into account the distribution of the maximum offset:

$$\bar{x} = \frac{\sum_{i=1}^{n} w_i x_i}{\sum_{i=1}^{n} w_i} \tag{4.1}$$

Where w_i is the maximum dip-slip offset for each fault and x_i is the strike of each fault.

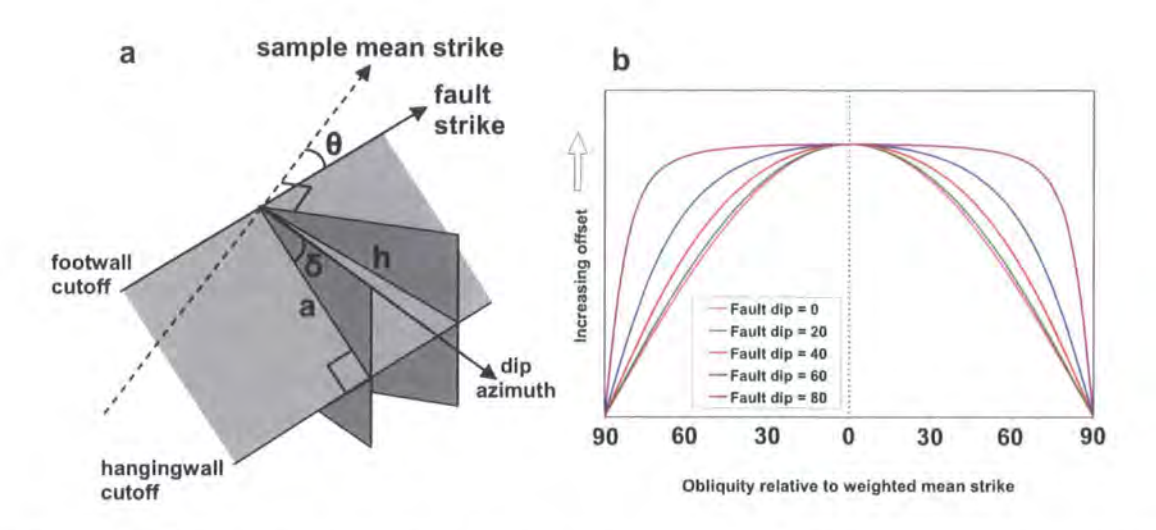


Figure 4.4: a) Geometric relationship between maximum offset and fault strike. a = maximum dip-slip offset, h = displacement, $\delta = dip$ of fault plane and $\theta = the$ difference between the fault strike and the weighted mean strike for the fault sample. b) Plot of curves with varying fault dip. A fault dip of 0° produces the flattest curve.

The curve that describes the sample distribution (Fig. 4.3b) represents the maximum dip-slip offset predicted by the model for a fault of given dip and strike relative to the weighted mean strike of the sample. It is defined as:

$$a = \frac{h\cos(\arctan(\tan\delta\cos\theta))\cos\theta}{\cos\delta}$$
(4.2)

Where a is the maximum dip-slip offset measured in the fault plane, h is the displacement, θ is the angle between the fault strike and the weighted mean strike of the sample and δ is the dip of the fault plane (Fig. 4.4a). A curve for a fault dip of 0° is the flattest possible curve (Fig. 4.4b). For any given fault dip, the curve defines the maximum predicted dip-slip offset because, in reality, faults will plot beneath the curve because of fault growth. The key point is that, regardless of fault dip, these curves predict the greatest dip-slip offset on faults with the ideal orientation, i.e. those whose strikes are close to the weighted mean strike.

4.3 APPLICATION TO THE NAM CON SON BASIN FAULT MODEL

The conceptual model outlined above has been tested using the fault model derived from detailed interpretation of a 3-dimensional seismic reflection dataset from the central Nam Con Son Basin. By using Badley's TraptesterTM software, the hangingwall and footwall intersections for each horizon can be accurately modelled on the fault surface. The hangingwall and footwall cutoffs of a given stratigraphic horizon on a fault surface define a fault polygon. Once modelled, TraptesterTM uses the fault polygons to calculate various fault attributes. The dataset and sampling methods used are fully described in section 3.3. The resulting database of fault attributes describes the dip and dip azimuth and the apparent throw and apparent heave on each horizon at regularly spaced points along the length of each fault. The apparent heave and apparent throw are then used to calculate the dip-slip offset at each point in the plane of the fault surface. Offset is used, rather than throw or heave because it is not affected by any later fault rotations, e.g. if the fault is steepened, for example, then the heave is reduced and the throw is increased but the offset remains unchanged. The measurements of dip-azimuth are used to calculate a vector mean dip azimuth for each fault surface using Equation 3.3. The vector mean dip azimuth is then used to calculate the fault strike, which has been used throughout this study.

Uncertainties in calculating the fault dip-slip offset arise due to inaccuracies in determining the vertical and horizontal position of the hangingwall and footwall cut-offs. The vertical accuracy is limited by the resolution of the seismic data, which is estimated to be ~15 m for this dataset. The uncertainty associated with the horizontal position of the cutoff is due to the accuracy of the interpreter and is estimated to be ~25 m. The seismic character is often disrupted either side of a fault and so it is difficult to

be precise when picking fault sticks and locating the fault/horizon intersections. The uncertainty in fault offset due to both vertical and horizontal positioning equates to error bars of ~60 m for most faults. In a minority of cases, 37 faults out of 225, it is not certain that the largest offset recorded is in fact the maximum dip-slip offset for that fault. This is due to an absence of fault polygons in areas where the horizon interpretations are incomplete because of poor quality seismic data or erosion. For these faults, the maximum offset is a best estimate based on the seismic data adjacent to the fault, any tentative horizon interpretation and a comparison with nearby faults.

The uncertainty associated with measuring the fault strike is very difficult to constrain. It results mainly from inaccuracies in the positions of the fault sticks or segments, which are picked manually by the interpreter and used to create the fault surface. However, because the fault strike is calculated from the vector mean dipazimuth, which is based on a number of sample points on the fault surface, the probability that the fault segments are misaligned in such a way that would result in a significant rotation of the fault strike relative to the fault's true orientation is considered to be very low.

4.4 THE NAM CON SON BASIN FAULT SAMPLE

The fault/horizon model reveals a dense, complex fault network pattern, with faults predominantly dipping east to southeast and west to northwest (Fig. 4.5).

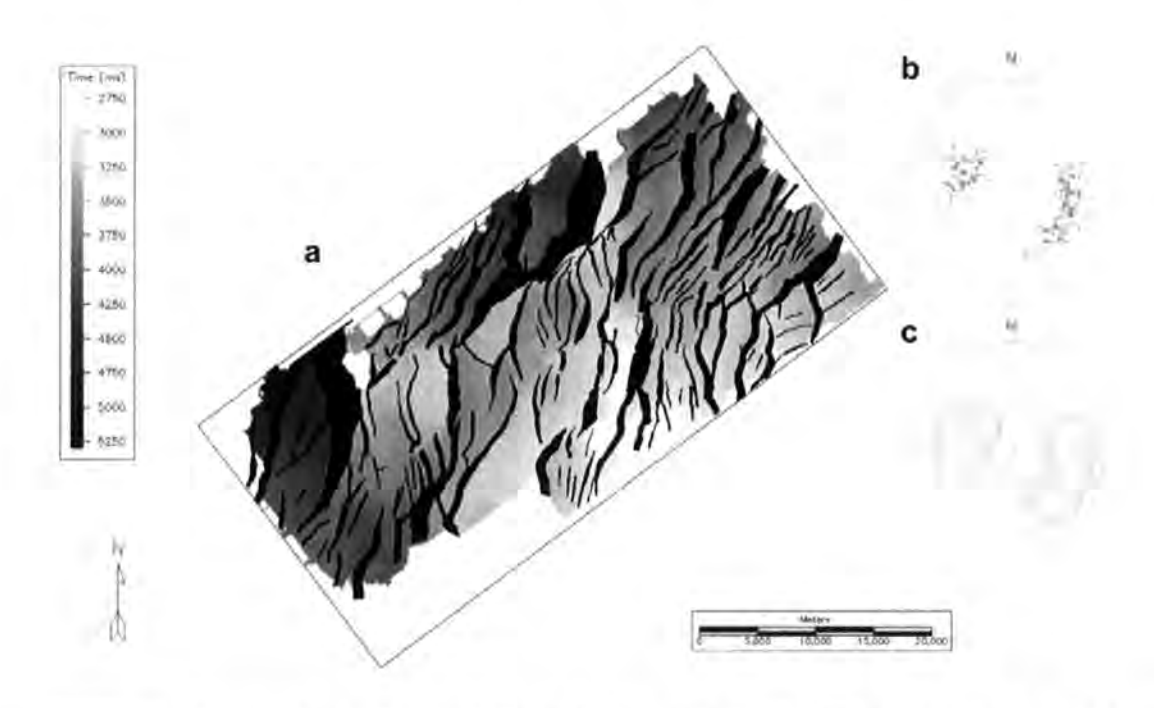


Figure 4.5: a) Structure map of horizon h2 (Early Miocene) in TWT with fault polygons shown in black. b) equal area stereonet of poles to planes for 225 faults. c) Equal area stereonet with density contours for the poles to planes of 225 faults.

The mean fault dip for the 225 faults is 43° with a standard deviation of 9.16°. The lower hemisphere stereographic projection shows faults with a range of dips from 19°-89° and a wide range of dip azimuths (Fig. 4.5 b-c). 93% of faults have dips between 30°-60°. The fault pattern changes little on the six stratigraphic horizons studied (Fig. 4.6), suggesting that the interpreted horizons all lie within a single rifted sequence. All faults appear to have normal offsets and there is no evidence for substantial amounts of inversion in the area studied here.

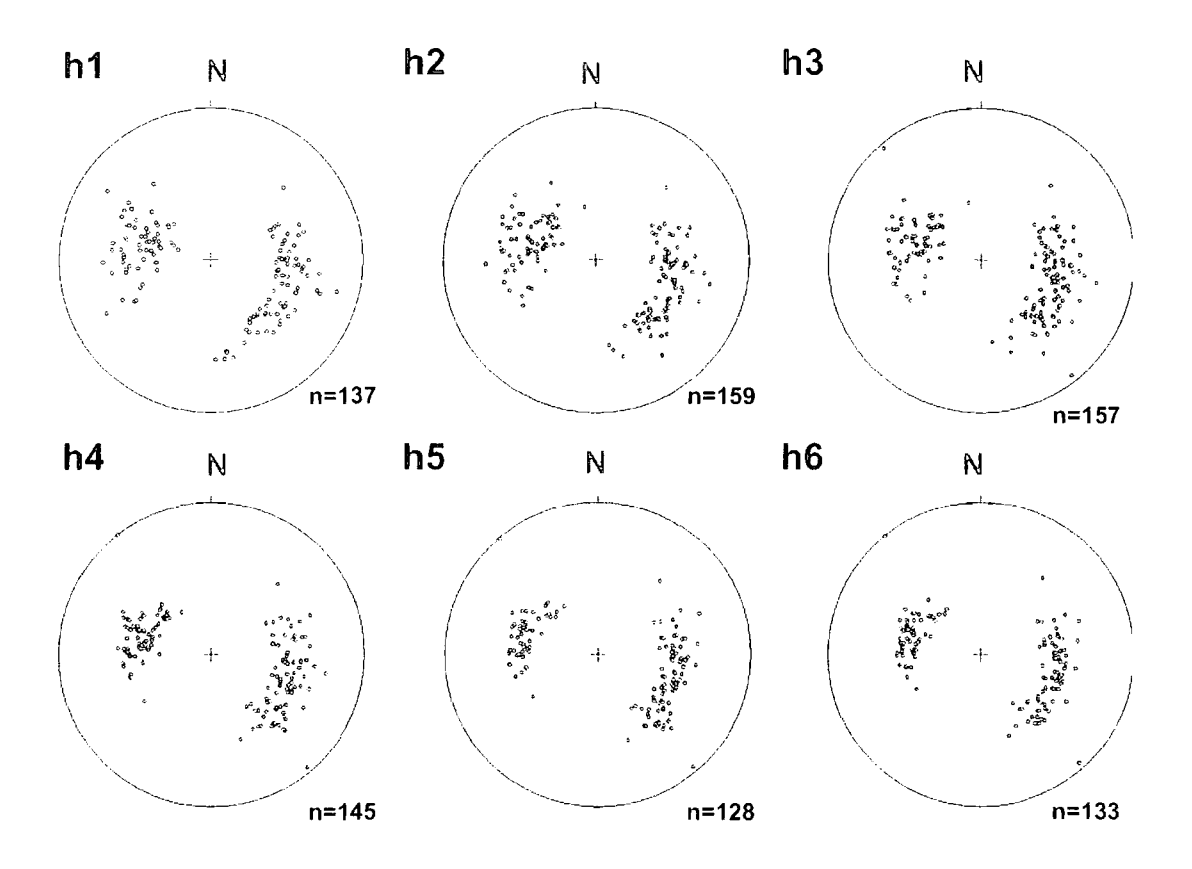


Figure 4.6: Equal area, lower hemisphere stereonet plots of poles to faults planes for all six stratigraphic horizons. Created using Georient.

It has been suggested in many publications that the Nam Con Son Basin may be a strike-slip or transtensional basin associated with movement along major sinistral or dextral shear zones, which cross the continental shelf and interact with South China Sea rifting (Tapponnier *et al.*, 1986; Tjia and Liew, 1996; Morley, 2002; Liu *et al.*, 2004). The 3-dimensional seismic data and additional 2-dimensional seismic lines from across the basin have been carefully examined for evidence of strike-slip structures using the criteria discussed by Harding (1990). No evidence has been found during the present study for their existence within the Nam Con Son Basin. Furthermore, the analyses discussed in Chapter 5 suggest that the faults have not significantly rotated about vertical axes during rifting.

4.5 STRAIN DISTRIBUTION WITHIN THE NAM CON SON BASIN

The wide range of fault orientations and the lack of inversion or vertical axes rotations within the area makes the Nam Con Son Basin fault sample ideally suited to analysis using the proposed model of strain distribution.

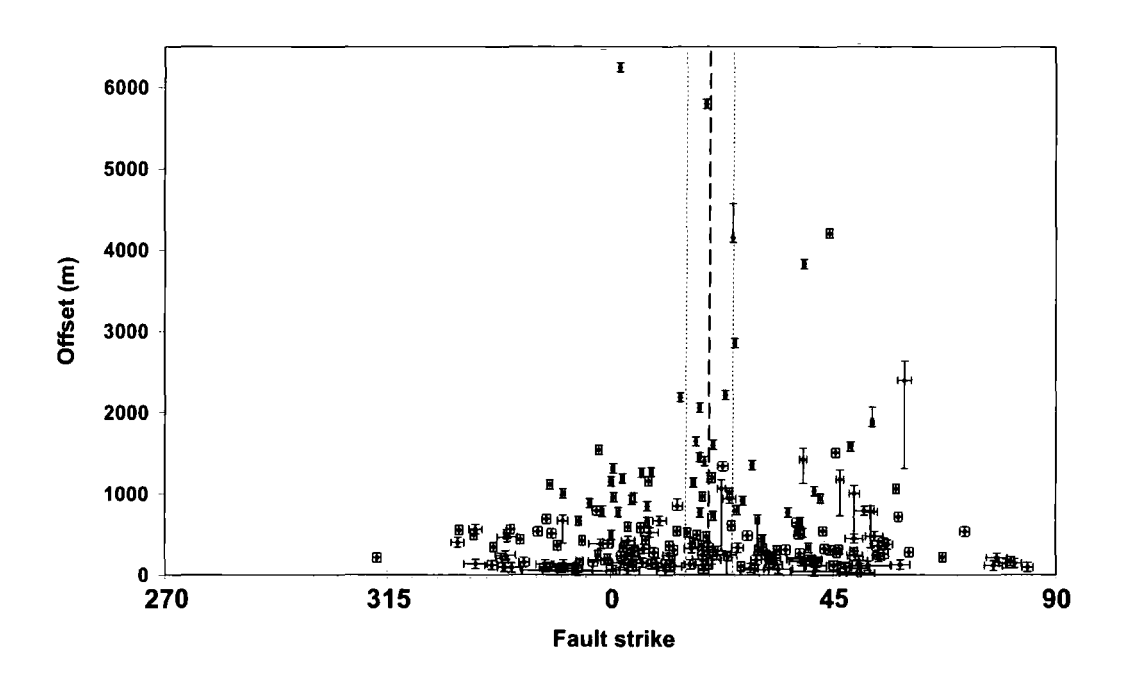


Figure 4.7: Plot of dip-slip offset versus fault strike for 225 faults. The dashed line represents the weighted mean strike for the sample at 021° and the dotted lines represent the confidence interval at a 95% significance.

Figure 4.7 shows a plot of dip-slip offset versus strike for all 225 faults that have been interpreted. As previously mentioned, a single offset is used for each fault, corresponding to the maximum offset on that fault. The plot shows a distribution very similar to that predicted by the model, in which the dip-slip offset increases towards a peak at the distribution centre. The weighted mean strike of the sample is 021°, which equates to a maximum horizontal extension direction (e_H) of 111°, WNW-ESE. The weighted mean strike, arithmetic mean strike, vector mean strike and median strike of the sample are all within 1°, which indicates that the maximum dip-slip offset is evenly

distributed about the sample centre. Furthermore, the fault strikes are approximately normally distributed, with a kurtosis which is slightly less than that of a normal distribution, -0.32 (Fig. 4.15a). The fault offsets have an exponential distribution and a wide range of values from 19 m to 6247 m (Fig. 4.8b).

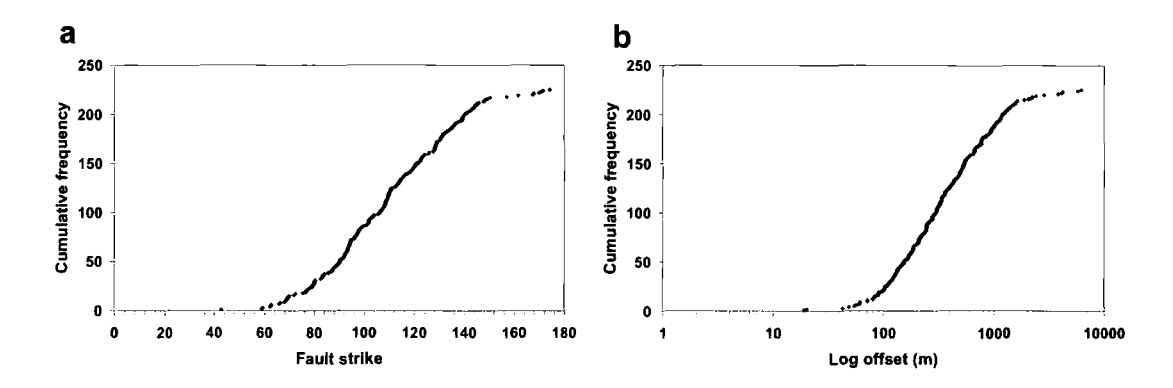


Figure 4.8: a) Cumulative frequency plot of strike, n = 225 b) Cumulative frequency plot of offset, n = 225.

As predicted by the model, the maximum offset of any fault reduces as the fault strike becomes more oblique to the weighted mean strike of the sample. The fault with the largest offset is an exception to this rule and is clearly inconsistent with the model. Despite having the largest offset of any fault, it has a strike 19° anticlockwise from the weighted mean strike of the sample. The fault with the second largest offset is consistent with the model as it coincides with the weighted mean strike of the sample. In both cases, the faults have extreme values of offset that are unrepresentative of the sample as a whole. It is difficult to draw statistically significant conclusions about the distribution of faults at any values above ~2500 m, where there are sparse faults with extreme values of offset.

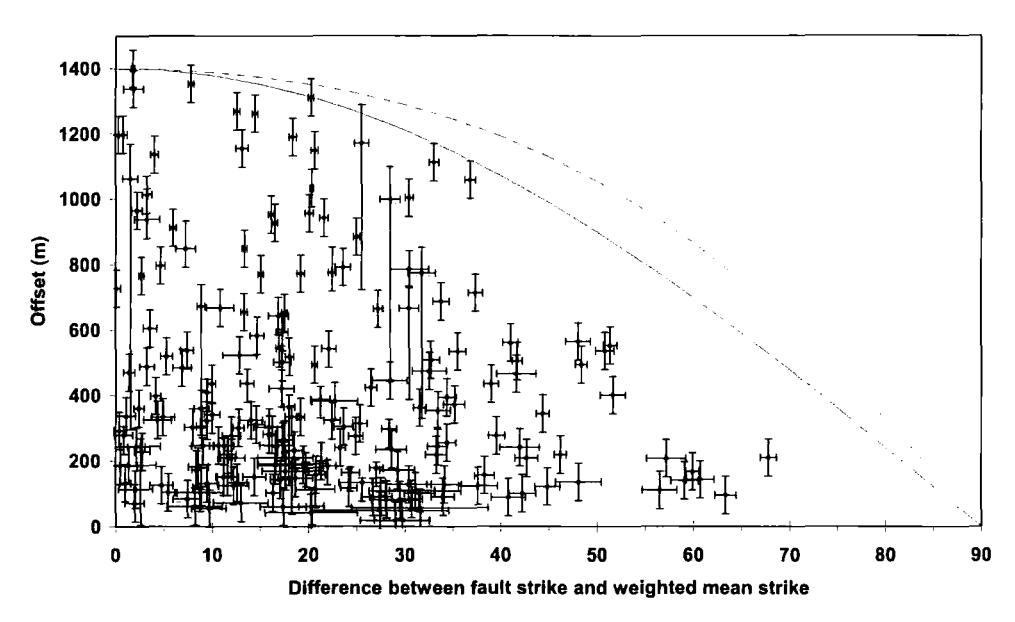


Figure 4.9: Plot of offset versus the difference between the strike for each fault and the weighted mean strike of the sample (Δ strike). Only those faults with offsets of +/- 1 standard deviation of the mean are plotted; 209 faults out of 225 (93%). The solid curve is that for a fault dip of 0°. Curves for greater dips are rounder than that for 0° dip. The dashed curve is that for a fault dip of 43°, the average dip of the sample.

In Figure 4.9 each fault is plotted as dip-slip offset versus the difference between the fault strike and the weighted mean strike of the sample, referred to as Δ strike. The curves represent the maximum offset for a fault of given strike and dip as predicted by the model (Eq. 4.2). The solid curve is that for a fault dip of 0°. Curves for greater dips are rounder than that for 0° dip. The dashed curve is that for a fault dip of 43°, the average dip of the sample. The plot includes all faults with an offset of less than 1400 m, which is within +/- 1 standard deviation of the mean offset of the sample (93% of the faults). This is done to ignore those faults with extreme offsets. To test that the faults plot beneath the curve as predicted, the interception of the curve with the y axis is set to 1400m, which is the dip-slip offset of an ideally oriented fault with a dip-slip offset within +/- 1 standard deviation of the mean dip-slip offset of the sample. The same result is achieved for an h value of 2200 m, which includes all faults within +/- 2 standard deviations of the sample mean offset, e.g. 97% of the faults.

These results clearly show that the data are consistent with the proposed model and that the distribution can be described by the bounding curve predicted from the model. However, two additional observations can be made with regards to the distribution. Firstly, none of the faults have a Δ strike greater than 70°, which suggests that in this dataset at least, the faults, whether dip-slip or oblique-slip, do not form at angles greater than ~70° to e_H. Secondly, the rate of reduction in dip-slip offset with increasing Δ strike appears to be greater than that described by the curves for any dip. As stated previously, the maximum possible dip-slip offset predicted by the curve is only achieved if the slip vector is parallel to e_H. Because the rate of reduction in offset appears to be greater, particularly above a Δ strike of 40°, it can be concluded that the displacement must also be reduced on faults that are not ideally oriented, even if the fault slip vector is parallel to e_H.

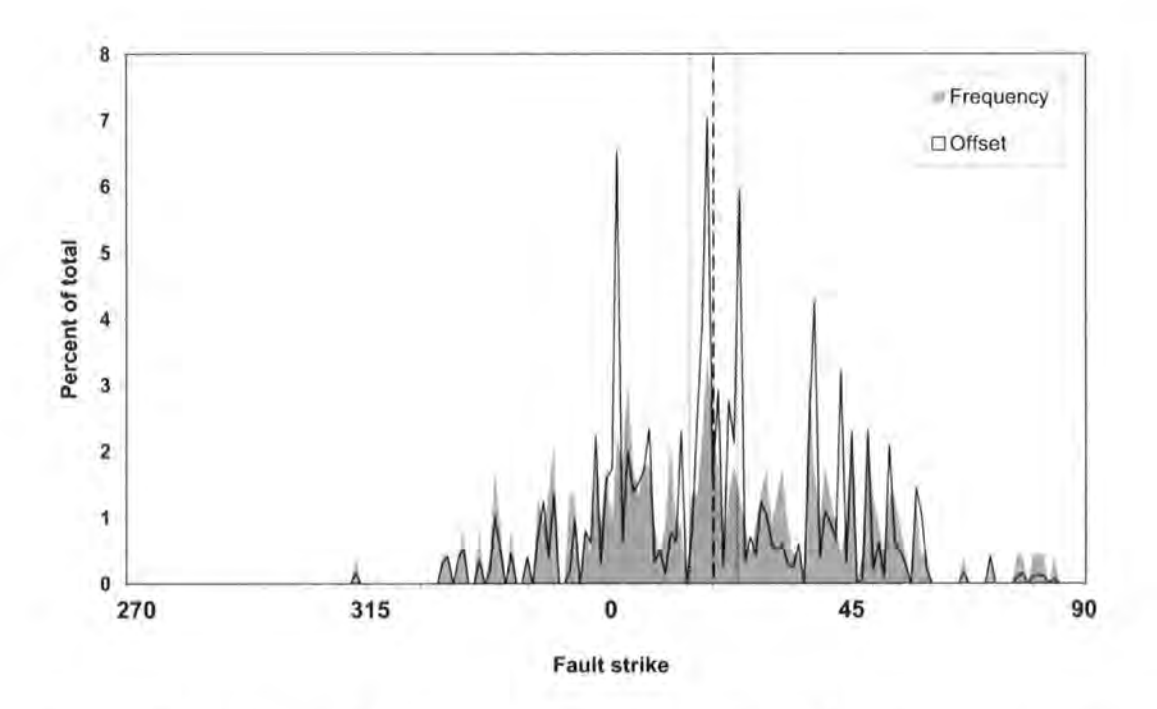


Figure 4.10: Plot of summed offset as a percentage of the total and fault number as a percentage of the total against fault strike, n = 225. The dashed line is the weighted mean strike of the sample at 021° and the dotted lines define the confidence interval at a 99% significance level.

In Figure 4.10 the offsets on all faults with a particular strike are summed and are plotted against the number of faults with that strike. The summed offset and fault number are plotted as a percentage of the total offset and the total number of faults (n=225), respectively. The plot shows the same overall pattern of increasing dip-slip offset towards the weighted mean of the sample. The distribution has numerous peaks in both offset and fault number, which increase in height towards the weighted mean of the sample. The peak with the greatest summed offset and greatest number of faults plots within 1° of the weighted mean of the sample. The peak in offset at strike 002° is a result of one large displacement fault. The modal fault number is within 1° of the sample mean at strike 019° and there are two additional peaks in fault number at strike 004° (n = 7) and strike 038° (n = 7). It is suggested that these peaks may reflect the orientations of the dominant pre-existing heterogeneities within the underlying basement. The 34° angle between the peaks at strikes 004° and 038° could be coincidental or could reflect the existence of an older set of faults with a conjugate pattern.

If the offsets are summed for 10° bins of strike and compared with the number of faults with that strike it is seen that a predictable relationship exists (Fig. 4.11). Nearer to the weighted mean strike of the sample, the amount of dip-slip offset, as a percentage of the total offset is greater than the number of faults, as a percentage of the total fault number. As the fault strikes become more oblique, this relationship reverses. This demonstrates that a greater amount of offset is not simply the result of greater fault numbers. More faults have strikes between 000° and 010° than in any other 10° range. However, in accordance with the model, these faults, which are further from the weighted mean strike of the sample, accommodate a smaller proportional of the offset compared to faults with strikes of between 010°-020° and 020°-030°.

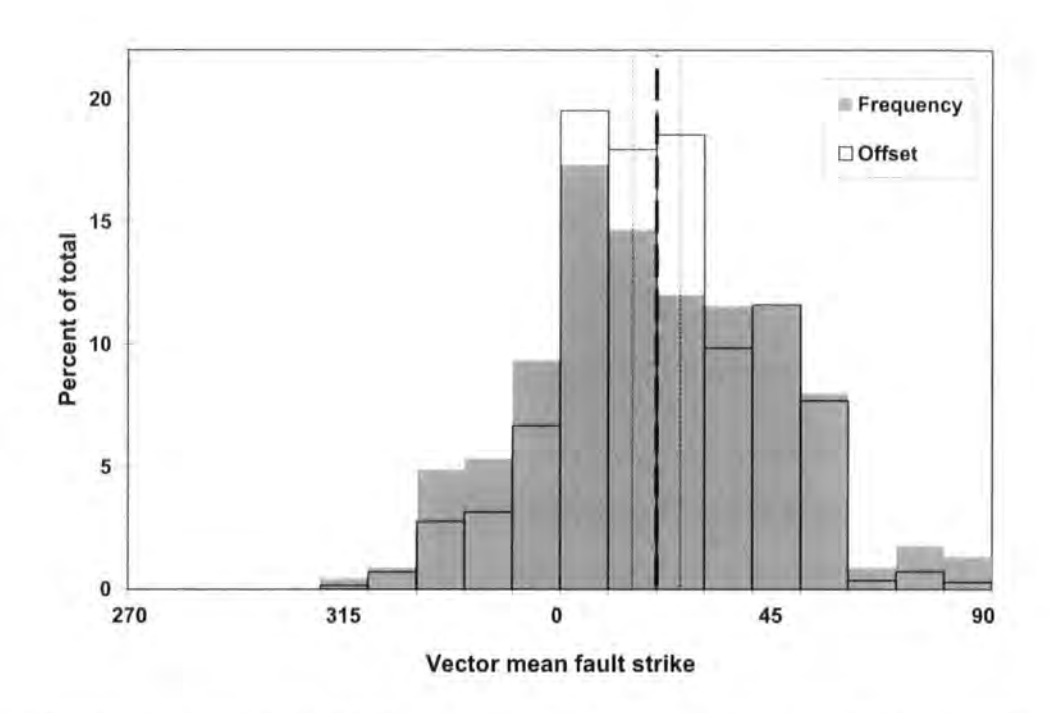


Figure 4.11: Summed offset for 10° bins as a percentage of the total offset and frequency for 10° bins as a percentage of the total number of faults. n=225. The dashed line is the weighted mean strike for the sample at 021° and the dotted lines are the confidence interval at a 99% significance level.

4.6 DISCUSSION

4.6.1 Maximum extension direction

The strain distribution model predicts a simple relationship between fault orientation and the magnitude of fault dip-slip offset. The model predictions fit the observed dip-slip offset data from the central Nam Con Son Basin very well, despite the apparent complexity of the fault system preserved. The analysis has been carried out without any prior knowledge of the fault kinematics, which are usually unknown in offshore datasets. The crust and lithosphere are typically mechanically heterogeneous, with reactivation and fault interaction likely adding complexity to all natural examples of fault populations. For this reason the fault pattern alone does not provide the means to quantify the maximum extension direction, as the relative contribution of the faults to the overall strain is generally unknown. The weighted mean strike of the sample takes into account the relative contributions of all faults to the overall strain and suggests a maximum extension direction, e_H, of 111°. This value is applied to the analyses in Chapter 5.

4.6.2 Strain distribution

For the Central Nam Con Son Basin fault sample, the weighted mean strike, arithmetic mean strike, vector mean strike (Eq. 3.3) and median strike are all within 1°. So for this dataset, the fault pattern alone could be used to infer the direction of maximum extension, without considering the distributions of dip-slip offset. However, this may not be the case for all fault populations. The similarity between the weighted mean strike and arithmetic mean strike or vector mean strike also shows that the offset distribution is approximately symmetrical. 45% of faults have strikes clockwise to the

weighted mean strike and they accommodate 45% of the total dip-slip offset. Conversely, the 55% of faults that have strikes counter-clockwise to the weighted mean strike accommodate 55% of the total dip-slip offset. The symmetry of the offset distribution supports the model because the faults that plot either side of the weighted mean strike represent two independent sub-samples. The prediction of decreasing dip-slip offset with increasing obliquity from the weighted mean strike is equally applicable to both sub-samples.

4.6.3 Fault growth rate

The model predicts the strain distribution of a fault sample without predicting a mechanism to explain the variations in offset. Two different mechanisms can be considered. Firstly, the orientation of the fault relative to e_H may control the rate of fault movement. Faults that are oblique to e_H would have slower rates of movement than ideally oriented faults. Alternatively, the orientation of the fault relative to e_H may determine the duration of activity, whilst the rate of fault movement remains constant. Ideally oriented faults would have relatively long lives compared to faults that are oblique to e_H. If the second mechanism is evident, there will be a correlation between the orientation of the fault relative to e_H and the duration of fault movement.

In Figure 4.12 the faults are grouped according to the relative duration of fault movement. This was established by counting the number of growth sequences for each fault, as constrained by the offsets of the six stratigraphic horizons. The available well data is sufficient to divide the faults into three groups, which is adequate for this analysis. The faults in Group 3 have the longest duration of activity as they were active throughout the entire constrained time period. The faults in Group 2 were not active

throughout the entire constrained time period but they do show growth during most of the sequence.

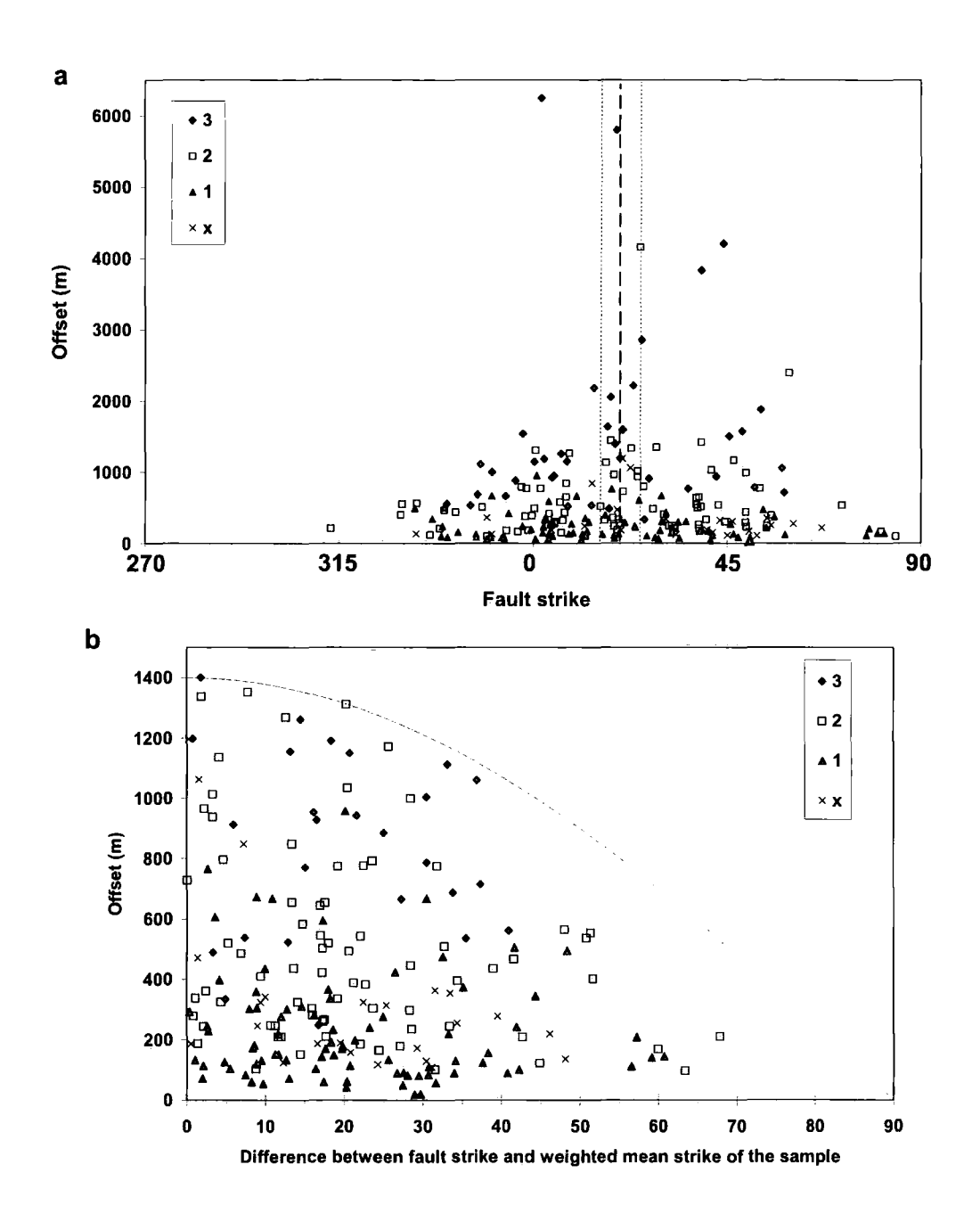


Figure 4.12: a) Fault strike vs. dip-slip offset with the faults divided into three groups according to the duration of fault activity. The faults in group 3 were active for longest and those in group 1 were active for the shortest length of time. Faults in group x have unknown durations of activity. b) Dip-slip offset vs. the difference between fault strike and the weighted mean strike with the faults divided into the same three groups. Only faults with dip-slip offsets within +/- 1 standard deviation of the mean sample offset are plotted, 209 faults out of 225 (93%). The curve describes the relationship between the maximum possible offset for a fault of a given strike and a dip of 0°.

The faults in Group 1 were only active for 1 or 2 growth sequences. A fourth group, Group x, includes faults with uncertain durations of activity. It is not possible to divide the faults into a greater number of groups because the amount of time that each growth sequence represents is not precisely constrained. For example, two faults, each active during a different growth sequence, can have different durations of fault activity depending on the length of time represented by the respective growth sequences.

The plot shows that a broad correlation exists between the amount of offset on a fault and the duration of activity. The faults with the largest offsets were active for a relatively long time, in particular, of the 16 largest faults, 14 belong to Group 3. Most of the smallest faults are from Group 1 and the faults from Group 2 have a range of offsets. Importantly, there is no correlation between the duration of fault activity and fault orientation. The faults of each group have a range of orientations. For example, the two faults that are most oblique to the weighted mean strike of the sample have relatively small offsets despite belonging to Group 2. This analysis suggests that faults with longer durations of activity do tend to accumulate larger offsets but this tendency is modified by the orientation of the fault relative to the weighted mean strike of the sample. However, it seems there is an additional control that results in ideally oriented, long lived faults with relatively small offsets. It is hypothesised that this could be an effect of fault interaction i.e. the growth of the fault has been subdued due to its proximity to a more dominant neighbouring fault.

4.6.4 Reactivation

The contribution of reactivation to a fault pattern is generally difficult to quantify (e.g. Holdsworth *et al.*, 1987). Often, faults are either parallel to the basement fabric or perpendicular to the regional extension direction, or some combination of these two

end-member types (Section 2.3). It is often difficult to confidently identify reactivation, particularly in offshore settings where the basement or deep structure may be below the range of the seismic data, whilst the relatively poor resolution of the data prevents the use of traditional outcrop-scale identification criteria. The strain distribution model predicts the amount of fault offset but does not predict the number of faults in a particular orientation. The Nam Con Son Basin data show a discrepancy between the orientation of faults with greatest offsets compared to the orientation associated with the greatest number of faults. It is suggested that this discrepancy could reflect the influence of a pre-existing fabric within the area.

Physical analogue models have been used to simulate the effects of reactivation on the structural development of faults. The experiments use a similar modelling technique in which a crustal analogue (sand or clay) is extended above a heterogeneity in the modelling apparatus that is oriented at an oblique angle to extension direction. This simulates the competing influences of the extension direction and the pre-existing structure. The models have shown that the interaction is not straightforward. In general fault populations include faults that are oriented parallel to the underlying heterogeneity and faults that are perpendicular to the extension direction (Section 2.1.3; Withjack and Jamison, 1986; McClay and White, 1995). This results in a fault population with a range of orientations and often curved or sigmoidal fault geometries, a very similar fault pattern to that seen within the central Nam Con Son Basin.

In the models of Dubois *et al.* (2002), the slip-vectors of the modelled faults were examined. In these models, the sandpack was extended to produce a fault-bound graben orthogonal to the extension direction and then extended a second time with an extension direction oblique to that graben. During the second extension phase the faults formed within the graben and parallel to the graben bounding faults but oblique to the

extension direction. The fault slip-vectors of the second phase faults were shown to be sub-parallel to the extension direction. Therefore, the orientation of the second phase faults was controlled by the pre-existing structure, whilst the fault kinematics reflected the orientation of the extension vector. This fault pattern may be an analogue for the Nam Con Son fault pattern on a regional scale. The preferred fault orientation of 000°-010° and the peaks in fault number at 019°, 004° and 038°, could be controlled by pre-existing structure but with reduced offset, relative to those with strikes nearer to the weighted mean strike, because of oblique-slip kinematics.

4.6.5 Application to fractured reservoirs

This work provides a predictive tool that can be used to improve models of fractured hydrocarbon reservoirs. The method can be used to provide more information for use in numerical models and in conjunction with fault orientation data from boreholes or 3-dimensional seismic data. It enables a prediction of those fault orientations that are more likely to have greater offsets than others and what the expected maximum offset could be for a fault with a given strike. For a particular stratigraphy, this information can help to predict the maximum expected stratigraphic juxtaposition on a fault of a given strike, which in turn, could provide an improved prediction of fluid flow pathways through fractured reservoirs.

4.7 CONCLUSIONS

A conceptual model to explain the relationship between dip-slip offset and fault strike within the central Nam Con Son Basin has been presented. The model is independent of fault kinematics, which are unknown, as is the case in most offshore subsurface datasets. The model provides an estimation of the direction of maximum extension, which is taken to be perpendicular to the weighted mean of the sample strike. For the Nam Con Son dataset the direction of maximum extension is 111°, WNW-ESE, which is broadly consistent with estimates of the extension vector for the South China Sea (Briais *et al.*, 1993) and most tectonic models for the region (Hall, 1997).

The analysis has shown that the distribution of strain is not simply a function of fault number, although the offset in the Nam Con Son fault sample is approaching an even distribution for almost all the faults. However, there are more faults with strikes of 000° to 010° compared to any other orientation and yet they accommodate consistently less offset than the faults nearer to the weighted mean strike. It is suggested that this increased fault number may reflect the influence of a ~N-S basement fabric in the area.

The model used in this case study needs to be tested with other datasets to see if it is equally applicable to other regions. Any datasets used must be able to demonstrate that the faults have not rotated about vertical axes and that there is no systematic variation in fault orientation with fault age. In addition, to produce a good estimate of the weighted mean strike, the sample should ideally have faults with a wide range of trends.

CHAPTER 5. THE RECOGNITION OF TRANSTENSIONAL RIFT BASINS USING SUB-SURFACE FAULT GROWTH DATASETS: A CASE STUDY FROM THE NAM CON SON BASIN, OFFSHORE VIETNAM

5.1 INTRODUCTION

It is increasingly recognised that many crustal deformation zones involve convergence or divergence that is significantly oblique. This is an inevitable consequence of plate motions on a sphere (Dewey, 1975; Woodcock, 1986; Dewey *et al.*, 1998). It is also likely since most continental deformation zones contain pre-existing structures (e.g. layering, foliation, faults, fractures, shear zones) lying oblique to the new regional transport direction which may undergo reactivation when subjected to renewed stress (Holdsworth *et al.*, 1997).

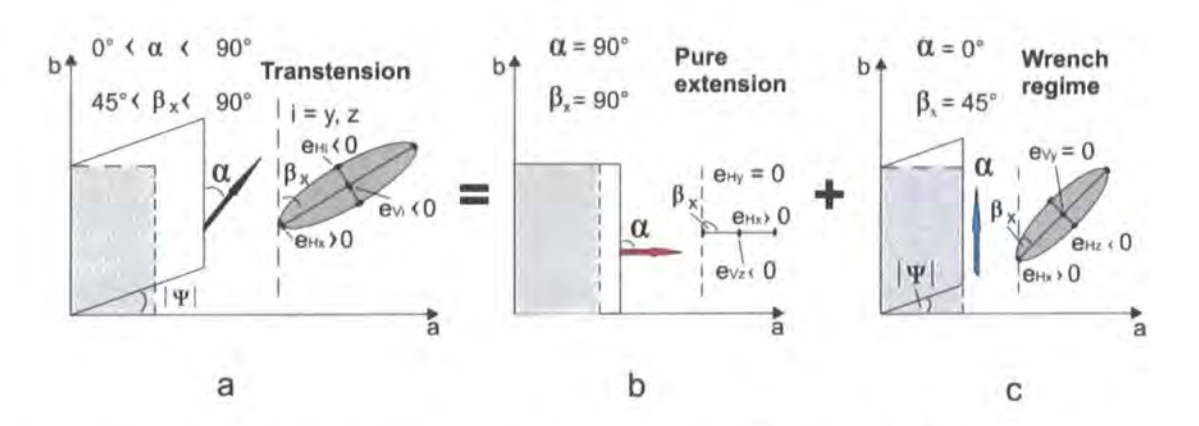


Figure 5.1: Plan views of vertical, fault confined transtension zones following the model of Sanderson & Marchini (1984). a) Transtensional infinitesimal strain will occur when the bulk displacement is at an oblique angle α to the deformation zone boundary faults (i.e. $0^{\circ} < \alpha < 90^{\circ}$). b, c) When the divergence direction is perpendicular ($\alpha = 90^{\circ}$) or parallel ($\alpha = 0^{\circ}$) to the boundary fault, there is pure shear coaxial extension (b) and non-coaxial wrench simple shear (c), respectively.

Parameters shown in the figure: β_x is the angle between the maximum horizontal extension axis and the boundary fault; $|\psi|$ is the infinitesimal angular shear; α is the divergence angle between the displacement and the boundary fault; x, y, z are the maximum, intermediate and minimum infinitesimal extension axes; eHi is the horizontal infinitesimal principal extension axis with i = x, y or z; eVi is the vertical infinitesimal principal extension axis with i = z or y. After De Paola et al. (2005a).

Oblique extension (or shortening) leads to transtension (or transpression) which can be defined as a strike-slip deformation that deviates from a simple shear due to a component of extension (or shortening) orthogonal to the deformation zone boundary (Fig. 5.1; Dewey et al., 1998). In all transtension (and transpression) zones, the relative displacement direction across the deformation zone, infinitesimal strain (or stress) and finite strain axes are all oblique to one another (Fig. 5.1). However, numerous theoretical (e.g. Sanderson & Marchini 1984; McCoss, 1986; Dewey et al., 1998; Dewey, 2002; De Paola et al., 2005a) and analogue experimental studies (e.g. Withjack and Jamison, 1986; Smith and Durney, 1992; Venkat-Ramani and Tikoff, 2002) have shown that predictable geometric relationships exist between the orientations of the deformation zone boundaries, the axes of infinitesimal strain (stress) and the relative displacement direction across the deformation zone. During transtension, the maximum principal extension axis (e_{Hx}) always lies in the horizontal plane during progressive deformation (Figs. 5.1a-c). The other horizontal infinitesimal principal extension axis can be either e_{Hz} (minimum principal extension axis) or e_{Hy} (intermediate principal extension axis), depending on the value of α . The switch of the minimum principal extension axis from a horizontal to a vertical orientation marks the transition between wrench- and extension-dominated transtension, respectively (De Paola et al., 2005a & b). The threshold angle α between wrench- and extension-dominated transtension has been termed the critical angle of displacement $\alpha_{critical}$ (Smith and Durney, 1992). It has a value of 20° if one assumes no volume change during deformation and following the other assumptions of the Sanderson and Marchini model (McCoss, 1986).

In many natural transtensional rifts, it should therefore be possible to apply an analysis using infinitesimal strain, which is broadly equivalent to the more widely-used stress-inversion techniques (e.g. Angelier, 1979 and 1984; Michael, 1984). Two

successful examples of this approach have been carried out in onshore regions by DePaola et al. (2005b) in the Northumberland Basin, UK and by Wilson et al. (2006) in Lofoten, Norway. An important caveat, however, is that this approach is only reasonable in regions where bulk finite strain – or more correctly, finite non-coaxial strains – are reasonably low, so that the misorientation between finite and infinitesimal strain axes is limited. If this condition is not met, the build-up in finite strain will lead to the progressive rotation of faults and their intervening fault-bounded blocks about vertical axes (Fig. 5.2; Allen et al. 1998; Waldron, 2005).

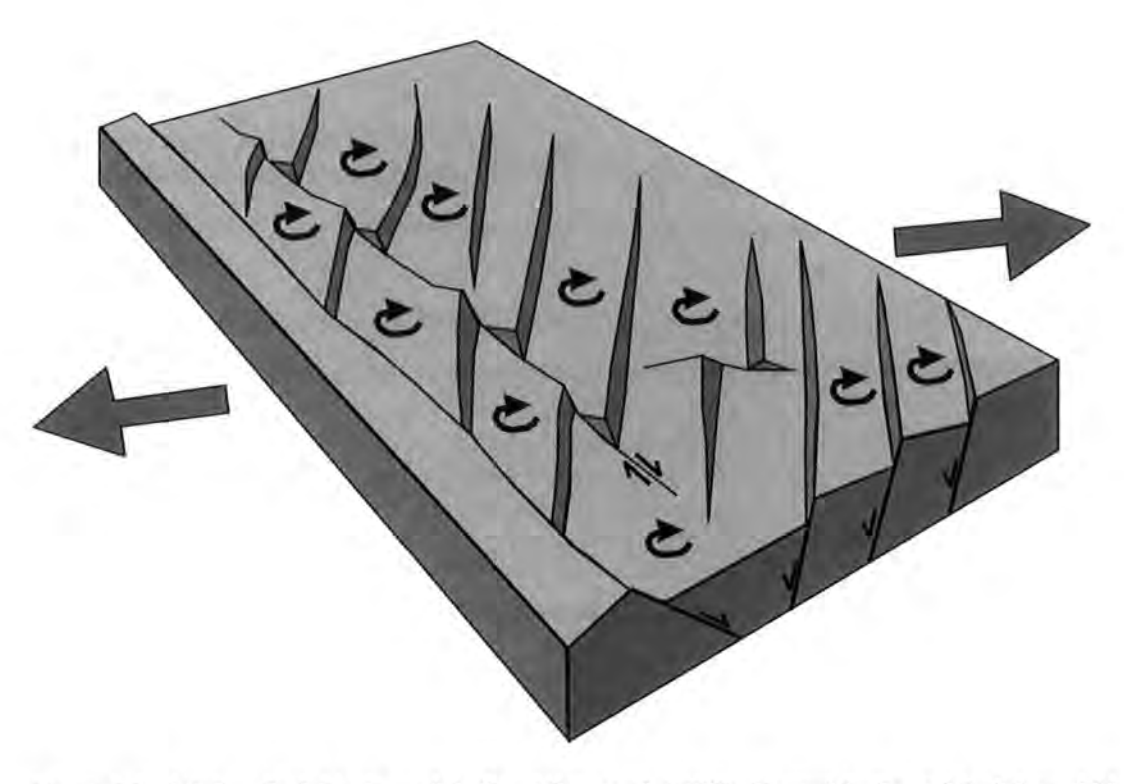


Figure 5.2: Rotating fault block model after Allen et al. (1998). Normal faults and fault bound blocks rotate about vertical axes during transtensional deformation.

Transtensional deformation zones present particular difficulties when dealing with deformation structures in the sub-surface due to a general lack of kinematic data, e.g. slickenline data from fault planes. It may also be difficult to independently constrain the orientation of the deformation zone boundaries. Furthermore, as the

deformation is not plane strain, it cannot generally be analysed using a single 2-dimensional cross-section or map views. In some cases extensional or shortening structures such as tight, symmetric graben or faulted anticlines can easily be misinterpreted as strike-slip flower structures (Harding, 1990). The key criteria most often used to confidently identify strike-slip tectonics in subsurface examples, is the presence of a through-going, laterally extensive master fault that shows laterally offset piercing points such as channels and fold hinges (Harding, 1990). In transtensional basins, however, the master 'fault' can be a wider zone of diffused deformation (Mann et al., 1983).

In this Chapter two further approaches to assist in the recognition of transtension in offshore, sub-surface basin settings are investigated. Firstly, new techniques for identifying fault rotations about vertical axes in offshore datasets are presented. Secondly, it is shown that it may be possible to establish the orientation of deformation boundaries in cases where geophysical data suggest a strong basement control on basin evolution. These methods are used to address the hypothesis that basement-influenced wrench tectonics played a significant role in the evolution of the Nam Con Son Basin.

5.2 SUMMARY OF THE REGIONAL TECTONICS AND BASIN STRUCTURE

The techniques are applied to the 225 faults from the Nam Con Son Basin model presented in Chapters 3 and 4. The analyses use the fault strike, which is calculated using the vector mean dip azimuth (section 3.4.3) and the fault timings, which are discussed in section 3.3.3 and 3.4.4. A full description of the regional tectonics, the basin structure and the fault pattern is included in Chapter 3 but the main points of particular relevance to this chapter are:

- A number of major strike-slip shear zones exist onshore throughout Indochina.
- Tertiary deformation may have been controlled by a north-south trending
 Mesozoic basement fabric to the east of the South China Sea.
- The NE-SW trend of the magnetic lineations in the South China Sea suggest a NW-SE regional extension direction.
- The Nam Con Son Basin has a rhomboidal geometry in plan view and a 2:1 length to width ratio.
- Faults have a wide range of strikes.
- All faults appear to have normal offsets; there is no evidence for inversion.
- The fault orientation patterns change little across the six stratigraphic horizons studied, suggesting that the interpreted horizons all lie within a single rifted sequence
- Seismic data shows no evidence for the existence of large strike-slip faults or shear zones within the basin.
- Fault offset patterns suggest a maximum extension direction of 111°.

5.3 TYPES OF FAULT ROTATION

Three related types of fault rotation are discussed here, each of which can be identified using a different technique. Common to all three models is the concept of non-coaxial strain, in which the axes of finite strain rotate in addition to material lines and planes. The techniques are designed to identify a consistent rotation that could be attributed to non-coaxial strain. If a consistent pattern of rotation is not detected or if the rotation is too subtle to account for the observed range of fault orientations then the model of non-coaxial strain alone is unlikely to be the dominant control over fault orientation. In this case, other controls such as rotations in the stress system, the reactivation of pre-existing anisotropy or the interactions between neighbouring faults may be of greater importance.

In the first type, normal faults initiate orthogonal to the axis of maximum incremental strain oriented at angles ≤ 45° to the deformation zone boundary and then rotate about vertical axes with the sense of rotation being determined by the sense of strike-slip shear (dextral – clockwise, sinistral – anticlockwise). To test this model, the faults were analysed to see if there is any systematic correlation between fault age and fault strike (Fig. 5.3a). A knowledge of the orientation or location of the shear zone boundary (shear plane) is not required.

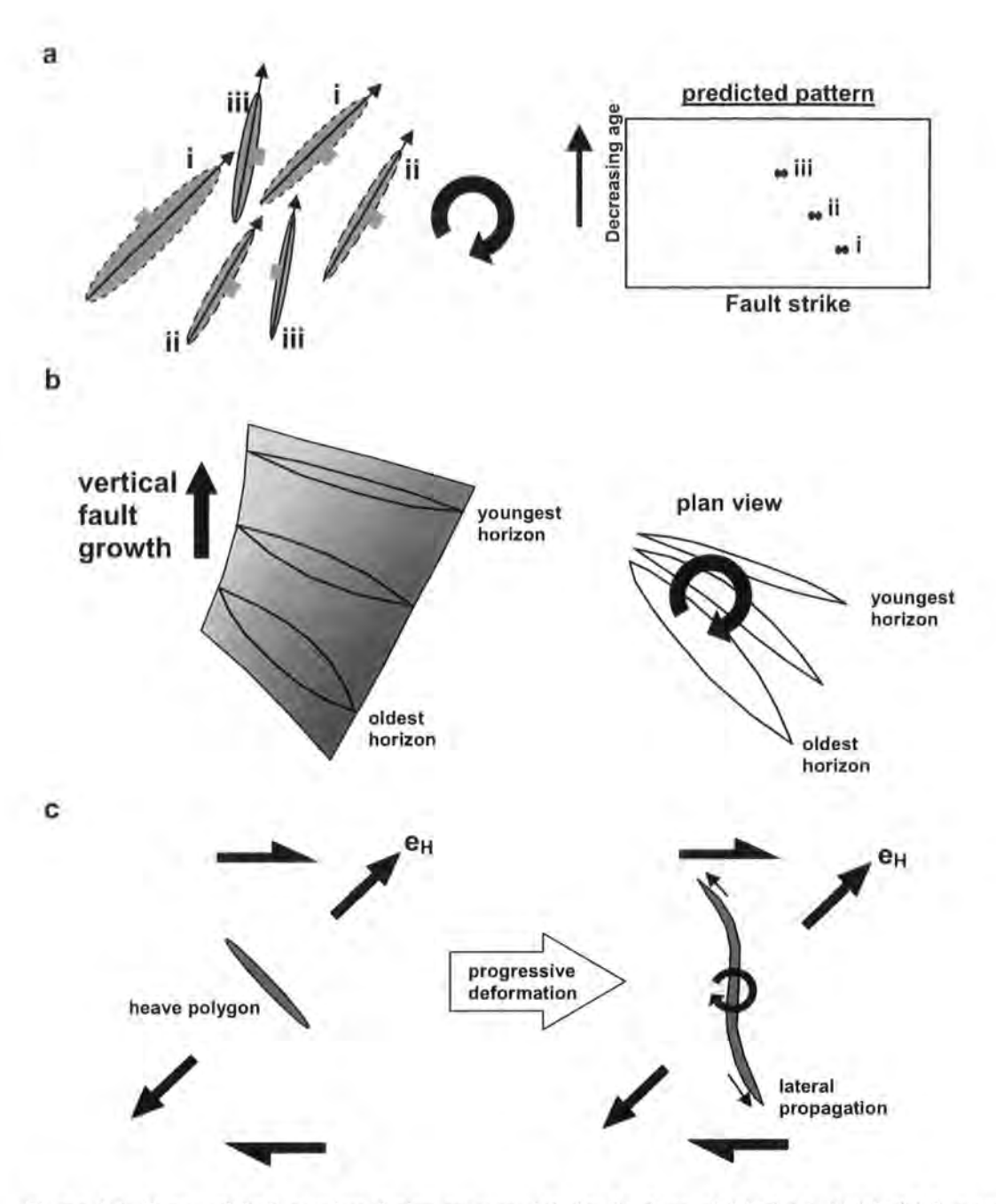


Figure 5.3: Types of fault rotation during non-coaxial simple shear. a) Model 1, b) Model 2, rotation during vertical propagation c) Model 3, rotation during lateral propagation.

Methods two and three identify rotations of the fault surface during vertical (Fig. 5.3b) and lateral fault growth (Fig. 5.3c), respectively. Again, fault nucleation is controlled by the axes of incremental strain and, following nucleation, the fault surface should rotate in a direction about a vertical axis determined by the sense of strike-slip shearing. Whilst the fault rotates, it continues to grow by vertical and lateral

propagation with the fault orientations near to the fault tips being controlled by the incremental strain axes which remain in a fixed orientation assuming steady state deformation. As a result, the oldest part of a fault surface, most likely the fault centre, is rotated relative to the younger part of the fault surface nearer to the tip line. This is analogous to tension gash propagation during shear zone development, which produces sigmoidal vein geometries (Fig. 5.3c; e.g. Ramsay, 1967).

The three types of rotation are tested using different methods but are likely to all be active within a given fault population where vertical axis rotation occurs due to strike-slip tectonics.

5.3.1 Type 1: Fault orientation vs. age

Figure 5.4 is a plot of fault strike versus fault age for 225 faults. The faults have been grouped into six sub-samples based on the relative age of the fault, as constrained using the methods described in section 3.3.3. The strike of each fault is calculated using the fault polygon of the oldest offset horizon only, as opposed to using all of the polygons for each fault. This is done to eliminate the effect of fault surface rotation during vertical growth, which will be addressed in section 5.3.2.

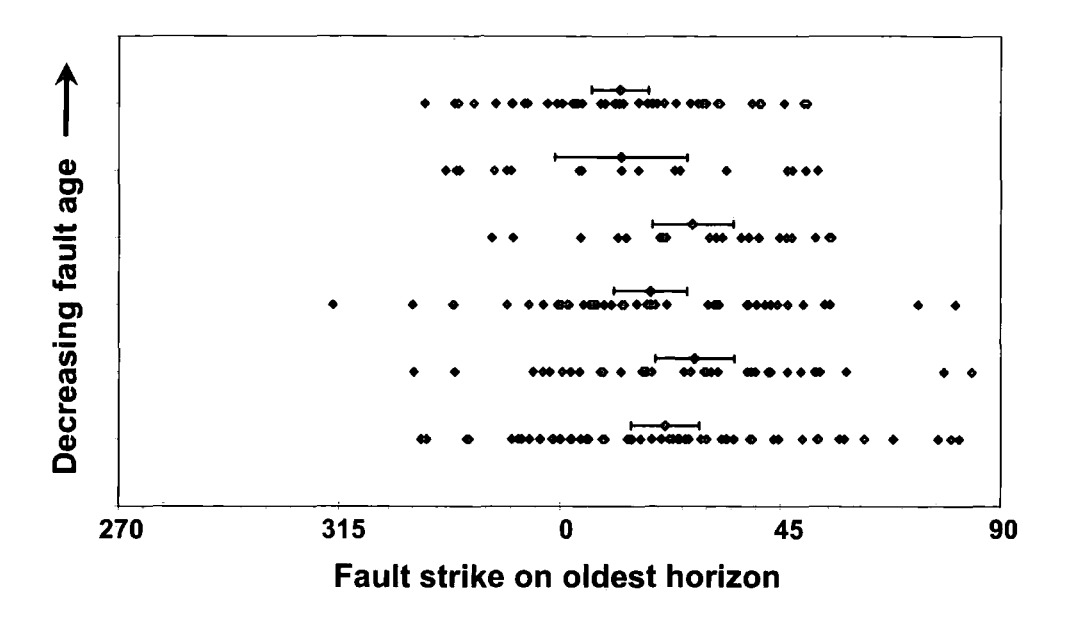


Figure 5.4: Plot of fault strike versus fault age. Each point represents a single fault. The vector mean strike of each fault is plotted against the. Each line of points is a sub-sample based on the relative age of the initiation of syn-sedimentary fault movement. The points with error bars represent the vector mean strike of each sub-sample with a 95% confidence interval.

For each sub-sample, the faults have a range of strikes of at least 80° (Fig. 5.4). This suggests that fault strike and fault age are not related and that, contrary to models of deformation during simple-shear, there is no constant orientation at which the faults have initiated. The vector mean of each sub-sample has been calculated and plotted (Fig. 5.4). Although the mean rotates by several degrees between each sub-sample, the sense of rotation is not constant. In total, the mean rotates 23° counter-clockwise and 30° clockwise, which equates to an overall clockwise rotation of 7° between the youngest and oldest sub-sample.

As previously stated, the range of strike of each sub-sample is at least 80°. Variations in the range of fault strike between sub-samples or faults sets of different age can provide insight into whether the faults have rotated. During strike-slip-related deformation, vertical axis rotation should be highest when a fault is oriented at a high angle to the deformation zone boundaries and should then decrease as the fault approaches parallelism with the boundaries. Therefore, even if the faults initiate with a

wide range of strike, through time the range of fault strike will decrease as the faults rotate, with varying rates, towards parallelism with the deformation zone boundaries. Therefore it is expected that the range of fault strike to be less on older fault sets compared to younger fault sets. However, there is no evidence for this pattern in Figure 5.4. In fact, the range of fault strike is greater for the older sub-samples.

5.3.2 Type 2: Rotation during vertical fault growth

This model can be tested by comparing the orientation of the fault polygons for each stratigraphic horizon within a growth sequence (Fig. 5.3b). The number of horizons included in the growth sequence varies between faults, as some were active for longer than others. A difference in the orientation of the polygons of two stratigraphic horizons that bound a growth sequence, indicates a rotation of the fault surface during vertical growth, and since the deposition of the older horizon. Of the 225 faults in the sample population, a sub-sample of 132 (59%) faults can be used for this analysis. 93 faults (41%) cannot be used because they either cut only one stratigraphic horizon or they do not show growth between horizons. Importantly, the 132 faults that are used represent, in effect, a random sample as they do not have preferred orientations, ages or locations. They are therefore a representative subset of the 225 fault sample.

The first analysis indicates whether a fault has consistent rotations between horizons within the growth sequence. Of the 132 fault sub-sample, 55 faults (42%) have both clockwise and counter-clockwise rotations. 43 (33%) faults have exclusively clockwise rotations and 34 (26%) faults have exclusively counter-clockwise rotations. However, these statistics are misleading as they do not take into account the number of rotations on each fault. This varies between faults depending on the number of horizons

within the growth sequence. For example, 36 faults have only one rotation but will be counted as having a consistent rotation sense.

Number of rotations	Number of faults	Both %	CW %	CCW %
0	93			
1	36	0	42	58
2	28	25	61	14
3	25	68	20	12
4	20	75	15	10
5	23	70	13	17
Total	225	42	33	26

Table 5.1: Rotations for each fault with the faults divided by the number of rotations.

Table 5.1 shows the number of faults with either exclusively clockwise, exclusively counter-clockwise or both rotations, as a percentage of the total number of faults with a given number of rotations. If the 36 faults with only one rotation are discounted, then the majority (57%) of faults have both clockwise and counter-clockwise rotations, whilst 29% of faults have exclusively clockwise rotations and 14% of faults have exclusively counter-clockwise rotations. In total, 362 rotations have been measured. Of these, 56% are clockwise and 44% counter-clockwise.

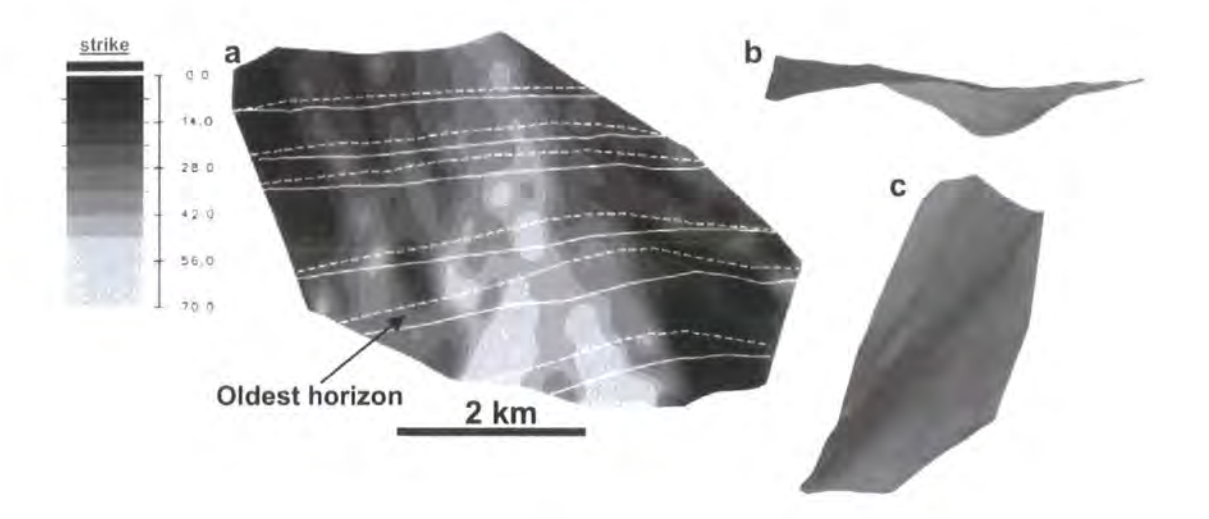


Figure 5.5: Example fault surface that shows counter-clockwise rotation of the fault trace between horizons. a) Normal to strike view of fault surface. Fault strike is displayed on the surface. On deeper horizons a greater proportion of the fault surface has a strike greater than ~40° but higher in the sequence the fault twists so that a greater proportion of the fault surface has a strike less than ~40°. b) view of the fault surface from above looking down dip. This highlights the curvature of the fault especially the left hand corner. c) side-on view of the fault.

Figure 5.5 shows an example of a fault with a counter-clockwise rotation between each horizon. In total, the strike of the fault trace rotates 12.8° relative to the earliest horizon. The variation in strike between horizons is due to the fault surface twisting. In Figure 5.5a the strike of the fault surface is displayed on the fault surface. On the older, deeper part of the fault, most of the surface strikes 040° to 070°. On the younger, upper part of the fault, this is not the case, as most of the fault surface strikes 000° to 040°. The twist of the fault surface can be seen in Figure 5.5b and c, and is particularly clear in the upper left hand corner of the fault surface.

The analysis so far has considered the number of rotations without regard for the magnitude of those rotations, which could be very small. If the magnitudes of the rotations are summed for each fault, with clockwise rotations having negative values and counter-clockwise having positive values, the cumulative rotation relative to the oldest horizon can be calculated. This analysis shows that 56% of faults have an overall clockwise rotation and 44% an overall counter-clockwise rotation. The total summed

magnitude of all fault rotations is 927°, of which 55% is clockwise and 45% counterclockwise.

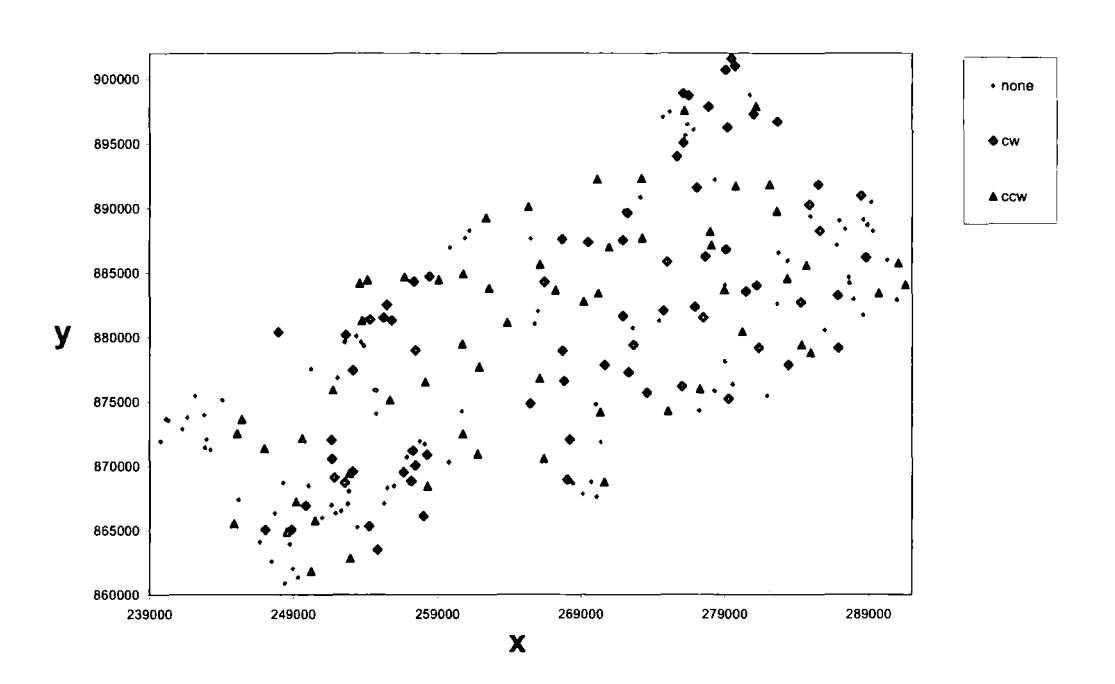


Figure 5.6: Spatial distribution of fault rotation. The locations of 225 faults are plotted. Each point represents a single fault and is located at the fault centre, which has been calculated by taking a mean of the x y coordinates for the fault. The faults are grouped into three groups according to their dominant sense of rotation. One group contains those faults for which the rotation cannot be constrained (see text). The rotations for 132 faults can be constrained. Of those 56% have overall clockwise rotations and 44% overall counter-clockwise rotations.

Figure 5.6 is a map showing the locations of the 225 faults. Each point represents a single fault and is located at the fault centre, which has been calculated by taking a mean of the x y coordinates for the fault. The faults are grouped into three groups according to their dominant sense of rotation. The analysis indicates that there is no spatial pattern associated with the dominant sense of rotation.

5.3.3 Type 3: Rotation during lateral fault growth

This type of rotation can be tested for by identifying those syn-sedimentary faults with lateral fault tips that post-date the majority of the fault surface. By identifying the

horizon that represents the base of the syn-sedimentary sequence, at each sample point along the fault surface, it is possible to establish the relative age of the fault at each sample point. In some cases this will vary along strike, which indicates that the fault tips are younger than the fault centre (Fig. 5.7) and that the fault has grown laterally through time (Section 3.3.3; Childs *et al.* 1993).

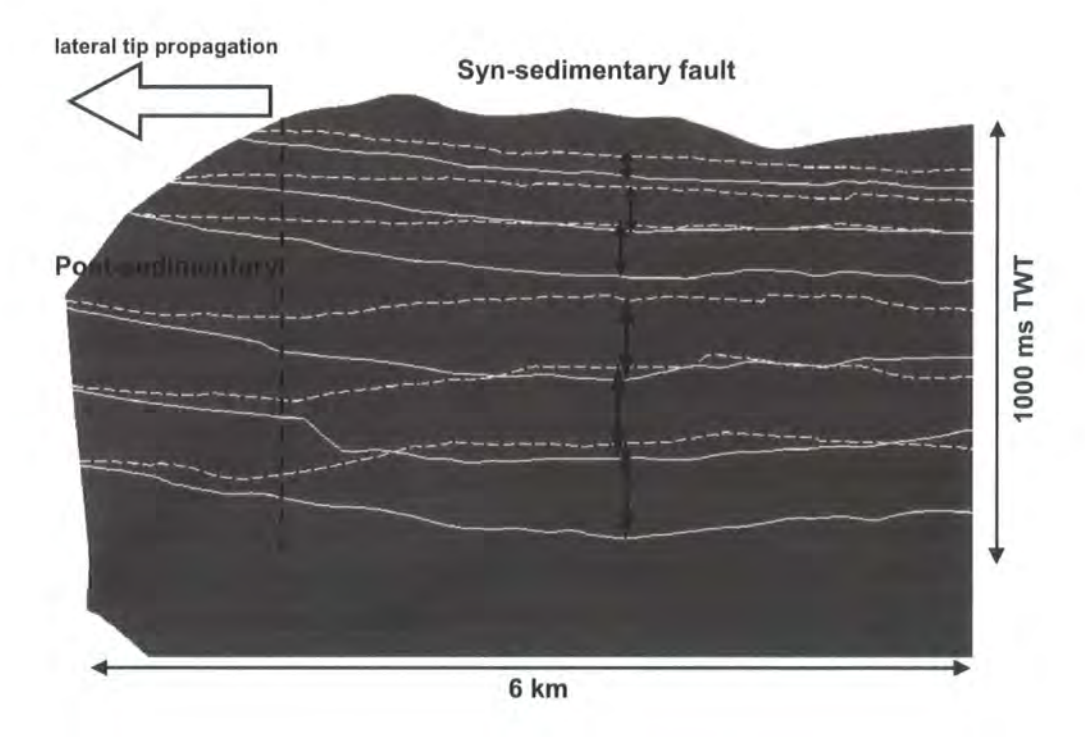


Figure 5.7: Strike view of a fault surface which shows a lateral propagation of the fault tip. Dashed white lines and solid white lines represent the footwall and hangingwall cutoffs respectively.

The orientations of new fault segments that form during lateral propagation of the fault are controlled by the orientation of the axes of incremental strain. Therefore, following initiation, if the fault is rotated about a vertical axis then younger tip zones will develop new segments that have different orientations to the older fault centre, i.e. a sigmoidal geometry (Fig. 5.3c). Using this method, 53 faults have been identified as having one or both tip zones younger than the majority of the fault surface, 60 tips in total (Fig. 5.8). More of the faults could have propagated laterally at the fault tips but were not detected due to the limits of the temporal resolution.

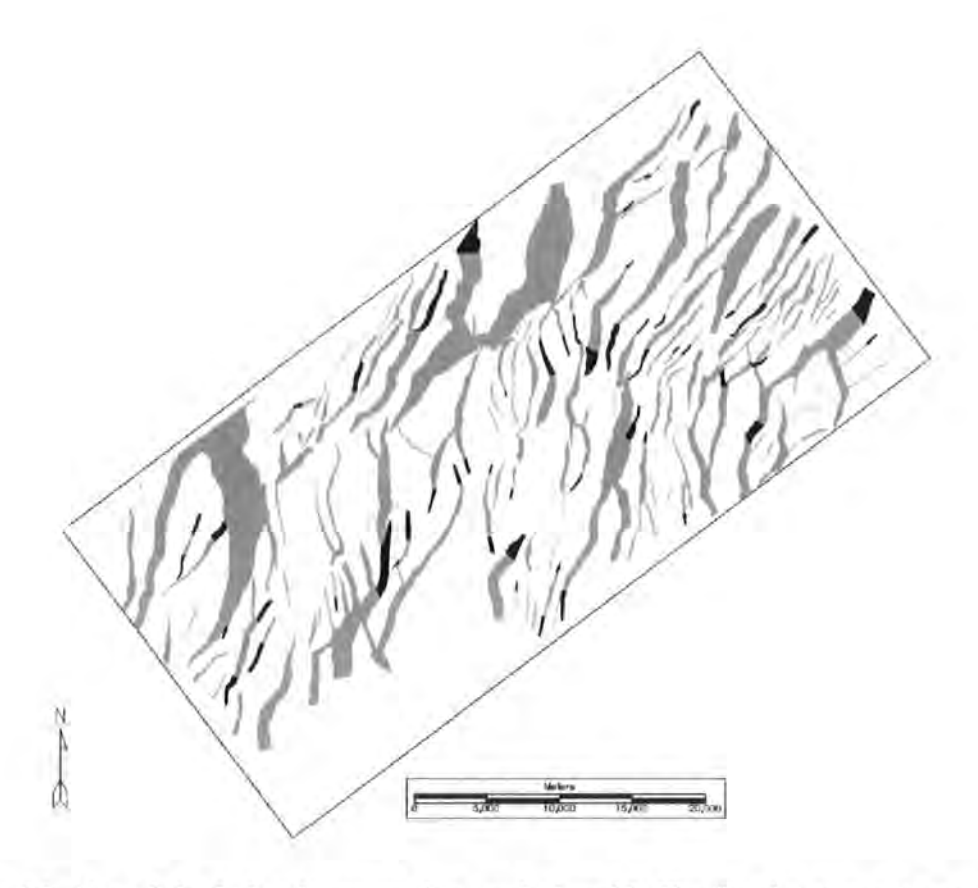


Figure 5.8: Map of the fault polygons as they cut horizon h2. The tips that appear to post-date the majority of the fault are highlighted in black. Not included are 5 additional fault tips from faults that do not offset horizon h2 and so are not displayed on this map. In all 5 cases the tips show no rotation.

Of the positively identified examples, a majority (59%) show no rotation relative to the rest of the fault surface, whilst 22% show a clockwise and 20% a counter-clockwise rotation. This indicates that once again there is no dominant sense of rotation and, in fact, that most faults show no rotation at all at their lateral tips. In addition, only two of the faults show rotation at both tips and in both cases the rotations of the tips are inconsistent, i.e. one tip rotates clockwise whilst the other rotates counter-clockwise. This is not consistent with a model in which the tips should have a common sense of rotation. Of the 25 tips that do show a rotation, 4 of them link to other faults whilst 6 are very close to neighbouring faults and may interact with them (section 2.2.3). Although 15 tips show no apparent interaction, the density of the faults in the sample, and the potential density of the sub-seismic fault population (Walsh *et al.*, 1991) means that

interaction at fault tips should not be ruled out for any fault within the present study area.

An interesting observation to come out of this analysis is that, of the 25 tips that show rotation, 21 of them (84%) rotate towards the direction of fault dip whilst only 4 rotate away from this direction. Of the 4 tips that break this rule, 2 are clearly linked to other faults whilst the other 2 are located very near to adjacent faults and so may interact. This observation echoes the sample population as a whole in which the vast majority of faults are concave towards the direction of fault dip.

5.4 DISCUSSION

Three possible types of fault evolution during vertical axis rotation have been identified for normal faults developing under a non-coaxial, strike slip or transtensional tectonic regime. Quantitative techniques have been developed to test for these types of growth and have been applied to the fault sample from the central Nam Con Son Basin. The techniques do not require knowledge of the location or orientation of the deformation zone boundaries. The main conclusions are:

- 1) There is no clear correlation between fault strike and fault age (Fig. 5.4). This suggests that the fault pattern is not the result of multiple rifting events, whilst the lack of any systematic shift in fault strike with fault age indicates that the fault pattern does not preserve strong evidence for a substantial amount of progressive vertical axis rotation of the faults over time. A small (7°) amount of clockwise rotation is apparent overall, however.
- 2) The second and third techniques identify rotations of an individual fault surface. The analysis shows that the geometries of the fault surfaces are not straightforward and that many faults clearly twist about vertical axes (Fig. 5.5), or curve along strike (Fig. 5.9). By demonstrating that the age of the fault surface varies from the centre to the tips, it can be seen that the curvature of the surface could reflect temporal variations in the orientations of the incremental strain axes. The absence of consistent pattern of rotations seems to rule out a regional scale rotation due to strike-slip-related shear. In general there is an approximate balance between the amount and magnitude of clockwise and counter-clockwise rotation. In particular, the analysis of the lateral fault tips has shown

that a majority 59% of those tips that have propagated during fault growth have not rotated relative to the fault centre. Those that have, show the same balance of clockwise and counter-clockwise rotation. Furthermore, the total magnitude of all measured rotations is evenly split with 55% of the total magnitude being clockwise and 45% counter-clockwise.

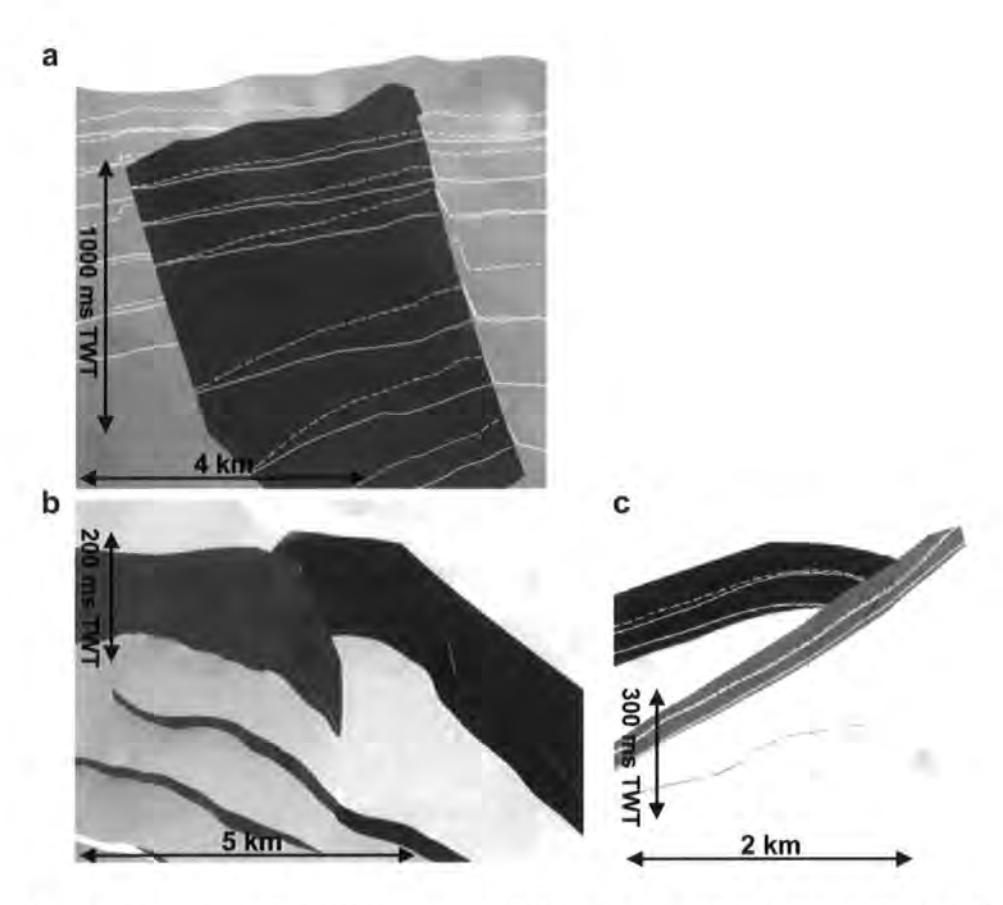


Figure 5.9: Examples of fault interaction and linkage. a) The dark fault links with the lighter fault along a branch line. The dark fault shows syn-sedimentary growth on the upper four horizons. The upper right hand corner of the dark fault curves towards parallelism with the light fault. b) and c) Two examples of fault linkage at the tips of faults. A fault surface can twist in cases where the faults link on younger horizons but not on older horizons.

3) The localised and irregular nature of some of the patterns may be related to fault interaction and linkage. Figure 5.9a shows another example of a twisted fault surface. Overall the fault polygons rotate 8° clockwise. However, in this example the fault is twisted in response to an interaction with a neighbouring fault. In Figure 5.9b and c the

fault surfaces curve along strike to link with neighbouring faults. In some cases the faults link at the upper surface but not at the lower surface, causing the fault surface to twist.

The results suggest that there have been no substantial amounts of fault rotation in a consistent sense about vertical axes in the Nam Con Son Basin during the Miocene main rifting episode. The quantitative analysis presented here may be precise enough to detect a subtle overall pattern of rotation. Although not substantial, there does appear to be a subtle clockwise rotation, which is revealed by all of the various techniques used (Table 5.2).

	CW	CCW
Number of rotations:		
% of faults	29	14
% of total rotations	56	44
% of lateral tips	22	20
Magnitude of rotation:		
% of faults	56	44
% of total magnitude	55	45

Table 5.2: Summary of results. There is a subtle preference for clockwise rather than counter-clockwise rotation.

In reality it is quite possible that the incremental strain axes may vary in response to local fault interactions within a basin, graben or hangingwall, whilst the axes of finite strain rotate systematically in response to the regional tectonics. It is therefore proposed that there may be a component of weak dextral shear resulting from oblique extension in the Nam Con Son Basin. It is manifested as a tendency for faults to

rotate clockwise rather than counter-clockwise but its influence seems to have remained subordinate compared to vertical axis rotation caused by the effects of fault interaction.

5.4.1 Transtension

The clay models of Withjack and Jamison (1986) provide a useful analogue for the Tertiary deformation seen along the east Vietnam coast (section 2.1.3). It is possible that the ~N-S trending rheological boundary between the Palaeozoic Indochina Craton to the west and Mesozoic accretionary crust to the east (section 3.2), creates a strong heterogeneity which acts in a similar way to the base-plate discontinuity of the analogue models (section 2.1.3).

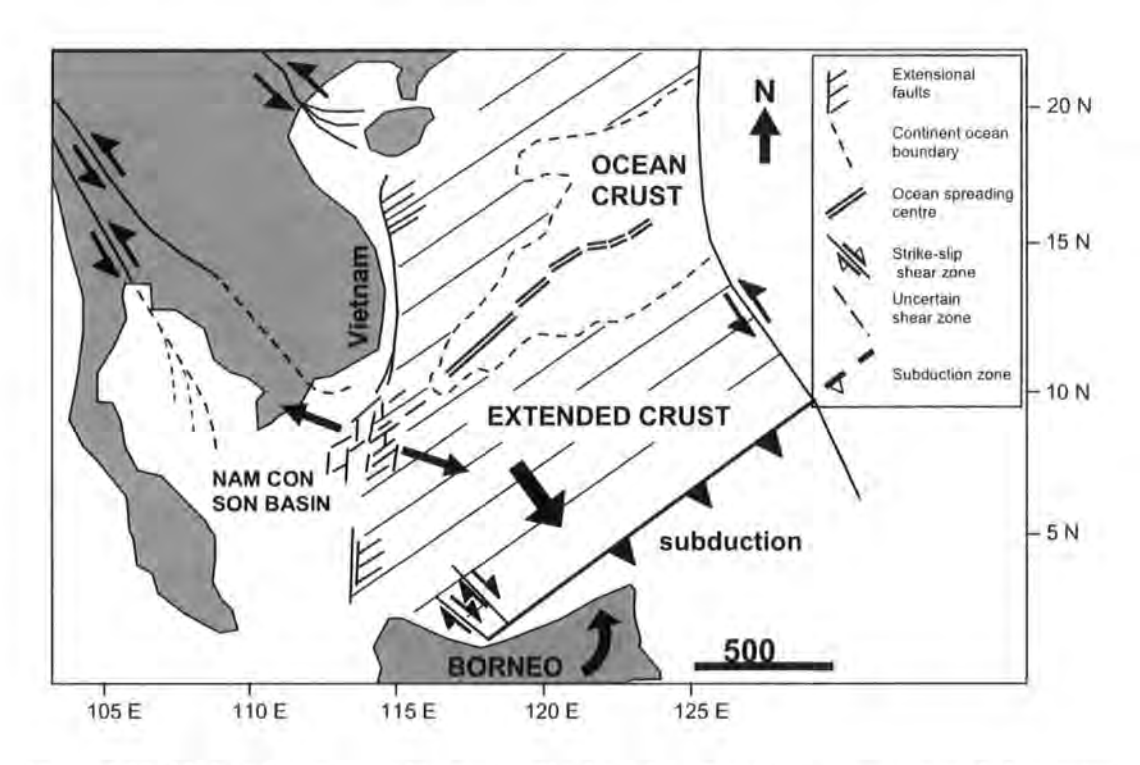


Figure 5.10: Model of the regional tectonics. The Nam Con Son Basin is an area of diffuse extension ahead of the South China Sea spreading centre. Extension is oblique to the dominant underlying basement fabric, which may represent the boundary between the Palaeozoic Indochinese craton and Mesozoic accretionary crust. The driving mechanism of rifting is that proposed by Hall (1997), in which extension is the result of slab pull as Mesozoic ocean crust is subducted to the east.

The regional ~NW-SE displacement vector, as suggested by the ~NE-SW trend of the magnetic lineations in the South China Sea, is oblique to this basement heterogeneity,

and if it has reactivated or influenced fault development could result in dextral transtension along the East Vietnam coast and throughout the Nam Con Son Basin (Fig. 5.10). Extension within the basin is not focussed onto a single, basin bounding, N-S trending fault but is more widely distributed. This could reflect the location of the basin ahead of the South China Sea spreading centre or the complexity of the underlying crust in this area.

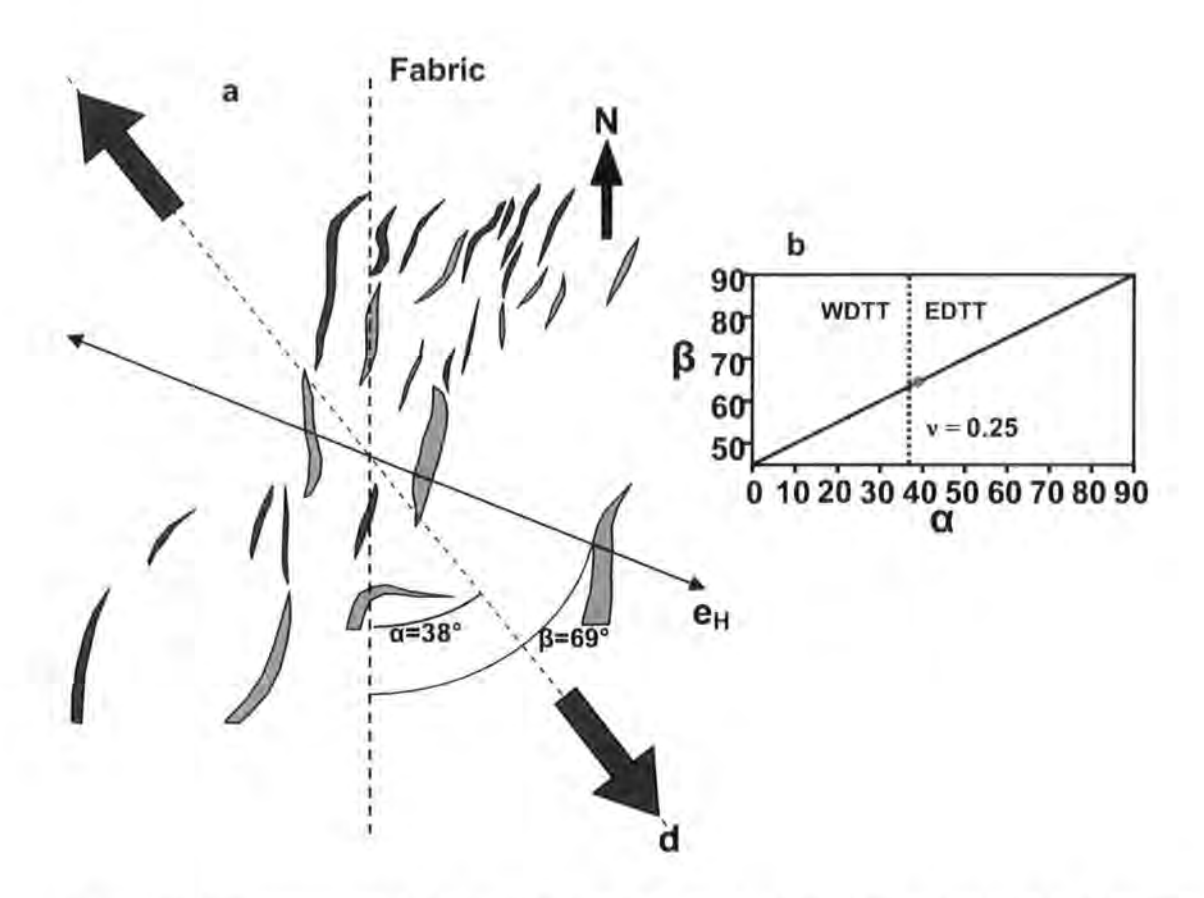


Figure 5.11: Transtension model for the Nam Con Son Basin. a) Nam Con Son Basin faults. Maximum extension direction (e_H) and regional displacement direction (d) are included. α and β are the angles between the N-S fabric and d and e_H, respectively. b) plot of the predicted relationship between α and β . The boundary between the wrench dominated and extension dominated domains is $\alpha_{critical} = 37^{\circ}$, for a poisson's ratio of 0.25, typical of shale (see text).

The methods employed by DePoala et al. (2005a and b) and Wilson et al. (2006) to quantify transtension in onshore settings using the bulk finite strain, can for the first time be applied to a sub-surface dataset and an offshore basin. By demonstrating that

the structures within the basin have not significantly rotated about vertical axes it is shown that the finite non-coaxial strain is reasonably low. The direction of maximum horizontal extension has therefore remained constant throughout the deformation with respect to the deformation zone boundary and the regional displacement direction.

By examining the variation in fault offset throughout the fault population, it has been possible to identify which orientation of fault accommodates the greatest strain and therefore which is most likely to be perpendicular to the axis of maximum horizontal extension (e_H) (see Chapter 4). This method has provided a maximum horizontal extension (e_H) vector for the basin of 111°. The angle between e_H and the ~N-S trending basement fabric (000°) is the angle beta of the transtensional model described in section 5.1 (Fig. 5.1), which in this case is $\beta = 69^{\circ}$. This equates to an α angle of 38° and a displacement direction of 142°, NW-SE (Fig. 5.11a), which fits neatly with the NE-SW orientation of the magnetic lineations in the South China Sea. On a plot of α vs β (Fig. 5.11b), an α angle of 38° plots just within the extension dominated transtension domain, where $\alpha_{critical}$ is 37°, assuming a Poisson's ratio of $\nu =$ 0.25, which has been calculated for shale (see chapter 2.1.1; Johnston & Christensen, 1992; Christensen, 1996; DePoala et al., 2005a) and is appropriate for the shale dominated stratigraphy in this part of the Nam Con Son Basin (Fig. 3.2). It is suggested that the proximity to the boundary of the wrench dominated domain accounts for the mild non-coaxiality of the strain, which resulted in a tendency for small clockwise rather than counter-clockwise rotations. The deformation is similar to that of the physical model of Withjack and Jamison, in which $\alpha = 30^{\circ}$, resulting in short extensional faults with a range of orientations but no evidence for rotations about vertical axes (section 2.1.3; Fig. 2.7c).

5.5 CONCLUSIONS

New techniques for quantitative fault analysis have been used to detect evidence for the rotations, about vertical axes, of normal faults that may occur in strike-slip influenced basins. The techniques presented are particularly suited to the analysis of 3-dimensional seismic data, in which the timing of fault activity and growth can often be constrained through the interpretation of multiple footwall and hangingwall cutoffs. Small variations in fault orientation and subtle fault geometries have been detected that could not have been recognised without this quantitative approach. In the case of the dataset from the central Nam Con Son Basin, the faults do not show a substantial and obviously dominant sense of rotation, which might be expected during large amounts of regional non-coaxial deformation in a wrench-dominated setting. It is also shown that the fault pattern observed in the basin is not the result of multiple rifting events. It may be influenced by the reactivation of pre-existing structures in the underlying pre-Tertiary basement, most notably features that parallel the major crustal boundary between Palaeozoic Craton and Mesozoic accretionary crust which runs beneath the centre of the Nam Con Son Basin. Local fault surface curvatures associated with growing fault tips probably reflect localised variations in the stress field, which are most likely the result of fault interaction. There is, however, evidence for a small amount of overall clockwise rotation, which could reflect a mild component of dextral shear during oblique extension.

In areas where fault rotations can be discounted by this technique, such as in the central Nam Con Son Basin, the finite bulk extension recorded by the fault offsets can be used to calculate the direction of maximum infinitesimal extension (minimum stress). The relationship between the kinematics of the deformation and the boundary conditions, taken to be the dominant pre-existing fabric in the region, predicts a regional

NW-SE displacement direction that is consistent with the ocean spreading vector in the South China Sea.

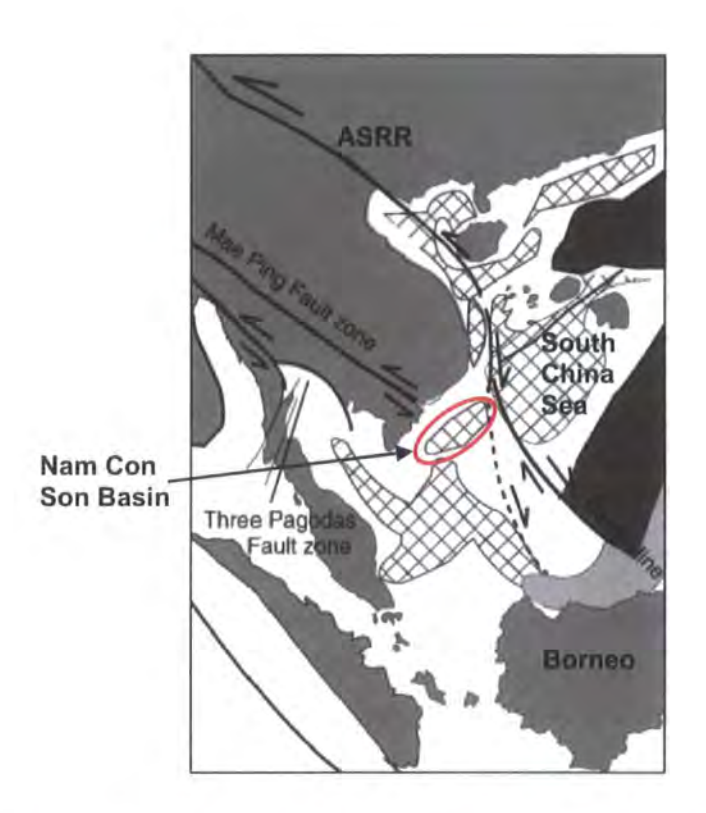


Figure 5.12: Possible location of major strike-slip shear zones offshore Indochina which could connect sea floor spreading in the South China Sea to northwest Borneo and to the ASRR shear zone in northern Vietnam (From Morley, 2002).

The analysis supports the tectonic model of Morley (2002) (Fig. 5.12) in which dextral shear along the eastern Vietnam coast accommodates NW-SE rifting and ocean spreading in the South China Sea during the Early-Middle Miocene. It is also consistent with dextral transtensional fault patterns recognised further north along the Vietnam coast. However, in the Nam Con Son Basin at least, there is no evidence that the dextral transtension is partitioned onto a major through-going strike-slip shear zone. Dextral strike-slip shear zones to the northwest of Borneo (Mat-zin and Swarbrick, 1997) may be responsible for accommodating the regional extension in this area and may provide a connection between the transtensional western margin of the South China Sea and

subduction of the crust beneath Borneo (Fig. 5.10). In this area the NW-SE displacement direction is sub-parallel to the shear zone boundaries and therefore may accommodate wrench-dominated transtension or plane strain simple shear.

The tectonic model of the region in which the western margin of the South China Sea has a dextral rather than sinistral shear sense is consistent with that of Hall (1996; 1997) in which Tertiary extension in the South China Sea region is driven by slab-pull, as older ocean crust, a proto-South China Sea, is subducted towards the southeast beneath Borneo (Fig. 5.10).

CHAPTER 6. DISCUSSION AND CONCLUSIONS

6.1 BASIN EVOLUTION

6.1.1 Eocene-Oligocene rifting

An accurate interpretation of the 3-dimensional seismic data has produced a very detailed model of the faults and stratigraphic horizons in the central area of the Nam Con Son Basin. The analysis shows that the dominant ~N-S and ~NE-SW fault set represents one rifting event that occurred during the Early and Middle Miocene resulting in >6 km of syn-rift sediment in the graben. However, in addition to this there is clearly a deeper sedimentary succession below the Miocene sediments, which could be ~6 km thick in the basin centre. Previous studies have shown that the Late Oligocene sequence, which was possibly deposited during thermal sag following the earlier Eocene rifting event, is a relatively thin sequence (up to 1 km thick) in the southeastern part of the basin (Matthews et al. 1997; Lee et al. 2001). If this succession was deposited as a response to thermally driven or loading induced subsidence it is likely that this thickness does not vary a great deal into the basin centre. Therefore, in the basin centre the Eocene-Early Oligocene rift fill must be considerably thicker than is seen in isolated graben in the southeast. This suggests the existence of a significant Eocene depocentre, with dimensions in the region of 150 km long, 75 km wide and 5 km deep, based on the top basement maps produced using 2-dimensional seismic data and gravity inversion (Huchon et al., 1998). The top basement that was mapped in the basin centre using 3dimensional data, dips towards the northwest and is not significantly offset by Miocene faults. It is possible that the basement dips towards a large south dipping Eocene fault to

the northwest, suggesting a trapdoor style half graben geometry for the Eocene rift in the basin centre. The basement dip may have been gently steepened by the Late Oligocene thermal subsidence.

6.1.2 Fault population growth

The fault timing has been constrained and reveals that the number of active faults increased throughout the Miocene rifting event (section 3.4.4). This is contrary to the strain localisation concept in which faults grow and link to form fewer larger faults through time (e.g. Walsh *et al.* 2003). An increase in the number of active faults must reflect changes in the orientation of the stress system or localised stresses due to ongoing deformation e.g. in deforming fault hangingwalls. The former is unlikely as there is no correlation between fault timing and fault orientation. The faults do not show a change in the preferred orientation through time, which would reflect a rotation of the stress system. Furthermore, the faults were not superseded by new, more efficient faults e.g. of a different orientation. Only 39 (17%) faults die out during the rifting episode and 40 of the faults (18%) were active throughout the entire constrained sequence, they initiated prior to h2 deposition and remained active until after the deposition of h6. The faults did not necessarily 'lock-up'.

The fault timing shows that the graben bounding faults were established at an early stage in the rifting and that subsequent faulting was concentrated within the graben and the subsiding ramp areas. These areas were deforming in response to continued movement on the graben bounding faults. An example of this can be seen on the ramp that connects Graben B to the structurally high centre (Fig. 6.1). The ramp is bound to the east by a large fault which initiated prior to h2 deposition. The smaller faults in the hangingwall of this fault, strike perpendicular to the master fault and to the

dip direction of the ramp. They systematically young towards the southwest, that is, in the direction of ramp dip.

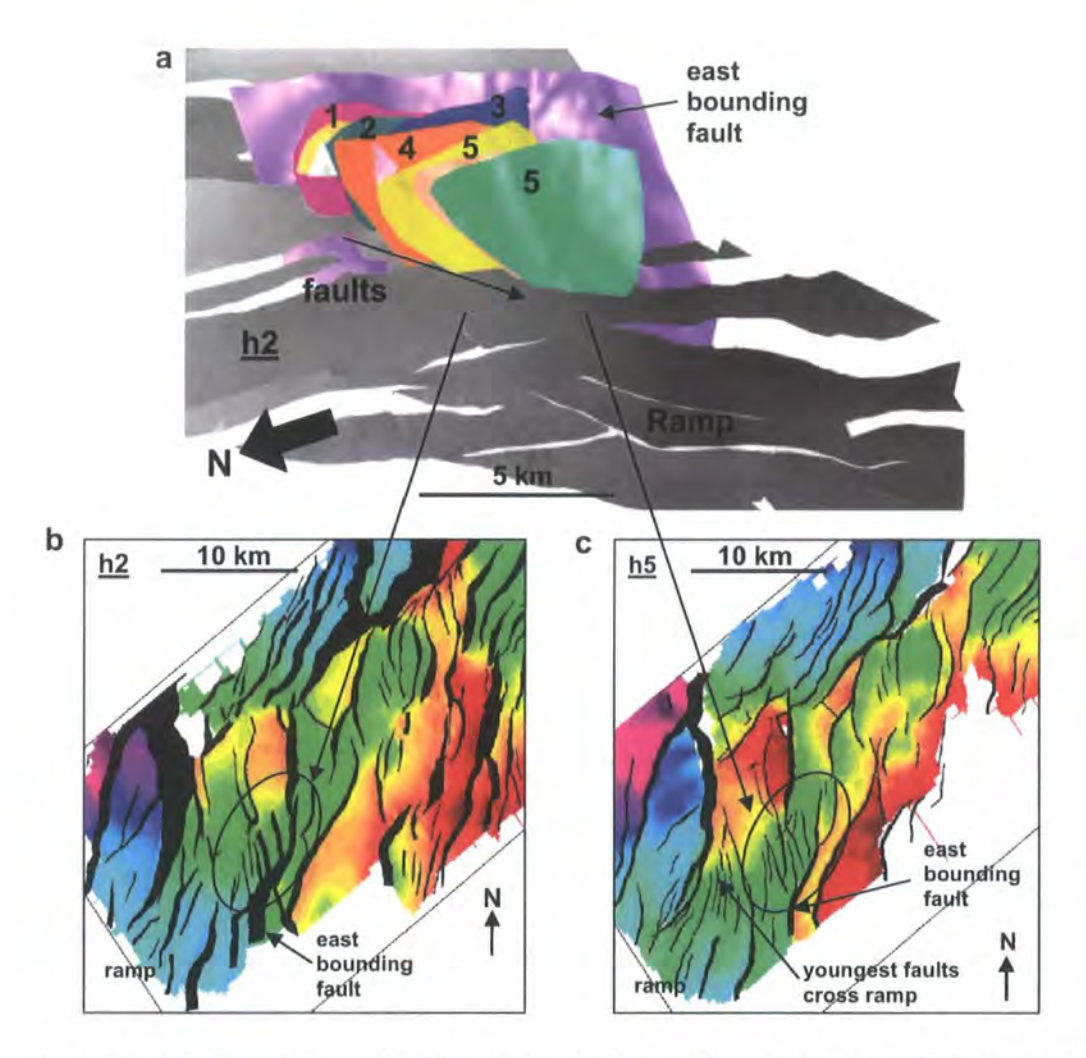


Figure 6.1: a) 3-dimensional model of the west graben ramp, the east bounding fault and several smaller faults that cross the ramp. The ages of the faults systematically decrease down the ramp. Fault numbers are relative ages, 1 is the oldest and 5 the youngest. The locations of the faults relative to the basin can be seen in the maps (b and c). b) Map of horizon h2. The faults discussed are circled. c) Map of horizon h5. The faults discussed are circled. The youngest faults on the ramp intersect h5 only and cross cut the ramp.

Throughout deformation the number of faults on the ramp increases. Initially there is only one fault on the ramp with a strike sub-parallel to the ramp dip direction. The number of faults increases with a final increase in fault numbers following the deposition of h6. The latest faults curve across the ramp, in effect breaching the structure.

Within the graben, the increased faulting is possibly the result of localised extension due to hangingwall rollover, in which a fault hangingwall is folded to form an anticline as the fault offset increases. This type of structure can occur on planar faults (Barnett *et al.*, 1987) but has the potential to be more pronounced on listric faults.

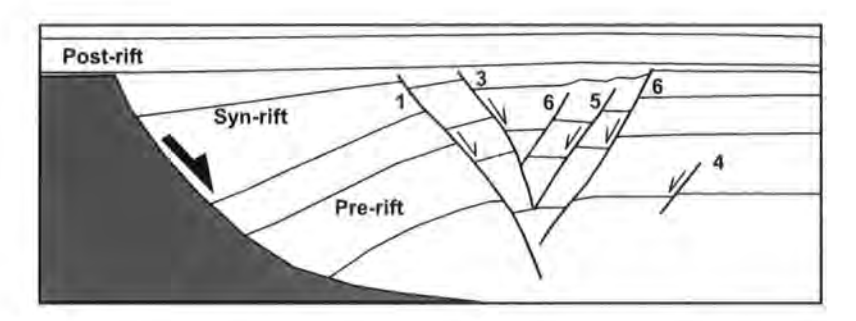


Figure 6.2: Physical sandbox model of extension in the hangingwall of a listric fault. The shaded grey area is a fixed footwall block. During deformation extensional faults formed in the hangingwall in the order that they are numbered. (After Buchanan and McClay, 1991).

Hangingwall rollover on a listric fault geometry has been modelled by McClay (1990a, b) using a sand hangingwall above a pre-cut listric fault template. As the hangingwall is folded, the convex, upper side of the hangingwall is extended. This is accommodated by the creation of smaller synthetic and antithetic normal faults within the hangingwall (Fig. 6.2).

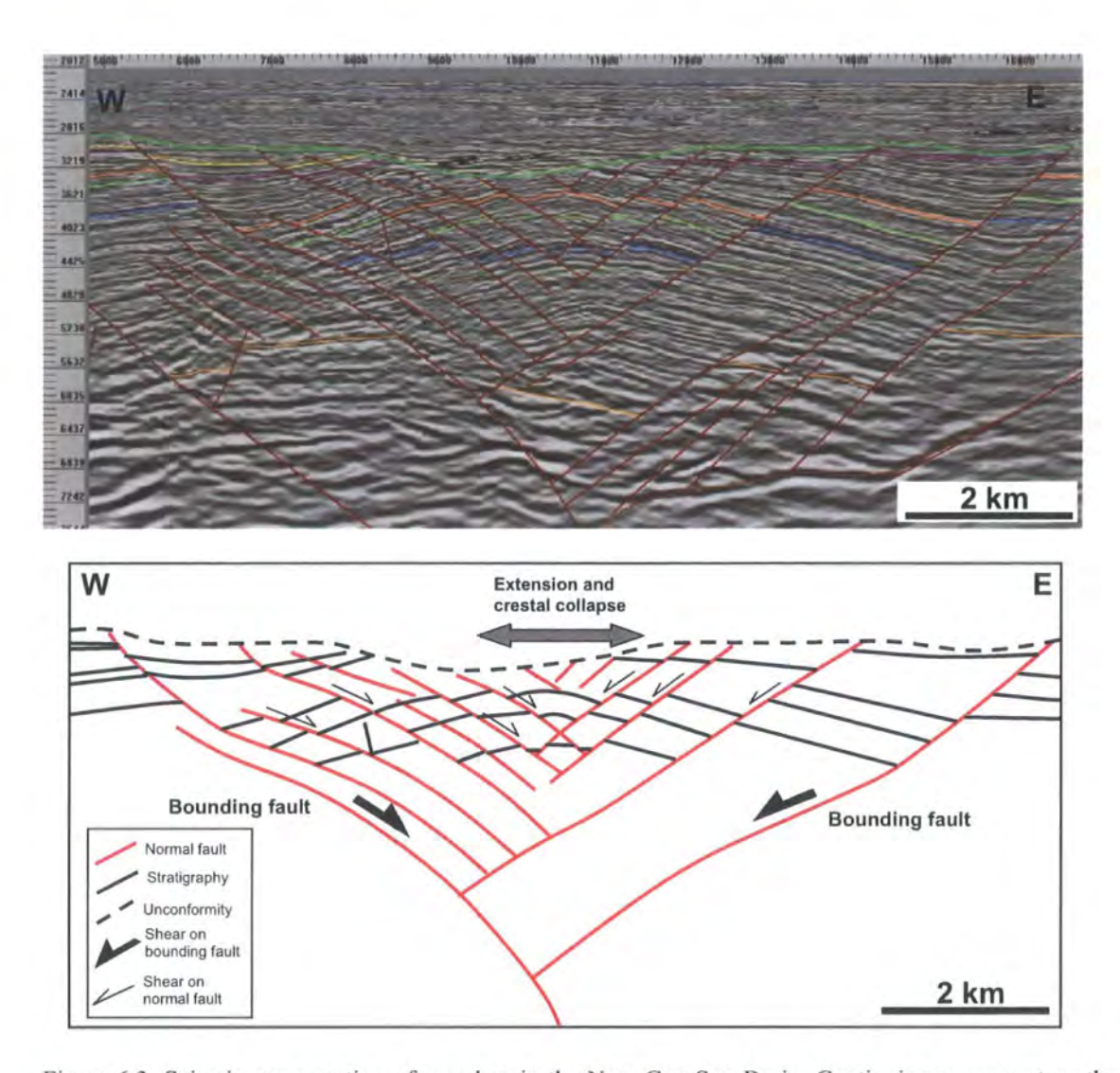


Figure 6.3: Seismic cross section of a graben in the Nam Con Son Basin. Continuing movement on the graben bounding faults produces deformation and folding of the stratigraphy. Orthogonal flexure causes extension across the convex side of the graben resulting in increased faulting similar to that demonstrated in sandbox models of crestal collapse. The deformation within the graben has rotated fault surfaces to produce sigmoidal fault geometries.

The sandbox models of hangingwall rollover are an analogue for the deformation observed within the graben but underestimate the degree of complexity. Rather than a hangingwall adjacent to a single fault or a hangingwall in an asymmetric half-graben, Graben C and D are bound at both sides by faults with similar offsets. This has produced symmetric rollover anticlines which more closely resemble compressional folds. The graben in the central Nam Con Son Basin show evidence of being extended across the convex side of the hangingwall. The amount of extension has been measured across the graben. In Graben C the amount of NW-SE extension increases upwards

through the sequence, with the greatest extension on horizon h3. Within the graben many of the faults have sigmoidal geometries. The sigmoidal faults dip towards the graben centre and the number of sigmoidal faults is greatest where the hangingwall fold becomes more pronounced. It is suggested that this fault geometry could reflect a bed parallel shear within the graben as the convex side of the fold is extended more than the concave side during orthogonal flexure (Fig. 6.3). The sense of shear flips across the fold hinge. The fault dips are lower within the graben than outside of the graben. This could suggest that during deformation, the faults initiated within the graben and were rotated about horizontal axes due to continuing fault movement on the bounding faults. This rotation is also evident in antithetic faults with normal offsets that have been steepened to sub-vertical. This supports the idea that continuing movement on the bounding faults created localised extension, which in turn lead to an increasing number of active faults. Faulting in the central Nam Con Son Basin is driven by the regional stress system and localised stresses resulting from hangingwall deformation. The increasing number of active faults during rifting can be attributed in part to hangingwall rollover or deformation of the subsiding ramp structures.

It has been questioned whether similar structures in the southeast of the basin have geometries resulting from extension only or whether they have been mildly inverted and uplifted due to compression (Fig. 6.4; Matthews *et al.*, 1997).

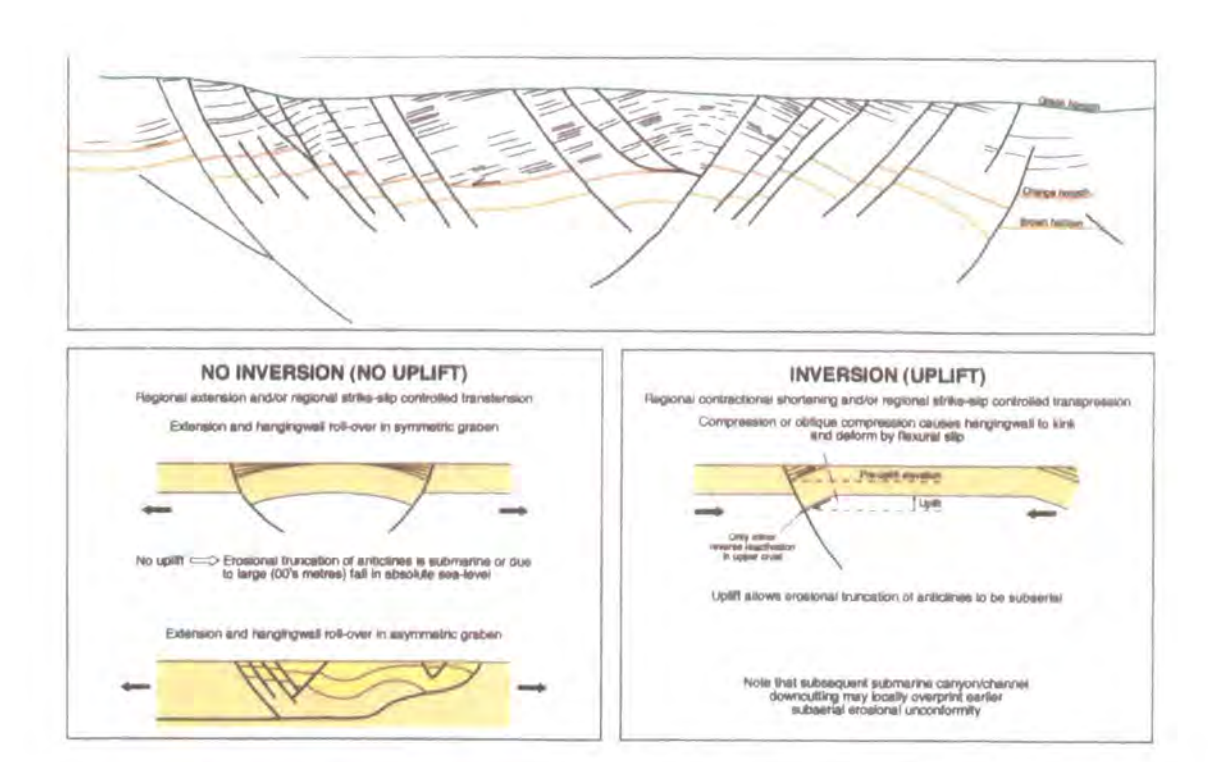


Figure 6.4: Competing models for graben anticline in the Nam Con Son Basin (after Matthews et al., 1997).

The crest of the structures in the southeast appear to have been eroded flat prior to the deposition of the post-rift sequence, with the truncation of seismic reflectors in places (Fig. 3.4). Graben C and D also show erosion across the hangingwall anticlines but the erosion appears to incise the syn-rift sequence to produce a more channel-like feature, which is passively infilled with post-rift sediment. The size, shape and seismic character of the erosional feature are similar to submarine channel complexes in the Kutei Basin, East Kalimantan (Fowler *et al.* 2004).

Graben D is structurally higher in the graben centre than at the margins, which does suggest that the graben has been inverted and uplifted. The amplitudes of the folds decrease upwards through the sequence, as shown by the measurements of shortening due to bed rotations and folding (section 3.4.6). This indicates that folding was synsedimentary and that the structures are probably rollover anticlines associated with extension on listric or sigmoidal faults. However, it is very difficult to establish whether the anticlines were then gently uplifted and tightened by subsequent E-W compression.

Small E-W trending folds within a horst appear to post-date the deposition of horizon h6 and so would be contemporary with the possible inversion (type 4 folds of section 3.4.5). However, the ~E-W trend of the folds is inconsistent with the idea of ~E-W compression. Also, there is no evidence for reverse fault offsets anywhere in the basin. Therefore, despite the unusual geometry and erosion of the anticlinal graben structures, a model of compressional tectonics during the Miocene cannot be reconciled with the available evidence.

6.2 THE EFFECTS OF TRANSTENSION AND REACTIVATION ON THE MIOCENE STRUCTURE

The presence of a strong \sim N-S trending fabric in the underlying crust has resulted in oblique extension or transtensional deformation during the Miocene. Quantitative fault analysis has been used to constrain the orientation of the maximum horizontal extension in relation to the dominant pre-existing fabric and the regional displacement direction (Chapter 4). The analysis indicates that during the Early-Middle Miocene the deformation was dextral extension-dominated transtension. In addition, assuming a poisson's ratio of \sim 0.25 (that of shale or sand), the deformation plots close to $\alpha_{critical}$, the boundary between wrench and extension dominated transtension (section 5.4.1).

The transtensional nature of the deformation has produced an unusual structural architecture. Immediately obvious is rhomboidal shape of the basin. The length to width ratio of <2:1 is similar to that of pull apart basins that form at releasing bends or stepovers in strike-slip shear zones. However, basins that formed as a direct result of movement along strike-slip shear zones, such as those found in the North Sea (Bartholomew *et al.*, 1993) or the classic examples associated with the San Andreas fault in California, are typically smaller than the Nam Con Son Basin. This reflects the transtensional nature of the basin and the absence of a through going shear zone.

The faults are relatively short, with most faults having offsets in the range of 100-1000 m and lengths in the range 1 km-10 km, measured at the longest part of the fault surface. The lengths of these faults are significantly lower than the normal faults with equivalent offsets described in Schlische *et al.* (1996), which have lengths of 5 km – 50 km. Furthermore, the physical model of oblique extension in which $\alpha = 30^{\circ}$ produced shorter faults than those models with higher angles of divergence (Fig. 2.7; Withjack and Jamison, 1996). It is suggested that short faults are a consequence of the

range of fault orientations and that lateral fault growth has been inhibited due to interactions between coeval faults with ~NE-SW and ~N-S trends.

In addition to fault interaction a potentially more important mechanism could be the influence of the E-W trending Eocene-Oligocene structures. Unfortunately the deeper sequence has not been interpreted due to the complexity of the seismic reflectivity at depth and the 'masking' effect of the Miocene faults but the existence of E-W trending structures in the basin centre is likely considering the thickness of the Eocene-Oligocene sequence in this area. These structures, which initiated during ~N-S extension, have not been reactivated during the Miocene because they are too oblique to the ~NW-SE regional extension. However, these structures have produced heterogeneity within the deeper sequence that has controlled subsequent faulting by acting as barriers to fault propagation, especially for ~N-S trending faults. A consequence of this is the along strike dip-polarity flips that are seen within the area.

6.2.1 Offset graben and along strike dip polarity flips

Along strike fault dip polarity flips are associated with offset depocentres. Graben A and B, in the western part of the area, contain Miocene sediment of a similar thickness, 6-8 km, and represent the southeastern part of the deep basin centre. Graben C and D to the east, have slightly thinner sedimentary infill of <5 km thick. In both cases, the graben have dextral offsets and the areas between Graben A and B and C and D are accommodation zones with complex fault patterns and along strike polarity flips. The ~N-S trending, east dipping fault that bounds the western edge of Graben C passes along strike to the west dipping fault that bounds the eastern edge of Graben D (Fig. 6.5).

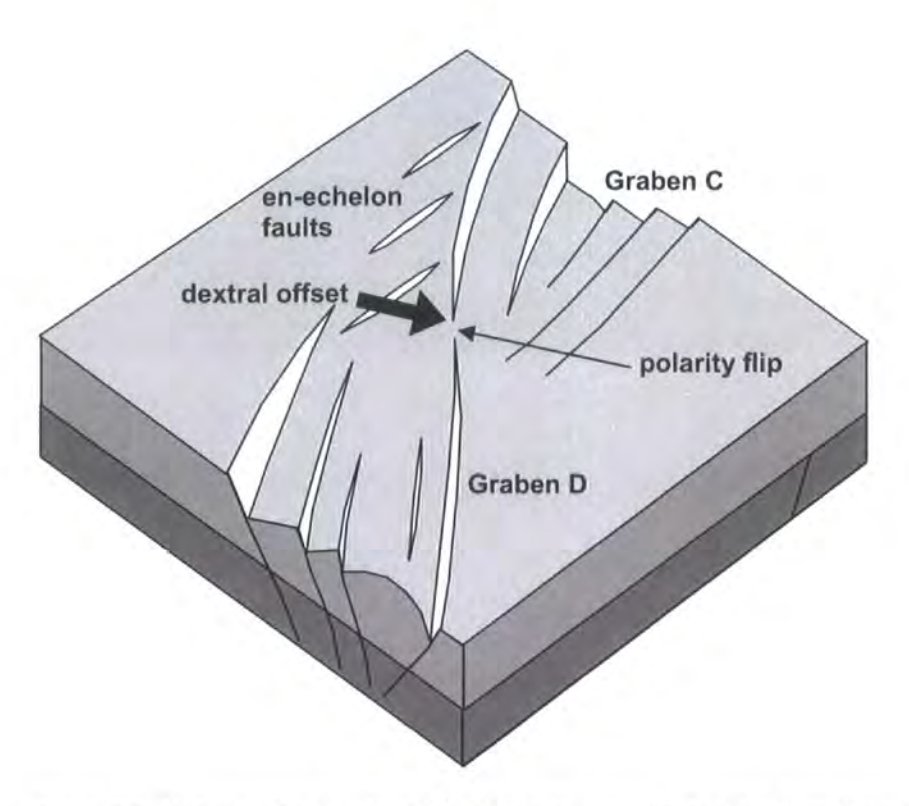


Figure 6.5: Cartoon of Graben C and D. The graben are offset with a dextral sense.

This structural style is observed in many natural rift basins (Lambiase and Bosworth, 1995), e.g. Lake Tanganyika, Africa (Rosendahl *et al.*, 1986) and has been reproduced by the sandbox models of McClay and White (1995) during oblique extension (Fig. 2.8). In accordance with the sandbox models, the offsets are accommodated solely by normal faulting, there is no evidence for strike-slip transfer zones. The offset of Graben C, relative to Graben D, could be accommodated by the en-echelon array of normal faults to the north of Graben D.

The offset graben mapped using the 3-dimensional seismic data reflects the structural style of the basin as a whole. The regional mapping work done by BP shows that the depocentres in the basin are offset (Fig. 6.6). Again the sense of offset is dextral, resulting in a NE-SW trending array of depocentres. The locations of the fault dip polarity flips and the depocentre offsets correspond to the locations of the

underlying ~E-W trending faults that offset Top basement but are buried beneath the Early-Miocene sequence (Fig. 3.3).

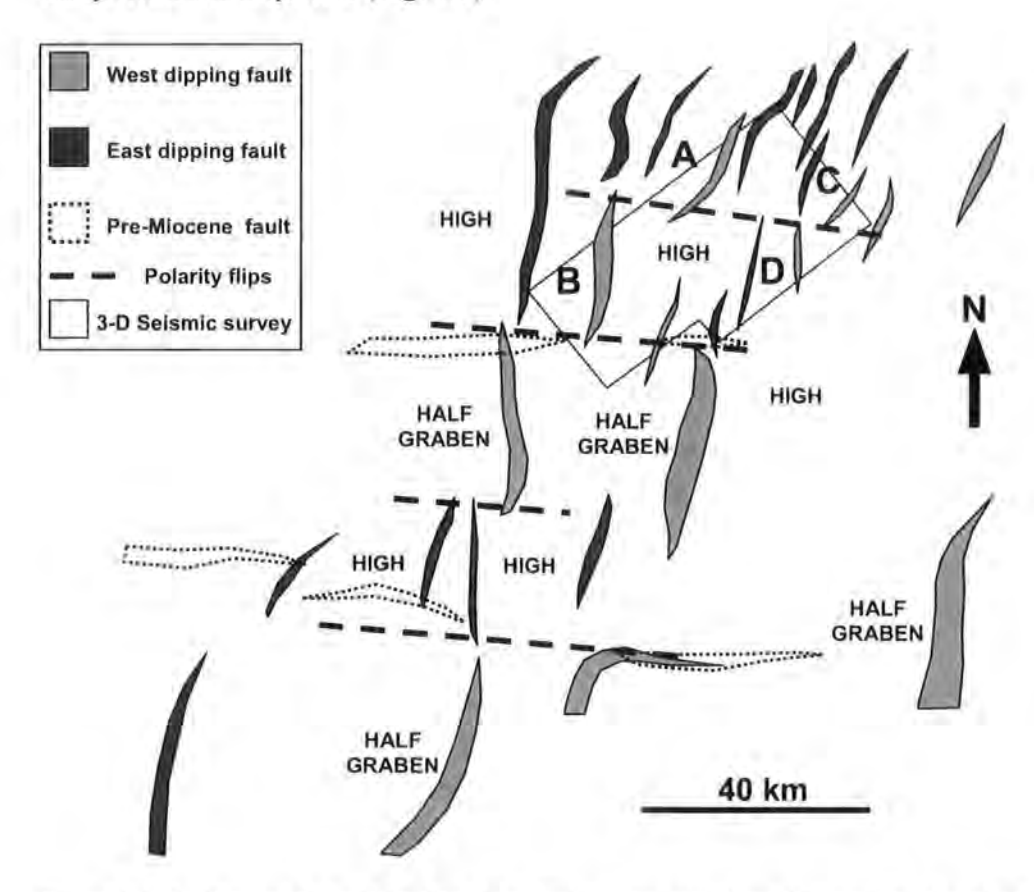


Figure 6.6: Fault map of the Nam Con Son Basin interpreted from the maps produced at BP (Fig.3.3). Solid faults offset the Early Miocene and are colour coded based on the dip polarity. Dashed faults offset the basement but are buried beneath the Early Miocene sequence. The dashed lines highlight the major polarity flips of the Early Miocene faults. The location of Graben A-D are labelled.

It is possible that the trend and locations of the Eocene-Early Oligocene faults have controlled the locations and trends of the Miocene accommodation zones. In this case the E-W trending faults have acted passively rather than actively, and have not reactivated as strike-slip shear zones as there is no evidence for strike-slip structures within the Miocene sequence. The dextral sense of offset has produced an array of basin depocentres with a trend perpendicular to the regional extension direction. This is similar to the Mae Moh Rift in Thailand in which the graben form an en-echelon array trending perpendicular to the extension direction (Morley, 2000).

6.2.2 Transtensional folding

Folding exists at a variety of scales within the Nam Con Son Basin (chapter 3.4.5). The folds are divided into four types based on their geometry, timing and the relationship to the adjacent faults. The majority of these folds trend ~E-W, sub-perpendicular to the adjacent faults. A minority of folds are classified as type 3, the only type of fold that is oriented sub-parallel to the adjacent faults. It is suggested that these folds are extensional forced folds that formed ahead of propagating fault tip (Fig. 6.7a; Withjack et al., 1990; Schlische, 1995; Hardy and McClay, 1999; Corfield and Sharp, 2000; Gawthorpe and Leeder, 2000; Jackson et al., 2006). The largest of these folds has a curved hinge that follows the curvature of the adjacent fault. The timing of fold growth may slightly pre-date fault movement.

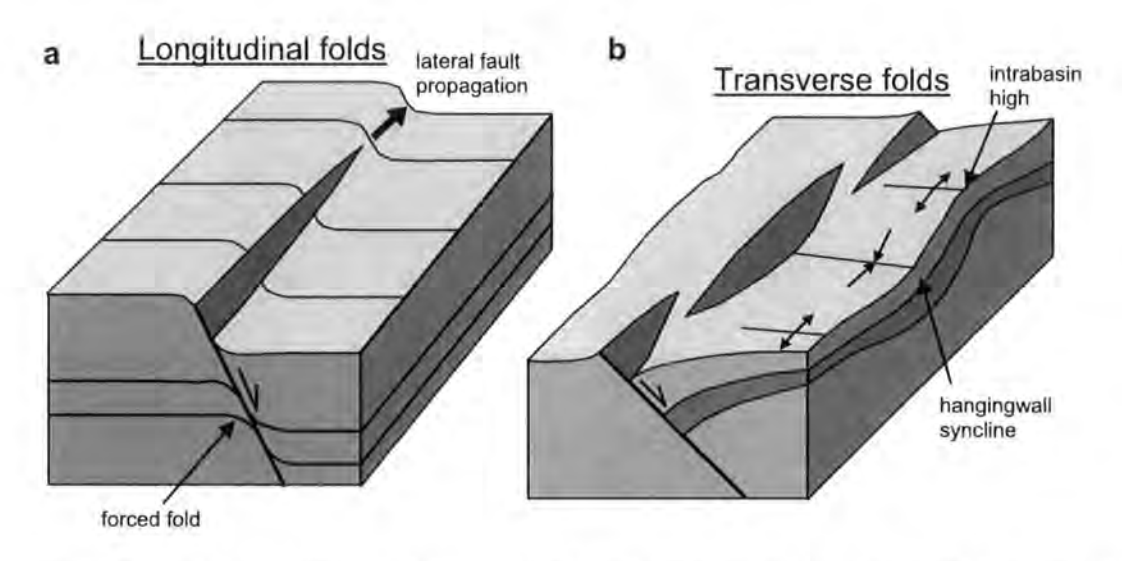


Figure 6.7: Cartoon of extensional folds. a) forced fold b) hangingwall syncline and intrabasin anticlines (After Schlische, 1995).

The majority of folds have ~E-W trends, roughly orthogonal to the adjacent faults. These folds are divided into three types and probably have different origins. Type 2 folds are the largest wavelength folds and are of a comparable scale to the adjacent faults. Furthermore, the timing of fold growth is contemporary with fault movement. It

is suggested that these folds are extensional hangingwall synclines and footwall anticlines that accommodate the decrease in offset from the fault centre to the tips (Fig. 6.7b).

A ~N-S contraction may have produced the type 1 and type 4 folds. This is consistent with the conclusions of Matthews *et al.* (1997), who suggested that an episode of N-S compression during the Middle Miocene had affected structures in the southeastern part of the basin. The growth of type 1 and 4 folds is synchronous with fault movement but in most cases post dates the initial fault activity. Folding initiated during the Middle Miocene, after the deposition of h3. Type 4 folds appear to post date the deposition of h6.

The ~E-W trend of the majority of the folds and the orthogonal relationship between the folds and faults is consistent with that predicted by models of wrench dominated transtension in which eh is a shortening strain (eh<1) and eH a lengthening strain (eH>1). However, models of transtension predict that there should be no horizontal shortening during extension dominated transtension. Transtensional folding within the Nam Con Son Basin is therefore inconsistent with the basin model of extension dominated transtension (chapter 5). Two alternative explanations can be put forward. Firstly, the faults are not transtensional in origin. Specifically, they do not accommodate a basin wide contraction but are a response to local stresses in the fault hangingwalls. In this case, a mechanism would be needed to explain the occurrence of the folds, including those in the horst (type 4 folds) that clearly do not accommodate hangingwall deformations. It could explain why some folds are not E-W trending but are instead sub-perpendicular to the adjacent fault surface, as seen in cases where the fold hinges diverge or converge when adjacent to curved faults (Fig. 3.39). Alternatively, the deformation could have a very mild wrench component, consistent

with the subtle clockwise rotations discussed previously (chapter 5). The majority of folding is very subtle relative to the extensional faulting and is local to the areas immediately adjacent to fault surfaces. The models of transtensional folding show that the amount of contraction and ergo the magnitude of the wrench component decreases as the divergence angle increases. The folding could reflect a very faint wrench component during a transtensional deformation that is barely within the extension dominated domain. This suggestion is consistent with the interpretation in section 5.4.1 that the deformation plots close to $\alpha_{critical}$, the boundary between wrench and extension dominated transtension.

The preferred ~E-W trend of the fold hinges is counter-clockwise from that predicted by models of transtensional strain, given the mean fault strike of 021° (see chapter 4). This pattern is evident on the fold hinge map (Fig. 3.36) in which a number of the folds show a subtle counter-clockwise rotation relative to the predicted orientation relative to the adjacent fault surface. It is possible that this realignment is another influence of the ~E-W trending Eocene-Early Oligocene structure. In addition to acting as barriers to lateral fault propagation, the earlier structures may have acted as buttresses that have somehow realigned the fold hinges.

6.3 IMPLICATIONS FOR HYDROCARBON PROSPECTIVITY

Potential source rocks in the Nam Con Son Basin are the Oligocene and Early Miocene shales (Tin *et al.*, 1994; Matthews *et al.*, 1997). Potential reservoir units exist throughout the stratigraphy, including coastal plain sandstones in the Oligocene and the Early-Middle Miocene syn-rift sequence, shelf carbonates in the Middle Miocene syn-rift sequence and shelf carbonates and turbiditic sandstones in the Late Miocene to recent post-rift sequence (Fig. 3.2). Well data from the centre of the basin suggests that the potential reservoir sands of the Oligocene sequence may be substantial but the sands within the Early-Middle Miocene sequence may be thinner than elsewhere. The post-rift sequence, which lies unconformably on the faulted blocks of the syn-rift sequence is dominated by mudrock and has the potential to provide a good regional seal. This discussion will focus on the potential of the Early-Middle Miocene syn-rift sequence and the influence of faulting and folding on the hydrocarbon prospectivity.

Assuming an average heat flow of 60 mW m² (Matthews *et al.*, 1997), it is probable that if Oligocene and Early Miocene source rocks exist in the deeper areas, they would have expelled hydrocarbons during the Middle Miocene and if they exist on the structural highs, they would have expelled hydrocarbons during the deposition of the Pliocene to Recent post-rift (Matthews *et al.*, 1997). In the case of the first scenario, in which hydrocarbons are expelled during the Middle Miocene, the expulsion would have been coeval with the Miocene rifting event. The Early Miocene faulting, in which the graben bounding faults were established has created fault bound structures relatively early in the rifting episode providing potential traps for any hydrocarbons that were expelled during the Middle Miocene. However, these faults were continuously active throughout the Middle Miocene, which increases the risk that any hydrocarbon charge

into those traps prior ~10 Ma was remigrated and possibly lost. A number of faults became inactive during the Middle Miocene but these are small structures compared to the larger faults, which remained active throughout rifting. Few faults offset the end Middle Miocene unconformity, which suggests that rifting had ceased by ~10 Ma. Any hydrocarbon charge since this time, including hydrocarbons expelled during the Pliocene to Recent has the potential to be trapped in a wide variety of fault bound structures.

The intensity of faulting has led to concern about the lack of continuous carrier beds and the reliance on vertical rather than lateral migration (Matthews *et al.*, 1997). However, the model of the central area suggests that lateral migration could have been facilitated by large ramp structures, which connect the deeper graben in the basin centre to the structural highs (Fig. 3.27). The ramps may have provided continuous pathways for fluid flow. Although the ramps are faulted, the faults are parallel to the dip of the ramps and therefore do not disrupt the continuity of the structure. This structural style has potentially enabled the structurally high areas of the basin centre to be charged from the Oligocene and Early Miocene oil prone source rocks in the drainage areas of the Dai Hung and Dua fields in the basin centre (Matthews *et al.*, 1997).

Oblique extension has resulted in the development of faults with a range of orientations that link at high angles to form trapping geometries (Fig. 6.8). In a number of cases two or more faults form a three-way closure, with the dipping hangingwall completing the trap. The hangingwall folds that have been mapped provide additional trapping potential. Many of the folds have hinges that are perpendicular to the fault surface and plunge away from the fault. In these cases the fold acts as a three way closure with the fault surface acting to prevent the hydrocarbons from escaping up-dip

(Fig. 6.8). The rollover hangingwall anticlines with crestal collapse faults are important features within the basin centre.

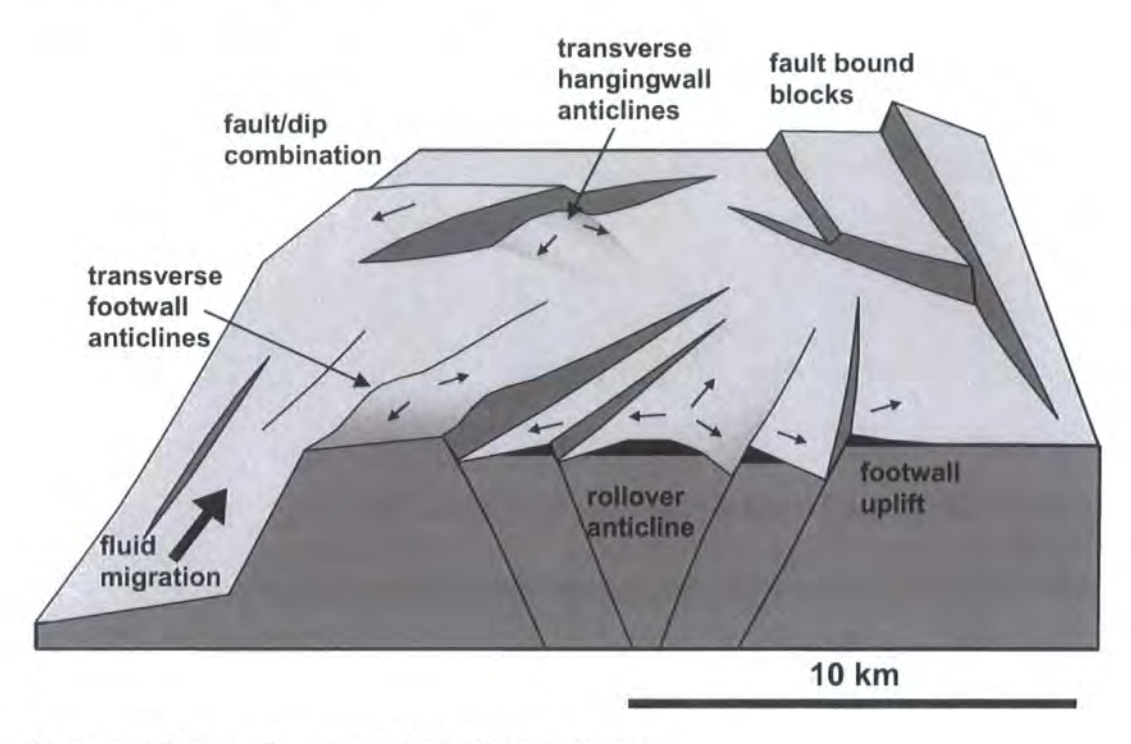


Figure 6.8: Cartoon of trapping styles in the basin centre.

These structures are similar to the hangingwall rollover anticlines associated with listric syn-sedimentary faults in the North Sea, which provide good structural traps (Hardman and Booth, 1991). The examples in the Nam Con Son Basin may be improved because of the symmetry of the graben, which has produced anticlines with symmetrical limbs that more closely resemble compressional folds than traditional rollover anticlines associated with asymmetrical half-graben. Fault seal is clearly important for the success of any structural traps within this area. The syn-rift sequence is dominated by mudrock with thinner interbedded sand units, giving it a low sand to shale ratio, particularly in the Middle Miocene section. Therefore there is good potential for clay smear or for the favourable juxtaposition of the sand and mud units.

It is unknown whether the fault pattern mapped using 3-dimensional seismic data is similar at smaller scales, including outcrop and reservoir scales. If this is the

case, the density of faulting and the range of fault orientations could serve to inhibit fluid flow within the reservoirs or lead to compartmentalisation. The strain distribution model presented in chapter 3 could potentially be used to improve models of fluid flow within heavily fractured reservoirs by predicting which orientation of fracture is likely to have greater dip-slip offsets and therefore which are more likely to seal and act as barriers to fluid flow. The amount of throw on a fault (vertical offset), is used in calculations of both shale gouge ratio and clay smear factor, two methods of estimating the likelihood of fault seal (Yielding *et al.* 1997).

6.4 CONCLUSIONS

The application of new and established quantitative fault analysis techniques to offshore 3-dimensional seismic data has provided new insight into the evolution of the fault population in the Nam Con Son Basin. Despite the wide range of fault orientations, by constraining the timing of fault movement it is shown that the faults are broadly contemporary, although the number of active faults did increase through time. This is attributed mainly to the continuing movement on graben bounding faults, which resulted in the extension and faulting being focused within the graben, as the basin evolved.

The variation in offset between faults of different orientations has revealed an ideal fault strike, which can be used to infer the direction of maximum extension. The range of fault orientations reflects the conflicting influences of the regional extension vector and the reactivation of pre-existing fabrics. The dominant regional fabric is ~N-S trending and relates to a strong rheological boundary in the crust that has controlled the western extent of South China Sea rifting and the orientation of faulting within the Nam Con Son and other basins. The regional extension direction during the Miocene is ~NW-SE and has controlled the orientation of South China Sea ocean spreading. The oblique angle between the dominant underlying basement fabric and the regional extension vector has resulted in dextral transtension in the Nam Con Son Basin. A quantitative analysis of the strain that has previously been applied to onshore datasets has for the first time been applied to an offshore sub-surface dataset. This analysis of the central Nam Con Son Basin has revealed a relationship between the boundary conditions, regional displacement direction and maximum extension vector that is consistent with an extension dominated transtension. The results of the analysis predict

that the deformation, although extension dominated is very close to the critical angle that defines the wrench dominated transtension domain. This may have led to mild contraction and folding, orthogonal to the maximum extension direction and to a tendency for faults to rotate clockwise about vertical axes, consistent with the dextral sense of obliquity.

A significant Eocene-Oligocene rifting episode resulted in the deposition of ~5 km of sediment in ~E-W trending graben. Although the Early to Middle Miocene extension vector was too oblique to reactivate these structures, this pre-existing structure has controlled the subsequent deformation by inhibiting lateral fault growth and resulting in numerous polarity flips and accommodation zones between offset graben.

The influence of pre-existing fabrics is shown to be crucial in the evolution of the Nam Con Son Basin during the Early-Middle Miocene. At a regional scale the N-S trending basement fabric, which is oblique to the regional extension direction, has been reactivated resulting in a transtensional rift basin. At a local scale within the basin, the Eocene-Oligocene structure has passively controlled the deformation by creating heterogeneity within the sedimentary cover sequence.

The implications of this work cover several areas, namely the development of quantitative fault techniques and their application to 3-dimensional seismic data, the evolution of fault populations, transtensional deformation and the role of pre-existing fabrics on subsequent deformation. The quantitative fault analysis techniques that have been developed can be applied to any other 3-dimensional seismic datasets in which the fault/horizon cutoffs have been modelled, as long as they meet a few assumptions (discussed herein). Further work would be to check that the strain distribution model is applicable to other areas of extensional faulting in which there is a wide range of fault

orientations. The techniques to identify fault rotations about vertical axes could be applied to areas in which there is good independent evidence for wrench tectonics e.g. in the Gulf of Tonkin, north Vietnam, offshore of where the onshore Red River Fault meets the continental shelf. If the techniques demonstrated a significant and dominant rotation in an area of strike-slip deformation then this would add confidence that the techniques can indeed be used to identify rotations of faults about vertical axes. The type of tectonics that created the Nam Con Son Basin, although complex, are not unique. The continental crust is heterogeneous and orthogonal extension is probably the exception rather than the rule. The deformation styles that have been observed and quantitatively analysed in the Nam Con Son Basin will be evident in countless other extensional basins, many of which will undoubtedly contain hydrocarbons.

REFERENCES

- Agterberg, F.P. 1974. Developments in Geomathematics. Elsevier, pp. 475-508.
- Allen, M.B., MacDonald, D.I.M., Xun, Z., Vincent, S.J., Brouet-Menzies, C. 1998. Transtensional deformation in the evolution of the Bohai Basin, northern China. In: Holdsworth, R.E., Strachan, R.A., Dewey, J.F. (Eds.), Continental Transpressional and Transtensional Tectonics. Geological Society, London, Special Publication 135, pp. 215-229.
- Anderson, E.M., 1951. The Dynamics of Faulting. Oliver & Boyd, Edinburgh.
- Angelier, J., 1979. Determination of the mean principle directions of stresses for a given fault population. Tectonophysics 56, 17-26.
- Angelier, J., 1984. Tectonic analysis of fault slip data sets. Journal of Geophysical Research 89, 5835-5848.
- Baas, J.H., 2000. EZ-Rose: a computer program for equal-area circular histograms and statistical analysis of two dimensional vectorial data. Computers and Geosciences 26, 153-166.
- Barnett, J.A.M., Mortimer, J., Rippon, J., Walsh, J.J., Waterson, J., 1987. Displacement geometry in the volume containing a single normal fault. AAPG Bulletin 71, 925 937.
- Bartholomew, I.D., Peters, J.M., Powell, C.M., 1993. Regional structural evolution of the North Sea: oblique slip and the reactivation of basement lineaments. In: Parker, J.R. (Ed.), Petroleum Geology of Northwest Europe: Proceedings of the 4th Conference. Geological Society, London, pp. 1109-1122.
- Blanton, T.L., 1982. An experimental study of interaction between hydraulically-induced and pre-existing fractures. SPE/DOE pre-print 10847, Proceedings of the Unconventional Gas Recovery Symposium, Pittsburgh, 559-571.
- Briais, A., Patriat, P., Tapponnier, P., 1993. Updated interpretation of magnetic anomalies and seafloor spreading stages in the South China Sea: implications for the Tertiary tectonics of Southeast Asia. Journal of Geophysical Research 98, 6299 6328.
- Buchanan, P.G., McClay, K.R., 1991. Sandbox experiments of inverted listric and planar fault systems. Tectonophysics 188, 97-115.
- Cartwright, J., 1991. The kinematic evolution of the Coffee Soil Fault. In: Roberts, A.M., Yielding, G., Freeman, B. (Eds.), The Geometry of Normal Faults. Geological Society, London, Special Publication 56, pp. 29-40.

- Childs, C., Easton, S.J., Vendeville, B.C., Jackson, M.P.A., Lin, S.T., Walsh, J.J., Watterson, J., 1993. Kinematics analysis of faults in a physical model of growth faulting above a viscous salt analogue. Tectonophysics 228, 313-329.
- Childs, C., Watterson, J., Walsh, J.J., 1995. Fault overlap zones within developing normal fault systems. Journal of the Geological Society, London, 152, 535-549.
- Childs, C., Nicol, A., Walsh, J.J., Watterson, J., 2003. The growth and propagation of synsedimentary faults. Journal of Structural Geology 25, 633-648.
- Christensen, N.I., 1996. Poisson's ratio and crustal seismology. Journal of Geophysical Research 101, 3139-3156.
- Christie-Blick, N., Biddle, K.T., 1985. Deformation and basin formation along strike-slip faults. In: Biddle, K.T., Christie-Blick, N. (Eds.), Strike-slip deformation, basin formation and sedimentation: SEPM Special Publication 37, pp. 1–34.
- Corfield, S. Sharp, I.R., 2000. Structural style and stratigraphic architecture of fault propagation folding in extensional settings: a seismic example from the Smørbukk area, Halten Terrace, Mid-Norway. Basin Research 12, 329-341.
- Davies, R.J., Turner, J.D., Underhill, J.R., 2001. Sequential dip-slip fault movement during rifting: a new model for the evolution of the Jurassic trilete North Sea rift system. Petroleum Geoscience 7, 371-388.
- Davies, R.J., Posamentier, H.W., 2005. Geologic processes in sedimentary basins inferred from three-dimensional seismic imaging. GSA Today 15, 4-9.
- De Paola, N., Holdsworth, R.E., McCaffrey, K.J.W., 2005a. The influence of lithology and pre-existing structures on reservoir scale faulting patterns in transtensional rift zones. Journal of the Geological Society, London, 162, 1-10.
- De Paola, N., Holdsworth, R.E., McCaffrey, K.J.W., Barchi, M.R., 2005b. Partitioned transtension in the late Carboniferous of Northern Britain a radical alternative to basin inversion models. Journal of Structural Geology 27, 607-625.
- Dewey, J.F., 1975. Finite plate evolution: some implications for the evolution of rock masses at plate margins. American Journal of Science 275A, 260-284.
- Dewey, J.F., Holdsworth, R.E., Strachan, R.A., 1998. Transpression and transtension zones. In: Holdsworth, R.E., Strachan, R.A., Dewey, J.F. (Eds.), Continental Transpressional and Transtensional Tectonics Geological Society, London, Special Publication 135, pp. 1–114.
- Dewey, J.F., 2002. Transtension in arcs and orogens. International Geology Review 44, 402-439.
- Dubois, A., Odonne, F., Massonnat, G., Lebourg, T., Fabre, R., 2002. Analogue modelling of fault reactivation: tectonic inversion and oblique remobilisation of grabens. Journal of Structural Geology 24, 1741-1752.

- Eisenstadt, G., Withjack, M.O., 1995. Estimating inversion: results from clay models. In: Buchanan, J.G., Buchanan, P.G. (Eds.), Basin Inversion. Geological Society, London, Special Publication 88, pp. 119-136.
- Fowler, J.N., Guritno, E., Sherwood, P., Smith, M.J., Algar, S., Busono, I., Goffey, G., Strong, A., 2004. Depositional architectures of Recent deepwater deposits in the Kutei Basin, East Kalimantan. In: Davies, R.J., Cartwright, J.A., Stewart, S.A., Lappin, M., Underhill, J.R. (Eds.), 3D Seismic Technology: Application to the exploration of sedimentary basins. Geological Society, London, Memoirs, 29, 25-33.
- Gawthorpe, R.L. and Hurst, J.M., 1993. Transfer zones in extensional basins: their structural style and influence on drainage development and stratigraphy. Journal of the Geological Society, London, 150, 1137-1152.
- Gawthorpe, R.L., Leeder, M.R., 2000. Tectono-sedimentary evolution of active extensional basins. Basin Research 12, 195-218.
- Hall, R., 1997. Cenozoic plate tectonic reconstructions of SE Asia. In: Fraser, A.J., Matthews, S.J., Murphy, R.W. (Eds.), Petroleum Geology of Southeast Asia. Geological Society, London, Special Publication 126, pp. 11-23.
- Haq, B.U., Hardenbol, J. & Vail, P.R., 1988. Mesozoic and Cenozoic chronostratigraphy and cycles of sea level change. In: Wilgus, C.K., Hastings, B.S., St C. Kendall, C.G., Posamentier, H.W., Ross C.A., and Van Wagoner, J.C., (Eds.), Sea-level Changes: an integrated approach. Spec. Publ. Soc. Econ. Paleont. Miner., 42, Tulsa.
- Harding, T.P., 1990. Identification of wrench faults using subsurface structural data: criteria and pitfalls. AAPG Bulletin 74, 1590-1609.
- Hardman, R.F.P., Booth, J.E., 1991. The significance of normal faults in the exploration and production of North Sea hydrocarbons. In: Roberts, A.M., Yielding, G., Freeman, B. (Eds.), The Geometry of Normal Faults. Geological Society, London, Special Publication 56, pp. 1-13.
- Hardy, S., McClay, K.,1999. Kinematic modelling of extensional fault-propagation folding. Journal of Structural Geology 21, 695-702.
- Holdsworth, R.E., Butler, C.A., Roberts, A.M., 1997. The recognition of reactivation during continental deformation. Journal of the Geological Society, London, 154, 73-78.
- Huchon, P., Nguyen, T.N.H., Chamot-Rooke, N., 1998. Finite extension across the South Vietnam basins from 3D gravimetric modelling: relation to South China Sea kinematics. Marine and Petroleum Geology 15, 619-634.
- Imber, J, Holdsworth, R.E., McCaffrey, K.J.W., Wilson, R.W., Jones, R.R., England, R.W., Gjeldvik, G. Early Tertiary sinistral transpression and fault reactivation in

- the western Vøring Basin, Norwegian Sea: Implications for hydrocarbon exploration and pre-breakup deformation in ocean margin basins. AAPG Bulletin 89, 1043-1069.
- Imber, J., Tuckwell, G.W., Childs, C., Walsh, J.J., Manzocchi, T., Heath A.E., Bonson, C.G., Strand, J., 2004. Three-dimensional distinct element modelling of relay growth and breaching along normal faults. Journal of Structural Geology 26, 1897-1911.
- Jackson, C.A.L., Gawthorpe, R.L., Sharp, I.R., 2006. Style and sequence of deformation during extensional fault-propagation folding: examples from the Hammam Faraun and El-Qaa fault blocks, Suez Rift, Egypt. Journal of Structural Geology 28, 519-535.
- Johnston, J.E., Christensen, N.I., 1992. Shear wave reflectivity, anisotropies, Poisson's ratios and densities of a southern Appalachian Palaeozoic sedimentary sequence. Tectonophysics 210, 1-20.
- Krantz, R.W., 1988. Multiple fault sets and three-dimensional strain: theory and application. Journal of Structural Geology 10, 225-237.
- Krantz, R.W., 1989. Orthorhombic fault patterns: The odd axis model and slip vector orientations. Tectonics 8, 483-495.
- Lambiase, J.J., Bosworth, W., 1995. Structural controls on sedimentation in continental rifts. In: Lambiase, J.J. (Ed.), Hydrocarbon Habitat in Rift Basins. Geological Society, London, Special Publication 80, pp. 117–144.
- Lee, G.H., Lee, K., Watkins, J.S., 2001. Geologic evolution of the Cuu Long and Nam Con Son basins, offshore southern Vietnam, South China Sea. AAGP Bulletin 85, 1055–1082.
- Leloup, P.H., Arnaud, N., Lacassin, R., Kienast, J.R., Harrison, T.M., Trong, T.T.P., Replumaz, A., Tapponnier, P., 2001. New constraints on the structure, thermochronology and timing of the Ailao Shan-Red River shear zone, SE Asia. Journal of Geophysical Research 66, 1083-6732.
- Liu, H., Yan, P., Zhang, B., Sun, Y., Zhang, Y., Shu, L., Qiu, X., Guo, L., 2004. Role of the Wan-Na fault system in the western Nansha Islands Southern South China Sea). Journal of Asian Earth Sciences 23, 221-233.
- McClay, K.R., Ellis, P.G., 1987. Geometries of extensional fault systems developed in model experiments. Geology 15, 341-344.
- McClay, K.R., White, M.J., 1995. Analogue modelling of orthogonal and oblique rifting. Marine and Petroleum Geology 12, 137-151.
- Mann, P., Hempton, M.R., Bradley, D.C., Burke, K., 1983. Development of pull-apart basins. Journal of Geology 91, 529-554.

- Marsden, D., 1992. V₀-K method of depth conversion. Geophysics: The Leading Edge of Exploration 11 (8), 53-54.
- Matthews, S.J., Fraser, A.J., Lowe, S., Todd, S.P., Peel, F.J., 1997. Structure, stratigraphy and petroleum geology of the SE Nam Con Son Basin, offshore Vietnam. In: Fraser, A.J., Matthews, S.J., Murphy, R.W. (Eds.), Petroleum Geology of Southeast Asia. Geological Society, London, Special Publication 126, pp. 89–106.
- Mat-Zin, I.C., Swarbrick, R.E., 1997. The tectonic evolution and associated sedimentation history of Sarawak Basin, eastern Malaysia: a guide for future hydrocarbon exploration. In: Fraser, A.J., Matthews, S.J., Murphy, R.W. (Eds.), Petroleum Geology of Southeast Asia. Geological Society, London, Special Publication 126, pp. 237–245.
- McCoss, A.M. 1986. Simple constructions for deformation in transpression/transtension zones. Journal of Structural Geology 8, 715-718.
- Metcalfe, I., 1996. Pre-Cretaceous evolution of SE Asian terranes. In: Hall, R., Blundell, D.J. (Eds.), Tectonic Evolution of SE Asia. Geological Society, London, Special Publication 106, pp. 97-122.
- Meyer, V., Nicol, A., Childs, C., Walsh, J.J., Watterson, J., 2002. Progressive localisation of strain during the evolution of a normal fault population. Journal of Structural Geology 24, 1215-1231.
- Michael, A.J., 1984. Determination of stress from slip data: faults and folds. Journal of Geophysical Research 89, 11517-11526.
- Morley, C.K., 1999. How successful are analogue models in addressing the influence of pre-existing fabrics on rift structure?. Journal of Structural Geology 21, 1267-1274.
- Morley, C.K., 2002. A tectonic model for the Tertiary evolution of strike-slip faults and rift basins in SE Asia. Tectonophysics 347, 189-215.
- Morley, C.K., Haranya, C., Phoosongsee, W., Pongwapee, S., Kornsawan, A., Wonganan, N., 2004. Activation of rift oblique and rift parallel pre-existing fabrics during extension and their effect on deformation style: examples from the rifts of Thailand. Journal of Structural Geology 26, 1803-1829.
- Nicol, A., Watterson, J., Walsh, J.J., Childs, C., 1996. The shapes, major axis orientations and displacement patterns of fault surfaces. Journal of Structural Geology 18, 235–248.
- Nicol, A., Walsh, J.J., Watterson, J., Underhill, J.R., 1997. Displacement rates of normal faults. Nature 390, 157-159.
- Nicol, A., 2008. Personal communication.

- Peacock, D.C.P., Sanderson, D.J., 1991. Displacements, segment linkage and relay ramps in normal fault zones. Journal of Structural Geology 13, 721-733.
- Peterson, K., Clausen, O.R., Korstgard, J.A., 1992. Evolution of a salt-related listric growth fault near the D-1 well, block 5605, Danish North Sea: displacement history and salt kinematics. Journal of Structural Geology 14, 565-577.
- Prosser, S., 1993. Rift-related linked depositional systems and their seismic expression. In: Williams, G.D., Dobb, A., (Eds.), Tectonics and Seismic Sequence Stratigraphy, Geological Society, London, Special Publication 71, pp. 35-66.
- Ramsay, J., 1967. Folding and fracturing of rocks. McGraw-Hill.
- Ramsay, J.G., Huber, M.I. 1983. The Techniques of Modern Structural Geology. Academic Press Ltd (London).
- Rangin, C., Van Trong, L., Klein, M., Roques, D., Le Pichon, X., 1995. The Red River fault system in the Tonkin Gulf, Vietnam. Tectonophysics 243, 209–222.
- Reches, Z., 1978. Analysis of faulting in three-dimensional strain field. Tectonophysics 47, 109-129.
- Reches, Z., 1983. Faulting of rocks in three-dimensional strain fields II. Theoretical analysis. Tectonophysics 95, 111-132.
- Reches, Z., Dieterich, J.H., 1983. Faulting of rocks in three-dimensional strain fields I. Failure of rocks in polyaxial, servo-control experiments. Tectonophysics 95, 111-132.
- Reinecker, J., Heidbach, O., Tingay, M., Sperner, B. & Müller, B., 2005. The release 2005 of the World Stress Map (available online at www.world-stress-map.org)
- Roques, D., Matthews, S.J., Rangin, C., 1997. Constraints on strike-slip motion from seismic and gravity data along the Vietnam margin offshore Da Nang: implications for hydrocarbon prospectivity and opening of the East Vietnam Sea. In: Hall, R., Blundell, D.J. (Eds.), Tectonic Evolution of SE Asia. Geological Society, London, Special Publication 106, pp. 341-353.
- Rosendahl, D.J., Reynolds, P.M., Lorber, C.F., Burgess, C.F., McGill, J., Scott, D., Lambiase, J.J., Derksen, S.J., 1986. Structural expressions of rifting: lessons from Lake Tanganyika, Africa. In: Frostick, L.E. (Ed.), Sedimentation in the African Rifts. Geological Society, London, Special Publication 25, pp. 29–43.
- Sanderson, D.J., Marchini, W.R.D., 1984. Transpression. Journal of Structural Geology 6, 449-458.
- Schlische, R.W., 1995. Geometry and origin of fault related folds in extensional settings. AAPG Bulletin 79, 1661-1678.

- Schlische, R.W., Young, S.S., Ackermann, R.V., Gupta, A., 1996. Geometry and scaling relations of a population of very small rift related normal faults. Geology, 24, 683-686.
- Schlische, R. W., Withjack, M.O., Eisenstadt, G., 2002. An experimental study of the secondary deformation produced by oblique-slip normal faulting. AAPG Bulletin 86, 885-906.
- Smith, J.V., Durney, D.W., 1992. Experimental formation of brittle structural assemblages in oblique divergence. Tectonophysics 216, 235-253.
- Smith, W.H.F., Sandwell, D.T., 1997. Global sea floor topography from satellite altimetry and ship depth soundings. Science 26, 1956-1962.
- Suppe, J., Sàbat, F., Muñoz, J.A., Poblet, J., Roca, E., Vergés, J., 1997. Bed-by-bed fold growth by kink-band migration: Sant Llorenç de Morunys, eastern Pyrenees. Journal of Structural Geology 19, 443-461.
- Tapponnier, P., Peltzer, G., Armijo, R., 1986. On the mechanism of collision between India and Asia. In: Coward, M.P., Ries, A.C. (Eds.), Collision Tectonics. Geological Society, London, Special Publication 19, pp. 115–157.
- Tjia, H.D., Liew, K.K. 1996. Changes in tectonic stress field in northern Sunda Shelf basins. In: Hall, R., Blundell, D. (Eds.), Tectonic Evolution of Southeast Asia. Geological Society, London, Special Publication 106, 291-306.
- Tin, N.T., Nguyen, D.T., Luu, T.H., 1994. Nam Con Son Basin. AAPG Bulletin 78, 1166.
- Twiss, R.J., Moores, E.M., 1992. Structural Geology. W.H. Freeman & Co., New York. 292-313.
- Venkat-Ramani, M.V., Tikoff, B., 2002. Physical models of transtensional folding. Geology 30, 523-526.
- Vietnam Licence Team, 1995. Well Evaluation: 05.2-KCT-1X & 05.2-KCT-1X ST1. BP Internal report EXT70287.
- Waldron, J.W.F. 2005. Extensional fault arrays in strike-slip and transtension. Journal of Structural Geology, 27, 23-34.
- Walsh, J.J., Watterson, J., 1988. Analysis of the relationship between displacements and dimensions of faults. Journal of structural geology, 10, 239-247.
- Walsh, J.J., Watterson, J., 1989. Displacement gradients on fault surfaces. Journal of Structural Geology 11, 307–316.
- Walsh, J.J., Watterson, J., 1991. Geometric and kinematic coherence and scale effects in normal fault systems. In: Roberts, A.M., Yielding, G., Freeman, B. (Eds.), The

- Geometry of Normal Faults. Geological Society, London, Special Publication 56, 193-203.
- Walsh, J.J., Watterson, J., Yielding, G. 1991. The importance of small-scale faulting in regional extension. Nature 351, 391-393.
- Walsh, J.J., Nicol, A., Childs, C., 2002. An alternative model for the growth of faults. Journal of Structural Geology 24, 1669–1675.
- Walsh, J.J., Childs, C., Imber, J., Manzocchi, T., Watterson, J., Nell, P.A.R., 2003. Strain localisation and population changes during fault system growth within the Inner Moray Firth, Northern North Sea. Journal of Structural Geology 25, 307-315.
- Watterson, J., 1986. Fault dimensions, displacements and growth. Pure and Applied Geophysics 124, 365–373.
- Williams, G.A., Turner, J.P., Holford, S.P. 2005. Inversion of the St. George's Channel basin, offshore Wales, UK. Journal of the Geological Society of London, 162, 97-111.
- Wilson, R.W., McCaffrey, K.J.W., Holdsworth, R.E., Imber, J., Jones, R.R., Welbon, A.I.F., Roberts, D., 2006. Complex fault patterns, transtension and structural segmentation of the Lofoten Ridge, Norwegian margin: Using digital mapping to link onshore and offshore geology. Tectonics 25.
- Withjack, M.O., Jamison, W.R., 1986. Deformation produced by oblique rifting. Tectonophysics 126, 99-124.
- Withjack, M.O., Olson, J., Peterson, E., 1990. Experimental models of extensional forced folds. AAPG Bulletin 74, 1038-1054.
- Woodcock, N.H., 1986. The role of strike-slip fault systems at plate boundaries. Philosophical Transaction of the Royal Society of London A317, 13-29.
- Woodcock, N.H., Schubert, C., 1994. Continental strike-slip tectonics. In: Hancock, P.L. (Ed.), Continental Deformation. Pergamon Press, Oxford.
- Yielding, G., Freeman, B., Needham, D.T., 1997. Quantitative fault seal prediction. AAPG Bulletin 81, 897-917.



